Millimeter-Wave Massive MIMO Communications with Restricted Architectures: Harness More with Less

A THESIS

SUBMITTED TO THE FACULTY OF THE GRADUATE SCHOOL

OF THE UNIVERSITY OF MINNESOTA

BY

Shijian Gao

IN PARTIAL FULFILLMENT OF THE REQUIREMENTS

FOR THE DEGREE OF

Doctor of Philosophy

Professor Georgios B. Giannakis, Advisor

April, 2022

© Shijian Gao 2022

ALL RIGHTS RESERVED

Acknowledgements

While the world is severely hit by Covid and hazed by war, I have also gone through a bumpy adventure. There were a few comments I was preparing to terminate the journey because of weary passion and strong diffidence. Completing exploration means a lot to me and would be mission impossible without the generous support offered by my respectful advisor Prof. Georgios B. Giannakis. I feel incredibly blessed to have such a seemingly impossible but somehow destined encounter. His overwhelming passion, penetrating insights, valuable suggestions, meticulous attitude, and transparent style will be my lifetime treasure to learn and follow.

I am also deeply indebted to Prof. Liuqing Yang, who guided me to into the research territory. I still remember how much effort she had put into polishing our first paper and how many comments she proposed to sharpen my presentation skills. Her encouragement and support are tremendous and critical to shaping me into an independent researcher. In this way, Prof. Xiang Cheng also instilled much time in supervision and collaboration. His diligence and enthusiasm demonstrate what a great scholar should be. Thank to their help, a raw idea can ultimately be turned into a publishable paper.

From Colorado to Minnesota, I have assembled three sets of dissertation committees. These committee members are Prof. Mingyi Hong, Prof. Jarvis Haupt, Prof. Demoz Gebre-Egziabher, Prof. Edwin Chong, Prof. Rockey Luo, Prof. Haonan Wang, and Prof. David Du, and Prof. Murti Salapaka. I am grateful for their precious time serving on my committee. Many comments raised by them have elevated the quality of this thesis.

It is my great privilege to work with so many wonderful SCANers and SPiNCOMer, including Prof. Rongqing Zhang, Prof. Xin Fang, Prof. Kesheng Zhang, Dr. Dexin Wang, Dr. Luoyang Fang, Dr. Yupeng Li, Dr. Hongfei Sun, Dr. Qin Lu, Dr. Jia Yan, Dr. Panagiotis Traganitis, Dr. Georgios Vasileios Karanikolas, Dr. Manish Singh, Xinhu Zheng, Bingcong Li, Yilang Zhang and Konstantinos Polyzos. Their constant support brightly shines on those gloomy mornings. I would like to deeply thank my manager Dr. Yi Huang and mentor Dr. Gokul Sridharan for offering a fulfilling and memorable internship at Qualcomm. Special thanks have to go to Meng Zhang, Yajun Fan, Kun Yuan, and Jinpeng Li for research collaboration and my wonderful friends Dr. Xiaofeng Ma, Jiefeng Sun, Bowen Li, and Xiaosong Shi for their generous encouragement and wishes.

Last but not least, I must extend heartfelt gratitude to my family, especially my wonderful parents, for their unconditional love. My sincerest condolence goes to my eldest uncle, who was among the many Covid victims in early 2020. So many force majeure factors inhibit me from saying goodbye to him, but his love and personality will always remain in my deepest heart.

Abstract

Communication at millimeter-wave (mmWave) frequencies (ranging from $30 \sim 300$ GHz) has been unanimously recognized as the essential remedy for addressing the current cellular spectrum bottleneck. The exploration of this uncharted band commenced by the lower end (28GHz) and now taps into the higher (60GHz) or even sub-Terahertz (100GHz) bands, making mmWave communication a powerful pillar in future wireless networks. Unlike the precedent generations deploying digital transceivers, the fifth-generation (5G) mmWave networks adopt the so-called restricted (*hybrid* or *low-bit*) architecture to alleviate power requirements and overall cost. Aside from hardware limitations, the unique channel propagation environment and remarkably augmented signal dimension necessitate a paradigm-shifting design. To this end, the research investigation in this thesis deals with physical-layer mmWave communications with restricted massive multiple-input multiple-output (mMIMO) structures.

The overarching goal throughout the technical design is to **harness more** (*namely improved error performance and higher spectrum efficiency*) **with less** (*that is, fewer pilot symbols and lower computational complexity*). The major efforts toward this target can be summarized as: i) development of a new-domain index modulation to break the restriction of multiplexing gain in narrowband hybrid systems; ii) a precoded index modulation scheme to boost spectrum efficiency in wideband hybrid systems; iii) design of a doubly-selective channel estimator leveraging the channel's double sparsity, iv) a generic wideband multi-user transceiver following hybrid block diagonalization framework; v) a model-enhanced learning-based detector to address the uplink access issue for 1-bit systems; and vi) a vector-based constellation generator to facilitate downlink multi-casting for 1-bit systems. The relevant findings and outcomes contribute to the fundamental research and practical deployment of mmWave communications.

Contents

List of Tables

List of Figures

Chapter 1

Introduction

1.1 Context and motivation

Since the first-generation wireless system launched in the early 1980s, cellular technologies have been undergoing an upgrade almost every decade [5]. From the primitive analog radio to today's entirely digital signal, and from the very basic voice telephony to today's high-definition mobile TV, claiming the evolution in the telecommunication sector to be "earth-shaking" is no exaggeration. Heading into the third decade of the 21st century, the fifth-generation (5G) wireless communication network has been poised for worldwide standardization and deployment. According to the blueprint regulated by the International Mobile Telecommunications 2020 (IMT-2020), three disruptive application domains, namely *enhanced mobile broadband* (eMBB), *massive machine-type communications* (mMTCs) and ultra-reliable low-latency communications (uRLLCs) have been rolling out in the 5G era [6]. Some key 5G capabilities include 20 Gbps peak data rate, 0.1 Gbps user experienced data rate, 1 ms end-to-end latency, supporting 500 km/h mobility, 1 million devices/Km^2 connection density, 10 Mbps/m^2 area traffic capacity, 3 times spectrum efficiency, and 100 times energy efficiency compared to fourth-generation long-term-evolution (4G-LTE) [7].

Such powerful 5G indicators breed numerous exciting applications, including augmented

reality, autonomous driving, and smart cities, which were technically incapable of being delivered by the peak data rate of around 100Mbps and latency up to dozens of ms in the 4G-LTE era. For all the 5G predecessors, their operating bands reside in the congested sub-6GHz microwave spectrum. Even more serious is that many frequency bands have been regulated for dedicated use. The outstanding spectrum bottleneck renders 4G-LTE incapable of supporting data-intensive and delay-sensitive applications, motivating the exploration of mmWave frequencies. Thanks to the maturity of semiconductor fabrication, deploying mmWave cellular has become practically feasible. Meanwhile, a concerted effort from multiple international organizations, including ECMA, IEEE 802.15.3 Task Group 3c, IEEE 802.11ad standardization task group, and the Wireless Gigabit Alliance, has also sped up the mmWave standardization [8]. Convincing evidence of mmWave's popularity is that major economic entities have basically finalized the spectrum planning for commercial use[1] .

Since the wavelengths are curtailed by magnitude at mmWave compared to the sub-6GHz microwave frequencies, diffraction and material penetration will incur more significant attenuation. Furthermore, the various resonances of oxygen and other gasses in the air also lead to pronounced signal absorption in the atmosphere [9]. For these reasons, mmWave has long been recognized as unsuitable for long-range transmission. Fortunately, mmWave's inherent short wavelength makes it a perfect companion for the massive multiple-input multiple-output (MIMO) technique [10]. The resulting diversity and multiplexing gain can be remarkable, helping mmWave overcome severe path loss and fulfill reliable communication. In principle, shifting to the higher mmWave band should not alter the digital baseband processing. However, many implementing concerns, such as power consumption and hardware expenditure, prohibit mmWave systems from inheriting fully-digital transceivers. In contrast, two economic yet restricted (*hybrid* [11] and *one-bit* [12]) structures come into practical use. In conjunction with

[1] Potential readers can refer to https://www.qualcomm.com/media/documents/files/spectrum-for-4g-and-5g.pdf for more details about mmWave spectrum regulation and deployment.

significantly augmented signal dimensions and complicated channel environments, it is imperative to investigate a paradigm-shifting design to accommodate the restricted mmWave structures.

Actually, mmWave technologies, embracing hybrid structures, have been a hot research area for nearly a decade. Some representative works include hybrid precoding [10], channel estimation [13], beam tracking [14], codebook design [15] and channel modeling[16]. Among these fruitful results, we find that existing works still exhibit three major limitations:

- *Limited expanding capacity based on the restricted structure.*
- *Lack of coherent treatment for the wideband multi-user setup.*
- *No dedicated strategy to combat potential time variation.*

This thesis will showcase a series of promising mmWave massive MIMO (mMIMO) techniques, with an emphasis on the physical layer to harness more with less. We anticipate the relevant results will partially mitigate the existing research deficiencies and contribute to mmWave cellular communication and networking.

1.2 Thesis Organization

The main body of this thesis comprises six chapters. For clarity, we visualize the organization in Fig.1.1 and summarize what **more** has been harnessed with **less**.

Specifically, the central theme of Chapter 2 is an advanced index modulation named generalized beamspace modulation (GBM) for a narrowband hybrid mmWave system. The key idea behind GBM is to project the spatial channel into a sub-beamspace via the existing hardware structure, and subsequently place an index mapper to activate the very few selected high-quality beams for bit embedding. By doing so, the resultant multiplexing gain can break the limit of radio-frequency (RF) chains without sacrificing power gains.

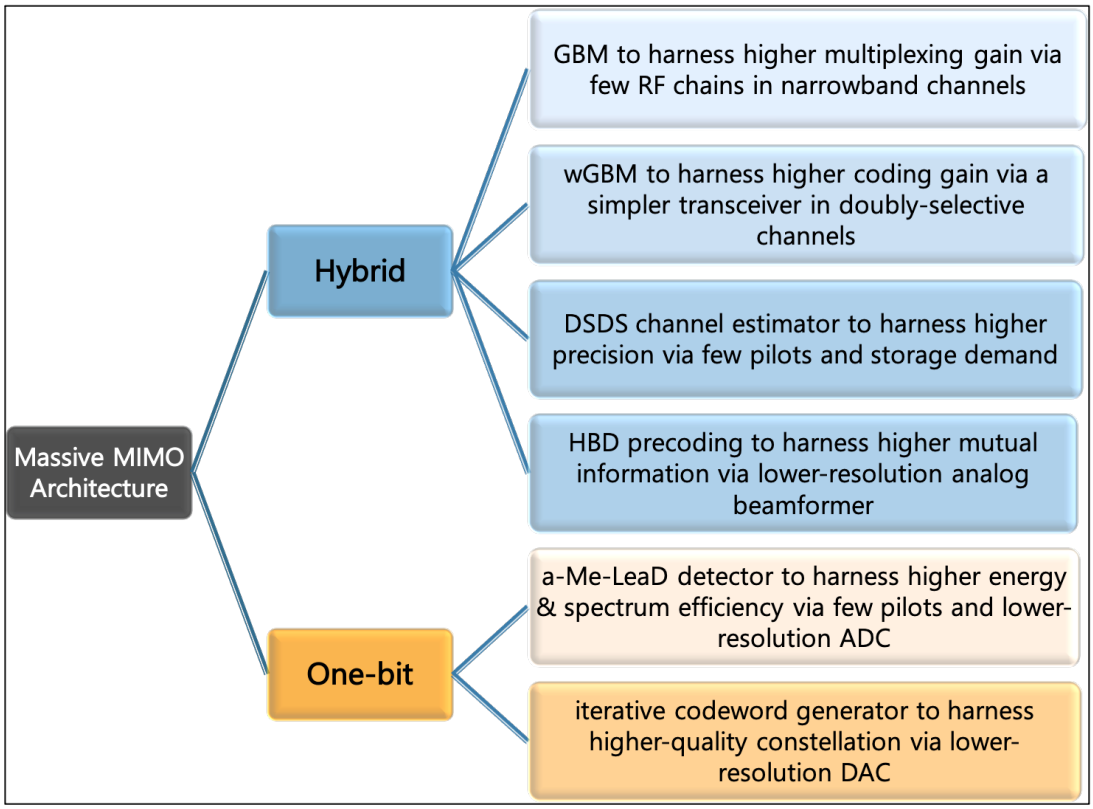

Figure 1.1: The hierarchical map of the thesis organization.

Building upon Chapter 2, Chapter 3 contributes a novel symbol-based modulation mechanism to extend GBM from narrowband to wideband channels. The developed wideband GBM (wGBM) retains all benefits of GBM while ensuring compatibility with the hybrid structure employing orthogonal frequency division multiplexing (OFDM). Aside from a general mapping and decoding design, wGBM is further refined via Doppler compensation at the receiver to combat time selectivity, along with a diagonal precoder at the transmitter to boost coding gain.

As accurate channel state information (CSI) is indispensable for GBM related designs, Chapter 4 henceforth develops a doubly-sparse doubly-selective (DSDS) channel estimator for hybrid systems. The overarching goal is to reduce the training overhead and storage demand by leveraging the channel's sparsity in the beamspace and delay domains. Specifically, with

the first-stage random probing, energy detection is applied to facilitate tap identification, and a compressive sensing algorithm is customized for the subsequent beam determination. Steerable probing then follows to estimate beam amplitudes and the associated Doppler shift accurately. The simple yet effective channel estimator outperforms existing counterparts by a large margin.

Chapter 5 deals with a general wideband multi-user setup and aims at an optimal transceiver. The core design adopts the prevalent hybrid block diagonalization (HBD) framework, but with two significant advances made. Firstly, the asymptotic optimality of HBD in terms of mutual information has been rigorously demonstrated. Secondly, both the upper and lower bounds regarding the mutual information have been derived. The obtained transceiver offers an attractive alternative to the available ad hoc designs by maximizing the lower bound. In addition, it remains applicable to inferior mmWave channel conditions and analog configurations.

Leaping from the more popular hybrid structure, Chapter 6 concentrates on the uplink access for ultra-simplified 1-bit structures. As the system suffers from severe non-linearity and the absence of CSI, a model-enhanced learning-based detector (Me-LeaD) is introduced by transforming detection into a classification problem. Moreover, the unveiled delay-domain information is tactfully incorporated into the learning network to guarantee a light overhead. The angular information is further introduced for dimension reduction via beam projection.

Still, in the context of a 1-bit structure, Chapter 7 switches the gear to downlink, and explores a pertinent multi-cast setting. As the 1-bit quantization prevents the use of the classic *one-vector-make-all* strategy, an iterative method is proposed by transforming the constellation design into a series of non-convex sub-problems, aiming to maximize the minimum Euclidean distance. The semi-definite relaxation tool is drawn to secure a decent solution. By utilizing the unique signal structure of the constructed constellation, the detection problem is accordingly formulated as a convex constrained least absolute shrinkage and selection operator (LASSO) [17] problem. In this manner, the achieved error rate is dramatically lower than the conventional linear equalization-based method.

Despite the best effort made over the course of this dissertation, it is prudent to recognize

that a PhD Thesis can only cover a tip of the iceberg of mmWave physical-layer communication. For this reason, Chapter 8 concludes by discussing some open problems and promising directions to inspire future studies.

1.3 Notation

a, $\boldsymbol{a}$ and $\boldsymbol{A}$ represent a scalar, a vector and a matrix, respectively. $\boldsymbol{A}^T(\boldsymbol{A}^{'})$, $\boldsymbol{A}^*(\boldsymbol{A}^H)$ and $\boldsymbol{A}^\dagger$ represent the transpose, the hermitian transpose, and the pseudo-inverse of $\boldsymbol{A}$, respectively. $\boldsymbol{a}[i]$ represents the i-th element of $\boldsymbol{a}$. $\boldsymbol{A}[m,n]$, $\boldsymbol{A}[m,:]$ and $\| \boldsymbol{A} \|_{\mathrm{F}}$ are denoted as the (m,n) entry, the m-th row and the Frobenius norm of $\boldsymbol{A}$. $\mathrm{Tr}(\boldsymbol{A})$ and $\mathrm{diag}(\boldsymbol{A})$ are the trace and the collection of all diagonal elements of $\boldsymbol{A}$. $|\mathcal{A}|$ is the cardinality of set $\mathcal{A}$. $\mathbb{C}_n^k$ denotes the number of k combinations from a given set of n elements. $\boldsymbol{I}_M$ is an $M \times M$ identify matrix. $\boldsymbol{F}_M$ is the M-dimensional discrete Fourier transform (DFT) matrix. $\mathrm{diag}\{\boldsymbol{A}_k\}_{k=1}^K = \mathrm{blkdiag}[\boldsymbol{A}_1, \boldsymbol{A}_2, \cdots, \boldsymbol{A}_K]$. $\lfloor \cdot \rfloor$ and $\lceil \cdot \rceil$ represent the floor and ceiling operation, respectively. $Q(\cdot)$, $\mathbf{I}(\cdot)$, $\mathbb{B}(\cdot)$, $\mathbb{E}(\cdot)$ and $\delta(\cdot)$ represent the Gaussian Q-function, the binary indicating function, the Beta function, the expectation function, and the Dirac function. respectively. $|| \cdot ||_2$ is the l_2-norm, and $| \cdot |$ is the l_1-norm. $\mathcal{U}$ and $\mathcal{CN}$ represent the uniform distribution and circular complex Gaussian distribution, respectively. $\bigotimes$ stands for the convolution operation and $\otimes$ for Kronecker product. $\boldsymbol{a}_I$ and $\boldsymbol{a}_Q$ stand for the real and imaginary parts of $\boldsymbol{a}$, respectively. mod stands for the modulo operation. $\mathrm{sgn(x)}$ is 1 if x is positive or -1 if x is negative.

Chapter 2

Generalized beamspace modulation (GBM) for mmWave massive MIMO

In mmWave mMIMO, the potential multiplexing gain (MG) is fundamentally limited by the minimum number of radio frequency (RF) chains at both ends. To cope with this fundamental limit and further boost the spectral efficiency (SE), there is an urgent need to develop index modulation (IM) techniques suitable for mmWave mMIMO.

As a matter of fact, similar problems have already been investigated in existing centimeter wave (cmWave) MIMO systems, and an effective solution is the generalized spatial modulation (GSM). The main idea of GSM is to convey the so-called index bits by utilizing the activation status of antennas [18, 19, 20, 21], therefore a higher MG can be achieved by activating a subset of RF chains [22, 23, 24]. Although GSM has demonstrated remarkable superiority in cmWave MIMO, it does not directly apply to mmWave mMIMO. First, unlike cmWave MIMO where a digital structure is employed, mmWave mMIMO typically adopts an economic hybrid structure for power consumption and hardware cost concerns [10, 3, 25]. Secondly, different from the typically isotropic environment in cmWave propagation, mmWave channels are well known to exhibit limited scattering [26, 27, 28, 29, 11], thus the highly correlated channels may severely affect the error performance. As a result, a simple transplantation of existing cmWave

IM techniques into mmWave mMIMO is not feasible. Instead, the ultimate solution requires a judicious design by accounting for the unique properties of mmWave mMIMO. To this end, the first step, which is also the top priority, is to seek a proper space where the index mapping can take place. We will first list existing options, and then introduce our proposed approach.

*IM in spatial domain:*A natural implementing space is the spatial domain; that is, the index bits directly determine which antennas are activated. In [30], an antenna-group (AG-) GSM is designed for mmWave MIMO, with transmitter structure shown in Fig. 2.1. Clearly, in mMIMO, directly (de-)activating each and every antenna will incur unbearable complexity, together with a huge number of RF chains. AG-GSM is adapted to hybrid mmWave structures by (de-)activating groups of (as opposed to individual) antennas. However, this approach essentially divides the entire array to a few groups of smaller ones, and will thus suffer from a severe loss of array gain and angle resolution. In addition, as the MG is dictated by the number of groups, there is clearly a tradeoff between the achievable MG and the array gain/angle resolution.

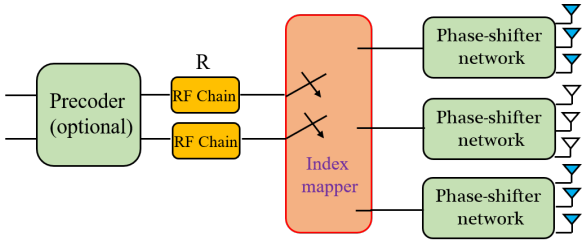

Figure 2.1: The transmitter of mmWave AG-GSM

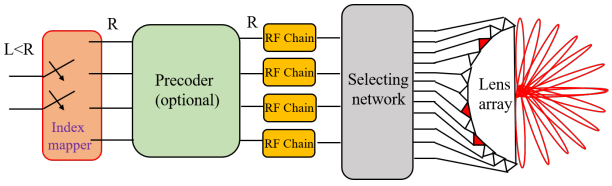

Figure 2.2: The transmitter of mmWave EDC-IM

IM in digital domain: Recall that GSM is essentially a digital technique, thus can be directly

applied to the equivalent digitized channel (EDC) that is encountered before the RF chains at the transmitter (Tx) and after the RF chains at the receiver (Rx). The Tx structure of EDC-IM is shown in Fig. 2.2. Although only a subset of RF chains are activated when performing IM, all antennas are employed for transmission. Hence EDC-IM is not only applicable to hybrid structures, but can also fully exploit the large array gain. However, its maximum MG is clearly limited by the minimum number of RF chains at the transceivers.

In view of the limitations of the abovementioned options, one may have realized that a proper domain has to leverage both the channel properties and the hybrid hardware structures that are unique to mmWave mMIMO. In this work, we innovatively resort to the beamspace, and the index mapping in GBM takes place neither at the antennas as the AG-GSM nor before the RF chains as the EDC-IM. Instead, the index mapping occurs after the RF chains but before the selecting network. Different from both aforementioned options, all RF chains and all antennas at the Tx are always active. As a result, not only that the array gain is fully exploited, but also the achievable MG is no longer restricted by the number of RF chains. The resultant GBM design is also perfectly compatible with prevalent mmWave mMIMO systems.

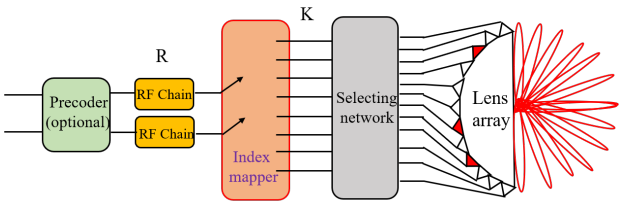

Figure 2.3: The transmitter of mmWave GBM

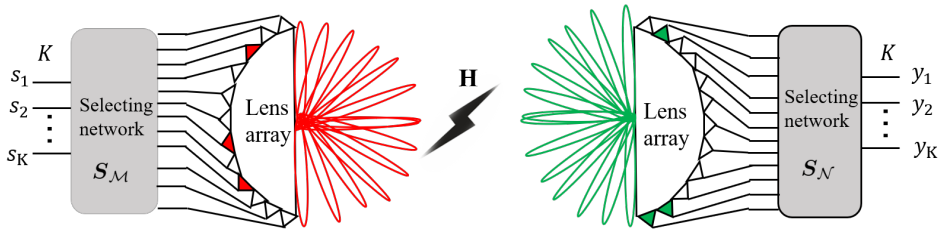

Figure 2.4: The system model of the uplink mmWave beamspace mMIMO

2.1 System and the beamspace

In this chapter, we consider an uplink mmWave mMIMO system, where the mobile station (MS) and the base station (BS) are equipped with lens arrays, each having M and N antennas, respectively. Essentially, an M-dimensional lens array plays the role of an $M \times M$ spatial fast Fourier transform (FFT) matrix, which contains orthogonal steering beams covering the entire beam domain [11]. To alleviate the high power consumption and deployment cost, the numbers of RF chains at both ends are much smaller than that of the antennas.

At the MS, let $\mathcal{M} = \{m_1, m_2, \cdots, m_K\}$ with $K \leq \min(M, N)$ be the set containing the indices of selected beams from the M-dimensional FFT matrix $\boldsymbol{F}_M$. The function of the selecting network (SN) can be described by

$$\boldsymbol{S}_{\mathcal{M}} = [\boldsymbol{e}_M(m_1), \boldsymbol{e}_M(m_2), \cdots, \boldsymbol{e}_M(m_K)] \tag{2.1}$$

where $\boldsymbol{e}_M(m)$ is the m-th column of $\boldsymbol{I}_M$. Let $\boldsymbol{s} = [s_1, s_2, \cdots, s_K]^T$ be the symbol vector to be transmitted from the SN port. After propagation through the $N \times M$ channel $\boldsymbol{H}$, the received signal at the BS is

$$\boldsymbol{r} = \boldsymbol{H}\boldsymbol{F}_M\boldsymbol{S}_{\mathcal{M}}\boldsymbol{s} + \boldsymbol{n} \tag{2.2}$$

where $\boldsymbol{n} \sim \mathcal{CN}(\boldsymbol{0}, \sigma^2\boldsymbol{I}_N)$ is the Gaussian noise vector.

Similar to [31, 32], we consider a narrow-band block fading channel. The propagation environments between the MS and the BS are modeled as the widely accepted geometric channel consisting of P paths[1] . With uniform linear array (ULA) antennas configured at both ends, the channel matrix is given by

$$\boldsymbol{H} = \sqrt{\frac{MN}{P}} \sum_{p=1}^{P} \alpha_p \boldsymbol{a}_r(\theta_p)\boldsymbol{a}_t^*(\phi_p) \tag{2.3}$$

where $\alpha_p \sim \mathcal{CN}(0, 1)$ is the complex gain of the p-th path; θ_p and ϕ_p represent the corresponding angle of arrival (AoA) and angle of departure (AoD), respectively, both modeled as

[1] Here, each path refers to a cluster of multipath components traveling closely in time and/or spatial domains [33].

uniformly distributed variables on $[0, 2\pi)$; $\boldsymbol{a}_t(\cdot)$ and $\boldsymbol{a}_r(\cdot)$ stand for the transmitting and receiving array responses, respectively. When half-wavelength spaced ULAs are employed at both ends, $\boldsymbol{a}_t(\cdot)$ and $\boldsymbol{a}_r(\cdot)$ can be written as

$$\boldsymbol{a}_t(\phi) = \frac{1}{\sqrt{M}}[1, e^{j\pi \sin\phi}, \cdots, e^{j(M-1)\pi \sin\phi}]^T \tag{2.4a}$$

$$\boldsymbol{a}_r(\theta) = \frac{1}{\sqrt{N}}[1, e^{j\pi \sin\theta}, \cdots, e^{j(N-1)\pi \sin\theta}]^T. \tag{2.4b}$$

At the BS, we define $\mathcal{N} = \{n_1, n_2, \cdots, n_K\}$, which contains the selected indices of the combing beams from the N-dimensional FFT matrix $\boldsymbol{F}_N$. Accordingly, the function of SN at the BS end can be expressed as

$$\boldsymbol{S}_{\mathcal{N}} = [\boldsymbol{e}_N(n_1), \boldsymbol{e}_N(n_2), \cdots, \boldsymbol{e}_N(n_K)]. \tag{2.5}$$

After analog combing, the signal to be detected in the digital baseband is given by

$$\boldsymbol{y} = \boldsymbol{S}_{\mathcal{N}}^* \boldsymbol{F}_N^* \boldsymbol{H} \boldsymbol{F}_M \boldsymbol{S}_{\mathcal{M}} \boldsymbol{s} + \boldsymbol{\xi} \tag{2.6}$$

where $\boldsymbol{\xi} = \boldsymbol{S}_{\mathcal{N}}^* \boldsymbol{F}_N^* \boldsymbol{n} \sim \mathcal{CN}(\boldsymbol{0}, \sigma^2 \boldsymbol{I}_K)$ remains white.

Let us now take a closer look to the effective $N \times M$ channel matrix

$$\overline{\boldsymbol{H}} = \boldsymbol{F}_N^* \boldsymbol{H} \boldsymbol{F}_M. \tag{2.7}$$

Note that the FFT basis is similar to the array responses shown in Eqs. (2.4a) and (2.4b). Therefore, $\overline{\boldsymbol{H}}[n, m]$ can be interpreted as the beam "path" coming from $\frac{2\pi(m-1)}{M}$ and arriving at $\frac{2\pi(n-1)}{N}$. From this perspective, $\overline{\boldsymbol{H}}$ essentially captures the channel in the "beamspace."

Proposition 2.1: *The beam with AoA θ_p and AoD ϕ_p is mainly captured by $\overline{\boldsymbol{H}}[n, m]$, with m and n satisfying $\left|\arcsin\left(\frac{\phi_p}{2}\right) - \frac{m-1}{M}\right| \leq \frac{1}{M}$ and $\left|\arcsin(\frac{\theta_p}{2}) - \frac{n-1}{N}\right| \leq \frac{1}{N}$, respectively.*

Proof. See Proof of Proposition 2.1. □

To illustrate the capturing effect in beamspace, we randomly generate a channel with three paths, and plot the channel amplitude in the spatial domain and beamspace, respectively. It is clear that each path is localized within a small bin in the beamspace.

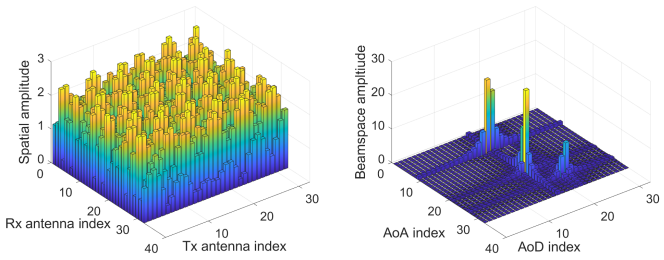

Figure 2.5: The amplitude comparison between the spatial domain and beamspace

Given the $N \times M$ effective beamspace channel matrix $\overline{\boldsymbol{H}}$, one can potentially apply GBM directly therein. It is worth noting that though $\overline{\boldsymbol{H}}$ has the same size as $\boldsymbol{H}$, GBM on $\overline{\boldsymbol{H}}$ is fundamentally different from AG-GSM (see Section I), because GBM implements selection of beams but activate all antennas and thus exploit the full array gain. Even though this is the case, it is not wise to apply GBM directly on $\overline{\boldsymbol{H}}$. With M and N both being large, GBM directly on $\overline{\boldsymbol{H}}$ will incur high complexity and imply a huge number of RF chains. In addition, the resultant MG and error performance will both be compromised due to the sparsity in $\overline{\boldsymbol{H}}$ (see Fig. 2.5) caused by the limited scattering of mmWave mMIMO channels.

To this end, the SN comes as a natural help, and one can obtain the sub-beamspace as follows

$$\overline{\boldsymbol{H}}_K = \boldsymbol{S}_{\mathcal{N}}^{*} \overline{\boldsymbol{H}} \boldsymbol{S}_{\mathcal{M}}. \tag{2.8}$$

The corresponding I/O relationship accordingly becomes

$$\boldsymbol{y} = \overline{\boldsymbol{H}}_K \boldsymbol{s} + \boldsymbol{\xi}. \tag{2.9}$$

Evidently, the system performance heavily relies on $\overline{\boldsymbol{H}}_K$ (SNs), whose optimization will be detailed in Section IV.

At this point, it is worth emphasizing that we are simply describing the practical mmWave transceiver without any alteration, except for revealing that the lens arrays naturally project the spatial domain to the beamspace and the SNs naturally facilitate the dimensional reduction and

beam selection. Next, we are going to introduce GBM that is judiciously designed for the (sub-)beamspace. As will be seen next, GBM will facilitate the multiplexing in ready-for-deployment mmWave systems under limited number of RF chains.

2.2 The digital part of GBM

In this section, we will focus on the digital part of GBM. The modulation along with the pattern selection is first introduced, followed by the demodulation design.

2.2.1 The GBM Modulator

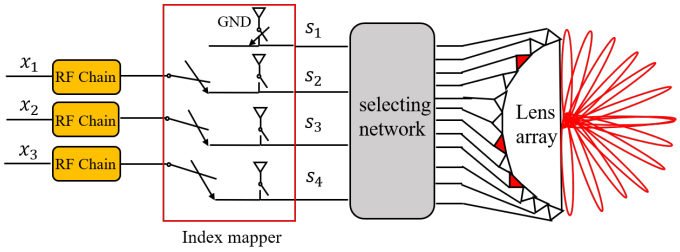

Figure 2.6: An illustration of GBM modulator.

The prototype of GBM modulator is shown in Fig. 2.6. With $R \leq K$ RF chains at Tx, there are $\eta = R\log_2 X + \lfloor \log_2(\mathbb{C}_K^R \rfloor$ incoming bits every transmission, with $R\log_2 X$ symbol bits and $\lfloor \log_2(\mathbb{C}_K^R) \rfloor$ index bits. The symbol bits are modulated into a symbol vector $\boldsymbol{x} = [x_1, \cdots, x_R]^T$, whose elements are chosen from $\mathcal{S}$, e.g., the constellation of an X-ary phase shift keying/quadrature amplitude (PSK/QAM) modulation. In this chapter, $\mathcal{S}$ is assumed to be normalized, so the signal-to-noise ratio (SNR) per bit is defined as $E_b/N_0 = R/(\eta\sigma^2)$.

Evidently, one only needs $R \leq K$ RF chains to transmit these R PSK/QAM symbols. However, it is worth emphasizing that this reduction in RF chains is not at the price of compromised SE, because the actual transmitted signal $\boldsymbol{s}$ has a higher dimension than $\boldsymbol{x}$. The conversion from $\boldsymbol{x}$ to $\boldsymbol{s}$ is realized by a $K \times R$ index mapping matrix $\boldsymbol{B}_{\mathcal{R}}$. Let $\mathcal{R}$ be a length-R lexicographical

sequence, whose elements range from $[1, K]$ and are sorted in an ascending order, then $\boldsymbol{B}_{\mathcal{R}}$ is constructed as follows:

- $\forall n \notin \mathcal{R}$, $\boldsymbol{B}_{\mathcal{R}}[n,:] = \mathbf{0}_{1\times R}^{T}$
- $\boldsymbol{B}_{\mathcal{R}}[\mathcal{R},:] = \boldsymbol{I}_R$.

To make it more clear, we take $(K = 4, R = 3)$ as an example. Suppose the 1^{st}, the 2^{nd} and the 4^{th} beams are selected, i.e, $\mathcal{R} = \{1, 2, 4\}$, then $\boldsymbol{s}$ is given by

$$\boldsymbol{s} = \boldsymbol{B}_{\mathcal{R}}\boldsymbol{x} = \begin{bmatrix} 1 & 0 & 0 \\ 0 & 0 & 0 \\ 0 & 1 & 0 \\ 0 & 0 & 1 \end{bmatrix} \begin{bmatrix} x_1 \\ x_2 \\ x_3 \end{bmatrix} = \begin{bmatrix} x_1 \\ 0 \\ x_2 \\ x_3 \end{bmatrix}. \tag{2.10}$$

Each $\boldsymbol{B}_{\mathcal{R}}$ corresponds to a unique $\mathcal{R}$, which essentially represents a specific index pattern. If $\log_2 \mathbb{C}_K^R$ is an integer, all index patterns will be used. However, if $\log_2 \mathbb{C}_K^R$ is not an integer, then $\mathbb{C}_K^R - 2^{\lfloor \log_2 \mathbb{C}_K^R \rfloor}$ index patterns become redundant.

For GSM, these $2^{\lfloor \log_2 \mathbb{C}_K^R \rfloor}$ index patterns are often just arbitrarily selected or lexicographically selected via a look-up table as in [34]. For GBM, K is not entirely a design parameter but is rather dictated by the channel as we will discuss in SectionVI. In addition, the beam quality may vary significantly. Therefore, if there are redundant index patterns, pattern selection is expected to have a non-negligible influence on the overall error performance.

An algorithm is henceforth proposed herein to select the preferred index patterns. The detailed procedure is described as follows

- *Let $\boldsymbol{p}_i$ and $\boldsymbol{p}_j$ represent two index patterns*[2] *, then the pattern distance (PD) between them is defined as $d_{i,j} = |\overline{\boldsymbol{H}}_K(\boldsymbol{p}_i - \boldsymbol{p}_j)|$;*
- *Choose the index combination with the maximal minimal PD (max-MPD), and the corresponding index patterns are recognized as preferred.*

[2] *For a mapping matrix, its corresponding index pattern is the sum of all its columns.*

The total number of index combinations is upper-bounded by $\max\left(\mathbb{C}_K^{\lceil \frac{K}{2} \rceil}, \mathbb{C}_K^{\lfloor \frac{K}{2} \rfloor}\right)$. Since the maximum K is restricted by the low-rank mmWave channels, it is typically very small (typically less than 12 as we will discuss in Section V). Thus the additional complexity involved by the pattern selection is minimal. From simulations in Section VI, we will see that such a simple scheme can bring a noticable performance improvement.

2.2.2 The GBM Demodulator

To meet different implementing requirements, we provide two detectors, namely the ML detector and the ZF-2Q detector.

ML detector

The ML criterion is expressed as

$$\widehat{\boldsymbol{s}} = \underset{\boldsymbol{s} \in \mathcal{G}}{\arg\min} \parallel \boldsymbol{y} - \overline{\boldsymbol{H}}_K \boldsymbol{s} \parallel^2 \tag{2.11}$$

where $\mathcal{G}$ is the ensemble containing all effective GBM vectors. Since the noise samples after RF combining remain uncorrelated, the ML detector can achieve the optimal detection performance. The overall computational complexity in terms of the number of multiplications is $O(2^\eta)$.

ZF-2Q

As a low-complexity alternative to the ML detector, the ZF detector is a popular option. A standard ZF detector consists of two components: i) the linear ZF filter $\overline{\boldsymbol{s}} = \overline{\boldsymbol{H}}_K^\dagger \boldsymbol{y}$; ii) the non-linear vector quantization:

$$\widehat{\boldsymbol{s}} = \underset{\boldsymbol{s} \in \mathcal{G}}{\arg\min} \parallel \overline{\boldsymbol{s}} - \boldsymbol{s} \parallel^2 . \tag{2.12}$$

However, in the context of IM as GBM here, the vector quantization actually induces exponential complexity $O(2^\eta)$, which is identical to ML! To this end, we propose the 2-step quantization (2Q) following the linear ZF filter.

2a: Quantization-I (Per-symbol quantization)

$$\widehat{\boldsymbol{s}}[i] = \arg\min_{s\in\mathcal{S}} |\overline{\boldsymbol{s}}[i] - s|^2. \tag{2.13}$$

2b: Quantization–II (Index pattern quantization)

$$\widehat{\boldsymbol{p}} = \arg\max_{\boldsymbol{p}\in\mathcal{P}} \sum_{i=1}^{K} \big(\mathbf{real}\{\overline{\boldsymbol{s}}[i]^* \times \widehat{\boldsymbol{s}}[i]\} - |\widehat{\boldsymbol{s}}[i]|^2/2\big)\boldsymbol{p}[i] \tag{2.14}$$

where $\mathcal{P}$ contains all preferred index patterns.

Along the lines of Page. 5 (L-C ML detector) in our earlier work [35], it can be readily proved that this 2-step quantization is equivalent to the vector quantization given in Eq. (2.12), but achieves a complexity reduction from $O(2^\eta)$ to $O(C_K^R)$. Plus the complexity of the first-step ZF equalization, the overall computational complexity of ZF-2Q is $O(C_K^R + K^3)$, which has polynomial complexity. It is worth noting that, when all beams are strictly orthogonal as the array size M and N approach infinity, no performance degradation will be incurred by ZF-2Q detector.

2.3 The analog part of GBM

In this section, we concentrate on the analog part of GBM. Via a careful beam selection design, highly reliable communications can be guaranteed by GBM.

2.3.1 Optimizing the size of $\overline{\boldsymbol{H}}_K$

Let $MG_{\rm GBM}$ denote the maximum achievable MG facilitated by mmWave mMIMO beamspace channel $\boldsymbol{H}$. We have the following result:

Proposition 2.2: *In mmWave mMIMO channels modeled as in Eq. 2.3, the maximum achievable MG $MG_{\rm GBM}$ is determined by the number of exclusively resolvable beams (ERBs) sharing no common AoA or AoD.*

Proof. See Proof of Proposition 2.2. □

Clearly, MG_{GBM} is upper bounded by the number of paths (P) in the channel. In conventional MIMO systems, MG_{GBM} is typically regarded as the rank of the channel matrix. The unique beamspace behavior of the mmWave mMIMO channels, together with the sparsity therein lead to Proposition 2.2. Though MG_{GBM} is in general not precisely equal to $rank(\overline{\boldsymbol{H}})$, they remain very close to each other. The difference of these two is induced by the finite beamspace (or angle-domain resolution of the antenna array). Such limited resolution leads to beamspace leakages which may contribute to $rank(\overline{\boldsymbol{H}})$ but does not contribute meaningful MG. As the array size M and N approach infinity, the beam resolution approaches zero and the beam leakage vanishes. In such an extreme case, one will find that both MG_{GBM} and $rank(\overline{\boldsymbol{H}})$ converge to the number of paths P. We further investigate the probability distribution of MG_{GBM} and obtain the following result.

Proposition 2.3: *In a mmWave mMIMO channel with P spatial paths, the maximum achievable MG MG_{GBM} follows a cumulative mass function (CMF) that can be upper bounded by*

$$\begin{aligned}\mathrm{CMF}_{\mathrm{MG}}(p) &\triangleq \Pr(MG_{\mathrm{GBM}} < p) \leq \overline{\mathrm{CMF}}_{\mathrm{MG}}(p) \\ &= \begin{cases} \left(1 - \prod_{i=0}^{p-1}\big(1 - f(i)\big)\right)^{\frac{P}{p}}, \text{if } \textit{mod}(P,p) = 0 \\ \left(1 \prod_{i=0}^{p-1}(1 - f(i))\right)^{\lfloor \frac{P}{p} \rfloor - 1} \left(1 - \prod_{i=0}^{p}(1 - f(i)) \right. \\ \quad \left. - \big(\sum_{i=1}^{p} f(i)\big) \prod_{i=1}^{p}\big(1 - f(i)\big)\right), \text{ o.w.} \end{cases} \end{aligned} \tag{2.15}$$

with $f(i) = \frac{i(M+N-i)}{MN}$.

Proof. See Proof of Proposition 2.3. □

As M and N approach infinity, $\overline{\mathrm{CMF}}_{\mathrm{MG}}(P) \to 0$, implying that $MG_{\mathrm{GBM}} \to P$. In addition, as the size of the array increases, the array resolution approaches zero and thus $rank(H) \to P$ as well. An example of $\overline{\mathrm{CMF}}_{\mathrm{MG}}(p)$ with a finite array size ($M = 32$ and $N = 64$) is presented in Fig. 2.7. Existing measurements show that mmWave channels typically have $8 \sim 12$ dominant paths in "rich" scattering environments [36], so we set $P = 8$, 10 and 12.

Lemma 2.1: The probability that the size of SNs K is no smaller than the maximum achievable MG MG_{GBM} can be lower bounded by

$$\Pr(MG_{\mathrm{GBM}} \leq K) \geq 1 - \overline{\mathrm{CMF}}_{\mathrm{MG}}(K) \tag{2.16}$$

where $\overline{\mathrm{CMF}}_{\mathrm{MG}}(\cdot)$ has been defined in Proposition 2.3.

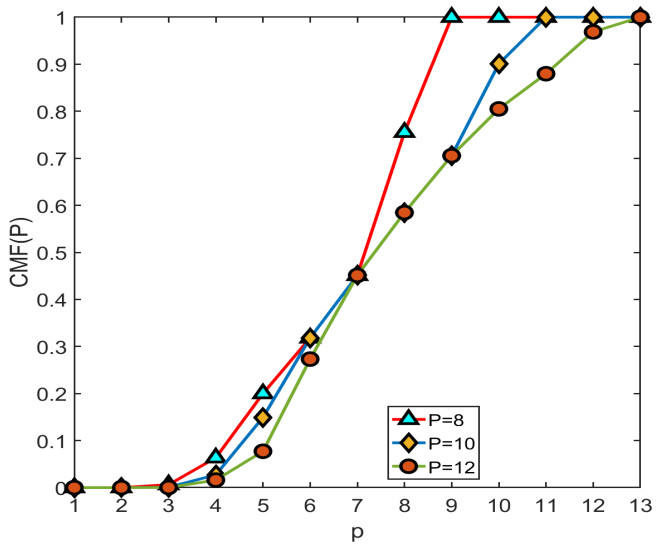

Figure 2.7: The upper-bound $\mathrm{CMF}_{\mathrm{MG}}$ of the achievable MG under different number of paths

Based on Lemma 2.1, one can learn that choosing the size of sub-beamspace channel K too large may lead to $\overline{\boldsymbol{H}}_K$ with insufficient beams to support GBM. Whereas choosing K too small will not fully exploit MG_{GBM} facilitated by the channel. Hence given M, N and P, Eq. (2.15) provides a valuable guidance for choosing the size of SNs.

2.3.2 Optimizing the entries of $\overline{\boldsymbol{H}}_K$

Even with K determined, not all $\overline{\boldsymbol{H}}_K$ candidates can support reliable communications because the beam quality may vary significantly. To optimize the entries of $\overline{\boldsymbol{H}}_K$, the immediate objective is to minimize the bit error rate (BER). Considering that the exact BER expression is

mathematically intractable, we resort to the APEP. We use $\mathrm{P}_{\mathrm{GBM}}(\overline{\boldsymbol{H}}_K)$ to stand for the conditional APEP under $\overline{\boldsymbol{H}}_K$. According to [35], $\mathrm{P}_{\mathrm{GBM}}(\overline{\boldsymbol{H}}_K)$ can be approximated as

$$\mathrm{P}_{\mathrm{GBM}}(\overline{\boldsymbol{H}}_K) \approx \frac{1}{\eta 2^{\eta}} \sum_{\forall \boldsymbol{s}} \sum_{\forall \widehat{\boldsymbol{s}}} Q\left(\sqrt{\frac{d^2(\overline{\boldsymbol{H}}_K, \mathbf{s}, \widehat{\boldsymbol{s}})}{2\sigma^2}}\right) e(\boldsymbol{s}, \widehat{\boldsymbol{s}}) \tag{2.17}$$

where $d(\overline{\boldsymbol{H}}_K, \boldsymbol{s}, \widehat{\boldsymbol{s}}) = \| \overline{\boldsymbol{H}}_K(\boldsymbol{s} - \widehat{\boldsymbol{s}}) \|_{\mathrm{F}}$; $e(\boldsymbol{s}, \widehat{\boldsymbol{s}})$ represents the number of differing bits between $\boldsymbol{s}$ and $\widehat{\boldsymbol{s}}$ after demodulation.

Existing IM-related works have shown IM manifests prominent advantages mainly at high SNR (see, e.g., [19] and [37, 38].) Therefore, we will seek a simplified form of Eq. (2.17) at high SNR. A proposition relating to $\mathrm{P}_{\mathrm{GBM}}(\overline{\boldsymbol{H}}_K)$ is made as follows.

Proposition 2.4: *At high SNR, the conditional APEP $P_{\mathrm{GBM}}(\overline{\boldsymbol{H}}_K)$ can be approximated as a monotonic decreasing function of $d(\overline{\boldsymbol{H}}_K)$, where $d(\overline{\boldsymbol{H}}_K) \triangleq \min\limits_{\forall \widehat{\boldsymbol{s}} \neq \boldsymbol{s}} d(\overline{\boldsymbol{H}}_K, \boldsymbol{s}, \widehat{\boldsymbol{s}})$.*

Proof. See Proof of Proposition 2.4. □

Note that this monotonicity is independent of the SNR, so the original SNR-coupled APEP minimization problem can be simplified to the SNR-independent problem of $d(\overline{\boldsymbol{H}}_K)$ maximization.

Ideally, the maximal $d(\overline{\boldsymbol{H}}_K)$ can be obtained via exhaustive search among all $\mathcal{M}$'s and $\mathcal{N}$'s. However, the computational burden would be badly severe under mMIMO (over 7.8×10^{12} for $M = 64$, $N = 32$ and $K = 4$). For practical implementation, it is necessary to shrink the searching space.

Thanks to the sparsity of $\overline{\boldsymbol{H}}$, a power-based criterion can be used to screen out weak beams:

$$\mathcal{P}_1 = \left\{ (i,j) \middle| \frac{|\overline{\boldsymbol{H}}[i,j]|^2}{\max\limits_{i,j} |\overline{\boldsymbol{H}}[i,j]|^2} \geq \lambda \right\}, \tag{2.18}$$

where λ is a small threshold (e.g., 0.05). Although the cardinality of $\mathcal{P}_1$ is much smaller than MN, further modifications are still required to avoid two extreme cases.

1) The cardinality of $\mathcal{P}_1$ may be too large such that the searching complexity is still unacceptable.

2) The cardinality of $\mathcal{P}_1$ may be too small such that it does not provide K entries for $\overline{\boldsymbol{H}}$.

Case.1 can be addressed via a trimming procedure if the cardinality of $\mathcal{P}_1$ exceeds a certain threshold. For case.2, we can choose the first K largest and exclusive indices from $\overline{\boldsymbol{H}}$, and these selected indices are collected by $\mathcal{B}$.

Proposition 2.5: *Define $\overline{\boldsymbol{H}}(A)$ to be the A-th ($A > K$) largest entry from $\overline{\boldsymbol{H}}$, then the searching space is given by*

$$\mathcal{P} = \begin{cases} \mathcal{P}_1 \bigcup \mathcal{B}; & \mathbf{Cal}(\mathcal{P}_1) \leq A \\ \left\{(i,j) \middle| |\overline{\boldsymbol{H}}[i,j]| \geq \overline{\boldsymbol{H}}(A)\right\} \bigcup \mathcal{B}; & \mathbf{Cal}(\mathcal{P}_1) > A. \end{cases} \tag{2.19}$$

The union of $\mathcal{B}$ in Eq. (2.19) is to guarantee the existence of a searching set. Denote (n_i, m_i) as the index of the i-th selected beam, then the optimal beam indices can be obtained via

$$\left\{(\overline{n}_1, \overline{m}_1), (\overline{n}_2, \overline{m}_2), \cdots, (\overline{n}_K, \overline{m}_K)\right\} = \underset{\forall i,(n_i,m_i)\in\mathcal{P}}{\arg\max}\ d(\overline{\boldsymbol{H}}_K, \overline{\boldsymbol{s}}). \tag{2.20}$$

Replacing $\mathcal{N} = (\overline{n}_1, \overline{n}_2, \cdots, \overline{n}_K)$ and $\mathcal{M} = (\overline{m}_1, \overline{m}_2, \cdots, \overline{m}_K)$ in Eq. (2.8), we can get $\overline{\boldsymbol{H}}_K$.

In summary, the GBM design procedures can be listed as follows:

1: Determine the number of selected beams at the transceiver SNs (K) based on MG_{GBM}.

2: Choose the number of RF chains R at the MS satisfying $R < K$;

3: Select the preferred beams based on the min-APEP criterion;

4: Trim redundant index patterns based on "max-MPD" algorithm; and

5: Choose the ML or ZF-2Q detector.

2.4 Analyses for GBM

To gain a better understanding of GBM and evaluate its performance, extensive analyses and discussions will be provided in this section.

2.4.1 APEP analysis

Due to the uncertainty of the sub-beamspace and the off-grid beam leakage, it is extremely difficult to derive an exact APEP. Here we attempt to derive an APEP bound to evaluate the error performance. As the array size approaches infinity, the actual APEP will also approach the derived bound.

Let $\boldsymbol{\beta} = [\beta_1, \cdots, \beta_K]^T$ with $\beta_i = \frac{P}{MN}\overline{\boldsymbol{H}}_K^2[i,i]$, and neglect the off-grid beam leakage. The pairwise error probability $\mathrm{P}_{\mathrm{GBM}}(\boldsymbol{s}, \widehat{\boldsymbol{s}})$ can be approximated as

$$\begin{aligned}\mathrm{P}_{\mathrm{GBM}}(\boldsymbol{s}, \widehat{\boldsymbol{s}}) &= Q\left(\sqrt{\frac{d^2(\overline{\boldsymbol{H}}_K, \mathbf{s}, \widehat{\boldsymbol{s}})}{2\sigma^2}}\right) \\ &\overset{(a)}{\approx} \mathbb{E}_{\boldsymbol{\beta}}\left\{\frac{1}{12}\exp\left(-\sum_{i=1}^{K} MN\beta_i\Delta s_i^2/4P\sigma^2\right) + \frac{1}{4}\exp\left(-\sum_{i=1}^{K} MN\beta_i\Delta s_i^2/3P\sigma^2\right)\right\}\end{aligned} \tag{2.21}$$

where (a) comes from $Q(x) \simeq \frac{1}{12}e^{-\frac{x^2}{2}} + \frac{1}{4}e^{-\frac{2x^2}{3}}$, which is a tight approximation of $Q(x)$ [39].

Proposition 2.6: *At high SNR, when K beams are selected from a mmWave channel with P paths, the pairwise error probability $\mathrm{P}_{\mathrm{GBM}}(\boldsymbol{s}, \widehat{\boldsymbol{s}})$ can be approximated as*

$$\begin{aligned}\mathrm{P}_{\mathrm{GBM}}(\boldsymbol{s}, \widehat{\boldsymbol{s}}) \simeq\ & \frac{(\mathbb{C}_{P-1}^{P-1-\kappa}P)^K}{12}\prod_{i=1}^{K}\mathbb{B}\left(\frac{MN\Delta s_i^2 E_b\eta}{4PRN_0} + P + 1 - \kappa, \kappa\right) \\ &+ \frac{(\mathbb{C}_{P-1}^{P-1-\kappa}P)^K}{4}\prod_{i=1}^{K}\mathbb{B}\left(\frac{MN\Delta s_i^2 E_b\eta}{3PRN_0} + P + 1 - \kappa, \kappa\right)\end{aligned} \tag{2.22}$$

where κ is the diversity gain ranging from 1 to P. In practice, the selected beams are generally strong, so the actual achieved diversity gain is very unlikely close to the lower-bound. However, the off-grid leakage not only incurs interference but also influences the beam selection, preventing one from achieving the diversity upper-bound. Therefore, we can infer that the actual diversity gain should be moderately high. This will be verified by simulations. In addition, Eq. (2.22) also reveals that the power gain achieved by GBM is MN, which is in fact the full array gain.

2.4.2 SE analysis

With R and K RF chains at the Tx and Rx, respectively, the achievable SE of GBM is

$$\mathcal{C} = \left\{ \lfloor \log_2 C_K^R \rfloor + R \log_2 X \middle| K \leq MG_{\text{GBM}}; R < K \right\}. \tag{2.23}$$

To understand the advantages of GBM over other alternatives, we will next compare their SE peformances. Considering that comparing SE under different setups is somewhat "unfair," we adopt the normalized spectral efficiency (nSE) for comparison, and the nSE is defined as the ratio of the SE and the number of Tx-end RF chains. According to [4], the energy efficiency (EE) is defined as the ratio of the SE and the sum of the transmit power consumption and hardware power consumption. The consumed power is roughly proportional to the number of RF chains, so nSE can roughly imply the EE as well.

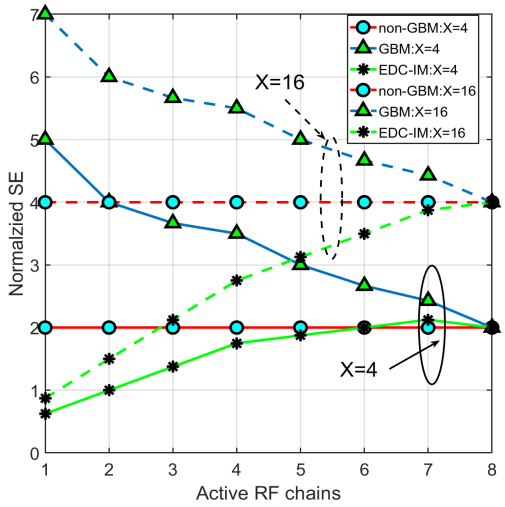

Figure 2.8: The nSE comparisons among GBM, non-GBM and EDC-IM.

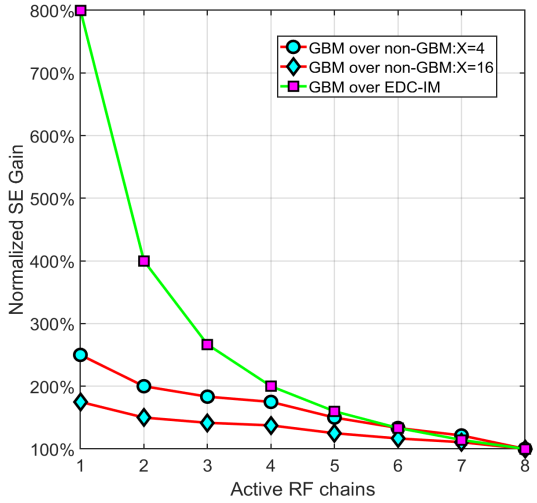

Figure 2.9: The nSE gain of GBM over non-GBM and EDC-IM.

In Fig. 2.8, GBM is compared with the EDC-IM and the non-GBM cases in terms of the nSE. In Fig. 2.9, the nSE gain of GBM over EDC-IM and non-GBM is further presented. For all cases, we adopt two modulation orders: $X = 4$ and $X = 16$, both with $K = 8$. Based on these two figures, we make the following remarks:

- *Using the same RF chains, GBM is always superior over non-GBM in terms of the nSE. This is because GBM can exploit a higher MG.*
- *Under the same MG, GBM is always superior over EDC-IM in terms of the nSE. This is because GBM requires less RF chains at the Tx.*
- *The nSE gain of GBM over non-GBM decreases with the modulation order, while the nSE gain of GBM over EDC-IM is irrelevant to the modulation order.*

2.4.3 GBM Variants

Recall that in Fig. 2.3, the optional precoder is essentially set as $\boldsymbol{I}$ in GBM. In this case, the Tx needs minimal or no CSI. The only information needed are the AoD indices of the selected beams, leading to a lightweight feedback overhead of $K \log_2 M$ (as apposed to MN with full CSI). Nevertheless, GBM can have different variants by altering the precoder or other system parameters.

Spatial scattering modulation (SSM): If only one RF chain is employed at the Tx, GBM is similar to SSM [40]. However, SSM assumes (and works if and only if) there is no leakage among the selected beams, whereas GBM explicitly cope with beam leakage that is inevitable due to the finite array size.

Generalized Eigenspace Modulation (GEM): The precoder in Fig. 2.3 can be configured such that the combined digital precoding and analog SN selection can approximate the (sub-)eigenspace of the channel. By selecting different hybrid precoders in each transmission, GBM subsumes to GEM, which is the mmWave counterpart of the authors' earlier work in [41]. By optimizing the power allocation, GEM can potentially achieve an improved end-to-end mutual information. If the array size approaches infinity, GBM and GEM become identical. However, the GEM variant of the GBM comes at much increased complexity and compromised practicality in that i) frequent transmitter reconfiguration; ii) complicated power allocation and bit loading; and iii) extremely heavy feedback overhead.

Precoded beamspace modulation (PBM): The precoder in Fig. 2.3 can also implement pre-equalization, such as the ZF precoding, to lower the receiver complexity at the cost of increased feedback overhead of CSI.

2.5 Simulations

In this section, extensive simulations are presented for an uncoded mmWave mMIMO system. The size of lens-array is set as $M = 32$ at the MS and $N = 64$ at the BS. Each BER curve is on the average of 20000 independent channel realizations, with a block length of 500 for each. For all figures, we set $P = 12$, $\lambda = 0.05$ and $A = 2P$. Without a specific statement, the receiver adopts ML detector to perform demodulation.

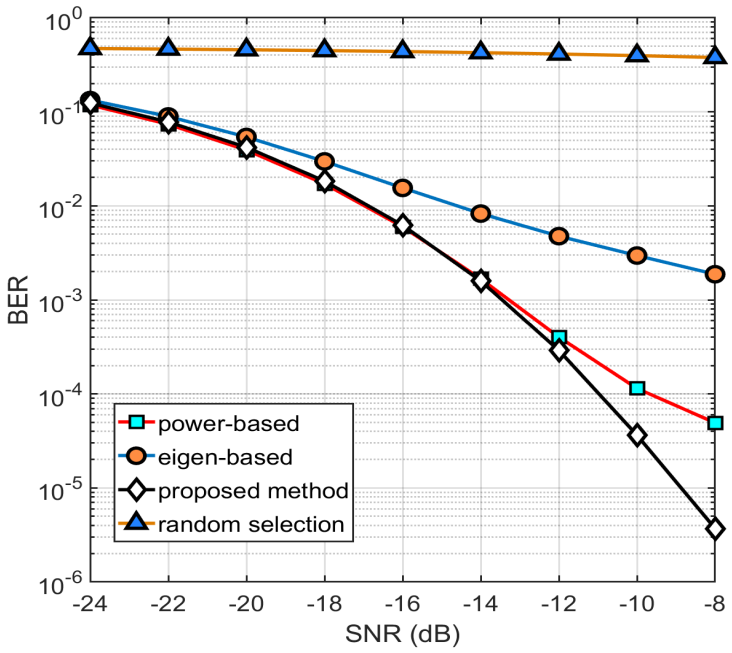

Figure 2.10: BER comparisons among different sub-beamspace construction methods

To understand the critical importance of $\overline{\boldsymbol{H}}_K$, in Fig. 2.10, we compare BER using different $\overline{\boldsymbol{H}}_K$ construction methods for non-GBM with $K = 4$ and BPSK modulation. It is clear to see

that a random construction will result in an unusable system. Another two methods, namely the power-based (PB) method and eigen-based (EB) method are also provided. For PB method, those strongest beams are selected. For EB method, those transmitting/receiving beams best matching the channel left/right singular vectors (EB) will be selected. Our proposed method can achieve an optimal performance at almost whole SNR region, even though the optimality is derived at high SNR.

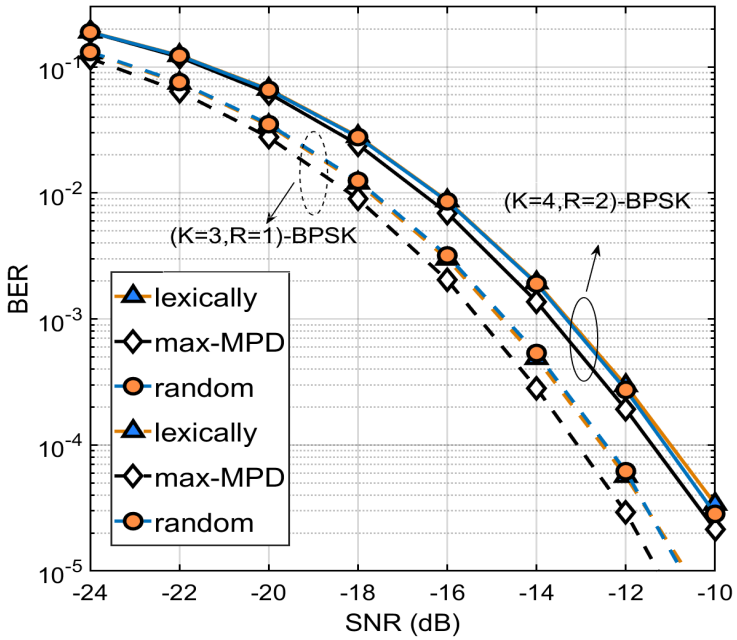

Figure 2.11: BER comparisons for different index pattern selection schemes

In Fig. 2.11, to validate the advantages of the proposed index pattern selection algorithm, we consider two GBM cases with binary phase-shift keying (BPSK) modulation: ($K = 3$, $R = 1$) and ($K = 4$, $R = 2$), both of which have a proportion of $1/3$ redundant patterns. Simulations show that with max-MPD scheme, more than 0.5dB BER advantage can be achieved over the lexicographically sequential selection (LSS) and random selection. Unlike LSS, max-MPD method requires an additional feedback of $\lceil \mathbb{C}_K^R \rceil$ bits to indicate the selected index combination,

but this overhead is obviously negligible. Therefore, our method is an appealing option when index patterns have redundancy.

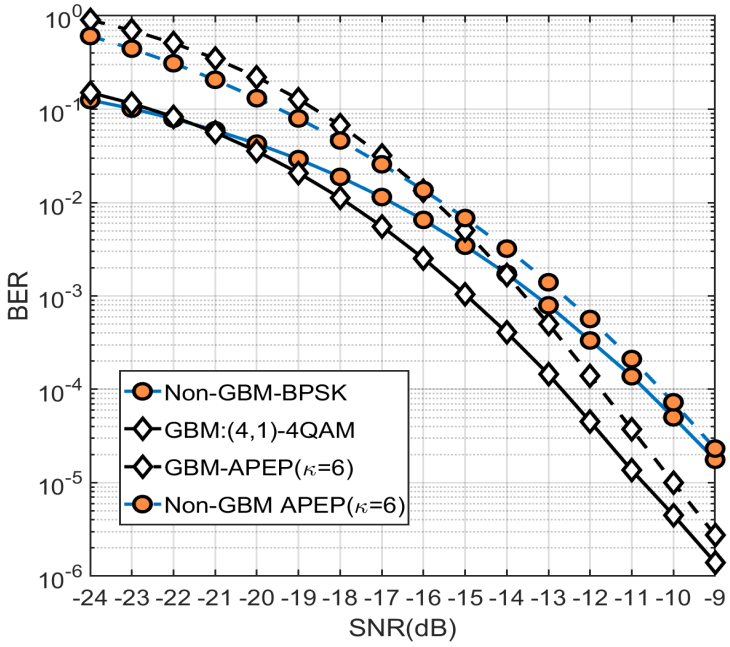

Figure 2.12: BER comparisons between GBM and non-GBM under η=4bits/Hz

In Fig. 2.12, we compare the BER performance of GBM and non-GBM with a spectral efficiency of 4 bits/Hz. For the GBM, we set $(K = 4, R = 1)$ with 4-QAM modulation. To achieve the same spectral efficiency, the non-GBM uses BPSK modulation. With an increase of SNR, the BER advantage of GBM over non-GBM gradually becomes noticeable. At high SNR, the BER advantage is over 2dB. This advantages owe to a large ratio (50%) of index bits, which are more robust compared to the index bits in high SNR region. Furthermore, we observe that the BER curves of GBM and non-GBM can be well described by Eq. (2.22), and the diversity gain of GBM is slightly larger than that of non-GBM. Besides, the actual diversity gain of both systems is about 6 ($1 < 6 < 12$), which is also consistent with our previous analysis.

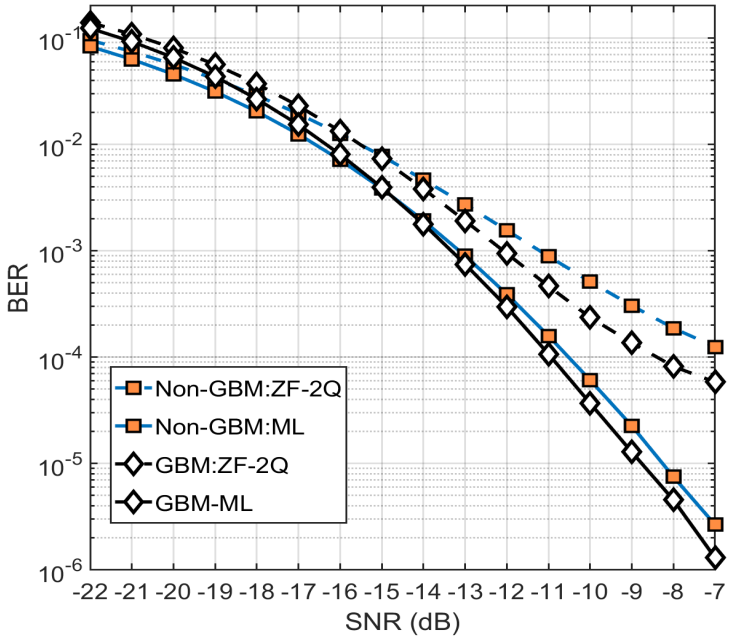

Figure 2.13: BER comparisons between GBM and non-GBM under η=8bits/Hz

Fig. 2.13 shows the BER performance with a higher spectral efficiency by setting $(K = 4, R = 3$, 4-QAM$)$ for GBM. The non-GBM adopts 4-QAM for the same spectral efficiency (8 bits/Hz). At low SNR, GBM is inferior to non-GBM, as the index bits are vulnerable to be wrongly detected. However, GBM soon outperforms non-GBM with a small increase of SNR. Even though the ratio of index bits is only 25%, the BER advantage is still over 0.5dB combined with a 33% nSE enhancement. In addition to the ML detector, the BER performance using ZF-2Q detector is also presented here. Although the detection complexity has been largely reduced, the performance gap compared to the ML detector is also notable. However, when both adopt ZF-2Q detector, we find the advantage of GBM over non-GBM is about 1.5dB. This signifies the GBM can partially compensate the performance loss due to sub-optimal equalizer.

2.6 Concluding Remarks

By exploiting the unique features of mmWave channels and the hybrid transceiver structures, a novel IM design termed as GBM has been judiciously devised for mmWave mMIMO. Under limited RF chains, GBM can achieve improved MG and SE, without compromising the array gain or the compatibility with prevalent mmWave mMIMO systems. Based on the (sub-)beamspace, a complete GBM transceiver is designed and optimized from the digital and analog parts. Extensive theoretical analyses and numerical simulations have demonstrated the remarkable advantages of GBM over non-GBM alternatives in terms of both the BER and SE.

2.7 Proof of Propositions for GBM

2.7.1 Proof of Proposition 2.1

Without loss of generality, we take the p-th path as an example. The 2-D beamforming gain at grid point $[n, m]$ is $\boldsymbol{F}_N^*[:, n]\boldsymbol{a}_r(\theta_p) \times \boldsymbol{a}_t^*(\phi_p)\boldsymbol{F}_M[:, m]$. Due to the symmetry, we consider the left part only, which is calculated as

$$\boldsymbol{a}_t^*(\phi_p)\boldsymbol{F}_M[:, m]=\frac{1}{M}\left|\frac{\sin \pi M\big(\arcsin\big(\frac{\phi_p}{2}\big)-\frac{m-1}{M}\big)}{\sin \pi\big(\arcsin\big(\frac{\phi_p}{2}\big)-\frac{m-1}{M}\big)}\right|. \tag{2.24}$$

The main-lobe of Eq. (2.24) is limited to $\big|\arcsin\big(\frac{\phi_p}{2}\big) - \frac{m-1}{M}\big| \leq \frac{1}{M}$, and the beamforming gain decreases rapidly in large M. Similarly, the main-lobe of the BS-end beamforming gain is limited to $\big|\arcsin\big(\frac{\theta_p}{2}\big) - \frac{n-1}{N}\big| \leq \frac{1}{N}$. Both M and N are quite large in mmWave mMIMO, thus the 2-D beamforming gain at $[m, n]$ tends to be negligible for either $\big|\arcsin\big(\frac{\phi_p}{2}\big) - \frac{m-1}{M}\big| > \frac{1}{M}$ or $\big|\arcsin(\frac{\theta_p}{2}) - \frac{n-1}{N}\big| > \frac{1}{N}$.

2.7.2 Proof of Proposition 2.2

The sufficiency is easy to be verified thus being omitted, so we focus on the necessity only. When less than K exclusive elements exist in beamspace, at least one common column (row)

will be shared by $\boldsymbol{S}_{\mathcal{N}}$ (or $\boldsymbol{S}_{\mathcal{M}}$), leading to two columns (rows) in $\overline{\boldsymbol{H}}_K$ linearly dependent. Therefore, the rank of $\overline{\boldsymbol{H}}_K$ will be smaller than K.

2.7.3 Proof of Proposition 2.3

Let $p(a,b)$ represent the probability that at least b out of $a(b \leq a)$ entries are exclusive, then one can readily get

$$p(m,m) = \prod_{i=0}^{m-1} \left(1 - \frac{i(M+N-i)}{MN}\right).$$

$p(m+1,m)$ includes two cases: all $m+1$ entries are exclusive, and only m entries are exclusive, thus $p(m+1,m)$ is lower-bounded by

$$p(m+1,m) \geq p(m+1,m+1) + \left(\sum_{i=1}^{m} \frac{i(M+N-i)}{MN}\right) \prod_{i=1}^{m} \left(1 - \frac{i(M+N-i)}{MN}\right).$$

If $\lfloor \frac{a}{b} \rfloor = 1$, it is clear that $P(a,b) \geq p(\min(b+1,a),b)$. Thus when $\lfloor \frac{a}{b} \rfloor > 1$, if mod$(a,b) = 0$, one can get $p(a,b) \geq 1 - (1-p(b,b))^{\lfloor \frac{a}{b} \rfloor}$; if mod$(a,b) \neq 0$, one can get $p(a,b) \geq (1-p(b+1,b))(1-p(b,b))^{\lfloor \frac{a}{b} \rfloor - 1}$.

2.7.4 Proof of Proposition 2.4

Let $d(\overline{\boldsymbol{H}}_K) = \min\limits_{\forall \widehat{\boldsymbol{s}} \neq \boldsymbol{s}} d(\overline{\boldsymbol{H}}_K, \boldsymbol{s}, \widehat{\boldsymbol{s}})$. By using the following result in [42] inductively

$$a_1 Q(x_1) + a_2 Q(x_2) \simeq a Q(\min(x_1, x_2))$$

$$\textit{with } a = \begin{cases} a_\mu, \mu = \arg\min\limits_{i=1,2} x_i; \textit{ if } x_1 \neq x_2 \\ 2; \textit{ if } x_1 = x_2 \end{cases}$$

at high SNR, $\mathrm{P}_{\mathrm{GBM}}$ in Eq. (2.17) can be approximated as

$$\mathrm{P}_{\mathrm{GBM}}(\overline{\boldsymbol{H}}_K) \simeq \frac{1}{\eta 2^\eta} Q\big(\sqrt{d(\overline{\boldsymbol{H}}_K)/2\sigma^2}\big)\mathcal{C}$$

where $\mathcal{C} = \sum\limits_{\forall \boldsymbol{s}} \sum\limits_{\forall \widehat{\boldsymbol{s}}} e(\boldsymbol{s}, \widehat{\boldsymbol{s}}) \mathbf{I}(d(\overline{\boldsymbol{H}}_K, \boldsymbol{s}, \widehat{\boldsymbol{s}}) == d(\overline{\boldsymbol{H}}_K))$. Hence P_{GBM} can be approximated as a monotonically decreasing function of $d(\overline{\boldsymbol{H}}_K)$.

2.7.5 Proof of Proposition 2.6

Since the amplitude of each path obeys a complex norm distribution, its square obeys a unit exponential distribution. The distribution of β_i corresponding to the strongest path is $f(\beta_i) = P(1-e^{-\beta_i})^{P-1}e^{-\beta_i}$. Denote $\mathcal{C} = \frac{E_b MN\eta}{N_0 P}$, and the first item in Eq. (2.21) can be bounded by

$$\frac{1}{12}\prod_{i=1}^{K}\int_0^{\infty} f(\beta_i)e^{-\mathcal{C}\beta_i\frac{\Delta s_i^2}{4}}d\beta_i \overset{(b)}{=} \frac{P^K}{12}\prod_{i=1}^{K}\mathbb{B}(\frac{\mathcal{C}\Delta s_i^2}{4R}+1,P)$$

where (b) is according to Eq.(3.251) in [43]. Thus lower-bound of Eq. (2.21) is derived as

$$\frac{P^K}{12}\prod_{i=1}^{K}\mathbb{B}\bigg(\frac{\mathcal{C}\Delta s_i^2}{4R}+1,P\bigg)+\frac{P^K}{4}\prod_{i=1}^{K}\mathbb{B}\bigg(\frac{\mathcal{C}\Delta s_i^2}{3R}+1,P\bigg).$$

For the weakest path,$f(\beta_i) = Pe^{-P\beta_i}$. Following the same procedure, the upper-bound of Eq. (2.21) can be derived as

$$\frac{P^K}{12}\prod_{i=1}^{K}\mathbb{B}\bigg(\frac{\mathcal{C}\Delta s_i^2}{4R}+P,1\bigg)+\frac{P^K}{4}\prod_{i=1}^{K}\mathbb{B}\bigg(\frac{\mathcal{C}\Delta s_i^2}{3R}+P,1\bigg).$$

At high SNR, it can be verified that

$$\begin{aligned}
&\prod_{i=1}^{K}\mathbb{B}\bigg(\frac{\mathcal{C}\Delta s_i^2}{4R}+P+1-\kappa,\kappa\bigg)\\
\simeq&\prod_{i=1}^{K}\frac{(\mathcal{C}\Delta s_i^2/4R+P-\kappa)!(\kappa-1)!}{(P+\mathcal{C}\Delta s_i^2/4R)!}\\
\simeq&\mathcal{M}_0\bigg(\frac{E_b}{N_0}\bigg)^{-\kappa}+o\bigg\{\bigg(\frac{E_b}{N_0}\bigg)^{-\kappa}\bigg\}
\end{aligned}$$

where $\mathcal{M}_0$ is a constant irrelevant to E_b/N_0. Therefore κ represents the diversity gain, whose lower-bound and upper-bound is 1 and P, respectively. Thus, the APEP can be described as the form of Eq. (2.22).

Chapter 3

Wideband Generalized Beamspace Modulation (wGBM) for Hybrid mmWave Massive MIMO

In Chapter 2, we have seen the remarkable superiority of GBM in boosting multiplexing gain. Yet, GBM was designed for narrowband channels and is inapplicable to practical wideband mmWave channels [44, 45, 46]. Therefore, how to make GBM immune to frequency selectivity deserves an extra research focus.

Many works have revealed that with the help of OFDM, extending IM to wideband channels in conventional fully-digital transceivers is straightforward by applying the corresponding narrowband IM on each subcarrier independently [35]. However, the mentioned similar approach fails for the broadband expansion of GBM due to two main reasons: i) the analog precoder in hybrid OFDM systems is shared by all subcarriers, therefore extending GBM requires joint consideration among all subcarriers; and ii) even with a decent analog precoder, simply inheriting GBM's index mapper will render the SE-enhanced merit disappearing in OFDM systems. In light of these challenges, wideband GBM (wGBM) is proposed via an innovative symbol-based modulating scheme. The resulting design promises to remain compatible with hybrid OFDM

systems and retain SE-enhanced advantage. To overcome the detection challenge arising from symbol-based modulation, we develop the minimum mean square error (LMMSE)-based detector and approximate message passing (AMP)-based detector by breaking the complicated block detection into the more manageable sub-block ones. Finally, we demonstrate that placing a first-order compensator at the receiver suffices to combat Doppler at a negligible cost. To the best of our knowledge, there is no IM technique designed for hybrid wideband mmWave systems except for the hybrid precoded spatial modulation (hPSM) [47]. Although hPSM can improve the error performance, its SE is still restricted by the number of RF chains. In this sense, wGBM is the first SE-enhanced wideband IM for hybrid mmWave systems and can be well-suited for time-varying channels.

3.1 wGBM Transceiver

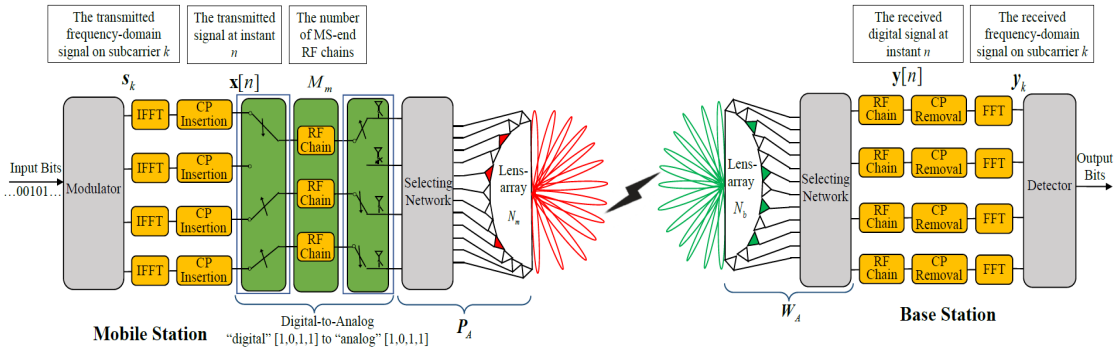

Figure 3.1: Illustration of uplink wideband mmWave mMIMO system.

3.1.1 System and Channel Models

We consider an uplink wideband mmWave mMIMO system, where N_m-dimensional lens-array antennas with M_m ($M_m << N_m$) RF chains and N_b-dimensional lens-array antennas with M_b ($M_b << N_b$) RF chains are deployed at the transmitter (mobile station) and receiver (base station), respectively. In the studied system shown in Fig. 3.1, the mobile station communicates with BS via L ($M_m \leq L \leq N_m$) streams. Without loss of generality, we further assume

$L = M_b$ and adopt OFDM for wideband transmission, with its number of subcarriers being K and the length of cyclic prefix (CP) being L_{cp}. All the channel and signal related notations are listed in Table. 3.1 for readers' reference.

Let $\boldsymbol{s}_k$ be the transmitted signal on subcarrier k. An inverse FFT (IFFT) operation is first applied to it, followed by CP insertion. The processed signal goes through the devised digital-to-analog module and be precoded by the analog precoder

$$\boldsymbol{P}_A = [\boldsymbol{p}_T(t_1), \boldsymbol{p}_T(t_2), \cdots, \boldsymbol{p}_T(t_L)], \tag{3.1}$$

where $\boldsymbol{p}_T(i)$ stands for the i-th column of $\boldsymbol{F}_{N_m}$. It is worth mentioning that $\boldsymbol{P}_A$ remains identical across all subcarriers in wideband hybrid system, forcing the subsequent wGBM design to be designed across all subcarriers. As will be detailed later, it is such a unique feature that renders the proposed wGBM distinctive from the existing wideband IMs.

To incorporate the angular-delay sparsity as well as the frequency-time selectivity exhibited by mmWave channels, we adopt a generic geometric channel model with N_c distinguishable delay taps and P dominant paths. According to [48], the tap-d channel at time instant-n $\mathbf{H}_d[n] \in \mathcal{C}^{N_b \times N_m}$can be written as

$$\mathbf{H}_d[n] = \sqrt{\frac{N_b N_m}{P}} \sum_{p=1}^{P} \alpha_p p_{rc}(dT_s - \tau_p) \boldsymbol{a}_r(\theta_p) \boldsymbol{a}_t^*(\phi_p) e^{jw_p n}, \tag{3.2}$$

where T_s is the sampling period; $p_{rc}(\cdot)$ is the response of the pulse-shaper. For the p-th path, τ_p is the propagation delay uniformly distributed within $[0, (N_c{-}1)T_s)$; $w_p = 2\pi f_c v_m T_s \sin(\theta_p)/c_v$ is its associated Doppler frequency shift, with f_c being the system carrier frequency, c_v being the speed of light, and v_m being the relative speed between mobile station (MS) and base station (BS); $\alpha_p \sim \mathcal{CN}(0,1)$ is the complex gain; θ_p and ϕ_p represent the AoA and AoD, respectively. $\boldsymbol{a}_t(\cdot)$ and $\boldsymbol{a}_r(\cdot)$ stand for the MS- and BS-end array responses, respectively. Define $\boldsymbol{f}_N(\psi) = \frac{1}{\sqrt{N}} \left[1, e^{j\psi}, \cdots, e^{j(N-1)\psi}\right]^T$. Then, under the commonly used half-wavelength spaced uniform linear arrays (ULAs), we have $\boldsymbol{a}_t(\phi_p) = \boldsymbol{f}_{N_m}(\pi \sin(\phi_p))$ and $\boldsymbol{a}_r(\theta_p) = \boldsymbol{f}_{N_b}(\pi \sin(\theta_p))$. In this section, channel state information (CSI) is assumed to be

available at the transceivers. This assumption is reasonable, because CSI can be accurately estimated in doubly-selective mmWave mMIMO channels by exploiting the delay-angular sparsity.

Table 3.1: Notations relating to uplink mmWave mMIMO system.

Notation			**Definition**
Type	**Time domain**	**Frequency domain**	
Channel	$\mathbf{H}_d[n]$	$\boldsymbol{H}_k[r]$	Spatial channel ($\mathbb{C}^{N_b \times N_m}, w_p \neq 0$)
	$\mathbf{H}_d$	$\boldsymbol{H}_k$	Spatial channel ($\mathbb{C}^{N_b \times N_m}, w_p = 0$)
	$\bar{\mathbf{H}}_d[n]$	$\bar{\boldsymbol{H}}_k[r]$	Equivalent channel incorporating analog parts ($\mathbb{C}^{L \times L}, w_p \neq 0$)
	$\bar{\mathbf{H}}_d$	$\bar{\boldsymbol{H}}_k$	Equivalent channel incorporating analog parts ($\mathbb{C}^{L \times L}, w_p = 0$)
Signal	$\mathbf{x}[n]$	$\boldsymbol{s}_k$	Signal before analog precoding
	$\mathbf{y}[n]$	$\boldsymbol{y}_k$	Signal after analog combing
	$\bar{\mathbf{y}}[n]$	$\bar{\boldsymbol{y}}_k$	Signal after compensation

Given the time-domain channel response in Eq. (3.2), the corresponding inter-subcarrier channel response $\boldsymbol{H}_k[r] \in \mathcal{C}^{N_b \times N_m}(k, r \in [0, K-1])$ can be expressed as [49]

$$\boldsymbol{H}_k[r] = \frac{1}{K} \sum_{i=0}^{K-1} \sum_{d=0}^{N_c-1} \mathbf{H}_d[L_{cp} + i] e^{-j2\pi(rd+(k-r)i)/K}, \tag{3.3}$$

where $\boldsymbol{H}_k[r]$ represents the channel response at subcarrier-k if $k = r$, or the inter-carrier interference (ICI) from subcarrier-r to k if $k \neq r$. Apparently, when $w_p = 0$, $\mathbf{H}_d[n]$ turns out

to be time-invariant. Denote the static version of $\mathbf{H}_d[n]$ as $\mathbf{H}_d$, then in this case, all the inter-subcarrier channels vanish except for leaving

$$\boldsymbol{H}_k[k] = \boldsymbol{H}_k = \sum_{d=0}^{N_c-1} \mathbf{H}_d e^{-j\frac{2\pi k}{K}d}. \tag{3.4}$$

After channel propagation, the received signal on subcarrier k is given by

$$\boldsymbol{r}_k = \boldsymbol{H}_k[k]\boldsymbol{P}_A\boldsymbol{s}_k + \sum_{r=0,r\neq k}^{K-1} \boldsymbol{H}_k[r]\boldsymbol{P}_A\boldsymbol{s}_r + \boldsymbol{w}_k, \tag{3.5}$$

where $\boldsymbol{w}_k \sim \mathcal{CN}\left(\mathbf{0}, \sigma^2\boldsymbol{I}_{N_b}\right)$ is the white Gaussian noise, with σ^2 representing the noise power. $\boldsymbol{r}_k$ is first combined by the analog combiner $\boldsymbol{W}_A = [\boldsymbol{f}_R(r_1), \boldsymbol{f}_R(r_2), \cdots, \boldsymbol{f}_R(r_L)]$ with $\boldsymbol{f}_R(i)$ being the i-th column of $\boldsymbol{F}_{N_b}$. After CP removal and FFT operation, the signal to be processed in digital baseband becomes

$$\begin{aligned}\boldsymbol{y}_k &= \boldsymbol{W}_A^*\boldsymbol{H}_k[k]\boldsymbol{P}_A\boldsymbol{s}_k + \sum_{r=0,r\neq k}^{K-1} \boldsymbol{W}_A^*\boldsymbol{H}_k[r]\boldsymbol{P}_A\boldsymbol{s}_r + \boldsymbol{W}_A^*\boldsymbol{w}_k \\ &= \bar{\boldsymbol{H}}_k[k]\boldsymbol{s}_k + \sum_{r=0,r\neq k}^{K-1} \bar{\boldsymbol{H}}_k[r]\boldsymbol{s}_r + \boldsymbol{\xi}_k,\end{aligned} \tag{3.6}$$

where $\boldsymbol{\xi}_k = \boldsymbol{W}_A^*\boldsymbol{w}_k \sim \mathcal{CN}\left(\mathbf{0}, \sigma^2\boldsymbol{I}_L\right)$ is the combined noise. Finally, the system I-O relationship can be expressed as

$$\underbrace{\begin{bmatrix}\boldsymbol{y}_0 \\ \vdots \\ \boldsymbol{y}_{K-1}\end{bmatrix}}_{\boldsymbol{y}} = \underbrace{\begin{bmatrix}\bar{\boldsymbol{H}}_0[0] & \cdots & \bar{\boldsymbol{H}}_0[K-1] \\ \vdots & \ddots & \vdots \\ \bar{\boldsymbol{H}}_{K-1}[0] & \cdots & \bar{\boldsymbol{H}}_{K-1}[K-1]\end{bmatrix}}_{\boldsymbol{H}} \underbrace{\begin{bmatrix}\boldsymbol{s}_0 \\ \vdots \\ \boldsymbol{s}_{K-1}\end{bmatrix}}_{\boldsymbol{s}} + \underbrace{\begin{bmatrix}\boldsymbol{\xi}_0 \\ \vdots \\ \boldsymbol{\xi}_{K-1}\end{bmatrix}}_{\boldsymbol{\xi}}. \tag{3.7}$$

Define $\bar{\boldsymbol{H}}_k = \boldsymbol{W}_A^*\boldsymbol{H}_k\boldsymbol{P}_A$. When $w_p = 0$, $\boldsymbol{H}$ in Eq. (3.7) can be further simplified as

$$\bar{\boldsymbol{H}} = \mathbf{diag}\left\{\bar{\boldsymbol{H}}_k\right\}_{k=0}^{K-1}. \tag{3.8}$$

3.1.2 wGBM over Static Channels

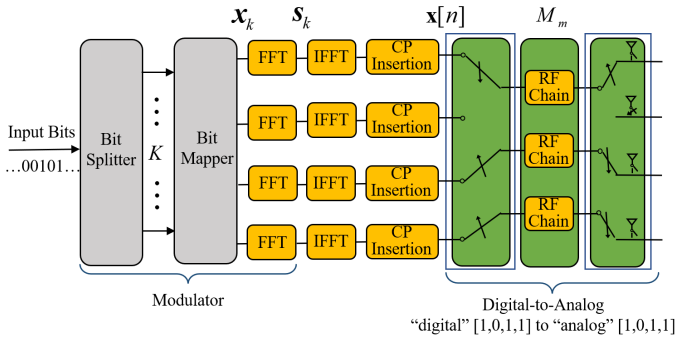

Figure 3.2: The prototype of wGBM modulator

The prototype of wGBM modulator shown in Fig. 3.2 comprises bit splitter, bit mapper, FFT module, OFDM modulator and digital-to-analog module. To be specific, the input bit stream is split into K branches, each having $b = M_m \log_2(M) + \left\lfloor \log_2(\mathbb{C}_L^{M_m}) \right\rfloor$ bits. Taking the k-th branch as an example to explain the specifics. The first $M_m \log_2(M)$ bits will be modulated into a symbol vector $\boldsymbol{u}_k = [u_{k,1}, u_{k,2}, \cdots, u_{k,M_m}]^T$, of which each entry is chosen from a normalized M-ary phase shift keying/quadrature amplitude (PSK/QAM) constellation χ. The remaining $\left\lfloor \log_2(\mathbb{C}_L^{M_m}) \right\rfloor$ bits will be mapped into a length-M_m sequence $I_k \subset S = \{S_1, \cdots, S_Q\}$, whose elements range from $[1, L]$ in an ascending order. As a result, the data vector after bit mapper can be written as

$$\boldsymbol{x}_k = \boldsymbol{I}_L[:, I_k]\boldsymbol{u}_k. \tag{3.9}$$

After FFT module, a stacked frequency-domain signal vector is obtained as

$$\boldsymbol{s} = [\boldsymbol{s}_0^T, \boldsymbol{s}_1^T, \cdots, \boldsymbol{s}_{K-1}^T]^T = (\boldsymbol{F}_K \otimes \boldsymbol{I}_L)\boldsymbol{x}, \tag{3.10}$$

with $\boldsymbol{x}$ being a concatenation of $\boldsymbol{x}_k$. By applying IFFT, the corresponding time-domain signal becomes

$$\boldsymbol{x} = (\boldsymbol{F}_K \otimes \boldsymbol{I}_L)^* \boldsymbol{s}. \tag{3.11}$$

Define $\widehat{\boldsymbol{x}}$ to be the concatenated signal after CP insertion. Then the corresponding time-domain signal at instant n is

$$\mathbf{x}[n] = \widehat{\boldsymbol{x}}[nL+1:(n+1)L](n < K + L_{cp} - 1). \tag{3.12}$$

Note that, with FFT applied before the OFDM modulator, $\mathbf{x}[n]$ always contains a fixed number of zero elements. Therefore, we can employ a simple digital-to-analog module to reduce the use of RF chains. That is, only those non-zero elements of $\mathbf{x}[n]$ will be up-converted via RF chains while the zero elements will be connected to the analog ground (essentially transmitting 0). It is worth mentioning that wGBM degenerates to GBM when K=1. By taking the CP consumption into account, the achievable SE of wGBM can be expressed as

$$\eta = \frac{K}{K + L_{cp}} \left(\lfloor \log_2 \mathbb{C}_L^R \rfloor + R \log_2 M \right). \tag{3.13}$$

1): *ML detector*: Based on Eqs. (3.7) and (3.10), the ML detector can be expressed as

$$\hat{\boldsymbol{x}} = \underset{\forall k, \boldsymbol{x}_k \in G}{\arg\min} \left\| \boldsymbol{y} - \bar{\boldsymbol{H}} \boldsymbol{s} \right\|^2 = \underset{\forall k, \boldsymbol{x}_k \in G}{\arg\min} \left\| \boldsymbol{y} - \bar{\boldsymbol{H}} (\boldsymbol{F}_K \otimes \boldsymbol{I}_L) \boldsymbol{x} \right\|^2, \tag{3.14}$$

where G contains all possible $\boldsymbol{x}_k$'s. Since the detection is performed across all subcarrier symbols, the computational complexity in terms of multiplications is $O \sim (2^{bK}(4K^2R + 4KL^2 + 2KL))$, which grows exponentially with K. The complexity would be badly high, driving us to seek a low-complexity alternative for practice use.

2): *LMMSE-based detector*: The high complexity of ML detector results from wGBM's symbol-based modulating nature. Therefore reducing complexity needs to decouple the intertwined relationship among subcarriers. Towards this objective, a two-step low-complexity detector is proposed. At first,the widely-used LMMSE equalizer $\boldsymbol{M} = \{\bar{\boldsymbol{H}}^* \bar{\boldsymbol{H}} + \sigma^2 \boldsymbol{I}_{LK}\}^{-1} \bar{\boldsymbol{H}}^*$ is applied to get estimated $\boldsymbol{s}$, i.e., $\bar{\boldsymbol{s}} = \boldsymbol{M}\boldsymbol{y}$, so with Eq. (3.10), $\boldsymbol{x}_k$ can be estimated as

$$\bar{\boldsymbol{x}}_k = (\boldsymbol{F}_K{}^*[k,:] \otimes \boldsymbol{I}_L) \bar{\boldsymbol{s}} = (\boldsymbol{F}_K{}^*[k,:] \otimes \boldsymbol{I}_L) \boldsymbol{M}\boldsymbol{y}. \tag{3.15}$$

In the next, ML detection is applied to the low-dimensional vector $\bar{\boldsymbol{x}}_k$, giving rise to

$$\hat{\boldsymbol{x}}_k = \underset{\boldsymbol{x}_k \in G}{\arg\min} \left\| \bar{\boldsymbol{x}}_k - \boldsymbol{x}_k \right\|^2. \tag{3.16}$$

In this manner, the detection complexity in terms of multiplications is $O \sim (2KL^3 + 8K^2L^3 + K(4KL + 2^{b+1}L))$, being polynomial with K and L. In essence, the LMMSE-based detector transforms complicated symbol detection into manageable subcarrier (sub-block) detection, thereby being more implementable.

3: *AMP-based detector*: LMMSE exhibits cubic-order complexity with respect to the signal dimension. To lower the detection burden, the AMP algorithm [50] comes into play to help reduce the complexity to square order. In brief, the AMP-based detector aims to break a joint KL-dimension estimation problem into KL simple ones, each dealing with a scalar estimation problem. The detailed procedures are summarized in Algorithm 1.

Recall that those L beams for constructing the analog parts should be determined in advance. Based on the estimated frequency-domain signal vector $\bar{\boldsymbol{s}}$, we can obtain the beam selection criterion of minimizing the mean square error function

$$\|\boldsymbol{e}\|^2 = \|\bar{\boldsymbol{s}} - \boldsymbol{s}\|^2 = \|\boldsymbol{M}\boldsymbol{y} - \boldsymbol{s}\|^2. \tag{3.17}$$

Ideally, those L beams can be obtained via exhaustive search within the set containing all possible beam candidates, but the computational complexity would be prohibitive in mMIMO. Thanks to the fact that beamspace sparsity still holds in wideband channels, we can apply the power-based exclusion as in [51] on each subcarrier to get a small-size beam set P_k. Let $P = \bigcup_{\forall k} P_k$ and $(\boldsymbol{r}, \boldsymbol{t}) = \{(r_1, t_1), \cdots, (r_L, t_L)\} \subset \mathcal{P}$ with $\forall i, (r_i, t_i) \in \mathcal{P}$. Those L beam indices for constructing the analog beamformer can be determined as

$$\begin{aligned}
\{(\bar{r}_1, \bar{t}_1), \cdots, (\bar{r}_L, \bar{t}_L)\} &= \underset{\forall(\boldsymbol{r},\boldsymbol{t})\subset\mathcal{P}}{\arg\min} \left\{ \left\| \boldsymbol{M}\bar{\boldsymbol{H}} - \boldsymbol{I}_{LK} \right\|^2 + \sigma^2 \|\boldsymbol{M}\|^2 \right\} \\
&\overset{(a)}{\simeq} \underset{\forall(\boldsymbol{r},\boldsymbol{t})\subset\mathcal{P}}{\arg\min} \left\{ \left\| \bar{\boldsymbol{H}}^{+}\bar{\boldsymbol{H}} - \boldsymbol{I}_{LK} \right\|^2 + \sigma^2 \left\| \bar{\boldsymbol{H}}^{+} \right\|^2 \right\} \\
&= \underset{\forall(\boldsymbol{r},\boldsymbol{t})\subset\mathcal{P}}{\arg\min} Tr\left\{ \{\bar{\boldsymbol{H}}^{*}\bar{\boldsymbol{H}}\}^{-1} \right\},
\end{aligned} \tag{3.18}$$

where (a) is for $\boldsymbol{M} \simeq \bar{\boldsymbol{H}}^{+}$ at high SNR. The approximation is reasonable because IM is well-known to manifest advantages at high SNR [37]. Based on the selected beams, the analog precoders are accordingly designed as $\boldsymbol{P}_A = [\boldsymbol{f}_T(\bar{t}_1), \boldsymbol{f}_T(\bar{t}_2), \cdots, \boldsymbol{f}_T(\bar{t}_L)]$ and $\boldsymbol{W}_A = [\boldsymbol{f}_R(\bar{r}_1), \boldsymbol{f}_R(\bar{r}_2), \cdots, \boldsymbol{f}_R(\bar{r}_L)]$.

Algorithm 1 AMP-based Detector for wGBM

1: **Initialization:** t=1, $\tilde{\boldsymbol{H}} = \bar{\boldsymbol{H}}(\boldsymbol{F}_K \otimes \boldsymbol{I}_L)$;

$\hat{x}_i^1 = \sum_{x\in\chi} x/2^b$, $\hat{v}_i^1 = \sum_{x\in\chi} \left|x - \hat{x}_i^1\right|^2/2^b$, $i = 1, \cdots, KL$; $V_j^0 = 1, Z_j^0 = \boldsymbol{y}(j), j = 1, \cdots, KL$;

2: **Decoupling step:** For $j = 1, \cdots, KL$ and $i = 1, \cdots, KL$, compute

$V_j^t = \delta \sum_i \left|\tilde{\boldsymbol{H}}[j,i]\right|^2 \hat{v}_i^t + (1-\delta)V_j^{t-1}$,

$Z_j^t = \sum_i \tilde{\boldsymbol{H}}[j,i]\hat{x}_i^t - V_j^t(\boldsymbol{y}(j) - Z_j^{t-1})/(\sigma^2 + V_j^{t-1})$

For $i = 1, \cdots, KL$, calculate

$\Sigma_i^t = \left[\sum_j \frac{\left|\tilde{\boldsymbol{H}}[j,i]\right|^2}{\sigma^2+V_j^t}\right]^{-1}$, $\bar{x}_i^t = \delta\hat{x}_i^t + (1-\delta)\bar{x}_i^{t-1}$

$R_i^t = \bar{x}_i^t + \Sigma_i^t \sum_j \tilde{\boldsymbol{H}}[j,i]^*(\boldsymbol{y}(j) - Z_j^t)/(\sigma^2+V_j^t)$

Here $\delta = 1$ is used in the first iteration.

3: **Denoising step:** For $i = 1, \cdots, KL$, $\tilde{k} = ceil(i/L) - 1$, $\bar{S}_q = \{1, \cdots, L\}\backslash S_q$, $q = 1, \cdots, Q$

$$D_i^t(x_i) = \exp\left(-\frac{|x_i|^2 - 2\mathrm{Re}(R_i^t x_i^*)}{\Sigma_i^t}\right) \times \sum_{q:(i-\tilde{k}L)\in S_q} \prod_{\substack{a\in S_q,\\ a\neq(i-\tilde{k}L)}} \left(\sum_{x\in\chi} \exp\left(-\frac{|x|^2 - 2\mathrm{Re}(R_{\tilde{k}L+a}^t x^*)}{\Sigma_{\tilde{k}L+a}^t}\right)\right)$$

$$E_i^t = \sum_{q:(i-\tilde{k}L)\in\bar{S}_q} \prod_{a\in S_q} \left(\sum_{x\in\chi} \exp\left(-\frac{|x|^2 - 2\mathrm{Re}(R_{\tilde{k}L+a}^t x^*)}{\Sigma_{\tilde{k}L+a}^t}\right)\right)$$

$$q^t(x_i) = \begin{cases} \frac{D_i^t(x_i)}{\sum_{x\in\chi} D_i^t(x) + E_i^t}, x_i \in \chi \\ \frac{E_i^t}{\sum_{x\in\chi} D_i^t(x) + E_i^t}, x_i = 0 \end{cases}$$

$\hat{x}_i^{t+1} = \sum_{x\in\chi} x q^t(x_i = x)$

$\hat{v}_i^{t+1} = \sum_{x\in\chi} |x|^2 q^t(x_i = x) - |\hat{x}_i^{t+1}|^2$

4: Set $t \leftarrow t+1$ and proceed to step 2) until $t < T_{max}$ or $\sum_i \left|\hat{x}_i^{t+1} - \hat{x}_i^t\right|^2 < 0.1$.

3.1.3 wGBM Error Performance

After accomplishing the wGBM transceiver design, we then analyze its error performance under the proposed LMMSE detection. Due to the similarity across all subcarriers, the asymptotic pairwise error probability (APEP) of wGBM can be approximated as

$$\begin{aligned} P_{\mathrm{APEP}} &= \frac{1}{Kb2^b} \sum_{k=0}^{K-1} \sum_{\boldsymbol{x}_k} \sum_{\hat{\boldsymbol{x}}_k} e(\boldsymbol{x}_k, \hat{\boldsymbol{x}}_k) P(\boldsymbol{x}_k \to \hat{\boldsymbol{x}}_k) \\ &\simeq \frac{1}{b2^b} \sum_{\boldsymbol{x}_k} \sum_{\hat{\boldsymbol{x}}_k} e(\boldsymbol{x}_k, \hat{\boldsymbol{x}}_k) P(\boldsymbol{x}_k \to \hat{\boldsymbol{x}}_k), \end{aligned} \tag{3.19}$$

where $e(\boldsymbol{x}_k, \hat{\boldsymbol{x}}_k)$ stands for the number of error bits between $\boldsymbol{x}_k$ and $\hat{\boldsymbol{x}}_k$, and $P(\boldsymbol{x}_k \to \hat{\boldsymbol{x}}_k)$ stands for the pair-wise error probability.

Proposition 3.1: *For wideband mmWave systems equipped with $M_m(M_b)$ RF chains at the MS (BS) and communicating through channels consisting of P dominant beam paths, the pair-wise error probability at subcarrier k can be approximated as*

$$\begin{aligned} P(\boldsymbol{x}_k \to \hat{\boldsymbol{x}}_k) \approx & \frac{P\mathbb{C}_{P-1}^{\nu-1}}{12} \mathbb{B}\left(\frac{N_b N_m A}{4\sigma^2 P} \sum_{l=1}^{L} |\Delta x_{k,l}|^2 + P - \nu + 1, \nu \right) \\ & + \frac{P\mathbb{C}_{P-1}^{\nu-1}}{4} \mathbb{B}\left(\frac{N_b N_m A}{3\sigma^2 P} \sum_{l=1}^{L} |\Delta x_{k,l}|^2 + P - \nu + 1, \nu \right), \end{aligned} \tag{3.20}$$

with $A = \int_0^{(N_c-1)T_s} \left(\frac{|p_{rc}(\lfloor\tau\rfloor-\tau)|^2 + |p_{rc}(\lfloor\tau\rfloor-\tau+T_s)|^2}{2(N_c-1)T_s} + \frac{(|p_{rc}(\lfloor\tau\rfloor-\tau)| - |p_{rc}(\lfloor\tau\rfloor-\tau+T_s)|)^2}{2(N_c-1)T_s} \right) d\tau$, $\Delta x_{k,l} = \boldsymbol{x}_{k,l} - \hat{\boldsymbol{x}}_{k,l}$, and ν denoting the diversity gain.

Proof. See Proof for Proposition 3.1. □

3.1.4 wGBM Accommodating Doppler

The above wGBM transceiver is designed in the absence of Doppler. In time-varying channels, the ICI may severely compromise the error performance. To address this issue, an additional operation, i.e., the first-order Doppler compensation, will be applied to the received signal

$\mathbf{y}[n]$ (see Fig. 3.3) before removing CP. Such an receiver operation does not change the existing wGBM design and will demand negligible computational complexity. The effectiveness is guaranteed by the following two arguments.

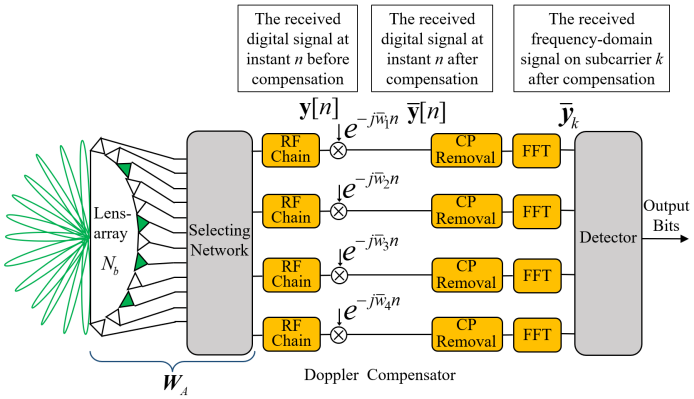

Figure 3.3: The schematic of the Doppler compensator at the receiver end.

Lemma 3.1: For two beams whose AoAs (BS side) are θ_1 and θ_2, respectively, once satisfying $|\sin(\theta_2) - \sin(\theta_1)| > 2/N_b$, these two beams are approximately orthogonal.

Proof. Let $\Delta = \sin(\theta_2) - \sin(\theta_1)$.The correlation between two beams can be calculated as

$$|\boldsymbol{a}_r(\theta_1)^* \boldsymbol{a}_r(\theta_2)| = \frac{1}{N_b} \left| \frac{\sin(\pi N_b \Delta/2)}{\sin(\pi \Delta/2)} \right|. \tag{3.21}$$

This value decreases rapidly as $|\Delta|$ increases in mMIMO, so two beams from distinct directions tend to be orthogonal, resulting in a tiny interference regardless of Doppler compensation. □

Lemma 3.2: *For two beams whose AoAs (BS side) are θ_1 and θ_2, respectively, once satisfying $|\sin(\theta_2) - \sin(\theta_1)| < 2/N_b$, the two beams experience a similar Doppler effect.*

Proof. The relative Doppler shift Δw for these two beams can be calculated as

$$\left| \frac{w_2 - w_1}{w_2} \right| = \left| \frac{2\pi f_c v_m T_s (\sin(\theta_2) - \sin(\theta_1))/c_v}{2\pi f_c v_m T_s \sin(\theta_2)/c_v} \right| = \left| \frac{\Delta}{\sin(\theta_2)} \right| < \left| \frac{2}{N_b \sin(\theta_2)} \right|. \tag{3.22}$$

Clearly this value can be very small in mMIMO, implying $w_2 \approx w_1$. □

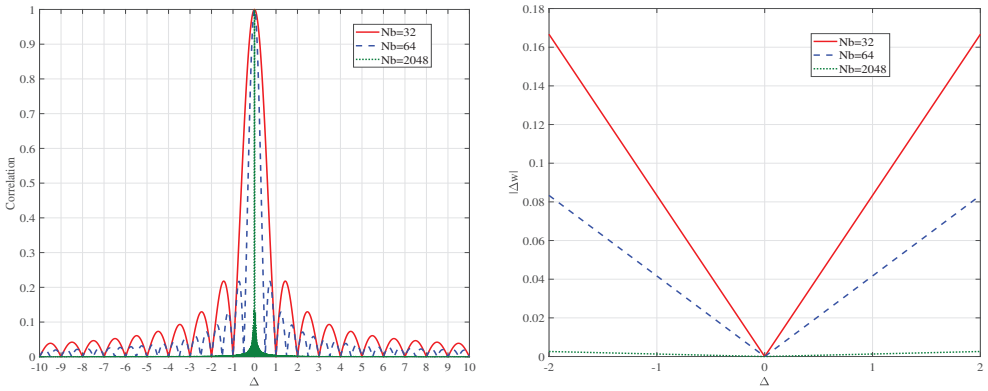

(a) (b)

Figure 3.4: Validation of first-order compensator's sufficiency: (a) The beam correlation versus the beam index gap; and (b) The Doppler difference versus the beam index gap.

Define $\bar{\mathbf{H}}_d[n] = \boldsymbol{W}_A^* \mathbf{H}_d[n] \boldsymbol{P}_A$, then the signal after down-conversion becomes

$$\bar{\mathbf{y}}[n] = \sum_{d=0}^{N_c-1} \mathbf{diag}\left\{e^{-j\bar{w}_l n}\right\}_{l=1}^{L} \bar{\mathbf{H}}_d[n]\mathbf{x}[n-d] + \bar{\mathbf{v}}[n], \tag{3.23}$$

where $\bar{w}_l$ is the Doppler associated with the l-th selected beam, and $\bar{\mathbf{v}}[n] \sim \mathcal{C}N\left(\mathbf{0}, \sigma^2 \boldsymbol{I}_L\right)$. With the two lemmas above, $\bar{\mathbf{y}}[n]$ can henceforth be approximated as

$$\bar{\mathbf{y}}[n] \simeq \sum_{d=0}^{N_c-1} \bar{\mathbf{H}}_d \mathbf{x}[n-d] + \bar{\mathbf{v}}[n]. \tag{3.24}$$

where $\bar{\mathbf{H}}_d = \boldsymbol{W}_A^* \mathbf{H}_d \boldsymbol{P}_A$. Unlike the original $\bar{\mathbf{H}}_d[n]$, $\bar{\mathbf{H}}_d$ here turns out to be irrespective of n. If neglecting the minimal interference or Doppler residue, $\mathbf{x}[n]$ is essentially transmitting through a time-invariant channel $\bar{\mathbf{H}}_d$. As N_b goes to infinity, it can be readily verified that the above compensation leads to an exact static channel $\bar{\mathbf{H}}_d$, such that ICIs can be completely vanished. Hence, the end-to-end I-O relationship degenerates into the case in static channels.

3.2 Simulations for wGBM

In this section, we first compare wGBM with the conventional spatial multiplexing (CSM) and the maximum beamforming (MBF). The pulse-shaper is set as the raised-cosine function

with $\beta = 0.8$. Other simulation parameters are: $K = 256$, $N_c = 64$, $L_{cp} = 64$, $P = 10$, $\psi \sim U[-\frac{7\pi}{16}, \frac{7\pi}{16}]$.

In Fig. 3.5, we make BER comparisons among wGBM, CSM and MBF in frequency-selective time-invariant (FSTI) channels. When η = 2.4 bps/Hz, the advantage of wGBM over CSM and MBF gradually becomes noticeable as SNR increases. At high SNR, the coding gains over CSM and MBF reach 2.5dB and 1.5dB, respectively. To achieve the SE of 5.6 bps/Hz, CSM adopts hybrid 4-QAM and 8-QAM modulation, while MBF adopts 128-QAM modulation. At low SNR, we observe that wGBM is inferior to CSM because the index bits are susceptible to strong noises, leading to more frequent erroneous detection. At high SNR, wGBM performs similar to CSM because the detection loss of wGBM caused by the MMSE detector can partially be bridged by the advantage of index modulation. With 14% index bits, wGBM also enjoys a coding gain of 6dB over MBF, whose adopted modulation order has to be every high. For wGBM, we further compare the theoretical and numerical results and the consistency hold for both the perfect and imperfect beam orthogonality.

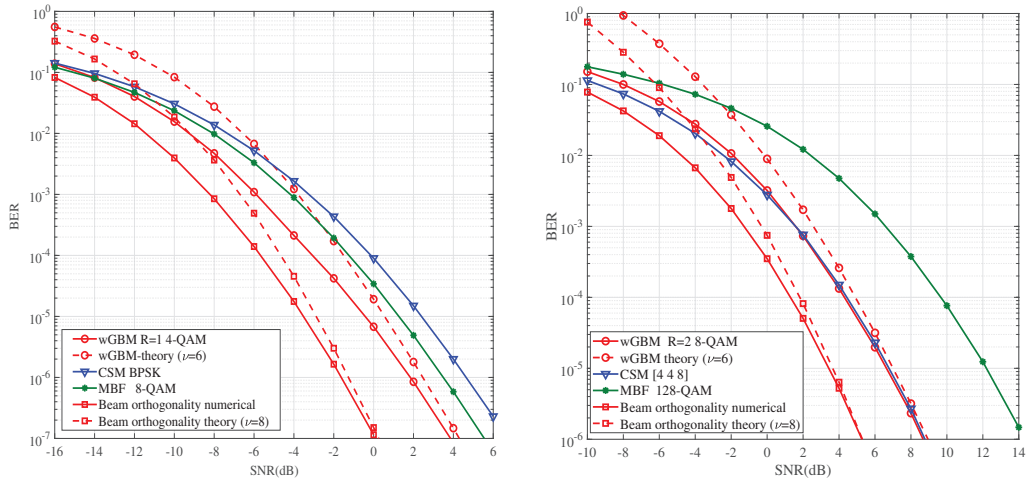

(a) (b)

Figure 3.5: BER comparisons among wGBM, CSM, and MBF in FSTI channels : (a) $\eta = 2.4$ bps/Hz, $N_m = 32$ and $N_b = 32$; and (b) $\eta = 5.6$ bps/Hz, $N_m = 32$ and $N_b = 32$.

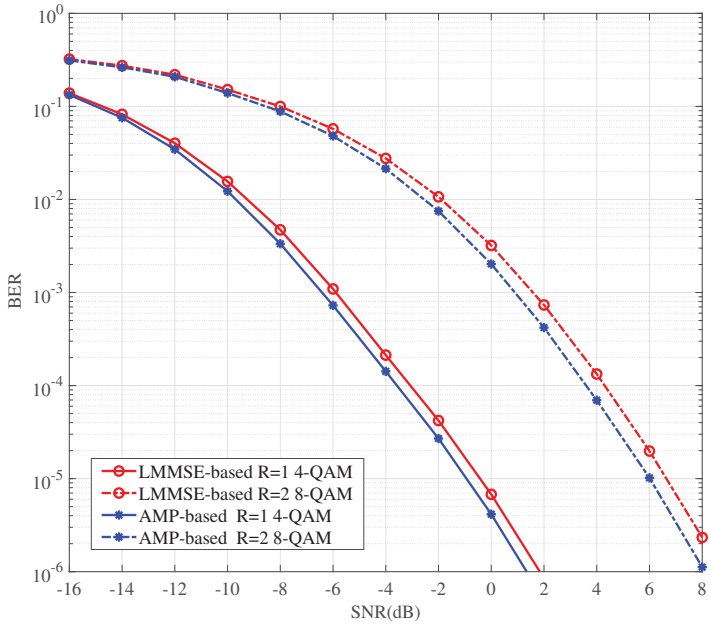

Figure 3.6: BER comparisons between LMMSE- and AMP-based detectors with $\eta = 2.4$bps/Hz and 5.6bps/Hz, $N_m = 32$ and $N_b = 32$.

Following the same system configuration, we then compare LMMSE- and AMP-based detectors in Fig. 3.6. We set $T_{max} = 5$ and $\delta = 0.4$ for AMP-based detection. Simulations show that AMP gains 0.5dB edge on the LMMS at BER = 10^{-6}. The reason is that the former algorithm can explore the structural sparsity of the transmitted signal.

In doubly-selective channels, we consider three different levels of maximum Doppler shift: 0.005, 0.01, and 0.015, corresponding to v_m = 40km/h, 80km/h, and 120km/h, respectively. As can be seen from Fig. 3.7, wGBM with compensation performs dramatically better than that without compensation. The gap between compensated wGBM and ideal benchmark is minimal at relatively low SNR. In the high SNR region, the former exhibits a BER floor as v_m increases. However, this error floor can be lowered by increasing N_b because higher angular resolution leaves a smaller interference residue after compensation.

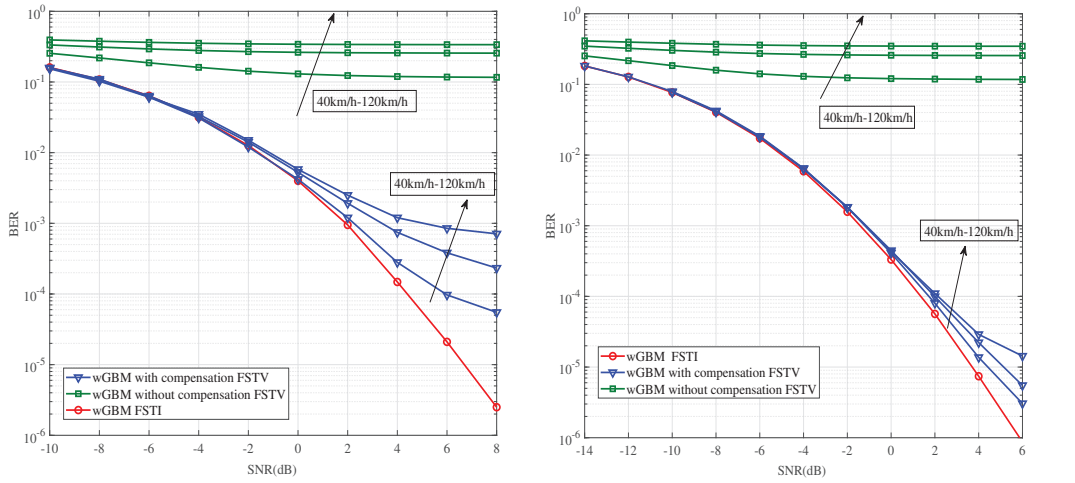

(a) (b)

Figure 3.7: BER comparisons in doubly-selective channels with η = 5.6 bps/Hz(a) $N_m = 32$ and $N_b = 32$; and (b) $N_m = 32$ and $N_b = 64$.

3.3 From wGBM to P-wGBM

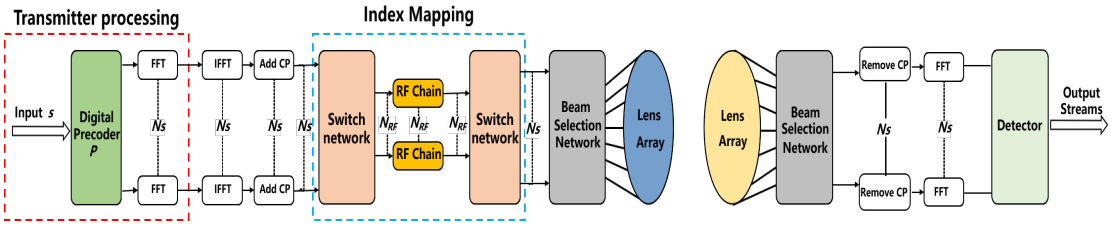

Figure 3.8: The schematic of P-wGBM for wideband hybrid mmWave m-MIMO.

3.3.1 Motivation of P-wGBM

Before going to RF domain, $\boldsymbol{s}_k$ is initially precoded by $\boldsymbol{P}_k \in \mathcal{C}^{N_s \times N_s}$. Stacking all precoded $\boldsymbol{s}_k$'s gives rise to a KN_s-dimensional vector

$$\boldsymbol{x} = \boldsymbol{P}\boldsymbol{s}, \tag{3.25}$$

where $\boldsymbol{P} = \mathrm{diag}(\boldsymbol{P}_1, \ldots, \boldsymbol{P}_K)$ and $\boldsymbol{s} = \{\boldsymbol{s}_k\}_{k=1}^K$. Note that wGBM fixes the digital precoder as an identity matrix. Motivated by the advantage of applying precoding in index modulation [52, 53], one would expect a positive yield to wGBM as well by activating the digital precoder. To enable the transmission of N_s streams via N_{RF} chains and RF switches. P-wGBM confines $\boldsymbol{P}_k$ to be a diagonal matrix such that the N_s-dimensional IFFT output remains N_{RF}-sparse. As $\boldsymbol{P}_k$ is a diagonal matrix, the precoding design boils down to finding an optimal KN_s-dimension vector. Let $P_e(\boldsymbol{p})$ stand for the corresponding error rate, which is commonly quantified as APEP. Then we can formulate the following optimization problem to guide the precoding design.

[P. 1: Original APEP-minimized precoding optimization]

$$\begin{aligned} & \arg\min_{\boldsymbol{p}} \quad P_e(\boldsymbol{p}) \\ \textit{s.t.} \quad & \left\| \boldsymbol{p}_{(k-1)N_s+1:kN_s} \right\|_F^2 \leq N_s, \forall k \in [1, K]. \end{aligned}$$

The constraint ensures that the transmit power in P-wGBM remains equal to wGBM.

3.3.2 Problem Transformation

The top priority in dealing with P.1 is of course to find a tractable alternative of $P_e(\boldsymbol{p})$. Denote S as the set containing all possible $\boldsymbol{s}$'s, and assume that the maximum-likelihood (ML) detection is adopted by the BS. Then the APEP for P-wGBM can be written as follows:

$$\begin{aligned} P_e(\boldsymbol{p}) &= \frac{1}{K\eta 2^{K\eta}} \sum_{\boldsymbol{s}\in\mathcal{S}} \sum_{\hat{\boldsymbol{s}}\neq\boldsymbol{s}} P_r\left(\boldsymbol{s} \to \hat{\boldsymbol{s}}\right) e\left(\boldsymbol{s}, \hat{\boldsymbol{s}}\right) \\ &= \frac{1}{K\eta 2^{K\eta}} \sum_{\boldsymbol{s}\in\mathcal{S}} \sum_{\hat{\boldsymbol{s}}\neq\boldsymbol{s}} Q\left(\sqrt{\frac{d(\boldsymbol{s}, \hat{\boldsymbol{s}})}{2N_0}}\right) e\left(\boldsymbol{s}, \hat{\boldsymbol{s}}\right), \end{aligned} \tag{3.26}$$

where $d(\boldsymbol{s}, \hat{\boldsymbol{s}}) = \left\| \overline{\boldsymbol{\Lambda}} \boldsymbol{P}(\boldsymbol{s} - \hat{\boldsymbol{s}}) \right\|^2$, K is the subcarrier number, and η is the information bits per subcarrier. $e(\boldsymbol{s}, \hat{\boldsymbol{s}}) = \sum_{k=1}^K e(\boldsymbol{s}_k, \hat{\boldsymbol{s}}_k)$ denotes the sum of bit-type Hamming distance, with $e(\boldsymbol{s}_k, \hat{\boldsymbol{s}}_k)$ calculated similar to [51] and [23].

Taking a closer look at Eq. (3.26), we discover its calculation involves $2^{2K\eta-1}$ items, while only $K2^{2\eta-1}$ items are required in precoded SM [54]. Such a vast disparity arises from their

different modulation mechanisms. That is, *P-wGBM is associated with the entire OFDM symbol while precoded SM is associated with one subcarrier.* As the subcarrier number K would be in the hundreds in mmWave systems, the primitive APEP is barely useful, forcing us to find a tractable alternative. Fortunately, the following two conclusions provide us with such an opportunity.

Proposition 3.2: $\overline{\boldsymbol{\Lambda}}^2 = \overline{\boldsymbol{\Lambda}}^H \overline{\boldsymbol{\Lambda}}$ *is a sparse matrix whose dominant energy is captured by the sub-matrices along its diagonal line.*

Proof. See Proof for Proposition 3.2. □

Following the derivation above, we can instantly get another useful result to simplify APEP.

Lemma 3.3: The sub-matrices $\overline{\boldsymbol{\Lambda}}^2_{k,k}$'s on the diagonal line of $\overline{\boldsymbol{\Lambda}}^2$ are exactly the same.

Proof. We have already arrived at $\overline{\boldsymbol{\Lambda}}^2 = \sum_{i=1}^{K} (\boldsymbol{f}_i^H \boldsymbol{f}_i) \otimes (\boldsymbol{\Lambda}_i^H \boldsymbol{\Lambda}_i)$. Since matrix $\boldsymbol{f}_i^H \boldsymbol{f}_i$ has an all-one diagonal line, the sub-matrices on the diagonal line of $\overline{\boldsymbol{\Lambda}}^2$ can be represented by

$$\overline{\boldsymbol{\Lambda}}^2_{k,k} = \left[\overline{\boldsymbol{\Lambda}}^2\right]_{(k-1)N_s+1:kN_s,(k-1)N_s+1:kN_s} = \sum_{i=1}^{K} \overline{\boldsymbol{H}}_i^H \overline{\boldsymbol{H}}_i. \tag{3.27}$$

□

As revealed by Proposition 3.2 that $\overline{\boldsymbol{\Lambda}}^2$ is near block-diagonal, the computation of Euclidean distance between two OFDM symbols can be transformed into per subcarrier. Therefore, the original APEP given in Eq. (3.26) can be approximated as

$$\frac{1}{K^2 \eta 2^{\eta}} \sum_{k=1}^{K} \sum_{\boldsymbol{s}_k \in \mathcal{G}} \sum_{\hat{\boldsymbol{s}}_k \neq \boldsymbol{s}_k} Q\left(\sqrt{\frac{d(\boldsymbol{s}_k, \hat{\boldsymbol{s}}_k)}{2N_0}}\right) e\left(\boldsymbol{s}_k, \hat{\boldsymbol{s}}_k\right), \tag{3.28}$$

where $\mathcal{G}$ represents the ensemble of $\boldsymbol{s}_k$, being common to all subcarriers; $d(\boldsymbol{s}_k, \hat{\boldsymbol{s}}_k) = \boldsymbol{p}_k^H \overline{\boldsymbol{\Lambda}}^H_{k,k} \overline{\boldsymbol{\Lambda}}_{k,k} \odot [(\boldsymbol{s}_k - \hat{\boldsymbol{s}}_k)(\boldsymbol{s}_k - \hat{\boldsymbol{s}}_k)^H]^T \boldsymbol{p}_k$. This step of approximation reduces the number of summations from $2^{\eta K}(2^{\eta K} - 1)$ to $K 2^{\eta}(2^{\eta} - 1)$.

Recall that lemma 3.3 points out all subcarriers share the same $\overline{\boldsymbol{\Lambda}}^2_{k,k}$. Also, they have a shared error pattern set. Hence, their behavior in terms of the error performance is the same,

leading to $\boldsymbol{p}_1 = \ldots = \boldsymbol{p}_K = \overline{\boldsymbol{p}}$. Using this property, we are able to absorb the summation over k on the outermost layer of Eq. (3.28), giving rise to a more compact form as follows:

$$\frac{1}{K\eta 2^{\eta}} \sum_{\boldsymbol{s}_i \in \mathcal{G}} \sum_{\boldsymbol{s}_j \neq \boldsymbol{s}_i} Q\left(\sqrt{\frac{\overline{\boldsymbol{p}}^H \overline{\boldsymbol{D}}_{i,j} \overline{\boldsymbol{p}}}{2N_0}}\right) e\left(\boldsymbol{s}_i, \boldsymbol{s}_j\right), \tag{3.29}$$

where $\overline{\boldsymbol{D}}_{i,j} = \overline{\boldsymbol{\Lambda}}_{i,i}^H \overline{\boldsymbol{\Lambda}}_{i,i} \odot [(\boldsymbol{s}_i - \boldsymbol{s}_j)(\boldsymbol{s}_i - \boldsymbol{s}_j)^H]^T$. As a result, APEP can be computed by summing up only $2^{\eta}(2^{\eta} - 1)$ items, even fewer than that required in precoded SM.

We replace $P_e(\boldsymbol{p})$ with Eq. (3.29) and further define

$$\overline{\boldsymbol{q}} = [Re(\overline{\boldsymbol{p}})^T, Im(\overline{\boldsymbol{p}})^T]^T \in \mathbb{R}^{2N_s \times 1}, \tag{3.30a}$$

$$\overline{\boldsymbol{R}}_{i,j} = \begin{bmatrix} Re(\overline{\boldsymbol{D}}_{i,j}) & -Im(\overline{\boldsymbol{D}}_{i,j}) \\ Im(\overline{\boldsymbol{D}}_{i,j}) & Re(\overline{\boldsymbol{D}}_{i,j}) \end{bmatrix}, \tag{3.30b}$$

then similar to [55], we rewrite the optimization problem in its equivalent real-valued form into

[P. 2: Simplified APEP-minimized precoding optimization]

$$\begin{aligned} \underset{\overline{\boldsymbol{q}}}{\arg\min}\ & \tilde{P}_e(\overline{\boldsymbol{q}}) = \frac{1}{K\eta 2^{\eta}} \sum_{\boldsymbol{s}_i \in \mathcal{G}} \sum_{\boldsymbol{s}_j \neq \boldsymbol{s}_i} Q\left(\sqrt{\frac{\overline{\boldsymbol{q}}^T \overline{\boldsymbol{R}}_{i,j} \overline{\boldsymbol{q}}}{2N_0}}\right) e\left(\boldsymbol{s}_i, \boldsymbol{s}_j\right) \\ & \textit{s.t.} \quad \|\overline{\boldsymbol{q}}\|^2 \leq N_s. \end{aligned}$$

3.3.3 Problem Solving

Our ultimate goal is to solve P.2, whose global optimum is generally not achievable. However, we will show that the obtained solution can be sufficiently close to the optimum if the signal-to-noise ratio (SNR) is high enough. In fact, this SNR range is also within our interest because index modulation is well-known to show an advantage over conventional modulations in that SNR range. Under the high-SNR assumption, the objective function of P.2 can be tightly approximated as

$$\tilde{P}_e(\overline{\boldsymbol{q}}) \approx \tilde{P}_{e,h}(\overline{\boldsymbol{q}}) = \frac{1}{K\eta 2^{\eta}} \sum_{\boldsymbol{s}_i \in \mathcal{G}} \sum_{\boldsymbol{s}_j \neq \boldsymbol{s}_i} Q\left(\sqrt{\frac{\overline{\boldsymbol{q}}^T \overline{\boldsymbol{R}}_{i,j} \overline{\boldsymbol{q}}}{2N_0}}\right) e\left(\boldsymbol{s}_i, \boldsymbol{s}_j\right) \mathbb{I}(\boldsymbol{s}_i, \boldsymbol{s}_j) \tag{3.31}$$

where $\mathbb{I}(\boldsymbol{s}_i, \boldsymbol{s}_j)$ is a binary indicator function taking on 1 if $\boldsymbol{s}_j$ and $\boldsymbol{s}_i$ differ in only one element. Once $\mathbb{I}(\boldsymbol{s}_i, \boldsymbol{s}_j) = 1$, $\overline{\boldsymbol{D}}_{i,j} = \overline{\boldsymbol{\Lambda}}_{i,i}^H \overline{\boldsymbol{\Lambda}}_{i,i} \odot [(\boldsymbol{s}_i - \boldsymbol{s}_j)(\boldsymbol{s}_i - \boldsymbol{s}_j)^H]^T$ contains a single non-zero element on its diagonal line. Then one can verify that altering the sign of an arbitrary element of $\overline{\boldsymbol{q}}$ does not change $\tilde{P}_{e,h}$. In consequence, minimizing $\tilde{P}_{e,h}$ over $\|\overline{\boldsymbol{q}}\|^2 \leq N_s$ equates to minimizing over $\mathcal{S} = \{\boldsymbol{q} | \, \|\overline{\boldsymbol{q}}\|^2 \leq N_s, \boldsymbol{q} \succ 0\}$.

Proposition 3.3: *$\tilde{P}_{e,h}(\overline{\boldsymbol{q}})$ is asymptotically convex w.r.t. $\overline{\boldsymbol{q}}$ over $\mathcal{S}$ at high SNR.*

Proof. See Proof for Proposition 3.3. □

Thanks to the asymptotic convexity of $P_{e,h}(\overline{\boldsymbol{q}})$, we can get a near-optimal solution to P. 2, denoted as $\overline{\boldsymbol{q}}$, at high SNR via a simple projected gradient algorithm. Accordingly, the precoder can be determined as

$$\boldsymbol{P}_k = \mathrm{diag}\left(\overline{\boldsymbol{q}}_{1:N_s}\right) + j\mathrm{diag}\left(\overline{\boldsymbol{q}}_{N_s+1:2N_s}\right), \forall k. \tag{3.32}$$

3.3.4 Simulations for P-wGBM

Numerical simulations will be carried out in this part to test the bit error ratio (BER) performance of P-wGBM. The well-known geometrical channel model [56] is adopted, with the tap-d channel ($d < N_c$) and the corresponding k-th subcarrier channel represented as

$$\mathbf{H}[d] = \sqrt{\frac{N_b N_m}{N_p}} \sum_{l=1}^{N_p} \alpha_l p(dT_s - \tau_l) \boldsymbol{a}_r(\phi_l) \boldsymbol{a}_t^H(\theta_l) \tag{3.33a}$$

$$\boldsymbol{H}_k = \sum_{d=0}^{N_c-1} \mathbf{H}[d] e^{-j\frac{2\pi k}{K}d}. \tag{3.33b}$$

Specifically, $p(\cdot)$ is the raised-cosine filter with roll-off factor $\beta = 0.8$ and N_c is the maximum tap. The uniform linear arrays with half-wavelength spacing are employed at the transceivers, so $\boldsymbol{a}_r(\phi) = \frac{1}{\sqrt{N_r}} \left[1, e^{j\pi \sin\phi}, \ldots, e^{j(N_r-1)\pi \sin\phi}\right]^T$. Other system and channel related parameters are listed in Table.3.2. The SNR is defined as $E_b/n_0 = N_{RF}/(\eta N_0)$. All BER curves are the average of 10000 independent channel realizations, each with a block of 2000 symbols.

Table 3.2: System and channel parameters for simulating P-wGBM

Parameter	Value
BS-end antenna number N_b	64
MS-end antenna number N_m	32
Subcarrier number K	32
Maximum delay tap N_c	8
Angle of arrival (departure) ϕ_l (θ_l)	$U[0, 2\pi)$
Tap delay τ_l	$U[0, (N_c - 1)T_s)$
Path amplitude α_l	$CN(0, 1)$
Sampling time T_s	10^{-9} s
Path number N_p	8

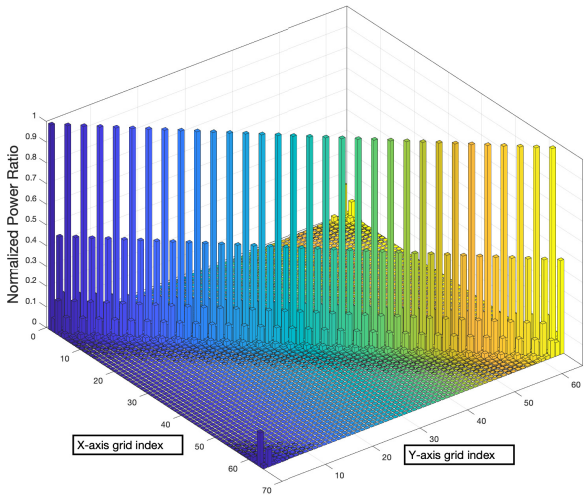

Figure 3.9: Normalized power map of $\overline{\boldsymbol{\Lambda}}^2$.

Recall that the success of APEP simplification counts on the unique structure of $\overline{\boldsymbol{\Lambda}}^2$. Actually, one can interpret $\overline{\boldsymbol{\Lambda}}^2$ as the autocorrelation of sub-beamspace channels. To gain more intuition, we visualize this matrix in a power map by averaging 10000 realizations. As seen

from Fig. 3.9, all sub-matrices along the diagonal line are exactly the same, amassing the majority of channel power. In contrast, the off-diagonal sub-matrices are suppressed to a very low level. The result implies that all subcarriers have a similar behavior regarding the error performance, so they share a common digital precoder.

Since ML detection is infeasible due to prohibitive complexity, we henceforth adopt near-ML detector proposed in [57] for both schemes. In brief, by leaving more effective candidates, whose number is denoted as m, the achieved performance is closer to the ML detector at the expense of higher complexity. As can be seen from Fig. (3.10), the coding gain is up to 2dB at high SNR under the setup of $\{N_{RF} = 1, N_s = 4$, 16-PSK$\}$. More configurations have been tested, and in general, we find that a large N_s and a high modulation order typically lead to a high coding gain. This is because in this case the beam quality exhibits a higher degree of discrimination, hence digital precoding can help compensate for the weak beams and reduce their adversary effects on the error performance.

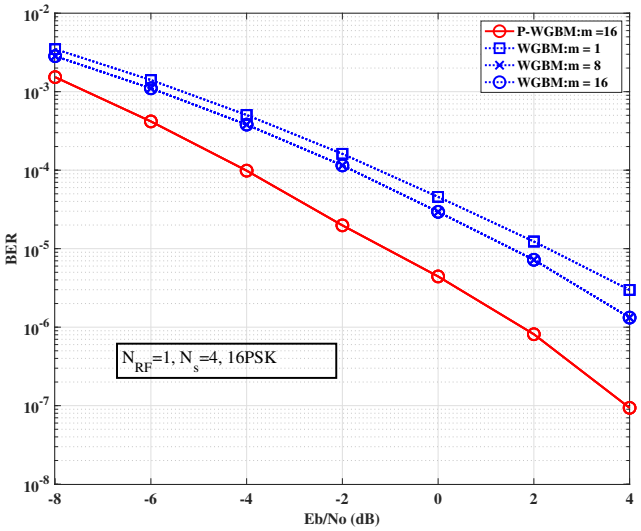

Figure 3.10: BER comparison between P-wGBM and wGBM under $N_{RF} = 1$, $N_s = 4$, and 16-PSK: $\eta = 6$ bits/Hz/s.

From the hardware perspective, wGBM and P-wGBM have equal complexity because no additional component is needed. From the computation perspective, P-wGBM requires digital

precoding whose complexity primarily relies on computing $\overline{\boldsymbol{D}}_{i,j}$ and updating gradient descent, each needing the number of flops in the order of $\mathcal{O}(KN_s^2)$ and $\mathcal{O}(N_{ite}N_s^2)$. The beam selection and detector complexity are $\mathcal{O}(K^3N_s^3)$ for both wGBM and P-wGBM. Although the latter is a bit more complicated, it shares the same cubic-order complexity concerning the subcarrier and stream number. Plus, the resulting nearly 1dB coding gain consolidates that such complexity cost is rather worthwhile.

3.4 Conclusions

In this chapter, we first generalized GBM from the narrowband to realistic wideband scenarios via a novel symbol-based IM framework. The developed wGBM is compatible with hybrid OFDM systems while retaining the SE-enhancing feature. Apart from the generic wGBM transceiver design, a simple first-order Doppler compensator is carefully designed to enhance the robustness against Doppler. Evolving from wGBM, P-wGBM was then developed by actively involving the digital precoder. Starting with determining a feasible precoding set, an optimization problem has been formulated, seeking the optimal precoder that retains multiplexing merit. To circumvent analytical intractability, we then devised a two-step simplification by exploiting the beamspace properties. Instead of resorting to complex processing, the resulting near-optimal precoder was efficiently obtained via projected gradient-descent algorithm. Simulations verified that a slightly increased complexity could yield more than 1dB coding gain over wGBM.

3.5 Proof of Propositions for wGBM

3.5.1 Proof for Proposition 3.1

Leveraging the fast-decaying nature of p_{rc}, we get

$$\begin{aligned}
\delta_l &= \frac{N_b N_m}{P}\left|\sum_{d=0}^{N_c-1}\alpha_l p_{rc}(dT_s-\tau_l)e^{-jd\frac{2\pi k}{K}}\right|^2 \\
&\approx \frac{N_b N_m}{P}|\alpha_l p_{rc}\left(\lfloor\tau_l/T_s\rfloor T_s-\tau_l\right)e^{-j\lfloor\tau_l/T_s\rfloor\frac{2\pi k}{K}} \\
&\qquad + \alpha_l p_{rc}\left((\lfloor\tau_l/T_s\rfloor+1)T_s-\tau_l\right)e^{-j(\lfloor\tau_l/T_s\rfloor+1)\frac{2\pi k}{K}}|^2 \\
&\approx \frac{N_b N_m}{P}|\alpha_l|^2\{(|p_{rc}\left(\lfloor\tau_l\rfloor-\tau_l\right)|^2+|p_{rc}\left(\lfloor\tau_l\rfloor-\tau_l+T_s\right)|^2)/2+ \\
&\qquad (|p_{rc}\left(\lfloor\tau_l\rfloor-\tau_l\right)|-|p_{rc}\left(\lfloor\tau_l\rfloor-\tau_l+T_s\right)|)^2/2\}.
\end{aligned} \tag{3.34}$$

Define $\boldsymbol{R}=\mathbf{diag}\left\{\frac{\delta_l}{\delta_l+\sigma^2}\right\}_{l=1}^{L}$. According to Eq. (3.15), we have

$$\begin{aligned}
\bar{\boldsymbol{x}}_k &= (\boldsymbol{F}_K{}^*[k,:]\otimes\boldsymbol{I}_L)\boldsymbol{M}\bar{\boldsymbol{H}}\boldsymbol{s}+(\boldsymbol{F}_K{}^*[k,:]\otimes\boldsymbol{I}_L)\boldsymbol{M}\boldsymbol{\xi} \\
&= (\boldsymbol{F}_K{}^*[k,:]\otimes\boldsymbol{I}_L)(\boldsymbol{I}_K\otimes\boldsymbol{R})\boldsymbol{s}+\boldsymbol{n}_k \\
&= (\boldsymbol{I}_1\otimes\boldsymbol{R})(\boldsymbol{F}_K{}^*[k,:]\otimes\boldsymbol{I}_L)\boldsymbol{s}+\boldsymbol{n}_k \\
&= \boldsymbol{R}\boldsymbol{x}_k+\boldsymbol{n}_k.
\end{aligned} \tag{3.35}$$

Thus, the LMMSE-based detector in Eq. (3.16) can be approximated as

$$\hat{\boldsymbol{x}}_k \simeq \underset{\boldsymbol{x}_k\in G}{\arg\min}\,\|\bar{\boldsymbol{x}}_k-\boldsymbol{R}\boldsymbol{x}_k\|^2. \tag{3.36}$$

The above equation can further lead to

$$\begin{aligned}
P(\boldsymbol{s}_k\to\hat{\boldsymbol{s}}_k) &= \mathbb{E}_{\bar{\boldsymbol{H}}_k}\left\{Q\left(\sqrt{\left(\|\boldsymbol{R}(\boldsymbol{x}_k-\hat{\boldsymbol{x}}_k)\|^2\right)^2/\sigma_k^2}\right)\right\} \\
&\overset{(b)}{\simeq} \mathbb{E}_{\bar{\boldsymbol{H}}_k}\left\{\frac{1}{12}\exp\left(-\left(\|\boldsymbol{R}(\boldsymbol{x}_k-\hat{\boldsymbol{x}}_k)\|^2\right)^2/2\sigma_k^2\right)\right\} \\
&\qquad + \mathbb{E}_{\bar{\boldsymbol{H}}_k}\left\{\frac{1}{4}\exp\left(-2\left(\|\boldsymbol{R}\left(\boldsymbol{x}_k-\hat{\boldsymbol{x}}_k\right)\|^2\right)^2/3\sigma_k^2\right)\right\},
\end{aligned} \tag{3.37}$$

where (b) comes from $Q(x) \simeq 1/12e^{-x^2/2}+1/4e^{-2x^2/3}$ [39], and $\sigma_k^2 = 2\sigma^2 \sum_{l=1}^{L} \frac{\delta_l^3}{(\delta_l+\sigma^2)^4}|\Delta x_{k,l}|^2$. Let $\boldsymbol{\gamma} = [\gamma_1, \cdots, \gamma_L]^T$ with $\gamma_l = |\alpha_l|^2$, and $\boldsymbol{\beta} = [\beta_1, \cdots, \beta_L]^T$ with

$$\begin{aligned}\beta_l =&(|p_{rc}(\lfloor\tau_l\rfloor - \tau_l)|^2 + |p_{rc}(\lfloor\tau_l\rfloor - \tau_l + T_s)|^2)/2+\\ &(|p_{rc}(\lfloor\tau_l\rfloor - \tau_l)| - |p_{rc}(\lfloor\tau_l\rfloor - \tau_l + T_s)|)^2/2.\end{aligned} \tag{3.38}$$

Recall that γ_l obeys unit exponential distribution, so by replacing all γ_l's with the p_0-th ($1 \leq p_0 \leq P$) largest one yields

$$f(\boldsymbol{\gamma}) = P\mathbb{C}_{P-1}^{P-p_0}\left(e^{-\gamma_L}\right)^{p_0}\left(1-e^{-\gamma_L}\right)^{P-p_0}\prod_{j=2}^{L}\delta(\gamma_j - \gamma_{j-1}). \tag{3.39}$$

Neglecting the constant term, the first expectation in Eq. (3.37) can be approximated as

$$\begin{aligned}&\int_0^\infty \cdots \int_0^\infty f(\boldsymbol{\gamma})\left\{\exp\left(-\left(\|\boldsymbol{R}(\boldsymbol{x}_k - \hat{\boldsymbol{x}}_k)\|^2\right)^2/2\sigma_k^2\right)\right\}d\gamma_1\cdots d\gamma_L\\ =&P\mathbb{C}_{P-1}^{P-p_0}\int_0^\infty e^{-(\frac{N_bN_m}{4\sigma^2P}\sum_{l=1}^{L}\mathbb{E}[\beta_l]\left|\Delta x_{k,l}\right|^2+p_0)\gamma_L}(1-e^{-\gamma_L})^{P-p_0}d\gamma_L\\ \overset{(c)}{=}&P\mathbb{C}_{P-1}^{P-p_0}\mathbb{B}\left(\frac{N_bN_m}{4\sigma^2P}\sum_{l=1}^{L}\mathbb{E}\left[\beta_l\right]|\Delta x_{k,l}|^2 + p_0, P-p_0+1\right)\\ \overset{(d)}{=}&P\mathbb{C}_{P-1}^{P-p_0}\mathbb{B}\left(\frac{N_bN_m}{4\sigma^2P}\sum_{l=1}^{L}\mathbb{E}\left[\beta_l\right]|\Delta x_{k,l}|^2 + P+1-\nu, \nu\right),\end{aligned} \tag{3.40}$$

where (c) comes from $\mathbb{B}(X,Y) = \int_0^1 \gamma^{X-1}(1-\gamma)^{Y-1}d\gamma$ and (d) is because $\nu = P - p_0 + 1$. As $p_{rc}(x) \approx 1/2\cos(\pi x/T_s)+1/2, x \in (-T_s, T_s)$, $\mathbb{E}\left[\beta_l\right] = \int_0^{(N_c-1)T_s}\beta_l\frac{1}{(N_c-1)T_s}d\tau_l, \forall l$, high SNR will lead to

$$P\mathbb{C}_{P-1}^{\nu-1}\frac{(\frac{N_bN_m}{4\sigma^2P}\sum_{l=1}^{L}\mathbb{E}\left[\beta_l\right]|\Delta x_{k,l}|^2 + P - \nu)!(\nu-1)!}{(\frac{N_bN_m}{4\sigma^2P}\sum_{l=1}^{L}\mathbb{E}\left[\beta_l\right]|\Delta x_{k,l}|^2 + P)!} \simeq M_0\left(\frac{S}{N_0}\right)^{-\nu} + o\left\{\left(\frac{S}{N_0}\right)^{-\nu}\right\}, \tag{3.41}$$

Apparently, ν ($1 \leq \nu \leq P$) represents the diversity gain.

3.5.2 Proof for Proposition 3.2

Let $\boldsymbol{f}_i$ be the i-th row of $\boldsymbol{F}_K$, then

$$\begin{aligned}\overline{\boldsymbol{\Lambda}}^2 &= (\boldsymbol{F}_K^H \otimes \boldsymbol{I}_{N_s})\boldsymbol{\Lambda}^H\boldsymbol{\Lambda}(\boldsymbol{F}_K \otimes \boldsymbol{I}_{N_s}) \\ &= \begin{bmatrix} \boldsymbol{f}_1 \otimes \boldsymbol{I}_{N_s} \\ \boldsymbol{f}_2 \otimes \boldsymbol{I}_{N_s} \\ \vdots \\ \boldsymbol{f}_K \otimes \boldsymbol{I}_{N_s} \end{bmatrix}^H \begin{bmatrix} \overline{\boldsymbol{H}}_1^H\overline{\boldsymbol{H}}_1 & & \\ & \ddots & \\ & & \overline{\boldsymbol{H}}_K^H\overline{\boldsymbol{H}}_K \end{bmatrix} \begin{bmatrix} \boldsymbol{f}_1 \otimes \boldsymbol{I}_{N_s} \\ \boldsymbol{f}_2 \otimes \boldsymbol{I}_{N_s} \\ \vdots \\ \boldsymbol{f}_K \otimes \boldsymbol{I}_{N_s} \end{bmatrix} \\ &= \sum_{k=1}^{K} (\boldsymbol{f}_k^H\boldsymbol{f}_k) \otimes \overline{\boldsymbol{H}}_k^H\overline{\boldsymbol{H}}_k \end{aligned} \tag{3.42}$$

Defining $\omega = e^{j\frac{2\pi}{K}}$, we have

$$\begin{aligned}\overline{\boldsymbol{\Lambda}}_{m,n}^2 &= \left[\overline{\boldsymbol{\Lambda}}^2\right]_{(m-1)N_s+1:mN_s,(n-1)N_s+1:nN_s} \\ &= \sum_{k=1}^{K} \omega^{(n-m)\cdot(k-1)}\overline{\boldsymbol{H}}_k^H\overline{\boldsymbol{H}}_k,\ m \neq n. \end{aligned} \tag{3.43}$$

$\forall k$, $\overline{\boldsymbol{H}}_k^H\overline{\boldsymbol{H}}_k$ is demonstrated to be asymptotically equal as antennas approach infinity [58]. Since $\frac{1}{K}\sum_{k=1}^{K}\omega^{n\cdot(k-1)} = 0$ if $k \neq 0$, $\overline{\boldsymbol{\Lambda}}_{m,n}^2$ is proved to be close to a zero matrix.

3.5.3 Proof for Proposition 3.3

The heart of demonstration lies in proving the convexity of Q-term. Let $\boldsymbol{R}_{i,j} = \overline{\boldsymbol{R}}_{i,j} + \overline{\boldsymbol{R}}_{i,j}^T$. Taking the second derivative of the Q-term *w.r.t.* $\overline{\boldsymbol{q}}$ results in

$$\begin{aligned}&\frac{\partial^2 Q}{\partial^2\overline{\boldsymbol{q}}} \propto e^{-\frac{\overline{\boldsymbol{q}}^T\overline{\boldsymbol{R}}_{i,j}\overline{\boldsymbol{q}}}{4N_0}} \left(\frac{\overline{\boldsymbol{q}}^T\overline{\boldsymbol{R}}_{i,j}\overline{\boldsymbol{q}}}{2N_0}\right)^{-\frac{1}{2}} \left(\frac{\boldsymbol{R}_{i,j}\overline{\boldsymbol{q}}\overline{\boldsymbol{q}}^T\boldsymbol{R}_{i,j}}{4N_0} - \boldsymbol{R}_{i,j} + \right. \\ &\left. \left(\frac{\overline{\boldsymbol{q}}^T\overline{\boldsymbol{R}}_{i,j}\overline{\boldsymbol{q}}}{2N_0}\right)^{-1} \frac{\boldsymbol{R}_{i,j}\overline{\boldsymbol{q}}\overline{\boldsymbol{q}}^T\boldsymbol{R}_{i,j}}{4N_0}\right) \propto \boldsymbol{R}_{i,j}\overline{\boldsymbol{q}}\overline{\boldsymbol{q}}^T\boldsymbol{R}_{i,j} - o(SNR^{-1})\boldsymbol{R}_{i,j}\end{aligned}$$

Note that if $\mathbb{I}(\boldsymbol{s}_i, \boldsymbol{s}_j) = 1$, $\boldsymbol{R}_{i,j}$ is rank-deficient, so $\boldsymbol{R}_{i,j}\overline{\boldsymbol{q}}\overline{\boldsymbol{q}}^T\boldsymbol{R}_{i,j} \succeq \boldsymbol{0}$. The Hessian matrix is non-negative, leading to the convexity (not strict convexity) of $\tilde{P}_{e,h}(\overline{\boldsymbol{q}})$.

Chapter 4

Doubly-Sparse Doubly-Selective (DSDS) Channel Estimator for Hybrid mmWave Massive MIMO

To facilitate the transceiver design including but not limited to the prior GBM and wGBM, the top priority is to acquire an accurate channel state information (CSI) [59]. However, compared to the cmWave MIMO systems, channel estimation for mmWave mMIMO faces unprecedented challenges. First, mmWave mMIMO typically adopts a hybrid structure for power and cost concerns [10], so the high-dimensional channel matrix has to be recovered via very few RF chains. Since the latter essentially determines the number of effective training symbols that can be transmitted simultaneously, it can take significant amount of time to transmit sufficient training symbols for mMIMO. When it comes to the mobile scenarios, the problem becomes even more challenging, because the channel turns out to be time-varying in the presence of Doppler.

As mmWave channels exhibit limited scattering, a unique sparsity holds in beamspace under mMIMO. Thanks to this sparsity, it may not be necessary to estimate the channel matrix element by element. Instead, one can resort to the compressed sensing (CS) theory to reduce the training

overhead while ensuring a high accuracy. Following this idea, in [13], a hierarchical beam training coupled with orthogonal matching pursuit (OMP) [60] is devised to estimate static narrowband mmWave channels. In [61], block-OMP (BOMP) is applied to estimate narrowband and time-varying mmWave channels. The static wideband channel estimation in the line-of-sight (LoS) scenarios is considered in [62], and the relevant work has been further extended to the non-LoS (NLoS) scenarios like [56] and [63], where OMP is applied either in the time-domain or the frequency-domain to assist channel estimation.

Due to the wideband nature of mmWave, the narrowband channel model suffers from severe limitations, motivating us to focus on the wideband channel model. Generally speaking, existing wideband channel estimation works can be divided into two main categories: time-domain estimation vs. frequency-domain. The former is to estimate all channel taps jointly, while the latter is to estimate individual subcarriers independently. By exploiting the sparsity in beamspace, both schemes achieve similar performance in the sense of the normalized mean square error (NMSE), with a largely reduced training overhead compared to the least-squares (LS) estimator. However, to effectively exploit the sparsity so that OMP could be applied, either the demanding storage requirement or the heavy computational burden is inevitable. On top of that, these works have not taken into account of the Doppler effects, rendering their feasibility in mobility scenarios questionable. To address these issues, there is an urgent need for a more generalized and more efficient channel estimation approach.

To achieve significant reduction in training overhead and computational complexity, we resort to the under-exploited delay-domain sparsity in combination with the well-known beamspace sparsity. Aiming at a high-performance and easy-to-implement channel estimator, a novel channel estimator is proposed by exploiting the double sparsity. As a matter of fact, the idea of using either the delay-domain sparsity or the double sparsity can be also found in some works, such as [64] and [65]. However, these works are not specifically designed for hybrid mMIMO, and their studied channels have not taken time selectivity into account. In fact, once the time selectivity is involved, how to exploit either the delay-domain sparsity or the beamspace sparsity becomes a thorny problem. Furthermore, the introduction of the hybrid structure makes channel

estimation a totally different topic as before, because the design flexibility is severely restricted by the hardware constraints. To address the aforementioned deficiencies, we propose a novel doubly-sparse approach to estimate mmWave mMIMO channels. Specifically, the so-called DSDS channel estimator comprises the following steps:

- To deal with the sparsity in delay domain, a special training pattern is judiciously designed to successfully separate each channel tap. Based on the energy detector, only a small proportion of channel taps will be identified effective regardless of Doppler effects and awaits a further processing.
- To deal with the beamspace sparsity, an enhanced OMP algorithm termed as A-BOMP is proposed to recover the beam direction. Given the maximum Doppler, A-BOMP can adjust basis matching and residue update with properly determined iterations, such that a high accuracy can be guaranteed even under strong Doppler effects.
- To jointly estimate the amplitudes and Doppler, repetitive steering-probing is applied based on the estimated beam direction. As a result, both the amplitudes and Doppler can be reliably estimated with low training overhead.

In the rest of chapter, we will detail these steps in sequence.

4.1 System and Channel Description

4.1.1 System Model

A mmWave mMIMO system is considered, where N_t and N_r antennas are employed at the transmitter (Tx) and receiver (Rx), respectively. Since the proposed channel estimation approach does not rely on the channel reciprocity, we simply assume channel estimation is implemented at Rx. For the power consumption and hardware cost concerns, mmWave mMIMO typically adopts a hybrid structure, in which the number of RF chains at the transceivers is much smaller than that of the antennas.

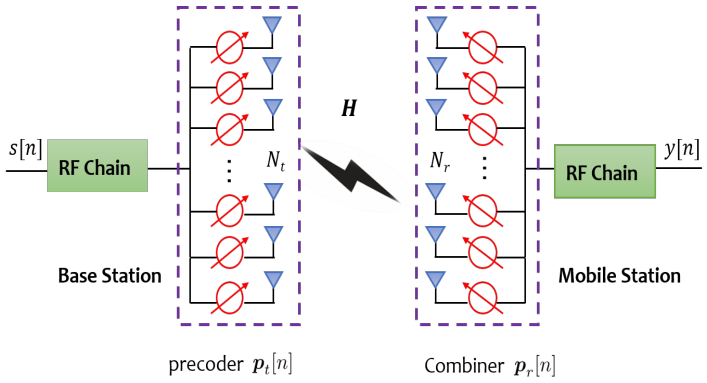

Figure 4.1: The system model of hybrid mmWave mMIMO with one RF chain deployed at transceivers.

Similar to [66], a fully-connected hybrid structure is studied here, where the RF chains and antennas are connected via a digitally controlled analog phase shifter (APS) network. Suppose each APS component has a resolution of b bits, then all adjustable angles are contained in

$$\mathcal{B} = \left\{0, 2\pi/2^b, \cdots, 2\pi(2^b-1)/2^b\right\} \tag{4.1}$$

with $\mid \mathcal{B} \mid = 2^b$. Accordingly, the angular quantization function is expressed as

$$\mathcal{Q}(x) = \mathcal{B}(i^*), i^* = \arg\min_i \operatorname{mod}\big(x - \mathcal{B}(i), 2\pi\big). \tag{4.2}$$

Let the transceivers each employ a single RF chain as shown in Fig. 4.1. Note that, since we focus on channel estimation in this chapter, this setup is without loss of generality and can be readily generalized to cope with arbitrary number of RF chains at the transceivers.

4.1.2 Geometric Channel

In this chapter, we adopt the modified Sen-Matolak channel model [67], which is an extension of the narrowband geometric model by taking the path delay and the Doppler effect into account. Denote the maximum number of delay taps as N_c. At time instant n, the sampled version of the tap-d channel $(0 \leq d < N_c)$ is given by

$$\boldsymbol{H}_d(n) = \sum_{p=1}^{P} \sqrt{\frac{N_t N_r}{P}} \alpha_p h(dT_s - \tau_p) \boldsymbol{a}_r(\theta_p) \boldsymbol{a}_t^*(\phi_p) e^{j\omega_p n} \tag{4.3}$$

where $\alpha_p \sim \mathcal{CN}(0,1)$ is the complex gain of the p-th path; $h(\cdot)$ is the pulse shaping filter response; τ_p is the propagation delay of the p-th path that obeys a uniform distribution on $[0,(N_c-1)T_s)$; θ_p and ϕ_p represent the angle of arrival (AoA) and angle of departure (AoD), respectively, both of which being modeled as uniformly distributed variables on $[0,2\pi)$. Define the system carrier frequency to be f_c, the velocity of light to be c_v, and the maximum relative velocity to be v_m. Then the normalized Doppler shift is $\omega_p = 2\pi f_c v_m T_s \sin(\theta_p)/c_v$. For notational simplicity, an array response generating function is defined as

$$\boldsymbol{f}_N(y) = \frac{1}{\sqrt{N}}\big[1, e^{j2\pi y}, \cdots, e^{j2\pi(N-1)y}\big]'. \tag{4.4}$$

With half-wavelength uniform linear arrays (ULAs) employed at the transceivers, we have $\boldsymbol{a}_t(\phi) = \boldsymbol{f}_{N_t}\big(\sin(\phi)/2\big)$ and $\boldsymbol{a}_r(\theta) = \boldsymbol{f}_{N_r}\big(\sin(\theta)/2\big)$.

4.1.3 Beamspace Representation

To simplify expression, one can rewrite the geometric model into a compact form [61]

$$\boldsymbol{H}_d(n) = \boldsymbol{A}_R \mathbf{diag}\big(\boldsymbol{g}_d(n)\big)\boldsymbol{A}_T^* \tag{4.5}$$

where $\boldsymbol{A}_T = \big[\boldsymbol{a}_t(\phi_1), \boldsymbol{a}_t(\phi_2), \cdots, \boldsymbol{a}_t(\phi_P)\big] \in \mathcal{C}^{N_t \times P}$ and $\boldsymbol{A}_R = \big[\boldsymbol{a}_r(\theta_1), \boldsymbol{a}_r(\theta_2), \cdots, \boldsymbol{a}_r(\theta_P)\big] \in \mathcal{C}^{N_r \times P}$ are steering matrices that remain unchanged during the channel estimation stage. The time-varying effects are incorporated in $\boldsymbol{g}_d(n)$ given by

$$\sqrt{\frac{N_t N_r}{P}}\big[\alpha_1 h(dT_s - \tau_1)e^{j\omega_1 n}, \cdots, \alpha_P h(dT_s - \tau_P)e^{j\omega_P n}\big]' \tag{4.6}$$

which contains the path gains at time instant n.

In Eq. (4.5), $\boldsymbol{A}_T$, $\boldsymbol{A}_R$ as well as $\boldsymbol{g}_d(n)$ are all associated with the physical channel taps, which are not always resolvable due to the finite resolution of the receiver in time and space, and thus cannot be directly estimated. To seek an equally general but more practical representation, we first construct the Tx-end and Rx-end angular dictionary matrices as in [13]

$$\boldsymbol{D}_t = \big[\boldsymbol{f}_{N_t}(0), \boldsymbol{f}_{N_t}(1/G_t), \cdots, \boldsymbol{f}_{N_t}\big((G_t-1)/G_t\big)\big] \tag{4.7a}$$

$$\boldsymbol{D}_r = \big[\boldsymbol{f}_{N_r}(0), \boldsymbol{f}_{N_r}(1/G_r), \cdots, \boldsymbol{f}_{N_r}\big((G_r-1)/G_r\big)\big] \tag{4.7b}$$

where G_t and G_r represent the size of corresponding dictionaries. Taking $\boldsymbol{D}_t$ as an example, it contains the steering vectors ranging from $[0, 2\pi]$ with resolution $2\pi/G_t$. As G_t approaches infinity, the resolution becomes zero, thus leading to a continuous dictionary. For practical implementation, most work show that setting G_t as $2 \sim 4$ times the array size can provide sufficient resolution for separating the AoAs/AoDs of the propagation paths. Based on the dictionary matrices, the channel representation in Eq. (4.5) can be re-expressed as

$$\boldsymbol{H}_d(n) = \boldsymbol{A}_R \mathbf{diag}\big(\boldsymbol{g}_d(n)\big) \boldsymbol{A}_T^* = \boldsymbol{D}_r \overline{\boldsymbol{H}}_d(n) \boldsymbol{D}_t^*. \tag{4.8}$$

Under the mMIMO setup, P propagation paths result in P dominant non-zero entries in $\overline{\boldsymbol{H}}_d$. As $\boldsymbol{D}_r$ and $\boldsymbol{D}_t$ are irrelevant to $\boldsymbol{H}_d$, $\overline{\boldsymbol{H}}_d$ essentially gathers the entire channel information that was originally contained by $\boldsymbol{A}_T$, $\boldsymbol{A}_R$ and $\boldsymbol{g}_d(n)$. Specifically, by omitting the time instant and assuming on-grid AoA/AoD pairs, $\forall p \in [1, P]$, $n_p = \frac{\phi_p}{2\pi/G_t}$, $m_p = \frac{\theta_p}{2\pi/G_t}$, $\overline{\boldsymbol{H}}_d(m_p, n_p) = \boldsymbol{g}_d[p]$. From this sense, $\overline{\boldsymbol{H}}_d$ can be interpreted as the channel representation in beamspace. Because a limited scattering effect in mmWave propagation leads to $P \ll G_r G_t$ [51], $\overline{\boldsymbol{H}}_d$ exhibits an evident sparse nature.[1]

Revisiting Eq. (4.3), the prior information available at both ends are N_t, N_r, N_c, the steering pattern of $\boldsymbol{a}_{t/r}$, while the remaining parameters are unknown to the transceivers, and thus have to be recovered via channel estimation. In the following, we will heavily rely on the beamspace representation to recover the beam direction (AoA and AoD), the beam amplitude, as well as the associated Doppler shift.

4.1.4 Input-output relationship

Let $s(n)$ be the training symbol at instant-n. At the Tx, $s(n)$ is first processed at the APS network, and the transmitted signal is $\boldsymbol{x}(n) = \boldsymbol{p}_t(n)s(n) \in \mathcal{C}^{N_t \times 1}$. Since each APS component

[1] In practice, the off-grid leakage may lead to extra non-zero entries in $\overline{\boldsymbol{H}}_d$. Since the leakage is typically very weak under mMIMO, the ensemble of dominant entries in $\overline{\boldsymbol{H}}_d$ is still similar to $\boldsymbol{g}_d$. Regardless of whether the non-zero entries of $\overline{\boldsymbol{H}}_d$ corresponds to a single channel path p or to some leakage terms, these entries are the resoluble ones that can be estimated.

can only adjust the phase, the probing vector $\boldsymbol{p}_t(n)$ bears the form as

$$\boldsymbol{p}_t(n) = \sqrt{1/N_t}\left[e^{j\alpha_1(n)}, e^{j\alpha_2(n)}, \cdots, e^{j\alpha_{N_t}(n)}\right]' \tag{4.9}$$

with $\alpha_i(n) \in \mathcal{B}, \forall i \in [1, N_t]$.

After channel propagation, the received signal is

$$\boldsymbol{r}(n) = \sum_{d=0}^{N_c-1} \boldsymbol{H}_d(n)\boldsymbol{x}(n-d) + \boldsymbol{\eta}(n) \tag{4.10}$$

which is the convolution of multiple time-varying channel taps. $\boldsymbol{\eta}(n) \sim \mathcal{CN}(\boldsymbol{0}, \sigma^2\boldsymbol{I}_{N_r})$ is the receiver noise vector. $\boldsymbol{r}(n)$ then goes through the Rx-end APS network, whose function is described by an $N_r \times 1$ probing vector $\boldsymbol{p}_R(n)$, so the received sample after APS becomes

$$y(n) = \sum_{d=0}^{N_c-1} \boldsymbol{p}_r^*(n)\boldsymbol{H}_d(n)\boldsymbol{p}_t(n-d)s(n-d) + \xi(n). \tag{4.11}$$

where $\xi(n) = \boldsymbol{p}_r^*(n)\boldsymbol{\eta}(n) \sim \mathcal{CN}(0, \sigma^2)$ remains white. Let $\overline{\boldsymbol{p}}_t(n) = \boldsymbol{D}_t\boldsymbol{p}_t(n)$ and $\overline{\boldsymbol{p}}_r(n) = \boldsymbol{D}_r\boldsymbol{p}_r(n)$. Based on the beamspace representation in Eq. (4.8), we have

$$y(n) = \sum_{d=0}^{N_c-1} \overline{\boldsymbol{p}}_r^*(n)\overline{\boldsymbol{H}}_d(n)\overline{\boldsymbol{p}}_t(n-d)s(n-d) + \xi(n). \tag{4.12}$$

Without loss of generality, we consider a general I-O relationship for the first frame only unless otherwise specified. The length-N_f training frame is simply denoted as $[s(0), s(1), \cdots, s(N_f-1)]$, and its specific form will be explained later. By concatenating all received samples, we write the I-O relationship in matrix form shown in Eq. (4.13) at the top of next page,

$$\begin{aligned}\boldsymbol{y} &= [y(0), y(1), \cdots, y(N_f-1)]' \\ &= \overline{\boldsymbol{P}}_r^* \begin{bmatrix} \overline{\boldsymbol{H}}_0(0) & \boldsymbol{0} & \boldsymbol{0} & \cdots & \boldsymbol{0} \\ \vdots & \overline{\boldsymbol{H}}_0(1) & \boldsymbol{0} & \cdots & \boldsymbol{0} \\ \overline{\boldsymbol{H}}_{N_c-1}(N_c-1) & \cdots & \ddots & \cdots & \vdots \\ \vdots & \ddots & \cdots & \ddots & \boldsymbol{0} \\ \boldsymbol{0} & \vdots & \overline{\boldsymbol{H}}_{N_c-1}(N_f-1) & \cdots & \overline{\boldsymbol{H}}_0(N_f-1) \end{bmatrix} \overline{\boldsymbol{P}}_t \begin{bmatrix} s(0) \\ \vdots \\ s(N_c-1) \\ \vdots \\ s(N_f-1) \end{bmatrix} + \boldsymbol{\xi}.\end{aligned} \tag{4.13}$$

$$\text{with } \overline{\boldsymbol{P}}_r^* = \begin{bmatrix} \overline{\boldsymbol{p}}_r^*(0) & \mathbf{0} & \cdots & \mathbf{0} \\ \mathbf{0} & \overline{\boldsymbol{p}}_r^*(1) & \cdots & \mathbf{0} \\ \vdots & \vdots & \ddots & \mathbf{0} \\ \mathbf{0} & \mathbf{0} & \cdots & \overline{\boldsymbol{p}}_r^*(N_f-1) \end{bmatrix} \text{ and } \overline{\boldsymbol{P}}_t = \begin{bmatrix} \overline{\boldsymbol{p}}_t(0) & \mathbf{0} & \cdots & \mathbf{0} \\ \mathbf{0} & \overline{\boldsymbol{p}}_t(1) & \cdots & \mathbf{0} \\ \vdots & \vdots & \ddots & \mathbf{0} \\ \mathbf{0} & \mathbf{0} & \cdots & \overline{\boldsymbol{p}}_t(N_f-1) \end{bmatrix}.$$

4.2 Exploit delay-domain sparsity

As described earlier, mmWave channels exhibit sparsity in beamspace. Apart from this well-known sparsity, this section will further show that mmWave channels exhibit sparsity in the delay domain as well. We first analyze why existing approaches fail to exploit the delay-domain sparsity, and then explain how one can effectively benefit this largely overlooked sparsity.

4.2.1 Sparsity in delay domain

To eliminate inter-frame interferences (IFIs) in block transmission, a commonly adopted approach amounts to zero-padding (ZP) a guard interval with length at least $(N_c - 1)$ to each frame. For example, the data-frame length is 512 in IEEE 802.11ad, while the prefix length can be up to 128. However, a long delay spread with large N_c due to the high symbol rate does not mean a rich multi-path environments. In fact, mmWave channels have very few dominant paths[2] Hence, a majority of the channel taps are actually too weak to be considered, rendering sparsity in the delay domain. To gain some intuitive insight, we plot the colormap of a randomly generated channel in Fig. 4.2, where the double sparsity in both the beamspace and delay domain can be clearly observed.

[2] typically $8 \sim 12$ even in "rich" scattering environments, and is much less in other environments [36].

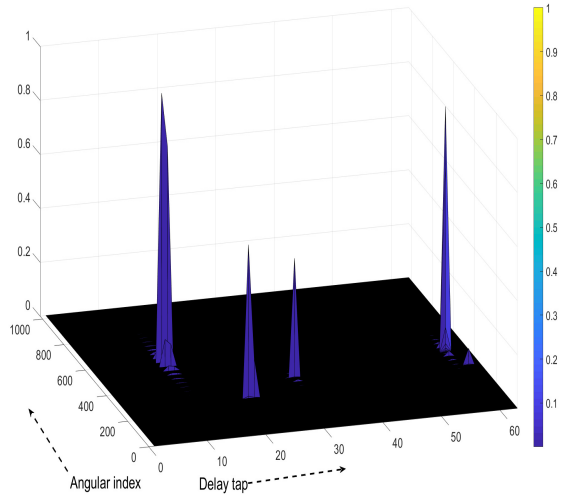

Figure 4.2: The delay-beamspace colormap of a randomly generated mmWave channel with $N_t = N_r = 32$, $N_c = 64$ and $P = 5$.

4.2.2 Conventional Training Pattern

The currently adopted training pattern [63] is given by

$$[s(0), s(1), \cdots, s(N_f - 1)] = \big[s_0, s_1, s_2, \cdots, s_{N-1}, \underbrace{0, \cdots, 0}_{N_c}\big]. \tag{4.14}$$

Specifically, each frame contains $N_f = N + N_c$ symbols, where N and N_c are the length of the data sequence and ZP, respectively. Clearly, the I-O relationship of this pattern still follows the general one in Eq. (4.13), but some specifics need to be clarified.

In wideband mmWave systems, symbols are pumped out at a very high rate, thus leaving insufficient buffer time for the APS network reconfiguration except for the ZP interval [56]. As a result, the probing vectors remain unchanged over the entire frame, that is

$$\boldsymbol{p}_{t/r}(n) = \boldsymbol{p}_{t/r}(0), \ \forall n \in [0, N_f). \tag{4.15}$$

Accordingly, $\overline{\boldsymbol{P}}_r^* = \boldsymbol{I}_{N_f} \otimes \overline{\boldsymbol{p}}_r^*(0)$ and $\overline{\boldsymbol{P}}_t = \boldsymbol{I}_{N_f} \otimes \overline{\boldsymbol{p}}_t(0)$.

Although the introduction of ZP ensures IFI-free, N_c channel taps remain unresolvable after convoluting with the training sequence. In consequence, channel estimation requires joint

processing across all taps, leading to high storage demand and heavy computational burden. More importantly, exploiting the delay-domain sparsity becomes an intractable task.

4.2.3 Proposed training pattern

To avoid these limitations, there is a great urgency to devise a new training pattern, by which the delay-domain sparsity could be exploited to facilitate channel estimation, and the pattern itself must be friendly to implementation. To this end, a new training pattern is designed as follows

$$[s(0), s(1), \cdots, s(N_f-1)] = \big[\underbrace{s_0, \overbrace{0, \cdots, 0}^{N_c-1}}_{(1)} \Big| \underbrace{s_1, \overbrace{0, \cdots, 0}^{N_c-1}}_{(2)} \Big| \cdots\cdots \Big| \underbrace{s_{L-1}, \overbrace{0, \cdots, 0}^{N_c-1}}_{(L)}\big]. \quad (4.16)$$

As can be seen, each frame is further divided into $L = N_f/N_c$ subframes[3] . Owing to the ZP in each subframe, sufficient buffer time is left to reconfigure the APS network after each non-zero training symbol. In other words, the probing vectors can be updated L times per frame, i.e.,

$$\boldsymbol{p}_{t/r}(n) = \boldsymbol{p}_{t/r}\big(N_c\lfloor n/N_c\rfloor\big), \forall n \in [0, N_f). \quad (4.17)$$

An interesting fact is that, when it comes to the frequency-selective channel estimation in conventional MIMO setup, the training pattern in Eq. (4.16) has been proved optimal in the sense of both the mean squared error (MSE) and system mutual information [68]. Before taking a closer look at the I-O relationship with the new pattern, we first make the following definition.

Random-probing vector*: At the random-probing stage, the probing vectors are generated by randomly adjusting the angle of each APS component from $\mathcal{B}$. The resultant vector is termed as the random-probing vector and denoted as*

$$\boldsymbol{p}^R_{t/r}(l) = \boldsymbol{p}_{t/r}(lN_c + n_c), (l < L, n_c < N_c). \quad (4.18)$$

Applying random probing is simply because no prior CSI is available at this stage. Note that, the above definition implies that $\boldsymbol{p}^R_{t/r}$ possesses both the randomness and subframe-updatability

[3] Without loss of generality, L is assumed to be an integer here. If N_f/N_c is not an integer, one can simply use $L = \lfloor N_f/N_c\rfloor$.

property. Applying a similar notational change to $\overline{\boldsymbol{p}}_{t/r}$, $\overline{\boldsymbol{P}}_r^*$ becomes Eq. (4.19),

$$\overline{\boldsymbol{P}}_r^* = \begin{bmatrix} \boldsymbol{I}_{N_c} \otimes \left(\overline{\boldsymbol{p}}_r^R(0)\right)^* & \boldsymbol{0} & \cdots & \boldsymbol{0} \\ \boldsymbol{0} & \boldsymbol{I}_{N_c} \otimes \left(\overline{\boldsymbol{p}}_r^R(1)\right)^* & \cdots & \boldsymbol{0} \\ \vdots & \vdots & \ddots & \boldsymbol{0} \\ \boldsymbol{0} & \boldsymbol{0} & \cdots & \boldsymbol{I}_{N_c} \otimes \left(\overline{\boldsymbol{p}}_r^R(L-1)\right)^* \end{bmatrix} \tag{4.19}$$

and $\overline{\boldsymbol{P}}_t$ is obtained likewise. Substituting the new $\overline{\boldsymbol{P}}_r^*$ and $\overline{\boldsymbol{P}}_t$, together with the training frame into Eq. (4.13), the received signal becomes

$$y(lN_c + n_c) = \left(\overline{\boldsymbol{p}}_r^R(l)\right)^* \overline{\boldsymbol{H}}_{n_c}(lN_c + n_c)\overline{\boldsymbol{p}}_t^R(l)s_l + \xi(lN_c + n_c). \tag{4.20}$$

Clearly, the received samples are now associated with a single channel tap. Hence, our proposed pattern facilitates separating channel taps and thus rendering it possible to exploit the delay-domain sparsity easily. Since the success of tap separation does not rely on the non-zero training symbol s_l in Eq. (4.16), s_l is set as 1 in the rest of chapter without loss of generality.

4.2.4 Identification of effective taps

To determine the existence of tap-d channel, we gather all $\overline{\boldsymbol{H}}_d$-related samples, i.e., $y(lN_c+d)$, $\forall l \in [0, L-1]$. If at least one dominant path exists in the tap-d channel, $y(lN_c + d)$ includes both the signal and noise parts. Otherwise, $y(lN_c + d)$ contains noise only. Hence, detecting the existence of the tap-d channel is a binary hypothesis testing problem that can be dealt with via energy detector. We first average the power of all samples associated with $\overline{\boldsymbol{H}}_d$, and get the test statistics (TS) and its normalized version nTS as

$$Y_d = \frac{1}{L}\sum_{l=0}^{L-1} \left|y(lN_c + d)\right|^2 \tag{4.21a}$$

$$\overline{Y}_d = \frac{Y_d - \sigma^2}{\max\limits_{0 \le m < N_c} (Y_m - \sigma^2, 0)}. \tag{4.21b}$$

When applying CS, random probing is necessary in estimating both the time-invariant and time-varying channels. While for the latter, another important function of random probing is to remain robust against Doppler.

Proposition 4.1 [Validity of test statistics with Doppler]: With sufficient random probings, the test statistics Y_d is approximately irrelevant to the channel's time variation.

Proof. Let $n = lN_c + d$ and $g_{d,p}(n)$ be the p-th element of $\boldsymbol{g}_d(n)$, then

$$\begin{aligned} y(n) &= \sum_{d=0}^{N_c-1} \overline{\boldsymbol{p}}_r^*(n)\overline{\boldsymbol{H}}_d(n)\overline{\boldsymbol{p}}_t(n-d) + \xi(n) \\ &= \sum_{p=1}^{P} \left(\boldsymbol{p}_r^R(l)\right)^* \boldsymbol{a}_r(\theta_p)\boldsymbol{a}_t^*(\phi_p)\boldsymbol{p}_t^R(l) g_{d,p}(n) + \xi(n). \end{aligned} \tag{4.22}$$

Denote $\rho_p(l) = (\boldsymbol{p}_R^R(l))^* \boldsymbol{a}_r(\theta_p)\boldsymbol{a}_t^H(\phi_p)\boldsymbol{p}_T^R(l)$. By using $g_{d,p}(n) = g_{d,p}(0)e^{j\omega_p n}$, we have

$$\begin{aligned} |y(n)|^2 = &\sum_{p=1}^{P} |\rho_p(n) g_{d,p}(0)|^2 + 2\mathcal{R}\Big\{ \sum_{p=1}^{P} \rho_p(l) g_{d,p}(0)\xi(n) e^{j\omega_{p_1} n} \Big\} \\ &+ 2\mathcal{R}\Big\{ \sum_{p_1} \sum_{p_2} \rho_{p_1}(l) g_{d,p_1}(0) \rho_{p_2}^*(l) g_{d,p_2}^*(0) e^{j(\omega_{p_1} - \omega_{p_2})n} \Big\}. \end{aligned} \tag{4.23}$$

Since $\boldsymbol{p}_t^R$ and $\boldsymbol{p}_r^R$ are random probing vectors with zero mean, it can be readily verified $\mathbb{E}\{\rho_p(l)\} = 0, \forall p \in [1, P]$. By averaging sufficient $|y(n)|^2$ terms, the last two terms in Eq. (4.23) approach zero, thus the TS becomes irrelevant to ω_p. □

Proposition 4.1 guarantees the exploitation of the delay-domain sparsity regardless of Doppler effects. With the energy detector, the effective taps can be roughly selected as

$$\mathcal{P}_1 = \left\{ d \;\middle|\; \overline{Y}_d \geq \mu \right\} \bigcap \left\{ d \;\middle|\; Y_d > \sigma^2 \right\}, \tag{4.24}$$

where μ is the threshold[4] . To avoid extreme cases where $\mathbf{cal}(\mathcal{P}_1)$ is either 0 or unreasonably large, a tuning procedure is added, and the ultimately determined taps are given by

$$\mathcal{P} = \begin{cases} \mathcal{P}_1, \quad 0 < \mathbf{cal}(\mathcal{P}_1) \leq A \\ \left\{ d | \overline{Y}_d \geq \overline{\lambda}_A \right\}, \ \mathbf{cal}(\mathcal{P}_1) > A \\ \left\{ d | Y_d \geq \lambda_A \right\}, \ \ \mathbf{cal}(\mathcal{P}_1) = 0. \end{cases} \tag{4.25}$$

[4] Evidently, the energy detector is somewhat heuristic. Recall that the energy detector actually plays the role of a binary classifier, a promising direction is to seek the power of deep neural networks. Specifically, given the channel model, a bunch of synthesized data can be generated to train the network for classification (tap detection) in a supervised manner. The offline trained network could then be used for online prediction.

with λ_A and $\overline{\lambda}_A$ representing the A-th largest TS and nTS, respectively.

Up till now, we have accomplished the first part of the random-probing stage. Summarizing, the main steps can be described as follows:

- Transmit judiciously designed training frames with random APS probing.
- Calculate the TS/nTS for each channel tap based on the corresponding received samples.
- Determine the non-negligible channel taps based on the energy detector $\mathcal{P}$.

4.3 Exploiting the Beamspace Sparsity

As outlined in Section II, the beamspace channel exhibits sparsity under mMIMO settings. Therefore, instead of estimating the original geometric channel matrix $\boldsymbol{H}_d$ with dimension $N_t N_r$, we estimate the sparse beamspace channel $\overline{\boldsymbol{H}}_d$. Since the time variation imposes a great difficulty in recovering the exact values of non-zero entries from $\overline{\boldsymbol{H}}_d$, we focus on locating the non-zero entries (essentially the angle support) first in this section, and leaving the estimation of exact values to the next section.

4.3.1 Sparse transformation

After tap detection, n_c out of N_c taps are recognized effective, with their indices collected by $\mathcal{D} = \{d_1, d_2, \cdots, d_D\}$. Using the samples already obtained at the random-probing stage, we proceed to determine the angle support for those taps belonging to $\mathcal{D}$. It has to be stressed that this step does not require extra training frames.

Due to the similarity, we take tap-d_i ($d_i \in \mathcal{D}$) for example, and the subscript of d_i is omitted for brevity. To apply CS, let us first derive the sparse representation for received samples. Stacking all $\overline{\boldsymbol{H}}_d$-related samples from $\boldsymbol{y}$ yields

$$\boldsymbol{y}_d = [y(d), y(N_c + d), \cdots, y((L-1)N_c + d)]^{'}. \tag{4.26}$$

Denoting $n_l = lN_c+d\ \big(\forall l \in [0, L)\big)$ and using matrix equality $\mathrm{vec}(\boldsymbol{ABC}) = (\boldsymbol{C}^{'} \otimes \boldsymbol{A})\mathrm{vec}(\boldsymbol{B})$, $y(n_l)$ can be rewritten as

$$y(n_l) = \underbrace{\left(\left(\overline{\boldsymbol{p}}_t^R(l)\right)^{'} \otimes \left(\overline{\boldsymbol{p}}_r^R(l)\right)^*\right)}_{\boldsymbol{\psi}(l)} \underbrace{\left(\mathbf{vec}\left(\overline{\boldsymbol{H}}_d(n_l)\right)\right)}_{\overline{\boldsymbol{h}}_{d(n_l)}} + \xi(n_l). \tag{4.27}$$

Neglecting the noises temporarily for brevity, $\boldsymbol{y}_d$ can be further expressed as

$$\boldsymbol{y}_d = \underbrace{\begin{bmatrix} \boldsymbol{\psi}(0) & \mathbf{0} & \cdots & \mathbf{0} \\ \mathbf{0} & \boldsymbol{\psi}(1) & \cdots & \mathbf{0} \\ \vdots & \vdots & \ddots & \vdots \\ \mathbf{0} & \mathbf{0} & \cdots & \boldsymbol{\psi}(L-1) \end{bmatrix}}_{\boldsymbol{\Psi}} \underbrace{\begin{bmatrix} \overline{\boldsymbol{h}}_d(n_0) \\ \overline{\boldsymbol{h}}_d(n_1) \\ \vdots \\ \overline{\boldsymbol{h}}_d(n_{L-1}) \end{bmatrix}}_{\overline{\boldsymbol{h}}_d}. \tag{4.28}$$

In the special case of time-invariant channels, all $\overline{\boldsymbol{h}}_d(n_l)$'s are exactly the same [61], thus giving rise to

$$\boldsymbol{y}_d = \begin{bmatrix} \boldsymbol{\psi}(0) \\ \boldsymbol{\psi}(1) \\ \vdots \\ \boldsymbol{\psi}(L-1) \end{bmatrix} \overline{\boldsymbol{h}}_d(n_0). \tag{4.29}$$

Determining the angle support of $\overline{\boldsymbol{H}}_d$ is equivalent to locating non-zero entries from the G_tG_r-dimensional vector $\overline{\boldsymbol{h}}_d$. Since $P \ll G_tG_t$, the "localization" can be effectively solved via OMP, through which $\mathcal{O}(P \log G_tG_r)$ instead of $\mathcal{O}(G_tG_r)$ samples suffice to guarantee a high accuracy.

However, Eq. (4.29) is no longer valid in the presence of Doppler shifts, motivating us to restudy the more general Eq. (4.28). Because $\overline{\boldsymbol{h}}_d$ remains sparse for $LP \ll LG_tG_r$, a natural option would be OMP as well. Reminisce that the variations of AoAs/AoDs are negligible during the channel estimation, thus a common angle support is shared by all $\overline{\boldsymbol{h}}_d(n_l)$'s. However, OMP cannot exploit such a unique structure because it treats $\boldsymbol{h}_d(n_l)$ as a generic sparse

vector. Fortunately, by utilizing the unique property of $\overline{\boldsymbol{h}}_d(n_l)$, a more general block-sparse representation can be derived. Specifically, constructing such a permutation matrix $\boldsymbol{P}$ satisfying $\boldsymbol{P}[:,(i-1)G_tG_r+j\big] = \boldsymbol{I}_{G_tG_r}[:,(j-1)G_tG_r+i]$ [69], $\boldsymbol{y}_d$ can be decomposed as

$$\boldsymbol{y}_d = \big(\boldsymbol{\Psi}\boldsymbol{P}\big)\cdot\big(\boldsymbol{P}^{'}\overline{\boldsymbol{h}}_d\big). \tag{4.30}$$

The "new" sparse signal and sensing matrix then become

$$\widetilde{\boldsymbol{h}}_d = \boldsymbol{P}^{'}\overline{\boldsymbol{h}}_d = \big[\widetilde{\boldsymbol{h}}_{d,1}^{'},\widetilde{\boldsymbol{h}}_{d,_2}^{'},\cdots,\widetilde{\boldsymbol{h}}_{d,G_tG_r}^{'}\big]^{'} \tag{4.31a}$$

$$\widetilde{\boldsymbol{\Psi}} = \boldsymbol{\Psi}\boldsymbol{P} = \big[\widetilde{\boldsymbol{\Psi}}_1,\widetilde{\boldsymbol{\Psi}}_2,\cdots,\widetilde{\boldsymbol{\Psi}}_{G_tG_r}\big] \tag{4.31b}$$

where $\widetilde{\boldsymbol{h}}_{d,i} = \big[\overline{h}_{d,i}(n_0),\overline{h}_{d,i}(n_1),\cdots,\overline{h}_{d,i}(n_{L-1})\big]^*$ and $\widetilde{\boldsymbol{\Psi}}_i = \mathbf{diag}\big[\psi_i(0),\psi_i(1),\cdots,\psi_i(L-1)\big]$, $\forall i\in[1,G_tG_r]$, with $\overline{h}_{d,i}(n_j)$ and $\psi_i(l)$ being the i-th entry of $\overline{\boldsymbol{h}}_d(n_j)$ and $\boldsymbol{\psi}(l)$, respectively. Unlike the original $\overline{\boldsymbol{h}}_d$, the rearranged $\widetilde{\boldsymbol{h}}_d$ exhibits block sparsity [70]. More importantly, the block sparsity of $\widetilde{\boldsymbol{h}}_d$ equals to the sparsity of $\overline{\boldsymbol{h}}_d(n_l)$.

Towards the issue of block or structured compressed sensing, quite a few methods are available in the existing literature. To be more specific, these methods can be categorized into the Bayesian type and non-Bayesian type. For the former, representative solutions include block-sparse Bayesian learning [71, 72], message passing based compresses sensing [73, 74], etc; while for the latter, representative solutions include structured Lasso [75], block OMP [76], etc. In this chapter, we choose the OMP-based method similar to many related works [13, 62, 56]. It should be mentioned that this choice has no optimality guarantee, and other methods could be attempted in the future.

Although block OMP seems to be a powerful tool to estimate $\widetilde{\boldsymbol{h}}_d$ in Eq. (4.28), accurate identification of the non-zero support still encounters two major difficulties:

P.1 How to properly set the number of iterations when applying CS algorithms.

P.2 How to avoid the potential degradation resulting from the strong Doppler effects.

To address these problems, we propose an algorithm termed as adaptive-block OMP (A-BOMP) that will be detailed next.

4.3.2 A-BOMP

When recovering the sparse signal via CS, a proper number of iterations is equal to (or a slightly higher than) the signal sparsity. Unfortunately, the actual sparsity of $\widetilde{\boldsymbol{h}}_d$ is unknown. To reduce the risks of estimation loss, most works adopt large iterations. However, once the iterations severely mismatch the signal sparsity, it may result in increased computational complexity and potential over-fitting errors. Albeit not knowing the sparsity either, we will show that, it is possible to set iterations properly after tap identification.

Since D out of N_c taps are regarded effective, the number of beams should be no greater than D, thus the signal sparsity is upper bounded by D. Surprisingly, the upper bound could be set even smaller for implementation. To verify this, we first provide the following result

Lemma 4.1: For the wideband channel with N_c taps, the probability that k out of K ($k \leq K$) beams reside within one tap is approximated as

$$P(K,k) = C_K^k \left(\frac{1}{N_c}\right)^k \left(\frac{N_c-1}{N_c}\right)^{K-k}. \tag{4.32}$$

A brief illustration is made under $N_c = 128$ and $K = 10$. In this case, $P(10,4) < 10^{-5}$, implying that it is virtually impossible for one tap containing over 3 beams, so k is expected to be smaller than 4, regardless to say 10 for $P(10,10) < 10^{-18}$. Combing above discussions, a proposition is made below to provide guidance on iterations setting:

Proposition 4.2 [Number of iterations]: *Let P_T be a small threshold (e.g, 10^{-3}) and D be the number of effective taps after tap identification. A proper iterations can be set as $k-1$, where k is the smallest integer satisfying $P(D,k) < P_T$.*

To address P.2, DPC-BEM model was used in [61] to capture the variations before implementing BOMP. This approach can dramatically lower the deterioration, but has two drawbacks. First, the estimation performance is heavily dependent on the basis order. Secondly, to construct orthogonal DPC basis, a large-scale eigenvalue decomposition (EVD) has to be involved [77] with complexity $\mathcal{O}(L^3)$. To lower complexity while remaining robustness against Doppler, A-BOMP is proposed with its pseudo-code presented in **Algorithm 2**. In A-BOMP, each outer iteration consists of three parts:

$\mathbf{S}_1$ (Lines.4-9) *partial basis matching*: select the angle pair having the largest sum of grouping correlations, and make sure that there is no overlapping with the selected ones.

$\mathbf{S}_2$ (Lines.10-16) *resolution refinement*: re-construct sensing matrix associated with the selected angle pair, and implement estimation procedure like $\mathbf{S}_1$ to refine resolution.

$\mathbf{S}_3$ (Lines.17-21) *partial residue update*: estimate the coefficients by the least-squared (LS) estimator, then update the residue $\boldsymbol{r}_d$ by subtracting the projection of each group.

In A-BOMP, another key parameter is the group size S (equivalent to the group number G). In the presence of Doppler, the size of the non-zero support always exceeds the number of measurements. In this case, accurately localizing the non-zero support is already challenging, not to mention to the recovery of the entire vector. The only exception is in the absence of Doppler, where the uncertainty could vanish when sufficient training frames are available.

The great shortage of measurements forces us to "shrink" the non-zero support. To this end, we divide $\widetilde{\boldsymbol{h}}_{d,i}$ defined in Eq. (4.31a) into S groups, and those entries belonging to one group are highly correlated thus being treated equally. Therefore, the group division essentially performs the signal compression, and S is nothing but the coherent interval.

Algorithm 2 Proposed A-BOMP Algorithm

Input: $\boldsymbol{y}_d$, $\widetilde{\boldsymbol{\Psi}}_d$, block-sparsity $\mathcal{K}$, group size S, group number $G = \frac{L}{S}$, threshold ϵ

Output: $\widetilde{\mathcal{A}}_d$ and $\widetilde{\mathcal{D}}_d$

Initialization: $\boldsymbol{r}_d = \boldsymbol{y}_d$, $C = 0$, $\beta = \infty$, $\boldsymbol{\Phi} = \varnothing$, $x = x_0 = 0$.
while $C < \mathcal{K}$ and $\beta > \epsilon$ **do**
  $C = C + 1$
  $g_i = \arg\max_{g} \sum_{i=1}^{G} \frac{\|[\widetilde{\boldsymbol{\Psi}}^*_{d,g} \boldsymbol{r}_d]((i-1)S+1:iS)\|_1}{\|\widetilde{\boldsymbol{\Psi}}_{d,g}\|_F}$
  $n_R = \lceil g_i / G_t \rceil$ and $n_T = g_i - (n_R - 1)G_t$.
  if $\exists\, i, \mathrm{mod}(\mid n_D/n_R - \mathcal{D}(i)/\mathcal{A}(i) \mid, G_t/G_r) \leq 1$ **then**
    goto 2
  end if
  $\mathcal{A} = \{\mathcal{A}, n_R\}$, $\mathcal{D} = \{\mathcal{D}, n_T\}$
  $\widehat{\boldsymbol{A}}_T = [\boldsymbol{f}_{N_t}(\frac{n_T - 1}{G_t} + \frac{2j_T}{G_t^2})]_{j_T \in [-\frac{G_t}{2}:1:\frac{G_t}{2}-1]}$
  $\widehat{\boldsymbol{A}}_R = [\boldsymbol{f}_{N}(\frac{n_R - 1}{G_r} + \frac{2j_R}{G_R^2})]_{j_R \in [-\frac{G_r}{2}:1:\frac{G_r}{2}-1]}$
  $\widehat{\boldsymbol{\psi}}[n_i] = (\boldsymbol{p}_A^{'}[n_i] \otimes \boldsymbol{w}_A^*[n_i])(\widehat{\boldsymbol{A}}_T^* \otimes \widehat{\boldsymbol{A}}_R)_{i=1\sim L}$
  $\widehat{\boldsymbol{\Psi}}_{d,i} = \mathbf{diag}\big[\widehat{\boldsymbol{\psi}}[n_1](i), \cdots, \widehat{\boldsymbol{\psi}}[n_{G_t G_r}](i)\big]_{i=1\sim G_t G_r}$
  $\widehat{g}_i = \arg\max_{g} \sum_{i=1}^{G} \frac{\|[\widehat{\boldsymbol{\Psi}}^*_{d,g} \boldsymbol{r}_d]((i-1)S+1:mS)\|_1}{\|\widehat{\boldsymbol{\Psi}}_{d,g}\|_F}$
  $\widehat{n}_R = \lceil \widehat{g}_i / G_t \rceil$ and $\widehat{n}_T = \widehat{g}_i - (\widehat{n}_R - 1)G_t$.
  $\boldsymbol{\Phi} = \big[\boldsymbol{\Phi}, \boldsymbol{M}(\boldsymbol{f}^*_{N_t}(\frac{G_t(n_T-1)+\widehat{n}_T}{G_t^2}) \otimes \boldsymbol{f}_{N_r}(\frac{G_r(n_R-1)+2\widehat{n}_R}{G_r^2})\big]$
  for $j = 1 : G$ **do**
    $\boldsymbol{j} = (j-1)S + 1 : mS$
    $x = x + \|\boldsymbol{\Phi}(\boldsymbol{j}, :)^{\dagger} \boldsymbol{y}(\boldsymbol{j})\|_2$
    $\boldsymbol{r}_d(\boldsymbol{j}) = \boldsymbol{y}_d(\boldsymbol{j}) - \boldsymbol{\Phi}(\boldsymbol{j}, :)\boldsymbol{\Phi}(\boldsymbol{j}, :)^{\dagger} \boldsymbol{y}(\boldsymbol{j})$
  end for
  $\beta = |x - x_0|/x$
  $x_0 = x$, $x = 0$
  $\widetilde{\mathcal{A}}_d = \big\{\widetilde{\mathcal{A}}_d, \frac{2\pi G_r(n_R-1)+\widehat{n}_R}{G_r^2}\big\}$ and $\widetilde{\mathcal{D}}_d = \big\{\widetilde{\mathcal{D}}_d, \frac{2\pi G_t(n_T-1)+\widehat{n}_T}{G_t^2}\big\}$
end while

Proposition 4.3: [Determination of the group size] *Let τ denote a high-correlation coefficient (e.g, 0.707). A proper group size can be set as the largest S satisfying* $\cos(\omega_{max}N_cS) \leq \tau$ *and* $\omega_{max}N_cS \leq \pi/2$.

Proposition 4.3 indicates that a smaller ω_{max} results in a larger S. For $\omega_{max} = 0$, i.e., a time-invariant channel, A-BOMP degenerates to BOMP as $G = L/S = 1$. Besides, one can readily verify that estimating $\widetilde{\boldsymbol{h}}_d$ via BOMP and estimating $\overline{\boldsymbol{h}}_d(n_i)$ via OMP are equivalent. Compared to BOMP, A-BOMP only introduces a few small-scale matrix inversions, and simulations show that such minimal computational cost will bring in a significantly improved accuracy. Based on the output of A-BOMP, the steering matrices for tap-d channel are estimated as

$$\widetilde{\boldsymbol{A}}_{r,d}=\big[\boldsymbol{f}_{N_r}\big(\widetilde{\mathcal{A}}_d(1)/2\pi\big),\cdots,\boldsymbol{f}_{N_r}\big(\widetilde{\mathcal{A}}_d(c_d)/2\pi\big)\big] \tag{4.33a}$$

$$\widetilde{\boldsymbol{A}}_{t,d}=\big[\boldsymbol{f}_{N_t}\big(\widetilde{\mathcal{D}}_d(1)/2\pi\big),\cdots,\boldsymbol{f}_{N_t}\big(\widetilde{\mathcal{D}}_d(c_d)/2\pi\big)\big] \tag{4.33b}$$

with $c_d = \mathbf{cal}(\widetilde{\mathcal{A}}_d)$. The approximate beamspace representation for tap-d bears a form as

$$\widetilde{\boldsymbol{H}}_d(n) = \widetilde{\boldsymbol{A}}_{r,d}\mathbf{diag}(\widetilde{\boldsymbol{g}}_d(n))\widetilde{\boldsymbol{A}}_{t,d}^*. \tag{4.34}$$

where $\widetilde{\boldsymbol{g}}_d(n)$ consists of unknown path gains. Despite that both the amplitudesand angle support can be simultaneously obtained via OMP in time-invariant channels, for the more general time-varying channels, an additional stage is still necessary to estimate the amplitudes and Doppler.

So far, we have completed the second part of the random-probing stage. Summarizing, the main steps are listed as

- Stack the receive samples for each identified tap.
- Transform the samples into a generic block-sparse form.
- Determine the iterations and group size for A-BOMP.
- Apply A-BOMP to estimate the angle support.

4.4 Joint Estimation of Path Gain and Doppler

At the random-probing stage, the effective taps are identified with their angle support obtained as well. In this section, we proceed to estimate the remaining unknown path gain/Doppler at the so-termed steering-probing stage.

4.4.1 Steering probing design

To accurately estimate path gains and Doppler shifts, steering-probing will be implemented based on the estimated beam direction. Specifically, for tap-d channel, construct set $\mathcal{I}_d$ whose i-th element is $(\mathcal{A}_d(i), \mathcal{D}_d(i))$. Because of the off-grid issues in beamspace and delay domain, different $\mathcal{I}_d$'s may share the same element, thus we get their union as

$$\mathcal{I} = \mathcal{I}_{d_1} \bigcup \mathcal{I}_{d_2} \bigcup \cdots \bigcup \mathcal{I}_{d_D}. \tag{4.35}$$

Further, all AoAs and AoDs are individually extracted from $\mathcal{I}$ and captured by $\mathcal{I}_A$ and $\mathcal{I}_D$, respectively. To facilitate beamforming, only the discrete AoD indices need to be fed back. Without causing ambiguity, we reset the time instant at the steering-probing stage, and making the following definition.

***Steering-probing vector**: At the steering-probing stage, denote $\boldsymbol{p}_t^S(n)$ and $\boldsymbol{p}_t^S(n)$ to be the RF vectors at time instant n. To improve receive SNR, $p_{p,t}^S(n)$ (the p-th element of $\boldsymbol{p}_t^S(n)$) and $p_{q,r}^S(n)$ (the q-th element of $\boldsymbol{p}_r^S(n)$) are designed as*

$$p_{p,t}^S(n) = \frac{1}{\sqrt{N_t}} e^{jQ\left((p-1)\mathcal{I}_D(\widehat{n})\right)}, p \in [1, N_t] \tag{4.36a}$$

$$p_{q,r}^S(n) = \frac{1}{\sqrt{N_r}} e^{jQ\left((q-1)\mathcal{I}_A(\widehat{n})\right)}, q \in [1, N_r] \tag{4.36b}$$

with $\widehat{n} = mod\big(\lfloor n/N_c \rfloor, cal(\mathcal{I})\big)$. As can be seen from Eq. (4.36), the probing vectors repeat every $cal(\mathcal{I})$ subframes, so that that each beam will be steered once during each polling.

4.4.2 Path gain/Doppler estimation

At the i-th polling, stacking all tap-d related samples yields

$$\boldsymbol{y}_{d,i} = \big[y\big(d+n_{i,0}\big), \cdots, y\big(d+n_{i,|\mathcal{I}|-1}\big)\big]^{'} \tag{4.37}$$

where $n_{i,j} = N_c j + \mathbf{cal}(\mathcal{I}) N_c i, \forall j \in [0, cal(\mathcal{I}))$. Using the compact beamspace representation obtained in Eq. (4.34), each sample in $\boldsymbol{y}_{d,i}$ is approximately equivalent to

$$\begin{aligned} y(n_{i,j}+d) &\approx (\boldsymbol{p}_r^S(n_{i,j}))^* \widetilde{\boldsymbol{A}}_{r,d} \mathbf{diag}(\widetilde{\boldsymbol{g}}_d(n_{i.j}+d)) \widetilde{\boldsymbol{A}}_{t,d}^* \boldsymbol{p}_t^S(n_{i,j}) + \xi(n_{i,j}+d) \\ &= \mathbf{vec}^{'}(\mathbf{diag}(\widetilde{\boldsymbol{g}}_d(n_{i,j}+d))) \boldsymbol{m}_d(n_{i,j}) + \xi(n_{i,j}+d) \end{aligned} \tag{4.38}$$

where $\boldsymbol{m}_d(n_{i,j}) = \big((\boldsymbol{p}_t^S(n_{i,j}))^{'} \widetilde{\boldsymbol{A}}_{t,d}^*\big) \otimes \big((\boldsymbol{p}_r^S(n_{i,j}))^* \widetilde{\boldsymbol{A}}_{r,d}\big)$. By capturing the amplitudes with the one sampling in the middle of current polling, $\boldsymbol{y}_{d,i}$ can be approximately represented as

$$\boldsymbol{y}_{d,i} \approx \underbrace{\begin{bmatrix} \boldsymbol{m}_d\big(n_{i,0}\big) \\ \boldsymbol{m}_d\big(n_{i,1}\big) \\ \vdots \\ \boldsymbol{m}_d\big(n_{i,cal(\mathcal{I})-1}\big) \end{bmatrix}}_{\boldsymbol{M}_{d,i}} \mathrm{vec}\Big(\mathbf{diag}\big(\boldsymbol{g}_d(\overline{n}_i)\big)\Big) + \boldsymbol{\xi}_{d,i} \tag{4.39}$$

with $\overline{n}_i = \big(n_{i,0}+n_{i,\mathbf{cal}(\mathcal{I})-1}\big)/2+d$ and $\boldsymbol{\xi}_{d,i} = [\xi(n_{i,0}+d), \xi(n_{i,1}+d), \cdots, \xi(n_{i,\mathbf{cal}(\mathcal{I})-1}+d)]^{'}$. Let $\widetilde{\boldsymbol{M}}_{d,i} = \big[\boldsymbol{M}_{d,i}[:,1^2], \boldsymbol{M}_{d,i}[:,2^2] \cdots, \boldsymbol{M}_{d,i}[:,C_d^2]\big]$, then Eq. (4.39) equals to

$$\boldsymbol{y}_{d,i} \approx \widetilde{\boldsymbol{M}}_{d,i} \boldsymbol{g}_d(\overline{n}_i) + \boldsymbol{\xi}_{d,i} \tag{4.40}$$

Since $\mathbf{cal}(\mathcal{I}) \geq c_d$, $\boldsymbol{g}_d(\overline{n}_i)$ can be recovered by LS estimator:

$$\widehat{\boldsymbol{g}}_d(\overline{n}_i) = \widetilde{\boldsymbol{M}}_{d,i}^{\dagger} \boldsymbol{y}_{d,i} = \boldsymbol{g}_d(\overline{n}_i) + \widetilde{\boldsymbol{M}}^{\dagger} \boldsymbol{\xi}_{d,i}. \tag{4.41}$$

Once getting a new $\widehat{\boldsymbol{g}}_d$, we pick its j-th element, which is the estimated amplitudesof the j-th beam in current polling. The polling lasts for $R = \lfloor L/\mathbf{cal}(\mathcal{I}) \rfloor$ times[5] , so a pseudo time series is finally obtained as $\widehat{\boldsymbol{g}}_{d,j} = \big[\widehat{g}_{d,j}(\overline{n}_0), \widehat{g}_{d,j}(\overline{n}_1), \cdots, \widehat{g}_{d,j}(\overline{n}_{R-1})\big]^{'}$.

[5] Similar to the random-probing stage, we introduce the steering-probing state based on one frame consisting of L subframes. In practice or numerical comparisons, one can simply replace L with the actual number of subframes, i.e., $\mathbf{cal}(I)R$.

Lemma 4.2: Through repetitive polling, the pseudo time series $\widehat{\boldsymbol{g}}_{d,j}$ has an equal sampling interval thus can be modeled as finite noisy samples of a single-tone sinusoid.

Many techniques have been proposed over the years for the frequency estimation of a complex sinusoid in complex additive white Gaussian noise. Here we adopt the WNALP estimator known for its computational efficiency and near-optimal performance [76]. The detailed procedures for path gain/Doppler estimation are described as below

- *Set* $M_0 = \lfloor R/2 \rfloor$.
- *Calculate the autocorrelation of* $\widehat{\boldsymbol{g}}_{d,j}$ *as*

$$R(m) = \frac{1}{R-m} \sum_{i=m+1}^{2M_0} \widehat{g}_{d,j}(\overline{n}_i)\widehat{g}^*_{d,j}(\overline{n}_{i-m}) \tag{4.42}$$

- *Calculate the smoothing coefficient* w_m *as*

$$w_m = \frac{3\big((M_0-m)(2M_0-m+1) - M_0^2\big)}{M_0(4M_0^2-1)} \tag{4.43}$$

- *Estimate the Doppler shift as*

$$\widehat{\omega}_{d,j} = \frac{1}{N_c cal(\mathcal{I})} \sum_{m=1}^{M_0} w_m \mathbf{angle}(R(m)R^*(m-1)) \tag{4.44}$$

- *Estimate the amplitudesas*

$$\begin{aligned} \widehat{g}_{d,j}(d) &= \frac{e^{-j\widehat{\omega}_{d,j}\frac{N_c cal(\mathcal{I})}{2}}}{R} \sum_{i=1}^{R} \widehat{g}_{d,j}(\overline{n}_i) e^{-j\widehat{\omega}_{d,j} N_c cal(\mathcal{I})(i-1)} \\ &= \frac{1}{R} \sum_{i=1}^{R} \widehat{g}_{d,j}(\overline{n}_i) e^{-j\widehat{\omega}_{d,j} N_c cal(\mathcal{I})(i-1/2)}. \end{aligned} \tag{4.45}$$

The rest beams can be estimated similarly thus being omitted.

4.5 Discussions and Simulations

4.5.1 Implementing Discussions

Implementing procedures: The implementation of the proposed DSDS channel estimator entails four key components:

1: Send multiple delta-like training pilots to separate channel taps with random probing applied.

2: Identify significant channel taps via energy detector to exploit the delay-domain sparsity regardless of Doppler.

3: Identify the direction of significant beams via A-BOMP with effective mechanism applied to combat time-variation.

4: Apply steering-probing to estimate the amplitudes and Doppler using high-quality received samples.

The proposed channel estimator is tailored for a general doubly-selective channels. In practice, the investigated channel may not exhibit double selectivity, so one can use part of the above steps to accommodate these special cases.

Storage demand: The major storage demand in channel estimation comes from the sensing matrix. Suppose p_1 frames ($p_1 L$ subframes actually) are allocated at the random-probing stage, then the size of sensing matrix in [56] is $C_1 = p_1 N \times U N_c G_t G_r$, with U being the up-sampling ratio. Although our estimation is conducted at each tap independently, the sensing matrix is shared by all taps with size $C_2 = p_1 L \times G_t G_r$. For $N_c = 128$ and $N = 512$, C_1 is more than 13000 times larger than C_2.

Computational complexity: The major computational complexity comes from the OMP-based algorithm, which comprises three parts: basis matching, orthogonal projection, and residue update. For a Q-dimensional sparse vector recovered via V measurements, the involved flops for these parts at iteration-k are $(2V-1)Q$, $4kV$, and $2kV$ flops, respectively [78]. The total flops of [56] and ours are $p_1 NV(2UN_c G_t G_r + 3p_1 N)$ and $p_1 LVG(2G_t G_r + 3p_1 L)$, both in the order of $\mathcal{O}(p_1^2)$. Thanks to our extremely small-scale sensing matrix, even for $p_1 < 300$, the former is still more than ten times larger than the upper-bound of the latter.

Sensing matrix construction: To ensure a reliable recovery via OMP, the sensing matrix should best satisfy the restricted isometry property (RIP). According to [79], the optimal sensing matrix in terms of the RIP is the independent and identically distributed (IID) Gaussian

matrix. Unfortunately, due to the constant-modulus limitation of APS, the optimal sensing matrix remains a open topic. In this work, we follow [62] and randomly adjust APS obeying a uniform distribution.

From a single RF chain to multiple RF chains: Although the DS-DS channel estimator is introduced based on a single RF chain, it can be readily generalized to multiple RF chains, because the proposed estimator is relevant to RF precoder only without a dedicated digital precoding design. Besides a slight change in the number of effective measurements each time, the algorithm can be carried out for arbitrary number of RF chains without any modification.

4.5.2 Simulation Verification

In this subsection, extensive numerical results are presented to verify the advantages of the proposed approach over existing works. In simulations, the system carrier frequency f_c is 60 GHz. The number of antennas is $N_t = N_r = 32$, The dictionary sizes are $G_t = G_r = 64$. $h(\cdot)$ is the raised-cosine filter with the roll-off factor $\beta = 1$. Each channel realization is generated according to Eq. (4.3) with P ranging from 1 to 4. One-stage refinement is applied for all cases when applying OMP-based methods. If not specified, the resolution of APS is 2-bit. Other simulation parameters include $N_c = 16$, $N = 64$, $T_s = 50ns$, $A = 8$, $P_T = 10^{-3}$, $\epsilon = 0.01$ and $\mu = 0.03$. The SNR (averaged TSNR) is defined as $\frac{L}{N\sigma^2}$. The estimation performance is weighted by the normalized MSE (NMSE) given by

$$\varepsilon = \frac{\sum_{d=0}^{N_c-1} \parallel \boldsymbol{H}_d - \widehat{\boldsymbol{H}}_d \parallel_F^2}{\sum_{d=0}^{N_c-1} \parallel \boldsymbol{H}_d \parallel_F^2}. \tag{4.46}$$

Each curve is on the average of 1000 channel realizations.

1: Verification of the functionality of tap identification

To verify the effectiveness of tap identification, we plot the averaged selected taps together with their power ratio in Fig. 4.3. $P = 3$ and 40 frames are allocated at the random-probing stage. Three different v_m's: 0, 12km/h, and 120km/h are considered. We see that the tap identification is regardless of Doppler effects. Fewer taps are selected with the increase of

SNR, and reduction is 75% at 0dB. As this work uses the raised-cosine pulse-shaper, the delay-domain also suffers from off-grid issues due to side-lobe leakage, so the number of identified taps is slightly larger that of actual paths. Note that, the large reduction in taps to be processed is not at the cost of power loss. As can be seen from Fig. 4.3, the averaged power ratio soon exceeds 97% at medium SNR. The effectiveness of tap identification is attributed to the delay-domain sparsity of mmWave channels.

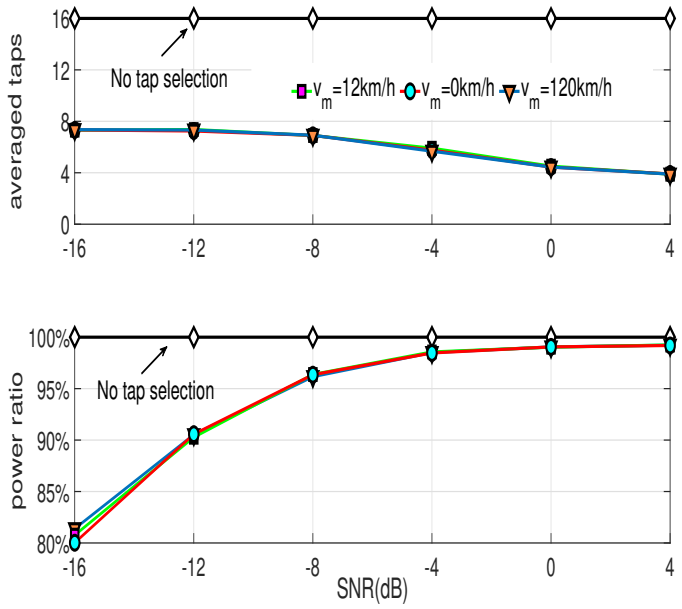

Figure 4.3: The averaged selected taps after tap identification.

We then compare the double-sparse approach (DSA) with state-of-the-art beamspace-sparse approach (BSA) [56] at the same averaged SNR in Fig. 4.4. The channel is generated with 3 paths and $\omega_m = 0$. For DSA, 40 training frames are allocated at the random-probing stage with repeating beamforming polling for $R = 4$ times at the steering-probing stage. 60 training frames are allocated for BSA and the regularized LS-estimator. For BSA, its sensing matrix size is 16384×131072, requiring a memory space over 18GB, in contrast to ours with size 200×4096 occupying 9Mb memory space. Due to the great shortage of training frames, the LS

estimator without utilizing any sparsity performs the worst. BSA performs much better than LS but still much worse than DSA. In addition, the shortage of probings makes the NMSE curve of BSA soon becomes flat. Even under the same peak SNR, we see that DSA still outperforms BSA at medium-to-high SNR region, implying that the benefits brought by DSA outweight the power inefficiency of the proposed training pattern.

2: NMSE comparisons in static and wideband channels:

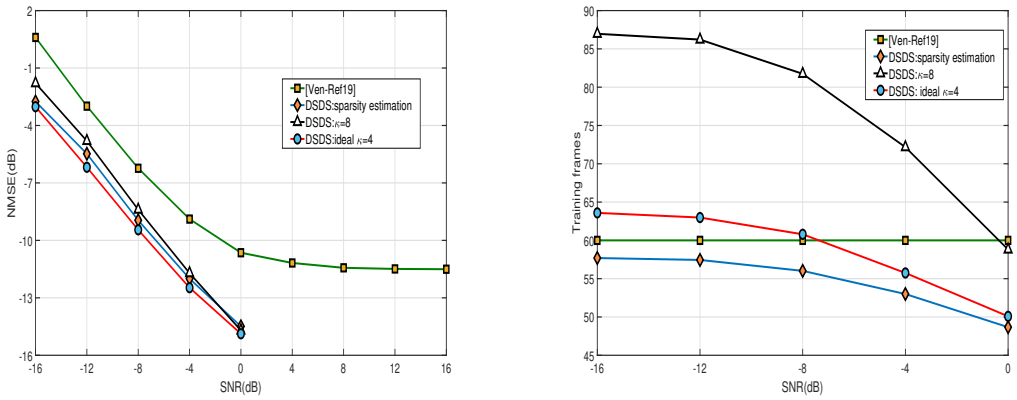

(a) (b)

Figure 4.4: A comparison in static wideband channels. (a) NMSE comparisons among different schemes; and (b) total training frames consumed by different schemes.

We further plot the averaged consumed training frames of different approaches. From two figures, it is clear that improper iterations ($\mathcal{K} = 8$) will result in additional training overhead without making any substantial performance improvement. Following proposition 4.2, iterations can be properly set for A-BOMP (A-BOMP is equivalent to OMP here), and the resultant NMSE performance is very close to the ideal benchmark ($\mathcal{K} = 4$). With pre-determined iterations, DSA requires the least training overhead, with a reduction of 20% compared to BSBA at high SNR.

3: NMSE comparisons in frequency-flat time-varying channels

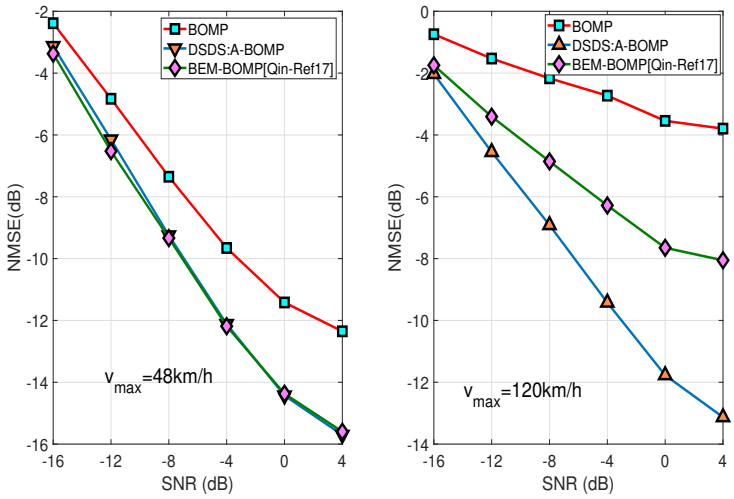

Figure 4.5: The NMSE comparisons in "frequency-flat"and time-varying channels in modest mobility.

In Fig. 4.5, the channel is generated with $P = 3$ with v_m=48km/h and v_m=120km/h, respectively. We compare the NMSEs with the angle support recovered via A-BOMP and DPC-BOMP [61], respectively. Since each tap channel is "frequency-flat" and time-varying (FTV), the results are essentially the comparison with state-of-the-art FTV channel estimator [61]. $p_1 = 60$ frames are allocated at the random-probing stage with repeating beamforming polling $R = 4$ times at the steering-probing stage. The DPC-basic order is 2 as in [61]. In modest mobility (v_m=48km/h), A-BOMP and DPC-BOMP achieve similar performances, both outperforming BOMP remarkably. In high mobility (v_m=120km/h), the advantage of A-BOMP over DPC-BOMP becomes notable. As described before, A-BOMP avoids the large-scale EVD required in DPC-BOMP, demonstrating that it is more efficient and superior.

4: NMSE performance in doubly-selective channels

To thoroughly evaluate the functionality of DSA, we fix SNR=-1dB and v_m=55km/h, and simulate NMSE versus frame duration under various conditions. In Fig. 4.6-a, we compare the NMSEs by varying the number of paths. Other parameters are $p_1 = 60$, $R = 4$, and $b = 2$.

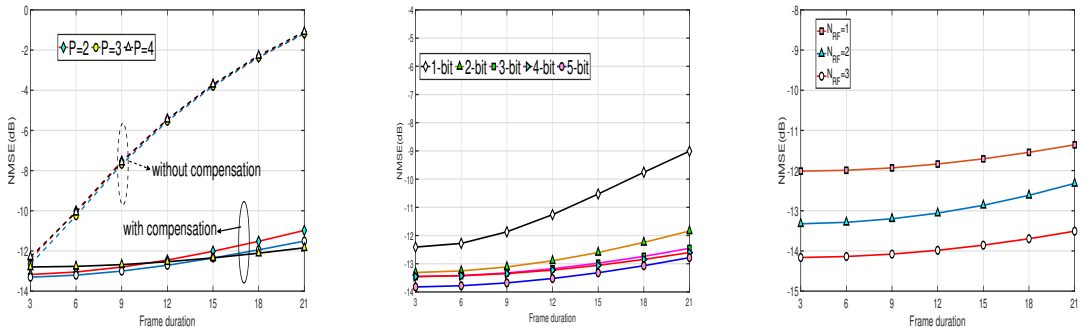

(a) Paths (b) APS (c) RF

Figure 4.6: Self-comparison in doubly-selective channels.(a) NMSE vs. the path number; (b) NMSE vs. APS resolution; and (c) vs. the number of RF chains.

The results show that, without Doppler compensation, the NMSE is soon to exceed -10dB, resulting in a great discrepancy with the actual channels. By compensating for the Doppler using the estimate, superb tracking ability can be guaranteed over up to 20 frames. Furthermore, there is a minimal performance degradation when increasing P from 2 to 4. In contrast, [56] suffers from a nearly 2dB degradation in a similar setup, implying that the proposed estimator is more robust against frequency selectivity.

In Fig. 4.6-b, we compare the NMSEs by varying the resolution (referring to b) of APS. Other parameters are set as $p_1 = 60$, $b = 2$, $R = 4$, and $P = 3$. A remarkable performance gap is noticed with the ultra-coarse 1-bit APS. However, increasing b by 1 bit will lead to a huge improvement. The performance gap compared to a finer APS (3$\sim$5-bit) in terms of the NMSE is very small (only 0.5dB), implying that the proposed channel estimator is insensitive to the resolution of APS.

In Fig. 4.6-c, we compare the NMSEs by varying the number of RF chains. Other parameters are set as $P = 3$, $b = 2$, $R = 6$, and $p_1 = 30$. As can be seen, multiple RF chains can lower the estimation error compared to the single RF chain. This is because multiple RF chains can generate more random beam probing patterns, which in turn benefits the recovery of the angle support using CS. We need to mention that throughout the estimation, all non-zero symbols are

set as one. Actually, if the peak to average power ratio (PAPR) is not a significant concern, one can potentially set these symbols as the Gaussian distributed variables like [62] to strengthen the randomness.

4.6 Conclusions

In this chapter, we investigated the doubly-selective channel estimation for hybrid mmWave mMIMO systems. The channel's beamspace- and delay-domain sparsity has been utilized via judiciously designed training pattern and analog probing to simplify the processing. The proposed channel estimator demonstrates strong robustness against double selectivity, without imposing any additional constraints on the hybrid structure itself. Compared with existing works, the DSDS approach proves to a more general and superior solution to channel estimation under hybrid mmWave mMIMO.

Chapter 5

Hybrid Block Diagonalization Based Transceiver for Wideband Multi-User mmWave Massive MIMO

In mmWave cellular, a mmWave mMIMO base station (BS) is expected to simultaneously serve multiple user equipments (UEs). Although both academia and industry have made remarkable efforts to design transceivers for mmWave mMIMO, relevant studies are congested in the single-UE scenarios. Driving by current research insufficiency, this chapter will concentrate on wMU transceiver design, hoping to improve the system capacity via inferior hardware structures.

There are three significant challenges encountered in transceiver design. The first stems from the hybrid structure that imposes more constraints on precoding [10] [51]. The second issue still associates with the unique structure, in which the per-subcarrier processing with OFDM applied is no longer independent due to a shared analog beamformer [66] [80]. Last but not least, unlike the P2P scenarios, the wMU scenarios have to jointly consider the user-specific signal quality variation and the multi-user interference (MUI) [81] [82]. To tackle these challenges, quite a few methods have been proposed (see e.g., [31, 83, 3, 84, 85, 82, 86, 87, 88, 89, 90]).

In the existing literature, a so-termed hybrid block diagonalization (HBD) framework is commonly adopted for transceiver design. Essentially, HBD requires the transmitter to eliminate the MUI with the help of CSI, such that independent detection can be applied individually at the UE end. For reference, we survey some of the most representative HBD schemes. The solution proposed in [66] and [85] entails analog beam steering and digital MUI cancellation. This one is easy-to-implement so long as a high-resolution analog beamformer is deployed, but its performance is mostly mediocre. Another solution proposed in [82] and [86] relies on the so-called equal-gain-transmission (EGT) processing. This technique does not demand a sparse channel, but it is a narrowband design and requires the BS to be operated at the multiplexing mode only. Another solution proposed in [87] and [88] consists of pre-beam separation and post-subspace projection. This one works relatively well if the multiplexing gain could perfectly match the rank of the channel, but a performance decline is likely to happen once such a condition is violated. In addition, its applicability to wideband channels is also questionable. Although HBD devised in [89] and [90] has taken the frequency-selectivity into account, it is essentially a greedy extension of its P2P ancestors, thereby inheriting their limitation and lacking a proper MUI management.

As can be seen, existing techniques fail to offer a performance guarantee for general wMU mmWave mMIMO systems due to their ad-hoc nature. To overcome the present limitations, we seek to design a systematic HBD-based transceiver framework explicitly for wMU mmWave mMIMO. Towards this aim, quite a few efforts have been made in this chapter, with the primary outcomes summarized as follows:

- By revealing the crucial role of analog processing in HBD-based transceiver design, we are able to transform the complicated hybrid processing into a well-tractable two-stage analog plus digital processing, and subsequently, establish the corresponding MI upper- and lower-bounds.

- By linking analog processing and channel decomposition, we prove that the upper and lower MI bounds will merge with probability 1 in the limit sense and demonstrate the

global optimality of HBD in the sense of MI optimization for wMU mmWave mMIMO.

- By optimizing the achievable yet asymptotically optimal MI lower-bound, we end up with sub-optimal yet high-performance analog processing. With the help of the post-digital processing, we accomplish the HBD-based transceiver designs for both the multi-aperture structure (MAS) and the multi-beam structure (MBS).

5.1 System and Channel Models

A downlink scenario is considered in this chapter, with an illustrative diagram shown in Fig. 5.1. Specifically, N_t antennas with M_t RF chains are employed at the BS, and N_r antennas with M_r RF chains are employed at each of the K UEs. The BS communicates with each UE via N_s data streams, satisfying $KN_s \leq M_t \leq N_t$ and $N_s \leq M_r \leq N_r$. Without loss of generality, we assume $M_r = N_s$ as in [87, 88, 89].

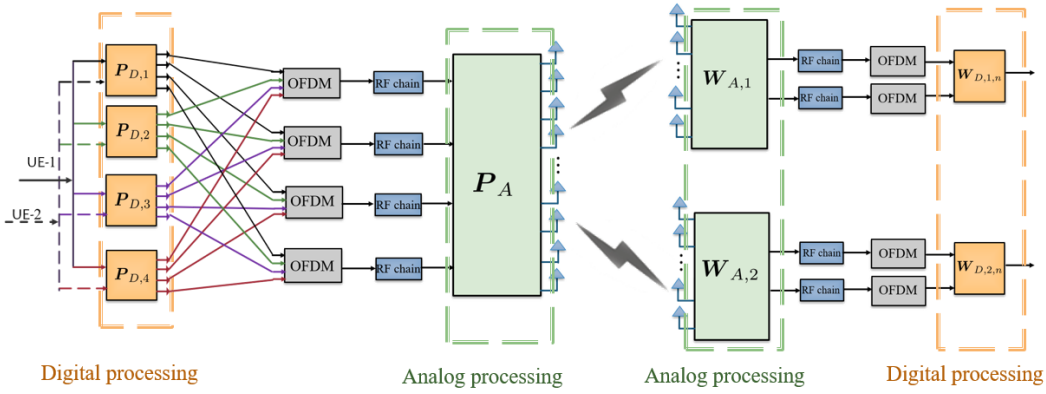

Figure 5.1: An illustrative wMU mmWave mMIMO system model with $K = 2$, $N = 4$, $M_t = 4$ and $M_r = 2$.

To incorporate the unique characteristics of mmWave channels, a commonly-used geometric wideband channel model is adopted. Let L and D represent the number of dominant paths and delay taps, respectively. Then according to [56, 63], the tap-d channel ($d \in [0, D)$) between

the BS and UE-k can be expressed as

$$\mathbf{H}_{k,d} = \sum_{l=1}^{L} \sqrt{\frac{N_t N_r}{L}} \alpha_{l,k} h(dT_s - \tau_{l,k}) \boldsymbol{a}_r(\theta_{l,k}) \boldsymbol{a}_t^*(\phi_{l,k}) \ . \tag{5.1}$$

For path-l, $\alpha_{l,k} \sim \mathcal{CN}(0,1)$ represents its amplitude; $h(\tau)$ is the pulse-shaping response sampled at τ; $\tau_{l,k}$ is the propagation delay uniformly distributed over $[0, (D-1)T_s)$; $\theta_{l,k}$ and $\phi_{l,k}$ are the AoA and AoD, respectively, both uniformly distributed within $[0, 2\pi)$. With the typical ULA, $\boldsymbol{a}_t(\phi) = \frac{1}{\sqrt{N_t}}[1, e^{j\pi \sin\phi}, \cdots, e^{j(N_t-1)\pi \sin\phi}]^T$.

For notational simplicity, we further define

$$\boldsymbol{A}_{t,k} = [\boldsymbol{a}_t(\phi_{1,k}), \boldsymbol{a}_t(\phi_{2,k}), \cdots, \boldsymbol{a}_t(\phi_{L,k})] \ , \tag{5.2a}$$

$$\boldsymbol{A}_{r,k} = [\boldsymbol{a}_r(\theta_{1,k}), \boldsymbol{a}_r(\theta_{2,k}), \cdots, \boldsymbol{a}_r(\theta_{L,k})] \ , \tag{5.2b}$$

$$\boldsymbol{\Lambda}_{k,d} = \text{diag}\{\alpha_{l,k} h(dT_s - \tau_{l,k})\}_{l=1}^{L} \ , \tag{5.2c}$$

then $\mathbf{H}_{k,d}$ can be rewritten as

$$\mathbf{H}_{k,d} = \boldsymbol{A}_{r,k} \boldsymbol{\Lambda}_{k,d} \boldsymbol{A}_{t,k}^* \ . \tag{5.3}$$

5.1.1 Input-Output Relationship

Let $\boldsymbol{x}_n = \left[\boldsymbol{x}_{1,n}^*, \boldsymbol{x}_{2,n}^*, \cdots, \boldsymbol{x}_{K,n}^*\right]^*$ be the input data on subcarrier-n ($n \in [1, N]$), satisfying $\mathbb{E}\{\boldsymbol{x}_{k,n} \boldsymbol{x}_{k,n}^*\} = \frac{1}{M_r} \boldsymbol{I}_{M_r}$. $\boldsymbol{x}_{k,n}$ will be sent to UE-k ($k \in [1, k]$) with its symbols selected from a Gaussian constellation. $\boldsymbol{x}_n$ is first precoded by the BS-end digital precoder

$$\boldsymbol{P}_{D,n} = [\boldsymbol{P}_{D,1,n}, \boldsymbol{P}_{D,2,n}, \cdots, \boldsymbol{P}_{D,K,n}] \in \mathcal{C}^{M_t \times K M_r} \ , \tag{5.4}$$

followed by M_t N-point IFFT's. The resultant time-domain signal will be appended by a length-D ($D \geq N_c - 1$) CP before being processed by the analog precoder $\boldsymbol{P}_A \in \mathcal{C}^{N_t \times M_t}$. In hybrid OFDM systems, $\boldsymbol{P}_A$ is applied after IFFT, thus it remains identical across all subcarriers. Note that this is drastically different from conventional fully digital OFDM systems, the precoders are independent and distinct across subcarriers.

After the BS-end hybrid precoding, the transmitted signal on subcarrier-n becomes

$$\boldsymbol{s}_n = \boldsymbol{P}_A \boldsymbol{P}_{D,n} \boldsymbol{x}_n \ . \tag{5.5}$$

Given the time-domain channel $\mathbf{H}_{k,d}$ in Eq. (5.1), we can obtain its frequency-domain channel on subcarrier-n as

$$\boldsymbol{H}_{k,n} = \sum_{d=0}^{D-1} \mathbf{H}_{k,d} e^{-j\frac{2\pi n}{N}d} \ . \tag{5.6}$$

Therefore the signal captured by UE-k on subcarrier-n is given by

$$\boldsymbol{r}_{k,n} = \boldsymbol{H}_{k,n} \boldsymbol{s}_n + \boldsymbol{\eta}_{k,n} \ , \tag{5.7}$$

where $\boldsymbol{\eta}_{k,n} \sim \mathcal{CN}(\mathbf{0}, \sigma^2 \boldsymbol{I}_{N_r})$ is the Gaussian noise. In this chapter, the SNR is defined as $\frac{1}{\sigma^2}$.

Upon the reception of $\boldsymbol{r}_{k,n}$, the analog combiner denoted as $\boldsymbol{W}_{A,k} \in \mathcal{C}^{N_r \times M_r}$, will be applied. By further removing CP and implementing M_r N-point fast Fourier transform's (FFT's), the frequency-domain signal will finally be combined by $\boldsymbol{W}_{D,k,n} \in \mathcal{C}^{M_r \times M_r}$, resulting in

$$\begin{aligned} \boldsymbol{y}_{k,n} &= \boldsymbol{W}_{D,k,n}^* \boldsymbol{W}_{A,k}^* \boldsymbol{H}_{k,n} \boldsymbol{P}_A \boldsymbol{P}_{D,n} \boldsymbol{x}_n + \boldsymbol{W}_{D,k,n}^* \boldsymbol{W}_{A,k}^* \boldsymbol{\eta}_{k,n} \\ &= \boldsymbol{W}_{D,k,n}^* \widetilde{\boldsymbol{H}}_{k,n} \boldsymbol{P}_{D,n} \boldsymbol{x}_n + \boldsymbol{\xi}_{k,n} \ , \end{aligned} \tag{5.8}$$

Here, $\widetilde{\boldsymbol{H}}_{k,n} = \boldsymbol{W}_{A,k}^* \boldsymbol{H}_{k,n} \boldsymbol{P}_A$ is termed as the equivalent digital channel (EDC) associated with UE-k on subcarrier-n. By stacking all $\{\boldsymbol{y}_{k,n}\}_{n=1}^N$ into a long vector, the multi-user I-O relationship accordingly becomes

$$\boldsymbol{y}_n = \boldsymbol{W}_{D,n}^* \underbrace{\begin{bmatrix} \widetilde{\boldsymbol{H}}_{1,n} \\ \widetilde{\boldsymbol{H}}_{2,n} \\ \vdots \\ \widetilde{\boldsymbol{H}}_{K,n} \end{bmatrix}}_{\widetilde{\boldsymbol{H}}_n} \boldsymbol{P}_{D,n} \boldsymbol{x}_n + \boldsymbol{\xi}_n \ , \tag{5.9}$$

with $\boldsymbol{W}_{D,n} = \text{diag}\{\boldsymbol{W}_{D,k,n}\}_{k=1}^K$, $\boldsymbol{\xi}_n$ being the concatenated noise vector, and $\widetilde{\boldsymbol{H}}_n$ being the multi-user EDC on subcarrier-n. It is worth mentioning that $\boldsymbol{W}_{D,n}$ and $\boldsymbol{P}_{D,n}$ in Eq. (5.9) correspond to the digital part, while $\widetilde{\boldsymbol{H}}_n$ corresponds to the analog part, for it has incorporated $\boldsymbol{P}_A$ and $\boldsymbol{W}_{A,k}$.

5.1.2 Problem Formulation

Our aim is to develop a systematic HBD scheme for wMU systems. More specifically, given $\mathbf{H}_{k,d}$, our task is to determine the digital part $\boldsymbol{P}_{D,n}$ and $\boldsymbol{W}_{D,k,n}$, as well as the analog part $\boldsymbol{P}_A$ and $\boldsymbol{W}_{A,k}$, to maximize the system MI while satisfying the following prerequisite for HBD:

$$\widetilde{\boldsymbol{H}}_n \boldsymbol{P}_D = \text{diag}\left\{\widetilde{\boldsymbol{H}}_n[(k-1)M_r+1:kM_r,:]\boldsymbol{P}_{D,k,n}\right\}_{k=1}^{K} \ . \tag{5.10}$$

Once each UE enjoys an MUI-free EDC, thus the achievable MI for UE-k on subcarrier-n can be computed as

$$I_{k,n} = \det\left(\boldsymbol{I}_{M_r} + \frac{1}{M_r\sigma^2}\left(\boldsymbol{W}_{D,k,n}^{*}\boldsymbol{W}_{A,k}^{*}\boldsymbol{W}_{A,k}\boldsymbol{W}_{D,k,n}\right)^{-1}\boldsymbol{H}_{e,k,n}\boldsymbol{H}_{e,k,n}^{*}\right) , \tag{5.11}$$

with $\boldsymbol{H}_{e,k,n} = \boldsymbol{W}_{D,k,n}^{*}\boldsymbol{W}_{A,k}^{*}\boldsymbol{H}_{k,n}\boldsymbol{P}_A\boldsymbol{P}_{D,k,n}$. As a result, the HBD-based transceiver design problem for wMU mmWave mMIMO can be formulated as:

P1. Problem Statement 1[***Generic HBD-wMU transceiver design***]:

$$\underset{\boldsymbol{W}_{D,k,n},\boldsymbol{W}_{A,k},\boldsymbol{P}_A,\boldsymbol{P}_{D,n}}{\arg\max} \quad I = \sum_{k=1}^{K}\sum_{n=1}^{N}\log_2 I_{k,n} \ , \tag{5.12a}$$

$$\textit{subject to} \qquad Eq.\ (5.10) \ , \tag{5.12b}$$

$$\boldsymbol{P}_A \in \mathcal{F} \ , \tag{5.12c}$$

$$\forall k, \quad \boldsymbol{W}_{A,k} \in \mathcal{W} \ , \tag{5.12d}$$

$$\forall k,n, \| \ \boldsymbol{P}_A\boldsymbol{P}_{D,k,n} \ \| \leq M_r \ . \tag{5.12e}$$

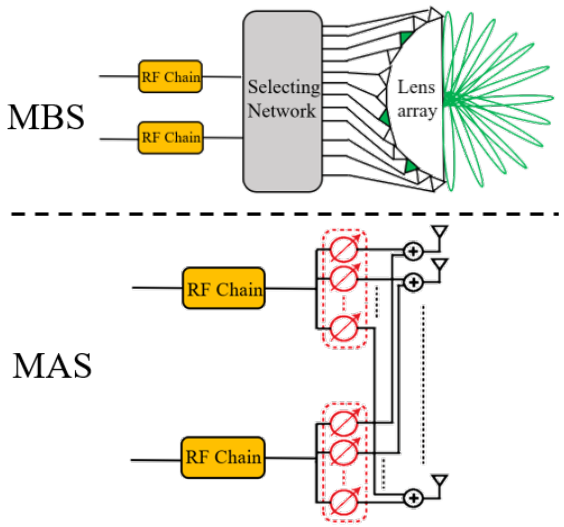

Figure 5.2: The diagram of MBS and MAS

In **P1**, $\mathcal{F}$ and $\mathcal{W}$ stand for the feasible sets of analog precoders[1] , which exhibit different constant-modulus forms in two mainstream hybrid mMIMO structures, namely MBS (shown in the upper part of Fig. 5.2) and MAS (shown in the lower part of Fig. 5.2). Briefly speaking, MBS corresponds to the so-called lens-array antennas, while MAS fits to the fully-connected analog phase shifter (APS) network. Both types will be investigated in-depth within a unified design paradigm.

5.1.3 Design Strategy

To obtain the optimal precoders, a common practice is to solve the formulated optimization problem **P1** directly. However, as an explicit objective function of **P1** is unavailable, the straightforward manner turns out to be intractable. Nevertheless, with a closer look at Eq. (5.10), we find that the BS-end digital precoder $\boldsymbol{P}_{D,k,n}$ resides in the null-space of $\widetilde{\boldsymbol{H}}_n$, indicating that the former is determined by the latter. Therefore, once Eq. (5.10) holds, UE-k will enjoy an MUI-free EDC $\boldsymbol{W}_{A,k}^{*}\boldsymbol{H}_{k,n}\boldsymbol{P}_{A}\boldsymbol{P}_{D,n}$, which is a function of $\widetilde{\boldsymbol{H}}_n$. It can be rapidly verified

[1] This chapter does not deliberately distinguish between the precoder and combiner, so both terms will be named precoder without causing ambiguity.

that a similar conclusion applies to $\boldsymbol{W}_{D,k,n}$ as well. In consequence, the digital part (including $\boldsymbol{P}_{D,n}$ and $\boldsymbol{W}_{D,k,n}$) is essentially a function of the analog part (including $\boldsymbol{W}_{A,k}$ and $\boldsymbol{P}_A$). Such a property makes it able to transform the original joint processing design into a sequential analog and digital processing.

To be more specific, given the analog part, an MI bound can be derived in replacement of the inexplicit I, thus the analog precoders can be determined via bound optimization. After analog processing, one can proceed with the digital processing to meet HBD condition and maximize MI. Based on this strategy, we will detail the HBD-based transceiver design in the ensuing sections.

5.2 MI Bounds and HBD Optimality

In this section, we first derive the MI upper- and lower-bounds via HBD. Then, we will investigate the properties of the derived bounds, and reveal the global optimality of HBD in the sense of MI optimization in wMU mmWave mMIMO transceiver design.

5.2.1 MI Upper-Bound

For notational simplicity, we express the system I-O relationship in a concise form as

$$\boldsymbol{y} = \underbrace{\text{diag}\{\boldsymbol{W}_{D,n}^*\}_{n=1}^N}_{\boldsymbol{W}_D^*} \underbrace{\text{diag}\{\widetilde{\boldsymbol{H}}_n\}_{n=1}^N}_{\widetilde{\boldsymbol{H}}} \underbrace{\text{diag}\{\boldsymbol{P}_{D,n}\}_{n=1}^N}_{\boldsymbol{P}_D} \boldsymbol{x} + \boldsymbol{\xi} \ . \tag{5.13}$$

In a multi-user setup, $\boldsymbol{W}_{D,n}$ bears a block-diagonal form, but this restriction could be relaxed if UEs are allowed to cooperate. If this is the case, by performing singular value decomposition (SVD) of $\widetilde{\boldsymbol{H}}_n$, i.e., $svd(\widetilde{\boldsymbol{H}}_n) = \widetilde{\boldsymbol{U}}_n \widetilde{\boldsymbol{\Sigma}}_n \widetilde{\boldsymbol{V}}_n^*$, setting $\boldsymbol{P}_{D,n} = \widetilde{\boldsymbol{V}}_n$ and $\boldsymbol{W}_{D,n} = \widetilde{\boldsymbol{U}}_n$ leads to $\boldsymbol{P}_D$ and $\boldsymbol{W}_D$ being the right and left singular matrices of $\widetilde{\boldsymbol{H}}$, and the corresponding MI can be

computed as

$$I_U = \sum_{n=1}^{N} \sum_{i=1}^{KM_r} \log_2 \left(1 + \frac{\widetilde{\Sigma}_n^2[i,i]}{M_r \sigma^2} \right) = \sum_{i=1}^{NKM_r} \log_2 \left(1 + \frac{\widetilde{\Sigma}^2[i,i]}{M_r \sigma^2} \right) , \tag{5.14}$$

with $\widetilde{\Sigma}[i,i]$ representing the i-th eigenvalue of $\widetilde{\boldsymbol{H}}$. Since Eq. (5.14) is obtained through the SVD of $\widetilde{\boldsymbol{H}}$ under user cooperation, it is clear that I_U is an MI upper-bound for HBD-based wMU transceivers.

5.2.2 MI Lower-Bound

If no cooperation is allowed among UEs, we set $\boldsymbol{W}_{D,n} = \boldsymbol{I}$ and $\boldsymbol{P}_{D,n} = \widetilde{\boldsymbol{H}}_n^{\dagger} \text{diag}\{\|\widetilde{\boldsymbol{H}}_n^{\dagger}[:,i]\|_F^{-1}\}_{i=1}^{NM_r}$. In this case, it can be verified that $\boldsymbol{P}_D$ acts as the zero-forcing (ZF) pre-equalizer for $\widetilde{\boldsymbol{H}}$, and the system MI can be calculated as

$$I_L = \sum_{n=1}^{N} \sum_{i=1}^{KM_r} \log_2 \left(1 + \frac{\left\|\widetilde{\boldsymbol{H}}_n^{\dagger}[:,i]\right\|_F^{-2}}{M_r \sigma^2} \right) = \sum_{i=1}^{NKM_r} \log_2 \left(1 + \frac{\left\|\widetilde{\boldsymbol{H}}^{\dagger}[:,i]\right\|_F^{-2}}{M_r \sigma^2} \right) . \tag{5.15}$$

In the above, the BS-end processing not only cancels out the MUI but also the inter-stream interferences for an individual UE, hence such a transceiver design is essentially a special type of HBD. Besides, achieving I_L does not involve any UE-end digital processing, so we can recognize I_L as the MI lower-bound for HBD-based wMU transceivers.

5.2.3 MI Relationship

Typically, I_L will be strictly smaller than I_U. Nevertheless, we will see that, as the number of antennas (N_t, N_r) approaches infinity, these two bounds will merge with probability 1. To

verify this point, we first rewrite Eq. (5.6) as

$$\boldsymbol{H}_{k,n} = \boldsymbol{A}_{r,k} \left(\sum_{d=0}^{D-1} \boldsymbol{\Lambda}_{k,d} e^{-j\frac{2\pi n}{N}d} \right) \boldsymbol{A}_{t,k}^{*} \ . \tag{5.16}$$

In the case of infinite N_t and N_r, we have

$$\boldsymbol{a}_{t(r)}^{*}(\theta_1)\boldsymbol{a}_{t(r)}(\theta_2) = \begin{cases} 0 & \theta_1 \neq \theta_2 \\ 1 & \theta_1 = \theta_2 \end{cases} , \tag{5.17}$$

so both $\boldsymbol{A}_{t,k}$ and $\boldsymbol{A}_{r,k}$ are semi-unitary matrices. Noticing that the term inside the bracket of Eq. (5.16) is a diagonal matrix, it can be concluded that $\forall n$, $\{\boldsymbol{H}_{k,n}\}_{n=1}^{N}$ share common singular vectors. Utilizing this property, the HBD-based transceivers as N_t and N_r go to infinity can be designed as

$$\boldsymbol{P}_A = \left[\overline{\boldsymbol{A}}_{t,1}, \overline{\boldsymbol{A}}_{t,2}, \cdots, \overline{\boldsymbol{A}}_{t,K}, \overline{\boldsymbol{A}} \right] \ , \tag{5.18a}$$

$$\boldsymbol{W}_{A,k} = \overline{\boldsymbol{A}}_{r,k} \ , \tag{5.18b}$$

$$\boldsymbol{P}_{D,n} = \left[\boldsymbol{I}_{KM_r}^{*}, \boldsymbol{0}_{M_t - KM_r}^{*} \right]^{*} \ , \tag{5.18c}$$

$$\boldsymbol{W}_{D,k,n} = \boldsymbol{I}_{M_r} \ . \tag{5.18d}$$

In the above, $\overline{\boldsymbol{A}}_{t,k} \in \mathcal{C}^{N_t \times M_r}$ is an arbitrary right singular sub-matrix extracted from $\boldsymbol{A}_{t,k}$, $\overline{\boldsymbol{A}}_{r,k}$ is the corresponding left singular sub-matrix extracted from $\boldsymbol{A}_{r,k}$, and $\overline{\boldsymbol{A}}$ is an arbitrary matrix bearing constant-modulus form. Such a design is valid because all analog precoders are constant-modulus, and $\| \ \boldsymbol{P}_A \boldsymbol{P}_{D,n} \ \|_F = M_r$ satisfies Eq. (5.12e), i.e., the transmit power constraint. On top of that, the above setting leads to $\widetilde{\boldsymbol{H}}$ defined in Eq. (5.13) being a diagonal matrix, hence I_U achieved via SVD equals to I_L achieved via ZF pre-equalization.

5.2.4 HBD Optimality

Although the proposed HBD solution above reveals that $I_L = I_U$ as N_t, $N_r \to \infty$, it does not guarantee the optimality of I_U or I_L. This is because $\overline{\boldsymbol{A}}_{r,k}$ (or $\overline{\boldsymbol{A}}_{t,k}$) defined in Eq. (5.18) has multiple choices, thereby awaiting further determination.

Note that, regardless of $\overline{\boldsymbol{A}}_{r,k}$, the above design always assures that $\boldsymbol{H}_{k,n}$ (see Eq. (5.16)) can be decomposed into M_r parallel single-input single-output (SISO) channels, each of which stands for a singular vector pair (SVP). Suppose that SVP-i_k ($i_k \leq L$) is selected for UE-k, then the MI contributed by this one can be individually computed as

$$I_{k,i_k} = \sum_{n=1}^{N} \log_2 \left(1 + \frac{|\sum_{d=0}^{D-1} \Lambda_{k,d}[i_k, i_k] e^{-j\frac{2\pi n}{N} d}|^2}{M_r \sigma^2} \right). \tag{5.19}$$

To maximize I_U or I_L, it suffices to choose M_r out of L SVPs with the most significant contribution to system MI. Then $\overline{\boldsymbol{A}}_{t,k}$ and $\overline{\boldsymbol{A}}_{r,k}$ are automatically determined. Interestingly, with this method, the ultimately achieved MI not only reaches the optimum among HBD-based wMU transceivers, but also among *any* wMU transceivers. For clarity, a proposition is expressly provided as follows.

Proposition 5.1: [Optimality of HBD] *With an infinite number of antennas employed at the transceivers, HBD is the optimal precoding technique in the sense of MI optimization for wMU mmWave mMIMO transceiver design.*

Proof. In P2P scenarios, it has been proven that the near-optimal analog precoder is the Karcher mean of the optimal unconstrained precoders on individual subcarrier (see Eqs. (26) and (27) in [66], where "$\approx$" is exactly "$=$" when N_t, $N_r \to \infty$, thus near-optimal accordingly becomes optimal). For UE-k, the optimal unconstrained precoder on each subcarrier is a sub-matrix of $\boldsymbol{A}_{t,k}$, hence the resultant Karcher mean is still a sub-matrix of $\boldsymbol{A}_{t,k}$, and a similar conclusion holds for $\boldsymbol{A}_{r,k}$ as well. Therefore, choosing the best M_r out of L SVPs to construct the analog precoder for UE-k clearly leads to optimality. Since all UEs enjoy MUI-free EDC, individual optimality automatically leads to overall optimality. Therefore, HBD is the optimal precoding technique in the sense of MI. □

5.3 wMU-HBD Transceiver Design

In this section, we will develop HBD-based transceivers for practical wMU mmWave mMIMO systems. Following the established design strategy, we start with the analog processing by

optimizing the MI bound, then complete the digital processing to facilitate MUI-free reception and individual MI improvements.

5.3.1 Analog Processing

Since the MI lower-bound I_L is always achievable and asymptotically optimal in the limit case, it is reasonable to use it as a replacement of the inexplicit I. For simplicity, we make a slight modification to I_L by omitting the "1" term in Eq. (5.15), giving rise to

$$\begin{aligned} I_L &= \sum_{i=1}^{NKM_r} \log_2 \left(1 + \frac{\left\| \widetilde{\boldsymbol{H}}^{\dagger}[:,i] \right\|_F^{-2}}{M_r \sigma^2} \right) \\ &\approx -\log_2 \left\{ \prod_{i=1}^{NKM_r} (\widetilde{\boldsymbol{H}} \widetilde{\boldsymbol{H}}^*)^{-1}[i,i] \right\} - NKM_r \log_2 M_r \sigma^2 \ . \end{aligned} \tag{5.20}$$

Eq. (5.20) monotonically decreases with the term inside the bracket, regardless of the SNR. Thus the analog processing problem can be formulated as the following one:

P2. Problem Statement 2 [***Analog processing via optimizing*** I_L]:

$$\underset{\boldsymbol{W}_{A,k}, \boldsymbol{P}_A}{\arg\min} \quad \prod_{i=1}^{NKM_r} (\widetilde{\boldsymbol{H}} \widetilde{\boldsymbol{H}}^*)^{-1}[i,i] \ , \tag{5.21a}$$

$$\textit{subject to} \quad \boldsymbol{P}_A \in \mathcal{F} \ , \ \ \forall k, \boldsymbol{W}_{A,k} \in \mathcal{W} \ . \tag{5.21b}$$

As has been mentioned before, there are two mainstream hybrid mmWave mMIMO structures, namely MBS and MAS. Since **P2** does not use any specialties in terms of the analog structures, both types could share a common design paradigm after taking their individual constraints into account.

MBS: Denote $\mathcal{F}_M$ as the set containing all M-dimensional DFT bases. Given the antenna dimension N_t and N_r, the analog constraints for MBS can be expressed as

$$\forall n, k, \boldsymbol{P}_A[:,n] \in \mathcal{F}_{N_t}, \ \boldsymbol{W}_{A,k}[:,n] \in \mathcal{F}_{N_r}. \tag{5.22}$$

Although the minimizer of **P2** can be acquired via $\mathbb{C}_{N_t}^{M_t} \left(\mathbb{C}_{N_r}^{M_r} \right)^K$ trials, the complexity would be formidable under wMU mMIMO setup($> 10^{14}$ trials for $N_r = 16$, $N_t = 64$, $M_r = 2$,

$M_t = 6$, $K = 3$), so a low-complexity remedy is necessary. A natural means to reduce complexity is by shrinking the search space as in [51], whereas two drawbacks will emerge in the studied problem. First, the effectiveness of this method is highly sensitive to the sparsity level of mmWave channels. Secondly, even if the mmWave channel is extremely sparse, the complexity is still huge for growing *exponentially* with the number of UEs. In light of these deficiencies, we judiciously devise a double-sequential-search (DSS) algorithm for the MBS, with the detailed pseudo-code provided in **Algorithm 3**.

The DSS algorithm entails greedy codeword selection for constructing the UE-end analog precoders and greedy codeword exclusion for constructing the BS-end analog precoder. As the BS-end precoder applies to all UEs, we start from the UE-end design by setting $\boldsymbol{P}_A = \boldsymbol{F}_{N_t}$ to eliminate the BS-end influence. Using the notation defined in **Step.1**, the criterion of codeword selection at the inner-loop (m, k) (**Step.2-Step.7**) can be mathematically described as

$$m^* = \arg\min_{m} \prod_{i=1}^{NKM_r} \left(\widetilde{\boldsymbol{H}}(m,k)\widetilde{\boldsymbol{H}}^*(m,k)\right)^{-1}[i,i] \ , \tag{5.23}$$

where $\widetilde{\boldsymbol{H}}(m,k) = \text{diag}\big\{\widetilde{\boldsymbol{H}}_n(m,k)\big\}_{n=1}^{N}$ satisfying

$$\widetilde{\boldsymbol{H}}_n(m,k) = \begin{bmatrix} \widetilde{\boldsymbol{W}}_{R,1}^* \boldsymbol{H}_{1,n} \\ \vdots \\ \widetilde{\boldsymbol{W}}_{R,k-1}^* \boldsymbol{H}_{k-1,n} \\ \left[\widetilde{\boldsymbol{W}}_{R,k}, \boldsymbol{F}_{N_r}[:,m]\right]^* \boldsymbol{H}_{k,n} \\ \widetilde{\boldsymbol{W}}_{R,k+1}^* \boldsymbol{H}_{k+1,n} \\ \vdots \\ \widetilde{\boldsymbol{W}}_{R,K}^* \boldsymbol{H}_{K,n} \end{bmatrix} \boldsymbol{F}_{N_t} \ . \tag{5.24}$$

The above criterion ensures a linear implementing complexity with the number of UEs as well as the fairness among UEs. After getting $\boldsymbol{W}_{A,k}$, the hybrid structure forces $\boldsymbol{P}_A$ to delete some redundant codewords and retain only M_t codewords. To this aim, the criterion of codeword

exclusion at the loop-j (**Step**.8-**Step**.13) is designed as

$$j^* = \arg\min_{j} \prod_{i=1}^{NKM_r} \left(\widetilde{\boldsymbol{H}}(j)\widetilde{\boldsymbol{H}}^*(j)\right)^{-1}[i,i] \ , \tag{5.25}$$

where $\widetilde{\boldsymbol{H}}(j) = \text{diag}\{\widetilde{\boldsymbol{H}}_n(j)\}_{n=1}^N$ with

$$\widetilde{\boldsymbol{H}}_n(j) = \begin{bmatrix} \widetilde{\boldsymbol{W}}_{R,1}^* \boldsymbol{H}_{1,n} \\ \widetilde{\boldsymbol{W}}_{R,2}^* \boldsymbol{H}_{2,n} \\ \vdots \\ \widetilde{\boldsymbol{W}}_{R,K}^* \boldsymbol{H}_{K,n} \end{bmatrix} \boldsymbol{F}_{N_t}[:, \mathcal{I} \backslash \mathcal{I}(i)] \ . \tag{5.26}$$

In each iteration, the codeword with the least contribution to system MI will be excluded. Such an exclusion terminates until only M_t codewords are left.

MAS: Assume MAS consists of b-bit APS, whose adjustable angles are given by

$$\mathcal{B} = \left\{0, 2\pi/2^b, \cdots, 2\pi \times (2^b - 1)/2^b\right\} \ . \tag{5.27}$$

The analog constraints in the MAS are imposed on each entry, giving rise to

$$\forall m, n, k, \boldsymbol{P}_A[m,n] \in \frac{e^{j\mathcal{B}}}{\sqrt{N_t}}, \boldsymbol{W}_{A,k}[m,n] \in \frac{e^{j\mathcal{B}}}{\sqrt{N_r}} \ . \tag{5.28}$$

In this case, **P2** is a large-scale NP-hard problem, whose minimizer is difficult to be obtained in a brute force manner. Furthermore, the DSS algorithm developed for the MBS is also inapplicable here because the MBS obeys a column-wise constraint, while the MAS obeys a more flexible entry-wise constraint. To secure a local minimizer within an acceptable complexity, we resort to the entry-wise update. First, we apply the DSS algorithm to get $\boldsymbol{P}_A^{(MBS)}$ and $\boldsymbol{W}_{A,k}^{(MBS)}$, then quantize them as

$$\boldsymbol{P}_R = \frac{1}{\sqrt{N_t}} e^{jQ(\angle \boldsymbol{P}_R^{(MBS)})} \ , \tag{5.29a}$$

$$\boldsymbol{W}_{A,k} = \frac{1}{\sqrt{N_r}} e^{jQ(\angle \boldsymbol{W}_{A,k}^{(MBS)})} \ , \tag{5.29b}$$

Algorithm 3 DSS analog processing algorithm for the MBS

Input: $\forall k, n$, $\boldsymbol{H}_{k,n}$, $\boldsymbol{F}_{N_t}$, $\boldsymbol{F}_{N_r}$, K, M_r and M_t;

Output: $\forall k$, $\boldsymbol{W}_{A,k}$, $\boldsymbol{P}_A$

Initialization $\forall k$, $\widetilde{\boldsymbol{W}}_{R,k} = \varnothing$, $\widetilde{\boldsymbol{P}}_A = \boldsymbol{F}_{N_t}$, $count = N_t$, $\mathcal{I} = \{1, 2, \cdots, N_t\}$;
for $m \leq M_r$ **do**
  for $k \leq K$ **do**
    Compute Eq. (5.23) to get m^* ;
    $\widetilde{\boldsymbol{W}}_{A,k} = \big[\widetilde{\boldsymbol{W}}_{A,k}, \boldsymbol{F}_{N_r}[:, m^*]\big]$;
  end for
end for
while $count > M_t$ **do**
  Compute Eq. (5.26) to get j^* ;
  $\mathcal{I} = \mathcal{I} \backslash \mathcal{I}(j^*)$;
  $\widetilde{\boldsymbol{P}}_A = \boldsymbol{F}_{N_t}[:, \mathcal{I}]$;
  $count = count - 1$;
end while
$\forall k$, $\boldsymbol{W}_{A,k} = \widetilde{\boldsymbol{W}}_{R,k}$, $\boldsymbol{P}_A = \widetilde{\boldsymbol{P}}_A$;

with $Q(x) = \mathcal{B}\big(\arg\min_i \text{mod}(x - \mathcal{B}(i), 2\pi)\big)$ representing the quantizer. Despite some differences between the MBS and MAS, $\boldsymbol{P}_R$ and $\boldsymbol{W}_{A,k}$ are expected to be decent initializers. Next, we take $\boldsymbol{P}_A[a, b]$ to exemplify the entry-wise update while assuming other $\boldsymbol{P}_A$ and $\{\boldsymbol{W}_{A,k}\}_{k=1}^K$ elements stay unchanged. By testing all candidates within $\frac{1}{\sqrt{N_t}} e^{j\mathcal{B}}$, the one minimizing Eq. (5.21a) will be selected to replace the current $\boldsymbol{P}_A[a, b]$. After refreshing the entire $\boldsymbol{P}_A$, a similar operation is then applied to $\{\boldsymbol{W}_{A,k}\}_{k=1}^K$. The updating process keeps running until triggering a specific terminating condition.

Subcarrier down-sampling

For either the MAS or MBS, the complexity regarding analog processing grows linearly with the subcarrier number. In mmWave systems, the ultra-wideband spectrum is very likely to be divided into a large number subcarriers. To alleviate the computational burden, we can apply the subcarrier down-sampling, such that only part of the subcarriers will be involved in analog processing. Specifically, if an r-time down-sampling operation is applied, the original multi-user EDC $\text{diag}\{\widetilde{\boldsymbol{H}}\}_{n=0}^{N}$ will be replaced by

$$\widetilde{\boldsymbol{H}}_{DS,r} = \text{diag}\{\widetilde{\boldsymbol{H}}_{1+nr}\}_{n=0}^{N/r-1} \ . \tag{5.30}$$

Consequently, the objective function in **P2** will be adapted to

$$\prod_{i=1}^{NKM_r/r} (\widetilde{\boldsymbol{H}}_{DS,r}\widetilde{\boldsymbol{H}}_{DS,r}^{*})^{-1}[i,i] \ . \tag{5.31}$$

The computational complexity will be reduced by r times from minimizing Eq. (5.21a) to Eq. (5.31). Later on, the simulations will show that even a relatively large r will cause a negligible MI loss.

5.3.2 Digital processing

After analog processing, we start to complete the digital processing targeting at MUI removal and MI maximization. Without loss of generality, we take UE-k on subcarrier-n as an example. To highlight the twofold functionality of digital processing, we specially decompose the associated digital precoder as

$$\boldsymbol{P}_{D,k,n} = \boldsymbol{P}_{D,k,1,n}\boldsymbol{P}_{D,k,2,n} \ , \tag{5.32}$$

where $\boldsymbol{P}_{D,k,1,n} \in \mathcal{C}^{M_t \times M_r}$ is for MUI removal, and $\boldsymbol{P}_{D,k,2,n} \in \mathcal{C}^{M_r \times M_r}$ is for individual MI maximization.

1^{st}**-step digital-processing**: Eq. (5.10) points out that, to get an MUI-free EDC, $\boldsymbol{P}_{D,k,1,n}$ must lie in the null-space (here referring to column space) of

$$\overline{\boldsymbol{H}}_{k,n} = \left[\widetilde{\boldsymbol{H}}_{1,n}^{*}, \cdots, \widetilde{\boldsymbol{H}}_{k-1,n}^{*}, \widetilde{\boldsymbol{H}}_{k+1,n}^{*}, \cdots, \widetilde{\boldsymbol{H}}_{K,n}^{*}\right]^{*} . \tag{5.33}$$

By performing $svd(\overline{\boldsymbol{H}}_{k,n}) = \overline{\boldsymbol{U}}_{k,n}\overline{\boldsymbol{\Sigma}}_{k,n}\overline{\boldsymbol{V}}^{*}_{k,n}$, the null-space of $\overline{\boldsymbol{H}}_{k,n}$ can be extracted as

$$\widehat{\boldsymbol{V}}_{k,n} = \boldsymbol{V}_{k,n}[:, (K-1)M_r + 1 : M_t]. \tag{5.34}$$

It is worth mentioning that $rank(\widehat{\boldsymbol{V}}_{k,n}) \geq M_r$ must hold, otherwise the HBD constraint cannot be satisfied anyhow.

When $M_t = KM_r$, $\boldsymbol{P}_{D,k,1,n} = \widehat{\boldsymbol{V}}_{k,n}$ is clearly the only viable option. Whereas for $M_t > KM_r$, $\boldsymbol{P}_{D,k,1,n}$ is non-unique because any M_r-dimensional subspace of $\widehat{\boldsymbol{V}}_{k,n}$ would suffice. Nevertheless, randomly selecting a subspace may compromise the EDC, especially for M_t and KM_r being significantly different. To harness power as well as removing MUI, we adopt the subspace projection method similar to [87]. Specifically, towards $\boldsymbol{H}_{k,n}$, denote its MUI-free space $\boldsymbol{P}^{n}_{k,n}$ and signal space $\boldsymbol{P}^{s}_{k,n}$ as

$$\boldsymbol{P}^{n}_{k,n} = \boldsymbol{I} - \overline{\boldsymbol{H}}^{*}_{k,n}(\overline{\boldsymbol{H}}_{k,n}\overline{\boldsymbol{H}}^{*}_{k,n})^{-1}\overline{\boldsymbol{H}}_{k,n} \ , \tag{5.35a}$$

$$\boldsymbol{P}^{s}_{k,n} = \widetilde{\boldsymbol{H}}^{*}_{k,n}(\widetilde{\boldsymbol{H}}_{k,n}\widetilde{\boldsymbol{H}}^{*}_{k,n})^{-1}\widetilde{\boldsymbol{H}}_{k,n} \ . \tag{5.35b}$$

By performing $svd(\boldsymbol{P}^{s}_{k,n}\boldsymbol{P}^{n}_{k,n}) = \overline{\boldsymbol{U}}_{k,n}\overline{\boldsymbol{\Sigma}}_{k,n}\overline{\boldsymbol{V}}^{*}_{k,n}$, $\boldsymbol{P}_{D,k,1,n}$ can be set as $\overline{\boldsymbol{V}}_{k,n}[:, 1 : M_r]$.

2^{nd}-step digital-processing: Thanks to $\boldsymbol{P}_{D,k,1,n}$, along with the analog precoders, UE-k ends up with an MUI-free EDC on subcarrier-n as follows:

$$\widetilde{\boldsymbol{H}}_{eff,k,n} = \widetilde{\boldsymbol{H}}_{k,n}\boldsymbol{P}_{D,k,1,n} \ , \tag{5.36}$$

The received signal can, therefore, be expressed as

$$\boldsymbol{y}_{k,n} = \widetilde{\boldsymbol{H}}_{eff,k,n}\boldsymbol{x}_{k,n} + \boldsymbol{\xi}_{k,n} \ . \tag{5.37}$$

According to [27], the analog precoder $\boldsymbol{W}_{A,k}$ is approximately semi-unitary under mmWave mMIMO setup, so the noise vector $\boldsymbol{\xi}_{k,n} = \boldsymbol{W}^{*}_{A,k}\boldsymbol{\eta}_{k,n}$ is almost white. Therefore, the optimal digital precoders for $\widetilde{\boldsymbol{H}}_{eff,k,n}$ correspond to its right and left singular matrix, denoted as $\widetilde{\boldsymbol{U}}_{eff,k,n}$ and $\widetilde{\boldsymbol{V}}_{eff,k,n}$, respectively. By setting $\boldsymbol{P}_{D,k,2,n} = \widetilde{\boldsymbol{V}}_{eff,k,n}$ and taking the transmit power constraint into account, the digital precoders are finally determined as

$$\boldsymbol{P}_{D,k,n} = \sqrt{M_r}\frac{\boldsymbol{P}_{D,k,1,n}\widehat{\boldsymbol{V}}_{eff,k,n}}{\|\boldsymbol{P}_{A}\boldsymbol{P}_{D,k,1,n}\widehat{\boldsymbol{V}}_{eff,k,n}\|_{F}} \ , \tag{5.38a}$$

$$\boldsymbol{W}_{D,k,n} = \widehat{\boldsymbol{U}}_{eff,k,n} \ . \tag{5.38b}$$

Up to this point, we have accomplished the entire HBD-based transceiver design for wMU mmWave mMIMO. Summarizing, the specific design can be carried out as follows:

1. Calculate the MI lower-bound according to Eq. (5.15);
2. Formulate **P2** according to Eq. (5.21);
3. Apply DSS algorithm for the MBS or the entry-wise update for the MAS to get the analog precoders;
4. Obtain the digital precoders according to Eq. (5.38)

5.3.3 Complexity analysis

As the end of Section IV, this part will quantify the complexity of the proposed HBD scheme and compare it with some representative alternatives. For all methods, their complexity regarding the low-dimensional digital processing tends to be relatively small, so we will only focus on the high-dimensional analog processing that occupies the primary computational burden. For simplicity, while without affecting the central conclusion, we will compare the complexity in the order of multiplications.

The major computing burden of the proposed MBS-HBD lies in calculating Eqs. (5.23) and (5.26), each requiring multiplications of $\mathcal{O}(KN_rN(KM_r)^3)$ and $\mathcal{O}(KN_tN(KM_r)^3)$, respectively. As $N_t \gg N_r$ usually holds, the sum of these two can be merged into $\mathcal{O}(KN_tN(KM_r)^3)$. In comparison with MBS-HBD, MAS-HBD further involves iterations with $\mathcal{O}((KM_r)^3)$ multiplications per update. Hence, the ultimate complexity comes to $\mathcal{O}(KN_t(N+n_pM_r)(KM_r)^3)$, with n_p representing the iteration times that is typically very small. When it comes to the existing schemes, the complexity of BS-HBD [32] can be easily obtained as $\mathcal{O}(KNN_t^2N_r^2)$. EGT-HBD proposed in [86] and AM-HBD proposed in [89] involve a one-time SVD and a per-UE per-subcarrier SVD, respectively, so their individual complexity can be roughly characterized by $\mathcal{O}(N_t^3 + NK(N_rM_r)^2)$ and $\mathcal{O}(KNN_t^3)$. As for IMD-HBD proposed in [87], although its applicability in wideband channels is unknown, its complexity is expected to be no

smaller than $\mathcal{O}(N(N_t^3 + n_a K M_r^3))$ given its narrowband realization, with n_a representing the iterations of matrix decomposition that is often large.

In most cases, BS-HBD enjoys the lowest complexity for free of cumbersome matrix inversions or decompositions, while IMD-HBD suffers from the highest complexity for many times of matrix decompositions. As for the proposed one, the corresponding implementing complexity is generally somewhere in between, and some more detailed remarks are in order.

- With a small number of UEs, the proposed HBD is highly efficient because no large-scale SVD (at least $\mathcal{O}(N_t^3)$) is required.
- With a large number of UEs, the proposed HBD tends to be less efficient because the complexity can reach to $\mathcal{O}(K^4)$.
- In a standard hybrid system, the proposed HBD has a modest complexity because the limited BS-end RF chains restricts the number of to-be-served UEs.

5.4 Simulations

In this section, simulations will be carried out to verify the superiority of the proposed HBD scheme over existing HBD counterparts. Unless otherwise specified, the transceiver-related parameters are set as: $N_t = 32$, $N_t = 16$, $M_t = 8$, $M_t = 2$, and $K = 4$; the channel-related parameters are set as: $D = 8$ and $N = 32$; $h(\cdot)$ is set as the raised-cosine filter with a roll-off factor $\beta = 0.2$. 3-bit APS will be used in the MAS, and the entry-wise update for analog processing will terminate in 5 iterations [2] or the relative changing ratio no exceeding 0.01. In simulations, the ideal MI upper-bound is obtained by neglecting the MUI and summing up the MI of each and every UE achieved in fully-digital structures. All curves are the average of 500 independent channel realizations.

[2] One iteration stands for a complete update of $\boldsymbol{P}_A$ and $\{\boldsymbol{W}_{A,k}\}_{k=1}^K$.

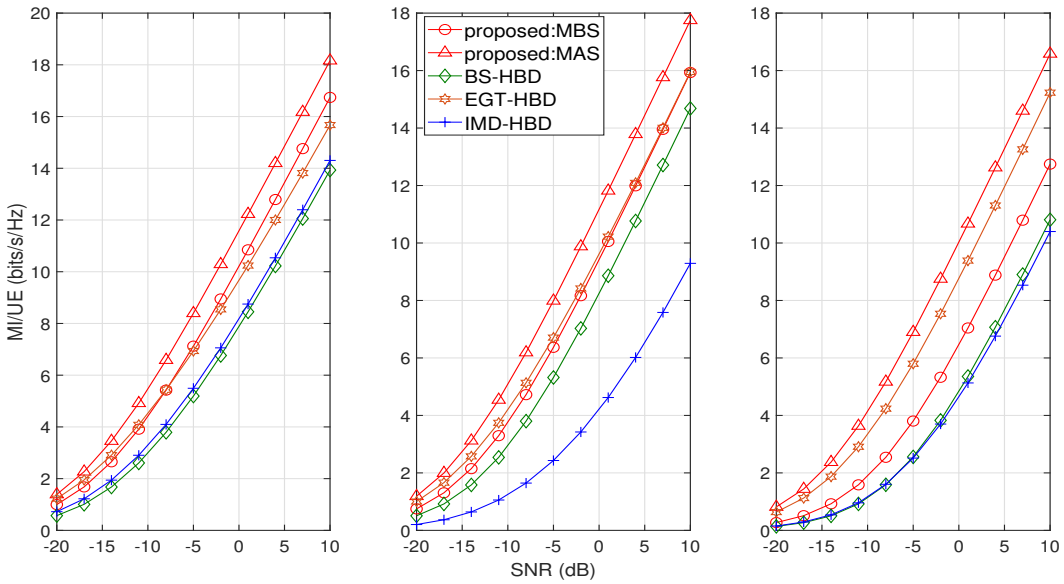

Figure 5.3: Averaged MI/UE for various HBD schemes in narrowband channels: $L = 6$, 12 and 100.

MI in frequency-flat channels: Before studying the wideband channels, we first focus on the narrowband channels. Three different levels of channel sparsity are considered with $L = 6$, $L = 12$, and $L = 100$. The first two cases are quite standard to mmWave channels, while the last case is unlikely to hold at mmWave frequencies as the the corresponding channel tends to be Rayleigh-fading. However, testing this extreme case is still important for us to speculate the applicability of the proposed scheme at lower frequencies.

For BS-HBD proposed in [32], the beam codewords are selected from the DFT matrix. For EGT-HBD proposed in [86], 5-bit APS is used at the BS and 4-bit APS is used at the UE. For IMD-HBD proposed in [87], continuous APS is adopted by the transceivers. Fig. 5.3 shows that the performance of IMD-HBD and BS-HBD is sensitive to the sparsity level. Although EGT-HBD is less insensitive, its performance is much worse than the proposed one. Specifically, the proposed MAS-HBD outperforms all schemes by over 2dB in the entire SNR region. The proposed MBS-HBD not only exceeds BS-HBD with the same hardware configurations, but also well matches and even excels IMD-HBD and EGT-HBD, both enjoying better hardware configurations. Despite being originally proposed in frequency-selective channels, it is clear the proposed HBD also works well in narrowband channels, regardless of channel sparsity.

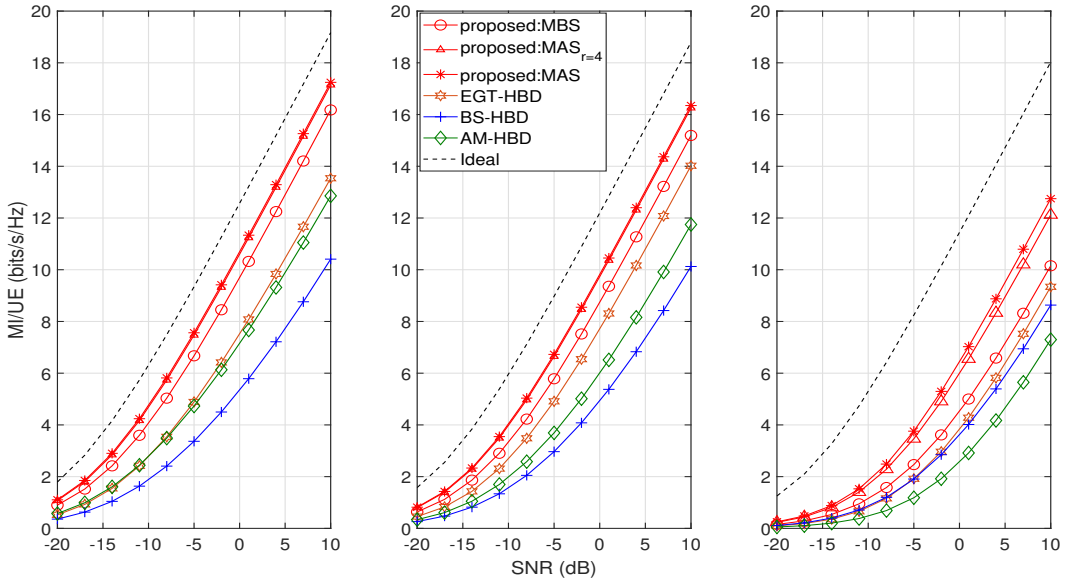

Figure 5.4: Averaged MI/UE for different HBD schemes in wideband channels with $L = 6$, 12 and 100.

MI in frequency-selective channels: We then compare MI performances in wideband mmWave channels. Apart from BS-HBD and EGT-HBD[3] , AM-HBD devised in [89] for wideband channels is also taken into comparison, and its analog configuration is set the same as EGT-HBD. Fig. 5.4 shows that, when the wideband mmWave channels exhibit strong sparsity, ($L = 6$ and $L = 12$), the proposed HBD is remarkably superior to others and its performance gap to the ideal upper bound is less than 3dB. Similar to the narrowband case, we also test the performance in wideband rich-scattering environments, by setting $L = 100$. The corresponding results reveal that all schemes suffer from certain performance degradation. It is worth mentioning that the degradation is inevitable and should be largely due to the limitations of hybrid structures. Even so, it can be observed that the proposed HBD still outperforms the rest and has the least degradation in comparison with the standard sparse scenarios.

With the $r = 4$ down-sampling applied, the resultant MI loss is very minimal for $L = 6$ and 12. Only until $L = 100$ will a small degradation (< 0.8dB) occurs as the correlation between

[3] For fairness, we have extended the narrowband EGT-HBD to the wideband channels, where a common RF precoder is calculated as the quantized Karcher mean of the RF precoder at each subcarrier.

two distant subcarriers diminishes in the Rayleigh-fading like channel. Based on the results, it can be safely concluded that the subcarrier down-sampling is an effective means to reduce the implementing complexity dramatically at the cost of little performance loss.

APS Impact: To verify the effectiveness of the entry-wise update in analog processing for the MAS, we fix $L = 6$ and plot the relative changing ratio versus the iteration times in Fig. 5.5-a. The result illustrates that three iterations suffice to reach a local optimum, implying that entry-wise update will not cause a heavy computational burden. By fixing SNR=-8dB, Fig. 5.5-b reveals that three iterations could harvest an over 20% MI improvement, and MAS with 2-bit APS could get a close performance as MBS. Basically, 3-bit APS could be sufficient for practical use for its good MI performance and economic hardware costs.

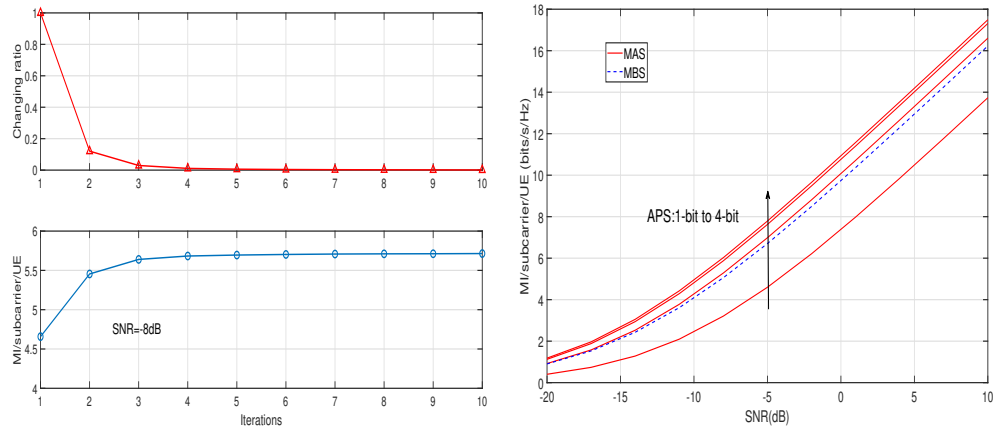

(a) (b)

Figure 5.5: (a) Averaged MI in MAS vs. iterations with SNR=-8dB; and (b) Averaged MI in MAS vs. APS resolution.

MI versus the number of RF chains: One may notice that the previous results are with $M_t = KM_r$. While in practice, the BS may utilize more RF chains to strengthen the signal quality (diversity gain). Since this operation mode can be supported by the proposed HBD and AM-HBD, we then take the MBS as an example to compare their MI performance versus the number of BS-end RF chains in Fig. 5.6.

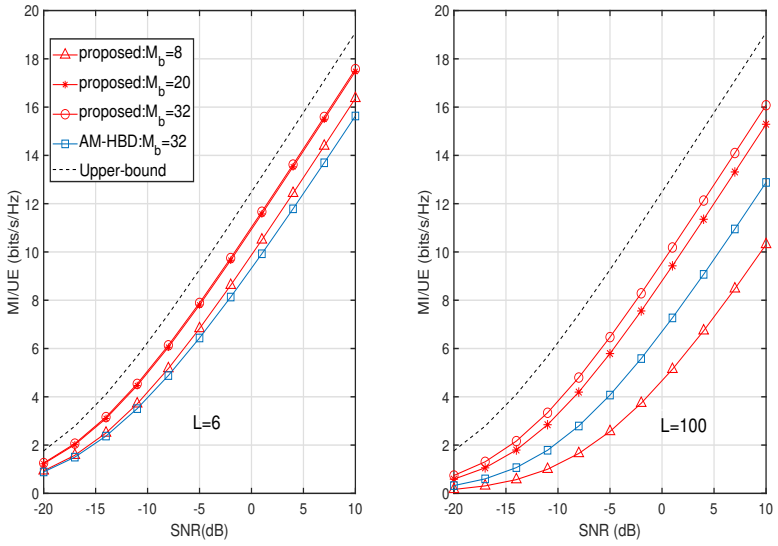

Figure 5.6: Averaged MI versus the number of BS-end RF chains. AM-HBD is with 5-bit APS at the BS and 4-bit APS at the UE.

As expected, a dramatic MI improvement is gained from $M_t = 8$ to $M_t = 20$. This can be explained by that the adversity arising from the coarse beam resolution is partly redeemed by the affluence of RF chains. However, in very sparse channels ($L = 6$), the positive compensation by RF chains will saturate rapidly, so a minimal MI improvement can be observed from $M_t = 20$ to $M_t = 32$. In contrast, the path energy is more dispersively distributed when $L = 100$, thus deploying more RF chains will make the path energy more accumulated, thus resulting in a higher MI. Under the same M_t, MI achieved via the proposed HBD is dramatically higher than that of AM-HBD. This is within our expectation because AM-HBD heavily relies on the strong correlation among subcarriers, while such a correlation will be weaker if L is large.

MI versus the number of UEs and antennas: By fixing the number of BS-end RF chains as 32, we then simulate the system MI versus the number of UEs. Fig. 5.7 shows that system MI increases with K in a roughly linear fashion at first. As K becomes relatively large, the adverse effects arising from the MUI emerge, reflected by a smaller slope of the curve. As K further increases, an MI decline takes place because a large number of UEs severely lower the freedom in constructing the MUI-free space, thus compromising the quality of the EDC.

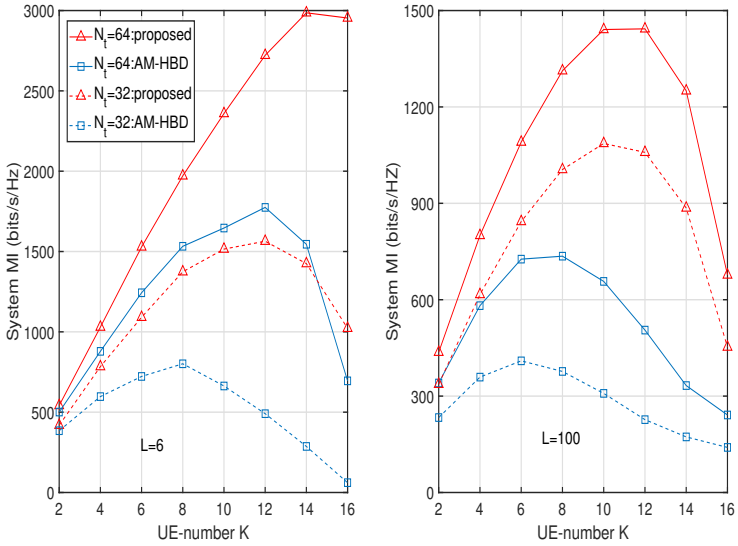

Figure 5.7: System MI versus the number of UE with $M_t = 32$ and SNR=-8dB. AM-HBD is with 5-bit APS at the BS and 4-bit APS at the UE.

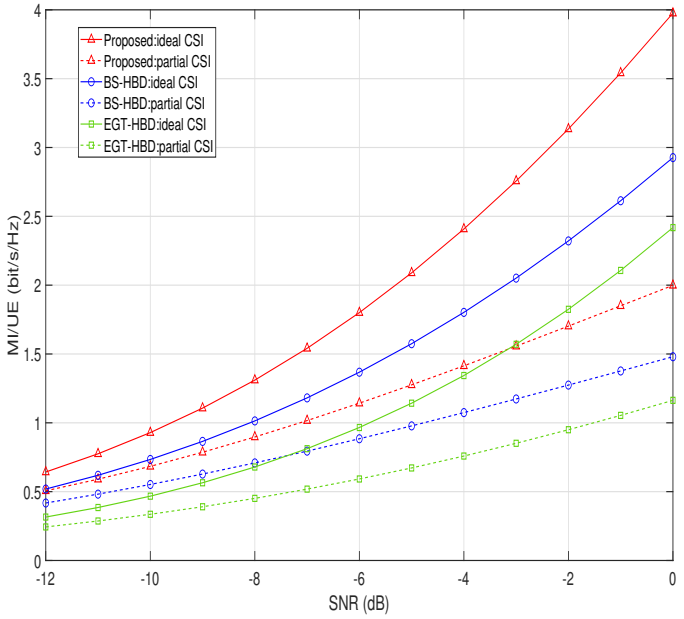

Figure 5.8: MI comparison in CDL-based channel model.

While increasing the number of antennas N_t from 32 to 64, we see a later appearance of the inflection point from which MI starts to decline. The reason is that more antennas bring

in a higher beam resolution, thereby easing the separation of UEs. When infinite antennas are deployed, the beam resolution also becomes infinite, and then it can be expected that the MI curve will monotonically increase with K.

MI in other deployment configurations: In Fig. 5.8, we compare MI performance over a modest range of transmit SNR in more specific conditions. The channel model used is the 3GPP type-A clustered-delay-line (CDL-) based model, with only the azimuth angles considered given the one-dimensional ULA setup. More details about how to generate the type-A CDL-based channel can be found in Chapter 7 in [91]. With perfect CSI, we see that the proposed method still achieves the highest MI. This result is of no surprise because the CDL-based model belongs to the generic geometric model. Another finding worth mentioning is that the BS-HBD performs rather well in this case because the adopted CDL-based channel contains line-of-sight clusters. As perfect CSI might be unattainable at the BS, a common practice is to report the best beams associated with their amplitude and propagating delay. To this end, we set the transmit SNR for channel estimation as 10dB. Only the best one-third of beams is fed back with their angles quantized to five bits. As can be seen, the proposed scheme yields the highest MI under limited feedback, and is even well-comparable to others with ideal CSI at low-to-medium SNR.

5.5 Conclusions

In this chapter, a systematic transceiver solution has been tailored for wMU mmWave mMIMO based on the criterion of MI maximization. The proposed scheme follows the popular HBD-based paradigm but mitigates the potential ad-hoc or empirical nature. For the limit case, we have demonstrated the asymptotic optimality of HBD in the sense of MI for wMU mmWave MIMO transceiver design. For the general case, we have devised high-performance HBD-wMU transceivers for both the MAS and the MBS, regardless of the resolution of the analog beamformers or the sparsity of mmWave channels. Extensive simulations have been carried out, demonstrating the superiority of the proposed HBD over existing counterparts.

Chapter 6

Model-Enhanced Learning-Based Detectors for Wideband Multi-user 1-bit mmWave Communications

In classic communication systems, each antenna is assigned an independent radio-frequency (RF) chain, including the high-bit (e.g., 8$\sim$12 bits [92]) analog-to-digital converters (ADC) and digital-to-analog converters (DAC), local oscillator (LO), low noise amplifier (LNA), mixers, base-band amplifier as well as automatic gain control (AGC) [1]. Such a system is deemed transparent in the sense that signal experiences negligible distortion when going through RF chains. However, three significant obstacles hinder a similar configuration being deployed in mmWave systems. First, the power consumption of converters increases linearly with the sampling rate and exponentially with the byte-width [93] [94]. Even for a single 8-bit mmWave converter this value has already reached 500mW [95]. Secondly, despite the advances in mmWave fabrication, the hardware cost is still far more expensive than its sub-6GHz counterparts. Besides, to accommodate high-bit mmWave converters, the peripheral RF circuitry also needs to be of high quality, thus further augmenting the expenditure. Given the concerns above, 1-bit mmWave communications, referring to the system equipped with 1-bit converters, comes as a promising

remedy. Undoubtedly, 1-bit communications face many limitations, but once combined with mmWave, they exhibit remarkable superiority in terms of energy efficiency.

In transparent systems, data detection typically incorporates two stages, namely *channel estimation* and *coherent demodulation*. Briefly speaking, a pilot-based method is often applied in stage-1 to obtain an estimated channel state information (CSI). Then in stage-2, detection can take place based on the input-output channel model. Unfortunately, in 1-bit systems, the severe non-linear distortion renders the model-based approach inapplicable. For this reason, quite a few new detection schemes have been proposed for 1-bit systems. They can be divided into two categories: The first (e.g., [96, 97, 98, 99, 100]) works on amending the model-based methods, while the second (e.g., [101, 102, 103, 104]) focuses on applying the learning-based methods. In general, the existing literature is mostly restricted to narrowband or point-to-point systems, with very few eceptions (e.g., [100]) where both the wideband and multi-user features are considered. However, these works either require infinitely dense channel taps or an ideal transmitter, lacking a solid foundation for practical use.

Despite the absence of an off-the-shelf solution, we find the method proposed in [101] might be helpful. The reason is, except for a narrowband assumption, this supervised-learning based detector does not rely on CSI and can support multi-user systems with 1-bit converters employed at both ends. Specifically, this design also consists of two phases similar to the model-based one. In phase-1, all users will transmit all possible data vectors. For an arbitrary transmitting vector, its index and the corresponding received vector are regarded as the label and template, if using the language of machine learning. Based on the collected labeled templates, a classifier can be trained. By doing so, the demodulation in phase-2 is equivalent to label prediction. Inspired by this idea, we will pursue a similar route in wMU 1-bit mmWave systems.

We first develop a so-termed learning-based detector (LeaD) based on the concept of the maximum likelihood (ML-) block detection. Nevertheless, we find such a mechanism comes with unaffordable computational complexity and training overhead in 1-bit wMU systems. To

mitigate the impracticability, we henceforth propose a more practical detector termed as model-enhanced LeaD (Me-LeaD). Me-LeaD converts the block detection into a serial detection by utilizing the channel delay-domain information. In this manner, the affordability can be markedly improved without sacrificing any data rate. To facilitate serial detection, we further design a compatible frame structure for Me-LeaD. Nevertheless, in 1-bit mmWave systems, Me-LeaD has an outstanding issue for the classifier has to be trained over high-dimensional inputs. To boost the efficiency of Me-LeaD, we then seek the assistance of channel angular-domain information, giving rise to the augmented (a-)Me-LeaD. In consequence, the training only involves low-dimensional inputs, which will dramatically reduce the complexity while causing negligible harm to the detecting performance. Note that applying (a-)Me-LeaD requires the channel domain information, which is, in fact, unknown in advance. To deal with this problem, we develop an effective method for extracting the model information. Owing to the exploitation of the unique underlying system features, a high precision can be guaranteed with low overhead.

6.1 System Descriptions

In this section, we will first explain the wMU 1-bit mmWave system and the adopted channel model, based upon which we will then introduce the corresponding I-O relationship.

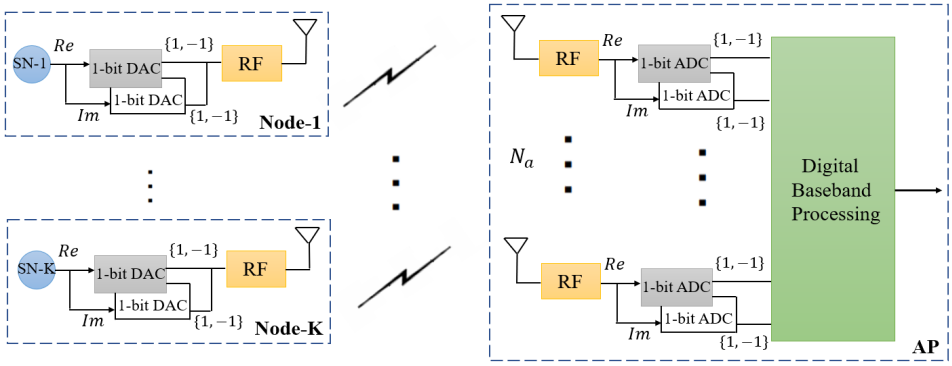

Figure 6.1: An illustrative diagram of the wMU 1-bit mmWave communication system.

6.1.1 System and channel models

A wMU 1-bit mmWave system consisting of K sensor nodes and one central access point (AP) is studied, with the schematic shown in Fig. 6.1. Each single-antenna node uses a pair of ultra-economic 1-bit DACs for data transmission. At the AP side, an N_a-dimensional uniform linear array (ULA) is deployed for data reception. Each receiving antenna is further connected with a pair of 1-bit ADCs applied to the real and imaginary parts of the received signal.

It is well-known that mmWave's propagation exhibits limited scattering and reflections. In addition, the ultra-wideband mmWave spectrum further leads to the frequency selectivity. To incorporate these channel properties, a generalized geometric model [105] is used. Then the uplink channel response between node-k and the AP can be characterized as

$$\boldsymbol{h}_{k,d} = \sqrt{\frac{N_a}{\rho}} \sum_{l=1}^{L_k} \alpha_{l,k} \boldsymbol{a}_r(\theta_{l,k}) \delta(d - d_{l,k}), d < d_m, \tag{6.1}$$

where d represents the delay tap. In Eq. (6.1), ρ is the distance-dependent large-scale fading (free-space loss); d_m represents the maximum distinguishable delay taps; L_k represents the number of paths; $\alpha_{l,k} \sim \mathcal{CN}(0,1)$, $d_{l,k}$ and $\theta_{l,k} \sim U[0, 2\pi)$ represent the small-scale fading, the propagation delay and the angle of arrival (AoA) associated with path-l, respectively. Without loss of generality, the antenna spacing is assumed to be half-wavelength. As a result, we have the array response as follows:

$$\boldsymbol{a}_r(\theta) = \sqrt{\frac{1}{N_a}} \left[1, e^{j\pi \sin\theta}, \cdots, e^{j(N_a-1)\pi \sin\theta}\right]^T. \tag{6.2}$$

Two points need to be mentioned here regarding the channel. First, no assumption is made in terms of the presence of a line-of-sight (LoS) path. Instead, all l_k paths may have similar power levels. Secondly, perfect CSI is unavailable at the AP because obtaining it would be challenging in 1-bit systems.

6.1.2 I-O Relationship

Orthogonal frequency-division multiplexing (OFDM) is the mainstream wideband transmission scheme in transparent communications for its outstanding ability to combat frequency selectivity. Whereas it 1-bit systems, OFDM becomes ineffective for the destroyed system linearity. In light of this, we will go back to the single-carrier (SC) transmission.

Let $s_{k,p}$ stand for the data sent from node-k at time instant-p, then

$$s_{k,p} \in \left\{ \pm\sqrt{\frac{1}{2}} \pm \sqrt{\frac{1}{2}}j \right\} \quad \rightarrow \text{Complex transmission} , \tag{6.3a}$$

$$s_{k,p} \in \{+1, -1\} \qquad \rightarrow \text{Real transmission} . \tag{6.3b}$$

In perfect synchronization, the AP will receive an aggregated signal as

$$\boldsymbol{r}_p = \boldsymbol{r}_{p,I} + j\boldsymbol{r}_{p,Q} = \sqrt{P_t}\sum_{k=1}^{K} \boldsymbol{h}_k \otimes s_{k,p} + \boldsymbol{n}_p \tag{6.4}$$

where P_t is the transmitting power; $\boldsymbol{n}_p \sim \mathcal{CN}(\boldsymbol{0}, n_0 B \boldsymbol{I}_{N_a})$ is the white Gaussian noise with n_0 being the noise power density and B being the communication bandwidth. Throughout this chapter, signal-to-noise ratio (SNR) is defined as $\varepsilon = \frac{P_t}{n_0 B}$. Note that, $s_{k,p}$, i.e., the output of one-bit DACs, has been implicitly incorporated the transmitter non-linearity, thus the linear model of $\boldsymbol{r}_p$ actually represents the channel part only. After 1-bit quantization, the signal to be processed in digital baseband becomes

$$\boldsymbol{y}_p = \mathrm{sgn}(\boldsymbol{r}_{p,I}) + j\mathrm{sgn}(\boldsymbol{r}_{p,Q}) . \tag{6.5}$$

In this work, our aim is to establish a general supervised-learning based detection framework such that $s_{k,p}$ can be efficiently detected in the absence of explicit CSI. For ease of description, the detection framework will be introduced based on the following configuration:

- Two sensor nodes, i.e., $K = 2$.
- Modulation order $X = 2$, i.e., $s_{k,p} = \pm 1, \forall k, p$.

- For node-1, its effective delay taps are contained in $\{d_{1,1}, d_{1,2}, ..., d_{1,k_1}\}$; $0 \leq d_{1,1} < d_{1,2} \cdots < d_{1,k_1} < d_m$.
- For node-2, its effective delay taps are contained in $\{d_{2,1}, d_{2,2}, ..., d_{2,k_2}\}$; $0 \leq d_{2,1} < d_{2,2} \cdots < d_{2,k_2} < d_m$.
- The starting instant is set as 0.

Note that restricting to two nodes will not sacrifice any loss of generality of the proposed detecting schemes.

6.2 Existing Works

Before developing detectors for wMU 1-bit mmWave systems, let us first make a quick review of two representative detectors that are applicable to wMU transparent systems and nMU 1-bit systems, respectively.

6.2.1 Model-Based Detection for wMU Transparent systems

The model-based approach consisting of channel estimation and coherent demodulation is commonly used in wMU transparent systems. In the following, we will explain the details under the prevalent OFDM regime.

Let the length of the cyclic prefix (CP) be d_m and the size of discrete Fourier transform (DFT)/inverse DFT (IDFT) be P. According to [100], the frequency-domain channel for node-k on subcarrier-p ($p < P$) can be expressed as

$$\overline{\boldsymbol{h}}_{k,p} = \sum_{d=0}^{d_m-1} \boldsymbol{h}_{k,d} e^{-j\frac{2\pi p}{P}d} \ . \tag{6.6}$$

Denote $\overline{s}_{k,p}$ as the data transmitted from node-k on subcarrier-p, then the system I-O relationship can be represented as

$$\boldsymbol{y}_p = \sqrt{P_t} \sum_{k=1}^{K} \overline{\boldsymbol{h}}_{k,p} \overline{s}_{k,p} + \boldsymbol{n}_p \tag{6.7}$$

Following the prevalent pilot insertion and post interpolation [106], we can first estimate $\overline{\boldsymbol{h}}_{k,p}$ ($\forall k, p$), with which the AP is able to equalize and demodulate $\boldsymbol{y}_p$. In fact, this approach is being used in LTE physical layer standard. The reason for its popularity and excellence should largely owe to an accurately modeled I-O relationship, based upon which abundant methods are available to tackle the detection therein.

6.2.2 Learning-Based Detection for nWU 1-bit Systems

The learning-based detection [101] [104] was originally designed for narrowband systems, corresponding to $d_{l,k} = 0, \forall k$, in Eq. (6.1). The main advantage over the model-based approach is the outstanding ability in coping with non-linear distortion.

According to [101], the learning-based approach incorporates the template learning and the label prediction. To make it clear, we illustrate the details based on formerly defined configurations. Let $\boldsymbol{s}_p = [s_{1,p}, s_{2,p}]^T$ representing the transmitting vector. All possible $\boldsymbol{s}_p$ is collected by

$$\mathcal{S} = \left\{ \begin{bmatrix} 1 \\ 1 \end{bmatrix}, \begin{bmatrix} 1 \\ -1 \end{bmatrix}, \begin{bmatrix} -1 \\ 1 \end{bmatrix}, \begin{bmatrix} -1 \\ -1 \end{bmatrix} \right\}. \tag{6.8}$$

In phase-1, two nodes obey the following transmission:

$$\boldsymbol{s}_p = \mathcal{S}\left\{\mathrm{mod}\left(p, 4\right)\right\} \ . \tag{6.9}$$

At least one complete scan over $\mathcal{S}$ is mandatory.

For a specific $\boldsymbol{s}_p$, its index and corresponding receiving vector can be regarded as the *label* and the *template*, denoted as L_p^L and T_p^L, respectively [104]. After R scans, a classifier can be trained as

$$f\left([T_{p,I}^L, T_{p,Q}^L]; \boldsymbol{\theta}\right) \mapsto L_p^L, p < 4R, \tag{6.10}$$

with $L_p^L = \mathrm{mod}\left(p, 4\right)$ and $T_p^L = \boldsymbol{y}_p$.

In phase-2, the two nodes will report their respective data to the AP, thus the received $T_p^L = \boldsymbol{y}_p$ accordingly becomes a testing data whose label awaits determination. By feeding it into the

classifier, the following label prediction actually plays a role of demodulation [101], resulting in

$$\widehat{\boldsymbol{s}}_p = \mathcal{S}\left\{f\left([T_{p,I}^L, T_{p,Q}^L]\right)\right\}, p \geq 4R\,. \tag{6.11}$$

As can be seen, demodulation via the learning-based approach does not need explicit CSI. This property is vital to 1-bit systems because accurate channel estimation is tough.

Remark: The model-based and learning-based methods do demonstrate their respective superiority in specific scenarios, but their applicability still exhibits substantial limitations. For the former, a violation of the system linearity will render it largely inferior and even inapplicable. For the latter, its ability to combat non-linear distortion only holds in narrowband channels. As a result, both types fail to undertake the demodulation tasks in wMU 1-bit mmWave systems.

6.3 Detectors for wMU 1-bit mmWave

In light of the existing deficiencies, new detectors will be explicitly designed to 1-bit wMU mmWave systems via model-enhanced learning.

6.3.1 Learning based Detector (LeaD)

We name the first detector LeaD. Although this one follows a similar route as the aforementioned narrowband detector, we will later see that it takes on strikingly different characteristics in wideband channels. Eq. (6.9) tells that the data transmission remains active in narrowband channels, but this manner does not apply to wideband channels. This is because the multi-path effects will render the interference arising from the next transmission falling into the current one, leading to the ambiguity in classification. To address this issue, our proposed LeaD will adopt a zero-padded block transmission given by:

$$\begin{bmatrix} s_{1,0} & s_{1,1} & \cdots & s_{1,P-1} & \mathbf{0}_{1\times(d_m-1)} \\ s_{2,0} & s_{2,1} & \cdots & s_{2,P-1} & \mathbf{0}_{1\times(d_m-1)} \end{bmatrix}. \tag{6.12}$$

To cover all transmit blocks, at least 4^P effective transmissions are required in the training phase. Define $\tilde{\mathcal{S}}$ to be the ensemble containing all possible blocks. We can write the templates and their corresponding labels as

$$\textbf{Template}: T_p^{LeaD} = \text{vec}\left(\boldsymbol{y}_{p(P+d_m-1)}\{\tilde{\mathcal{S}}(p)\}\right) \ , \tag{6.13a}$$

$$\textbf{Label}: L_p^{LeaD} = \text{mod}\left(p, 4^P\right). \tag{6.13b}$$

After R complete scans, all labeled templates can be used for training a 4^P-classes classifier as:

$$\textbf{Classifier}: f\left([T_{p,I}^{LeaD}, T_{p,Q}^{LeaD}]; \boldsymbol{\theta}\right) \mapsto L_p^{LeaD}, \ p < 4^P R. \tag{6.14}$$

Moving on to phase-2, the transmission still follows Eq. (6.12) except for replacing $s_{1,p}$ and $s_{2,p}$ with the nodes' effective data. By feeding the obtained T^{LeaD} into the classifier, the entire block can be demodulated as

$$\textbf{Demodulator}: \tilde{\mathcal{S}}\left(f\left([T_{p,I}^{LeaD}, T_{p,Q}^{LeaD}]\right)\right) \ , \tag{6.15}$$

$$\text{with} \ \ p \geq 4^P R \ \ \text{and} \ \ \text{mod}(p, P + d_m - 1) = 0. \tag{6.16}$$

As can be seen, LeaD is analogous to the ML block detector, a well-recognized optimal solution in transparent systems in the sense of error performance. Unfortunately, gaining such an optimality is impractical in wMU 1-bit systems even with a modestly large P. The reason is that demodulation via LeaD is through predicting one out of a total of 4^P classes, thus the training overhead and computational complexity would be 4^{P-1} times higher than the narrowband case. Let us consider a special form of LeaD, namely LeaD-1 by setting $P = 1$. This case enjoys supreme affordability, but it suffers from huge data loss because each UE transmits only one symbol per d_m instants. In this regard, LeaD-1 is also an "impractical" solution.

Remark: Summarizing, LeaD is capable of demodulating without explicit CSI, but its applicability is severely restricted by the block size P; that is, either decreasing or increasing P cannot decently balance the data rate and complexity.

6.3.2 Model Enhanced (Me-)LeaD

Being aware of the impracticability of block detection in 1-bit systems, we decide to adopt serial detection that is presumably more tractable. To enable this mechanism, we will seek the help of channel unique domain information, giving rise to Me-LeaD.

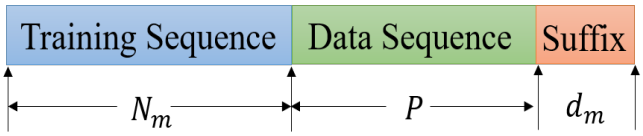

Figure 6.2: Proposed frame structure to accommodate serial detection.

Suppose the effective channel delay taps are available at the AP. For an arbitrary symbol $s_{1,p}$, its associated receiving vectors form the following matrix:

$$\boldsymbol{Y}_{p,1} = \left[\boldsymbol{y}_{p+d_{1,1}}, \boldsymbol{y}_{p+d_{1,2}}, ..., \boldsymbol{y}_{p+d_{1,k_1}}\right] . \tag{6.17}$$

To detect $s_{1,p}$, we need to depend on $\boldsymbol{Y}_{p,1}$ comprising k_1 vectors, each having at most $2^{k_1+k_2}$ combinations if neglecting the noise term. $\boldsymbol{Y}_{p,1}$ has $2^{k_1^2+k_1k_2}$ options, which encompass all patterns associated with $s_{1,p}$. Therefore, one can treat $\boldsymbol{Y}_{p,1}$ as the template and $s_{1,p}$ as the lable. Using them a binary-classifer can be trained and used for later demodulation).

Recall that mmWave channels generally exhibit notable sparsity in the delay domain [94, 99, 48], implying k_1 and k_2 are very small. As a result, the size of the template ensemble for node-1, i.e., $2^{k_1^2+k_1k_2}$, is significantly smaller than 4^P via LeaD. Meanwhile, the much smaller template size as well as the much fewer associated classes also brings a huge reduction in training complexity[1] .

Applying Me-LeaD requires each to-be-decoded symbol entails a full-order interference pattern, whereas this requirement cannot be met by those upfront and trailing symbols in zero-padded transmission. To facilitate serial detection, we propose a new transmission scheme with its frame structure presented in Fig. 6.2. Specifically, the training part is designed as a

[1] It is worth mentioning that a complete scan of all patterns is not a must for Me-LeaD because the number of classes is only two.

length-N_m pseudo sequence composed of modulated symbols, aiming to serve sufficient labeled templates for classifier training; the data part is divided into two segments, with the first being a length-P sequence padded with effective data and the second being a length-d_m suffix to meet the pattern requirement.

Take node-1 as an example, whose templates and associated labels can be represented as

$$\textbf{Template} : T_{1,p}^{Me} = \text{vec}\left([\boldsymbol{Y}_{p,1,I}, \boldsymbol{Y}_{p,1,Q}]\right) \ , \tag{6.18a}$$

$$\textbf{Label} : L_{1,p}^{Me} = s_{1,p} \ , d_{k,1} \leq p < N_m \ . \tag{6.18b}$$

With these labeled templates, we can train a binary-classifier for node-1 as

$$\textbf{Classifier} : f(T_{1,p}^{Me}; \boldsymbol{\theta}_1) \mapsto L_{1,p}^{Me}, d_{k,1} \leq i < N_m \ . \tag{6.19}$$

By feeding $T_{1,p}^{Me}$, whose associated transmit symbol belongs to the segment of effective data, into the classifier, we can get the demodulated data as

$$\textbf{Demodulator} : \widehat{s}_{1,p} = f(T_{1,p}^{Me}), N_m \leq p < N_m + P. \tag{6.20}$$

Remark: Note that, there is a tradeoff between the block-detection based LeaD and the serial-detection based Me-LeaD. That is, the former enjoys a better error performance at the price of higher computational complexity and reduced data rate. Although reducing the block size of LeaD will render its computational complexity more affordable, the computation load increases so steeply with the block size such that the block size would have to be extremely small in order for LeaD to become computationally practical. In other words, the tradeoff between LeaD and Me-LeaD is largely theoretical without much practical implication, making Me-LeaD much more favorable than LeaD in practical use. Nevertheless, Me-LeaD has a notable drawback for the classifier has to be trained over high-dimensional inputs. To streamline the training process, we will resort to additional model information to augment Me-LeaD.

6.3.3 Augmented (a-)Me-LeaD

Abundant mmWave literature (e.g., [11, 31, 86]) has revealed that in transparent systems, the mixed multi-user signals can be separated from the angular domain, transforming the original

high-dimensional spatial processing into the low-dimensional angular processing [86]. Despite the non-transparency of 1-bit systems, we will show that by introducing the angular information to Me-LeaD, the resultant augmented (a-)Me-LeaD still enjoys a similar benefit, thereby notably accelerating training with minimal performance degradation.

Proposition 6.1: *The core angular information of the unquantized signal $\boldsymbol{r}_p$ still retains in its quantized version $\boldsymbol{y}_p$.*

Proof. Rewrite the unquantized signal $\boldsymbol{r}_p$ in Eq. (6.7) as

$$\boldsymbol{r}_p = \underbrace{\begin{bmatrix} \boldsymbol{a}_r^H(\theta_{1,d_{1,1}}) \\ \vdots \\ \boldsymbol{a}_r^H(\theta_{1,d_{1,k_1}}) \\ \boldsymbol{a}_r^H(\theta_{2,d_{2,1}}) \\ \vdots \\ \boldsymbol{a}_r^H(\theta_{2,d_{2,k_2}}) \end{bmatrix}^H}_{\tilde{\boldsymbol{H}}_p} \times \underbrace{\begin{bmatrix} \alpha_{1,d_{1,1}} s_{1,p-d_{1,1}} \\ \vdots \\ \alpha_{1,d_{1,k_1}} s_{1,p-d_{1,k_1}} \\ \alpha_{2,d_{2,1}} s_{2,p-d_{2,1}} \\ \vdots \\ \alpha_{2,d_{2,k_2}}, s_{2,p-d_{2,k_2}} \end{bmatrix}}_{\tilde{\boldsymbol{s}}_p} + \boldsymbol{n}_p \ . \tag{6.21}$$

Both the Bussgang and AQNM methods [107] are commonly used to linearly model a low-bit quantizer. For instance, applying the former gives

$$\begin{aligned} \boldsymbol{y}_p &= \operatorname{sgn}(\boldsymbol{r}_p) \\ &\simeq \operatorname{sgn}\left(\tilde{\boldsymbol{H}}_p\left(\tilde{\boldsymbol{s}}_p + \tilde{\boldsymbol{H}}_p^{\dagger}\boldsymbol{n}_p\right)\right) \\ &\approx 0.64[\operatorname{diag}(\tilde{\boldsymbol{H}}_p\tilde{\boldsymbol{H}}_p^H)]^{-\frac{1}{2}}\tilde{\boldsymbol{H}}_p\left(\boldsymbol{s}_p + \tilde{\boldsymbol{H}}_p^{\dagger}\boldsymbol{n}_p\right) + \boldsymbol{q}_B \\ &= \mathcal{C}\tilde{\boldsymbol{H}}_p\tilde{\boldsymbol{s}}_p + \boldsymbol{q} \ , \end{aligned} \tag{6.22}$$

where $\mathcal{C} = 0.64(k_1 + k_2)^{-\frac{1}{2}}$ and $\boldsymbol{q}$ is a colored noise whose covariance can refer to [107]. A similar linear form can also be obtained via the AQNM method, which reveals that the quantized signal retains the core angular information. It is worth mentioning that the approximated linear model $\boldsymbol{y}_p$ only includes the channel and receiver part without the transmitter part. Therefore, $\boldsymbol{y}_p$ cannot be treated as an end-to-end linear system model where OFDM can be applied. □

Following proposition 6.1, we can quicky arrive at the following conclusion that will help in developing a-Me-LeaD.

Lemma 6.1: The unitary transformation $\boldsymbol{F}_{N_a}$ is also a sparse transformation concerning the quantized signal $\boldsymbol{y}_p$.

Proof. Eq. (6.22) shows that $\tilde{\boldsymbol{y}}_p \approx \mathcal{C}\boldsymbol{F}_{N_a}^H \tilde{\boldsymbol{H}}_p \tilde{\boldsymbol{s}}_p + \boldsymbol{F}_{N_a}^H \boldsymbol{q}$. Since $\boldsymbol{F}_{N_a}^H \boldsymbol{a}_r(\theta) \approx \boldsymbol{e}_{i^*}^T$ with $i^* = \underset{i\in[0,N_a)}{\arg\max} \cos(\pi \sin\theta - \frac{2\pi i}{N_a})$, $\tilde{\boldsymbol{y}}_p$ has very few prominent entries, implying $\boldsymbol{F}_{N_a}$ performs a sparse transformation. □

Based on Eq (6.18a), we define

$$\tilde{T}_{1,p}^{Me} = \boldsymbol{F}_{N_a}^H T_{1,p}^{Me} \ . \tag{6.23}$$

Theoretically, using either $\tilde{T}_{1,p}^{Me}$ or $T_{1,p}^{Me}$ to train the classifier is of no difference. Nevertheless, is focusing on a practical scenario with restricted training overhead and transmit power, using the later would be better because the underlying features of $T_{1,p}^{Me}$ has already been unveiled by $\boldsymbol{F}_{N_a}$. Furthermore, if those few prominent features are reliably identified, then using them as templates should greatly simplify the training process.

Assume that all AoAs are known by the AP, then applying "matched filtering" gives rise to

$$\begin{aligned}\hat{\boldsymbol{Y}}_p &= \tilde{\boldsymbol{H}}_p^H \boldsymbol{Y}_p \\ &\approx \mathcal{C} \begin{bmatrix} \boldsymbol{I}_{k_1} & \boldsymbol{0} \\ \boldsymbol{0} & \boldsymbol{I}_{k_2} \end{bmatrix} \begin{bmatrix} \tilde{\boldsymbol{s}}_{1,p+d_{1,1}} & \cdots & \tilde{\boldsymbol{s}}_{1,p+d_{1,k_1}} \\ \tilde{\boldsymbol{s}}_{2,p+d_{2,1}} & \cdots & \tilde{\boldsymbol{s}}_{2,p+d_{1,k_1}} \end{bmatrix} + \begin{bmatrix} \widehat{\boldsymbol{q}}_1 \\ \widehat{\boldsymbol{q}}_2 \end{bmatrix},\end{aligned} \tag{6.24}$$

and $\tilde{\boldsymbol{s}}_{1,p} = [\alpha_{1,d_{1,1}} s_{1,p-d_{1,1}} \cdots \alpha_{1,d_{1,k_1}} s_{1,p-d_{1,k_1}}]^T$, $\tilde{\boldsymbol{s}}_{2,p} = [\alpha_{2,d_{2,1}} s_{2,p-d_{2,1}} \cdots \alpha_{2,d_{2,k_2}} s_{2,p-d_{2,k_2}}]^T$. Eq. (6.24) reveals that the multi-user signal has been approximately separated via filtering. Hence one can only use $\hat{\boldsymbol{Y}}_{p,1}$ formed by the first k_1 rows of $\hat{\boldsymbol{Y}}_p$ to detect node-1's data. In consequence, the templates and labels related to node-1 become

$$\textbf{Template}: T_{1,p}^{a-Me} = \text{vec}\left([\hat{\boldsymbol{Y}}_{p,1,I}, \hat{\boldsymbol{Y}}_{p,1,Q}]\right) \ , \tag{6.25a}$$

$$\textbf{Label}: L_{1,p}^{a-Me} = s_{1,p}. \tag{6.25b}$$

Based on Eq. (6.25), a binary classifier can be trained as

$$\textbf{Classifier}: f(T_{1,p}^{a-Me};\boldsymbol{\theta}_1) \mapsto L_{1,p}^{a-Me}, d_{k_1} \leq p < N_m \ . \tag{6.26}$$

Then node-1's data is demodulated as

$$\textbf{Demodulator}: \widehat{s}_{1,p} = f(T_{1,p}^{a-Me};\boldsymbol{\theta}_1), N_m \leq p < N_m + P. \tag{6.27}$$

Remark: Summarizing, a-Me-LeaD performs serial detection for each user after suppressing the multi-user interferences. The corresponding complexity is only $\frac{k_1}{N_a}$ of the Me-LeaD's. Despite a potential performance degradation at high SNR, a-Me-LeaD is still appealing because the transmit power at the user end is usually constrained to extend battery life. To apply (a-)Me-LeaD, the channel model information is indispensable, while acquiring it is no easy task in wMU mmWave 1-bit systems. Due to the space limitation, we will leave the specifics in the next section.

6.3.4 Design Considerations

Classifier Option

In the application of (a-)Me-LeaD, we adopt the linear support vector machine (SVM) to train the classifier. The reason is twofold. First, the labeled templates should be limited in communication applications, so deep learning related techniques are unsuitable. Secondly, the linear SVM is trained over a small-scale dataset with few tuning parameters, which will not impose a heavy computational burden on on-line learning.

According to [108], SVM aims at finding an optimal hyperplane to separate two classes. The hyper-parameters $(\boldsymbol{w}, b)$ are obtained through solving the following optimization problem

$$\begin{aligned} \underset{\boldsymbol{w},b,\zeta}{\text{mininize.}} \quad & \frac{1}{2}\boldsymbol{w}\boldsymbol{w}^T + C\sum_{i=1}^{m}\zeta^{(i)} \\ \text{subject to.} \quad & t^{(i)}(\boldsymbol{w}^T\boldsymbol{x}^{(i)} + b) \geq 1 - \zeta^{(i)} \\ & \zeta^{(i)} \geq 0. \end{aligned} \tag{6.28}$$

where C is a regularization parameter and $t^{(i)} = \pm 1$ is the label of the input data $\boldsymbol{x}^{(i)}$. The primitive SVM is designed for binary classification. To handle the multi-class classification, One-vs-Rest and One-vs-One are commonly used [109]. As the number of classes is at most 4 (QPSK), these two types do not differ much. In simulations, we choose the One-vs-One strategy. This type takes one class as positive and all the rest as negative, so it will train n classifiers for the data having n classes. In the scoring phase, all the n-classifiers predict the probability of a particular class, and the class with the highest probability will be selected.

Training Sequence

It is speculated that the quality of templates will hugely impact the detection performance of (a-)Me-LeaD. To ensure a balanced set of labeled templates, the training sequence is preferably adjusted according to the current channel delay-domain information. However, this approach is impractical for a high-volume feedback. For this reason, we devise an "inflexible" scheme by fixing the training sequence as a modulated m-sequence. Furthermore, the m-sequence generator at each node will be allotted a mutually different stage. Such a design enjoys two remarkable benefits:

- Each class contains an almost equal number of templates thanks to the near-perfect randomness of m-sequence.
- Whenever varying the length of the training sequence, the only parameter in feedback is the order of m-sequence.

Table 6.1: Characteristics of different detectors.

	Applicable range	Data Rate	Input dimension	Classes	Complexity
Model-based	wMU transparent	OFDM: $\frac{P}{P+d_m}$	N_a	N/A	$\mathcal{O}(N_a^2)$
Learning-based	nMU 1-bit	SC:1	N_a	X^K	$\mathcal{O}(X^K)$
LeaD	wMU 1-bit	ZP: $\frac{P}{P+d_m}$	$N_a(d_m+P)$	X^{KP}	$\mathcal{O}(X^{KP})$
Me-LeaD	wMU 1-bit	SC: $\frac{P}{P+d_m}$	N_aL_k	X	$\mathcal{O}(N_a^2L_k^2)$
a-Me-LeaD	wMU 1-bit	SC: $\frac{P}{P+d_m}$	L_k^2	X	$\mathcal{O}(L_k^4)$

Up to this point, we have explained the principles for all proposed detectors. Their characteristics are listed in Table.6.1 for reference.

6.4 Model Information Extraction

As mentioned before, applying (a-)Me-LeaD needs channel angular-delay information. Therefore in this section, we will investigate how to get these required domain information.

6.4.1 Angular-Domain Information

Without loss of generality, we explain the AoA estimation based on an arbitrary beam $\alpha\boldsymbol{a}_r(\theta)$. In transparent systems, it is well-known that θ can be estimated as

$$\widehat{\theta} = \frac{2\pi i^*}{N_a} \text{ with } i^* = \arg\max_i \left|\boldsymbol{F}_{N_a}^H[:,i](\alpha\boldsymbol{a}_r(\theta))\right| \ . \tag{6.29}$$

The effectiveness of Eq. (6.29) is attributed to the following fact:

$$\boldsymbol{a}_r^H(\theta_1)\boldsymbol{a}_r(\theta_1) \gg \boldsymbol{a}_r^H(\theta_1)\boldsymbol{a}_r(\theta_2), \ \ \mid \theta_1-\theta_2 \mid > \frac{2\pi}{N_a} \ . \tag{6.30}$$

Perhaps a little bit surprising, we find that a similar fact also holds for the studied 1-bit systems.

Proposition 6.2: *In 1-bit mmWave systems with N_a antennas, $\mid \theta_1-\theta_2 \mid > \frac{2\pi}{N_a}$ will lead to* $\operatorname{sgn}\left(\boldsymbol{a}_r^H(\theta_1)\right)\operatorname{sgn}\left(\boldsymbol{a}_r(\theta_1)\right)$ *being much larger than* $\operatorname{sgn}\left(\boldsymbol{a}_r^H(\theta_1)\right)\operatorname{sgn}\left(\boldsymbol{a}_r(\theta_2)\right)$.

Proof. We first define the following matrix[2] :

$$\boldsymbol{F}_C = \frac{1}{2N_a}\left(\mathrm{sgn}(\boldsymbol{F}_{N_a,I}^T)\mathrm{sgn}(\boldsymbol{F}_{N_a,I}) + \mathrm{sgn}(\boldsymbol{F}_{N_a,Q}^T)\mathrm{sgn}(\boldsymbol{F}_{N_a,Q})\right) . \tag{6.31}$$

Proposition 6.2 can be proved through elucidating the following two properties:

- The largest off-diagonal element (denoted as L_m) of $\boldsymbol{F}_C$ is much smaller than 1.
- $\epsilon_D = \| \boldsymbol{F}_C - \boldsymbol{I}_{N_a} \|_F / \| \boldsymbol{I}_{N_a} \|_F \simeq 0$.

A rigorous demonstration of these properties is hard, whereas numerical validation can be quickly done by testing N_a, i.e., the antenna array size, over a wide range. The relevant results are presented in Table.6.2, from which we are convinced of the validity of the above properties in 1-bit mmWave systems. □

Table 6.2: L_m and ϵ_D under different N_a.

N_a	16	32	64	128	256	512	1024
L_m	0	0.25	0.25	0.313	0.313	0.328	0.328
ϵ_D	0	0.063	0.054	0.047	0.047	0.027	0.021

Now that 1-bit quantization does not really affect the low-correlation relationship between $\boldsymbol{a}_r(\theta_1)$ and $\boldsymbol{a}_r(\theta_2)$, then it is fair to speculate that the criterion of AoA estimation can mimic Eq. (6.29) by replacing $\boldsymbol{F}_{N_a}^H[:,i]$ and $\alpha\boldsymbol{a}_r(\theta)$ with their quantized version. Unfortunately, this naive implantation is invalid because $\mathrm{sgn}\left(\alpha\boldsymbol{a}_r(\theta)\right) \neq \mathrm{sgn}\left(\boldsymbol{a}_r(\theta)\right)$. In other words, the amplitude $\alpha = |\alpha|e^{j\beta}$ may change where the highest correlation occurs. Recall that $\boldsymbol{a}_r(\theta) = [1, e^{j\pi\sin\theta}, \cdots, e^{j(N_a-1)\pi\sin\theta}]^T$, from which we observe that $e^{j\beta}|\alpha|\boldsymbol{a}_r(\theta)$ is a cyclic-shift version of $|\alpha|\boldsymbol{a}_r(\theta)$. To find the original peak position, we first generate $[\boldsymbol{a}_r(\theta)]_j$ by cyclically

[2] It is recommended to use $e^{j\pi/N_a}\boldsymbol{F}_{N_a}$ instead of $\boldsymbol{F}_{N_a}$ throughout angle estimation. This is for the purpose of mitigating the ambiguity in quantizing the on-axis element. All the results achieved in this chapter are based on $e^{j\pi/N_a}\boldsymbol{F}_{N_a}$.

shifting $\boldsymbol{a}_r(\theta)$ by j elements; then, by projecting $\mathrm{sgn}\left([\alpha \boldsymbol{a}_r(\theta)]_j\right)$ $(\forall j < N_a)$ into $\mathrm{sgn}(\boldsymbol{F}_N)$, we locate the angular index as

$$\widehat{\theta} = \frac{2\pi i^*}{N_a} \text{ with } i^* = \arg\max_i \left\{ \max_j \left| \mathrm{sgn}\left(\boldsymbol{F}_{N_a}^H[:,i]\right) \mathrm{sgn}\left([\alpha \boldsymbol{a}_r(\theta)]_j\right) \right| \right\}. \tag{6.32}$$

6.4.2 Delay-Domain Information

The only work left now is to acquire the channel delay-domain information. In our prior work [48], the following training pattern is used in a similar task but without 1-bit constraints

$$[1, 0, 0, ..., 0]_{1\times d_m} \ . \tag{6.33}$$

Here, we continue to use this pattern for its capability of decoupling the delay taps regardless of quantization. In the estimation stage, all nodes are assumed to operate in the time-division-duplex (TDD) mode. Once a node is scheduled a time slot, it will send the above training pattern for a specified number of times.

Owing to the channel's sparsity in the delay domain, we can quickly identify the useful delay taps in transparent systems per the received power. However, this method is invalid in the studied 1-bit system as the received power is a constant, i.e.,

$$\| \boldsymbol{y}_d \|_2 = \| \mathrm{sgn}(\boldsymbol{r}_{p,I}) \|_2 + \| \mathrm{sgn}(\boldsymbol{r}_{p,Q}) \|_2 \doteq 2N_a \ , \tag{6.34}$$

forcing us to propose an enhanced power-based method. To this end, let us first define

$$C(\boldsymbol{y}_d) = \frac{1}{2N_a} \max_{i,j} \left| \mathrm{sgn}\left(\boldsymbol{F}_N^H[:,i]\right) \mathrm{sgn}\left([\boldsymbol{y}_d]_j\right) \right|. \tag{6.35}$$

For an ineffective tap, say tap-d, $\boldsymbol{y}_d \simeq \mathrm{sgn}\left(\boldsymbol{\eta_d}\right)$ holds, so both the real and imaginary parts of $y_d[i]$ can be approximately modeled as a bernoulli variable with

$$\Pr\left(y_d[i] = 1\right) = \Pr\left(y_d[i] = -1\right) = \frac{1}{2} \ . \tag{6.36}$$

We can readily verify that the mean and the variance of $\mathrm{sgn}\left(\boldsymbol{F}_N^H\right) \mathrm{sgn}\left([\boldsymbol{y}_d]_j\right)$ are 0 and $\frac{1}{2N_a}$, respectively. Since N_a is typically very large in 1-bit mmWave systems, the variance tends to

be zero, implying that $C(\boldsymbol{y}_d)$ is densely distributed around 0. On the other hand, if tap-d is effective, then $C(\boldsymbol{y}_d)$ will be much deviated from 0 and approaches to 1 at high SNR. In this sense, $C(\boldsymbol{y}_d)$ acts as a reliable indictor signifying the strength of the tap-d channel. Inspired by this insight, an off-line learning strategy is henceforth proposed, aiming at constructing a look-up table from which we can get an estimated channel strength. The detailed procedures are listed as follows:

1: Giving P_m, randomly generate a bunch of synthesize data

$$\boldsymbol{y}_s = \mathrm{sgn}\left(\sqrt{P_m}e^{j\beta}\boldsymbol{a}_r(\theta) + \boldsymbol{\eta}\right) \tag{6.37}$$

according to $\beta, \theta \sim U[0, 2\pi]$ and $\boldsymbol{\eta} \sim \mathcal{CN}(\mathbf{0}, \boldsymbol{I}_{N_a})$.

2: Calculate $C(\boldsymbol{y}_s)$ according to Eq. (6.35), then store a key-value pair $< \mathbb{E}\{C(\boldsymbol{y}_s)\}, P_m >$.

3: Repeat Steps.1 and 2 by varying P_m.

In the on-line stage, we first calculate $\mathbb{E}\{C(\boldsymbol{y}_d)\}$, then from the constructed table we pinpoint the closest P_m to which $\mathbb{E}\{C(\boldsymbol{y}_d)\}$ corresponds. Only those taps with notable P_m will be selected, and the rest with minimal power contributions are simply excluded. Within the selected taps, their AoAs are estimated according to Eq. (6.32) except for replacing $\alpha\boldsymbol{a}_r(\theta)$ with $\boldsymbol{y}_d$[3] . With the estimated delay-angular information, one can apply (a-)Me-LeaD for demodulation.

[3] When one tap contains more than one prominent path, the estimated AoA is expected to be the one associated with the strongest path.

Table 6.3: Hardware power consumption according to [1] [2]. c =494fJ/step/Hz according to state-of-the-art HPADC structure.

,

Device	Notation	Value
Low Noise Amplifier	P_{LNA}	39mW
Local oscillator	P_{LO}	5mW
Low pass filter	P_{LPF}	14mW
Base-band amplifier	P_{BAMP}	5mW
Mixer	P_M	16.8mW
b-bit ADC(DAC)	P_{ADC}	$cB2^b$

6.5 Simulations

In this section, simulations will be carried out to compare the performance among different detectors. The system parameters for simulation are given in Table.6.4. Apart from BER, EE and EDR will also be included in comparison. In this work, EE (bit/Joule) is defined as the ratio between EDR and the overall system power consumption (hardware and communication). The latter value for a b-bit system is estimated as

$$P_{tol}(b) \approx KP_t + (N_a + K)(\underbrace{P_M + P_{LO} + P_{LPF} + P_{BAMP} + P_{LNA}}_{P_{RF}} + 2P_{b-ADC}) \ . \quad (6.38)$$

The definition and the typical value of each term within Eq. (6.38) are given in Table. 6.3. In the following, we use $P_{tol}(8)$ to stand for the power consumption in transparent systems.

Table 6.4: System parameters for simulation.

System Parameters	Value
ULA size N_a	128
System bandwidth B	1GHz
Carrier frequency f_c	60GHz
Noise power density n_0	-174dbm/Hz
CP length d_m	64
OFDM size P	512
Path Loss ρ	110dB
Modulation	QPSK
SVM regularization parameter	10

Simulation parameters: Without loss of generality, the channel between each node and AP has an equal number of paths, denoted as L. When $K = 3$, the model-based detector and LeaD take up two OFDM symbols for channel estimation and template training, respectively. The proposed Me-LeaD uses one symbol duration to estimate channel domain information and the other one to pad training sequence. When $K = 6$, the model-based detector and LeaD take up three OFDM symbol durations for channel estimation and template training, respectively. Me-LeaD uses two symbol durations to estimate channel domain information and the remaining one to pad training sequence. The least-squares estimator is used for channel estimation in model-based detection. All the curves are the average of 300 independent channel realizations.

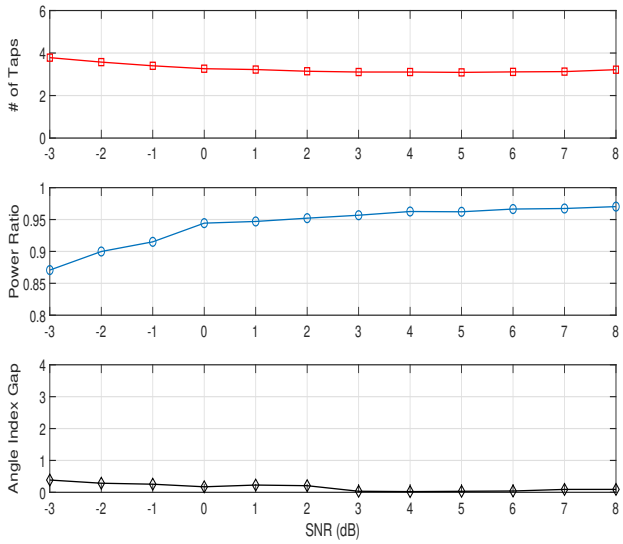

Figure 6.3: Validation of the high-accuracy in obtaining the delay-angular information.

Validation of model-information estimation: We first verify the effectiveness in estimating the model information by setting $K = 3$ and $L = 3$. As can be seen from Fig. 6.3, only a small proportion of taps are identified from a total of 64 taps, making up over 95% of the channel power at a modest training SNR. Among those correctly identified taps, we then compare the gap between the estimated AoA index and the actual quantized one. If the gap is no larger than one, we treat the estimation as a successful one. Fig. 6.3 shows that the averaged gap is small than 1 even at a low training SNR, indicating that the proposed AoA estimation is very reliable. In Table.6.5, we further present the standard deviation for the estimated number of taps as well as the index gap within the correctly identified taps. Both types have small deviations, implying a high stability of the estimation method. Since only one OFDM symbol duration is used to get all the required model information, the proposed method is very efficient.

Table 6.5: Standard deviation of the estimated number of taps and angle index gap.

SNR(dB)	-2	0	2	4	6	8
$\mathrm{Dev}_{\mathrm{tap}}$	1.37	0.89	0.49	0.55	0.076	0.078
$\mathrm{Dev}_{\mathrm{ang}}$	0.94	0.81	0.75	0.67	0.66	0.65

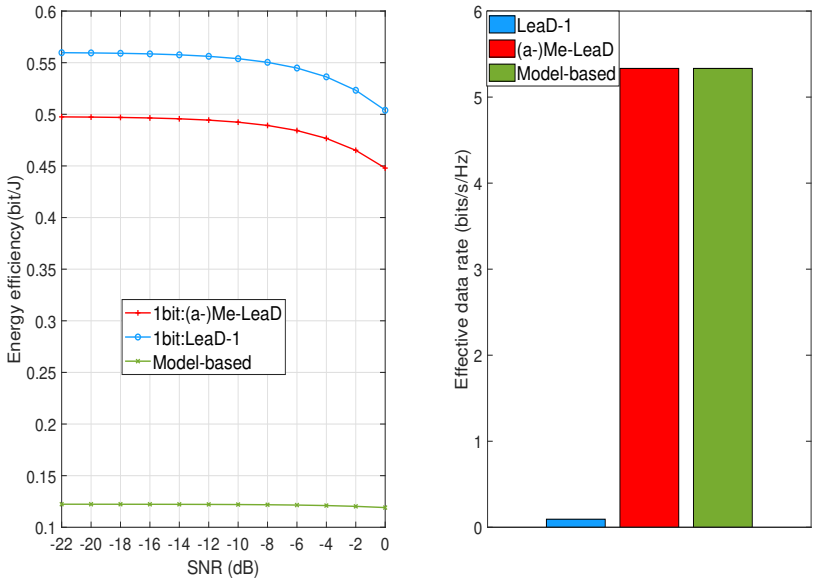

Figure 6.4: EE and EDR comparisons among different detectors with $K = 3$.

Performance comparisons among different detectors: In Fig. 6.4, we compare the EE and EDR performance among LeaD, Me-LeaD, and the model-based detector by setting $K = 3$. As can be seen, the model-based detector achieves the lowest EE because the hardware consumption in transparent systems is significantly higher than their 1-bit counterparts. Under the adopted configurations, LeaD and Me-LeaD achieve a similar EE performance. LeaD is slightly more energy efficient than Me-LeaD is because it remains idle most of the time. However, such a tiny advantage comes at a significant sacrifice of EDR.

We then compare the error performance by setting $L = 2$ The transmission power is set as $P_t = 1W$ (SNR≈3dB) when either estimating the entire channel or domain information only. Note that, only 18 out of 64 combinations can be scanned via LeaD within the pre-defined training duration. Assume the scanned ones can always be correctly detected, while the rest is randomly determined to be one of these 18 combinations. By doing so, the resultant BER can be treated as the BER lower-bound via LeaD. Fig. 6.5shows that LeaD performs worst merely for an incomplete scan.

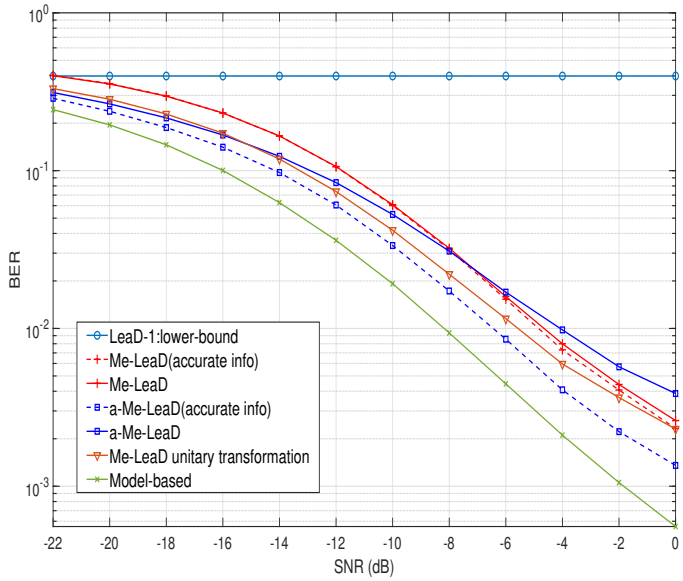

Figure 6.5: BER comparisons among different detectors with $K = 3$, $L = 2$ and QPSK modulation.

With an equal amount of training overhead, Me-LeaD performs remarkably better than LeaD because the former performs serial detection, thereby significantly lowering the requirement of templates. When using the estimated model information, Me-LeaD with sparse transformation is superior to its plain version and a-Me-LeaD. At a low-to-modest SNR, the most-efficient a-Me-LeaD also enjoys a lower error rate than Me-LeaD. But as SNR increases, a-Me-LeaD gradually becomes inferior to Me-LeaD. The inferiority mainly comes from the AoA mismatch, including both the resolution error and estimation error. Although Me-LeaD suffers from a 3dB gap compared to the model-based detector, its EE is more than 4 times higher than the latter. Therefore, through a comprehensive evaluation, Me-LeaD stands out as an appealing detection solution for wMU 1-bit mmWave system owing to its overall decent performance.

BER performance in more special cases: In this part, we compare the BER performance in two special cases. In case-1, we keep $K = 3$ but change L from 2 to 1, so the channel is frequency-flat. In case-2, we set $K = 6$ and $L = 4$, doubling both the number of nodes and the number of paths used in Fig. 6.5. From Fig. 6.6-a, one may surprisingly observe that Me-LeaD still well matches the model-based detector, and Me-LeaD with sparse transformation even

performs best. Their excellent performances should owe to the fact that the training templates (512) are way ampler than required ($4^3 = 64$). We have to admit this case is somewhat unfair to the model-based because it remains workable if assigned to one symbol duration for channel estimation, while Me-LeaD cannot.

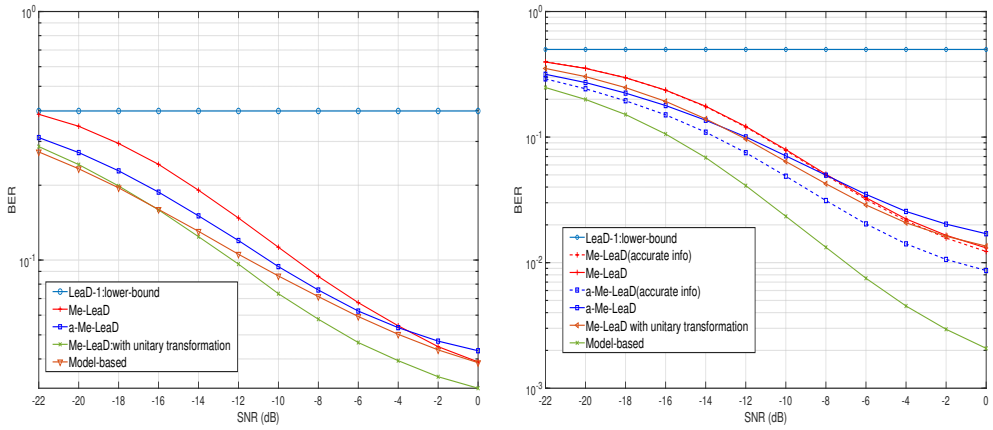

(a) (b)

Figure 6.6: BER comparisons among different detectors (a) $K = 3$ and $L = 1$ with QPSK; and (b) $K = 6$ and $L = 4$ with QPSK.

In case-2, Me-LeaD unsurprisingly performs much worse than the model-based detector. This reason is that 512 training templates are far from sufficient to cover a total of 4^{24} interference patterns. Thanks to the serial detection, an incomplete pattern scan does not paralyze Me-LeaD. From the above results, we conclude that the training overhead has a huge impact on the performance of Me-LeaD. In practice, it is advisable to properly prolong the training sequence, as a small increase in overhead may harvest a notable performance improvement.

6.6 Conclusions

To address the detection problem for wMU 1-bit mmWave systems, the supervised-learning techniques were utilized to cope with the challenges arising from the non-linear distortion. Starting from a generally optimal yet impractical block detector LeaD, two additional practical

serial detectors termed as Me-LeaD and a-Me-LeaD have been developed by exploiting the channel model information. To facilitate (a-)Me-LeaD, we further designed an efficient method to estimate the required domain information. Owing to an innovative integration of learning and modeling, the proposed (a-)Me-LeaD can effectively complete the detection task for wMU 1-bit mmWave systems without relying on explicit CSI or sacrificing data rate.

Chapter 7

Wireless Multi-casting for Wideband mmWave System with 1-bit DAC

Centering at a 1-bit mmWave system as in Chapter 6, we will study a downlink transmission scenario. A particular focus will be placed on wireless multi-casting, a crucial transmission modality frequently used for network control and information sharing. Actually, multi-casting has been extensively studied either in digital sub-6GHz systems (e.g., [110, 111]) or hybrid mmWave systems (e.g., [112, 113]). Despite pronounced distinctions in their hardware architectures, nearly all the examined systems are transparent in the sense that the end-to-end linearity holds. And thanks to this property, the resultant multi-casting design boils down to finding an optimal beam-forming vector under a specific quality-of-service (QoS) target. With the obtained vector, one can multiply it with an arbitrary symbol, by convention a PSK or QAM symbol for information delivery. The entire process imposes no challenges on detection, so a single-tap linear equalizer generally suffices. For this reason, we term the conventional strategy as "*one-make-all*."

Unfortunately, such an elegant framework does not work for 1-bit systems. To clarify this argument, one needs to realize that in conventional multi-casting modulation occurs in the scalar symbol rather than the beamforming vector. As a 1-bit DAC component enables to output at

most four distinct value, associating an arbitrary symbol with a vector is not permitted by hardware. This tightening restriction drives us to complicate modulation via customizing M vectors for an M-ary constellation. By doing so, each vector acts as an independent codeword that is not necessarily co-linear to another as in convention. Following this overarching methodology, we first investigate the achievable constellation size for different types of 1-bit structures, including the analog, the digital, and the hybrid setup. In addition, energy efficiency has been analyzed to measure their individual modulation efficiency. Starting from the low-order modulation case ($M \leq 4$), we demonstrate the optimal pattern is akin to a standard M-ary PSK constellation that can be produced from a basis. Leveraging this property, we are capable of constructing a constellation with arbitrary size by iteratively solving formulated *max-min* problems, each giving rise to a basis vector. Semi-definite relaxation (SDR-) programming is exploited to bypass non-convexity and NP-hardness, followed by carefully designed rank-1 approximation to make sure the codeword is valid. To further streamline the generation of high-order constellations, we also provide a low-complexity alternative that performs comparably to the generic SDR-based approach.

Owing to a different modulation paradigm at the transmitter, the receiver is found to call for adaption in demodulation for twofold reasons. First, as the transmitter applies non-linear quantization, the OFDM scheme cannot diagonalize the convoluted end-to-end channel, making the single-tap equalizer ineffective at each subcarrier. Secondly, when the codewords become linearly independent, the resulting signal model used for block detection tends to be underdetermined. As a result, the classic linear equalizer suffers from performance deficiency. Aspiring to a lower error rate, we resort to investigating detection from an optimization perspective, via which the sparse signal structure can be incorporated conveniently to boost detection performance. Via a series of manipulations, the original detection problem is transformed to a constrained LASSO optimization problem, whose optimum can be assured thanks to its convexity. Simulations show that the achieved error rate with this approach can be dramatically lower than that via the linear equalization.

7.1 System Descriptions

In this section, we will introduce the generic system and channel models adopted for mmWave 1-bit multi-casting. We consider a downlink multi-user mmWave system consisting of K single-antenna sensor nodes and one multi-antenna access point (AP) with N_a antennas. To alleviate power consumption and hardware cost, we suppose the AP, whose number of antennas is massive, deploys a so-called ultra-economic 1-bit-DAC structure for information transmission. At the receiver, each node still adopts conventional high-resolution analog-to-digital converters for data reception because a single RF chain incurs very limited expenditure.

7.1.1 System Model

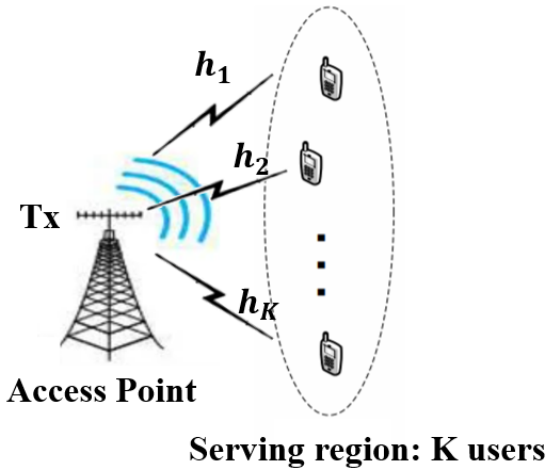

Figure 7.1: The system model of multi-casting.

In the studied 1-bit-DAC system, we focus on a multi-casting scenario where the AP broadcasts common information content to all sensor nodes. Such an means of information delivery is frequently used in wireless downloading and system reconfiguration. In spite of facing a potentially frequency-selective channel, we are prevented from adopting the prevalent OFDM regime because the system linearity is severely corrupted after 1-bit quantization at the AP side. Therefore, we opt to apply the primitive single-carrier (SC) scheme for block transmission.

Let $\boldsymbol{w}_p$ stand for the transmit vector at time instant p. After multi-casting, the received signal at node-k can be represented as

$$r_{k,p} = \boldsymbol{h}_{k,p}^H \otimes \boldsymbol{w}_p + n_{k,p} \ , \tag{7.1}$$

where $n_{k,p} \sim \mathcal{CN}(0, \sigma^2)$ is the additive Gaussian noise with power σ^2. Throughout this chapter, we set $|\boldsymbol{w}_p| = \sqrt{N_a}$, and the SNR is defined as $\epsilon = \frac{1}{\sigma^2}$. Note that $\boldsymbol{w}_p$ in Eq. (7.1) does not involve any user-related subscript. This is because in the context of multi-casting, $\boldsymbol{w}_p$ conveys information common to all users.

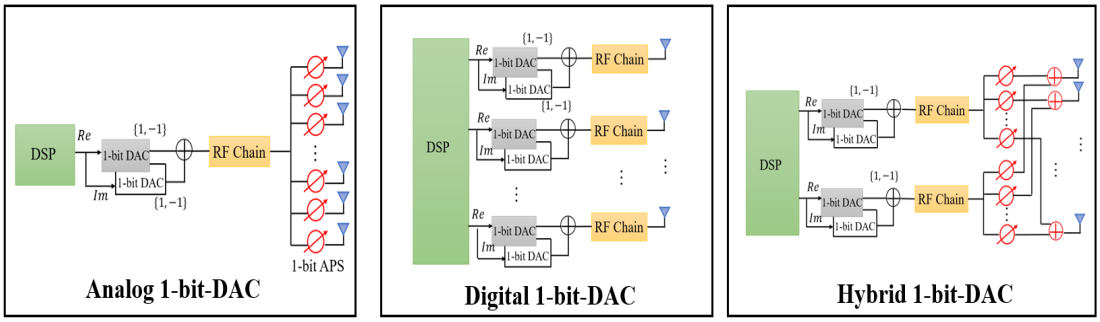

Figure 7.2: The block diagrams for analog, digital, and hybrid 1-bit-DAC setups.

7.1.2 Channel Models

Similar to [62], we adopt the widely used Saleh-Valenzuela channel model to characterize the propagation environment between AP and node-k. Using this model, the channel response for the d-th delay tap can be expressed as

$$\boldsymbol{h}_{k,d} = \sqrt{\frac{N_a}{1 + (L_k - 1)\mathcal{K}}} \left(\alpha_{0,k} \boldsymbol{a}_t^H(\theta_{0,k} + \sum_{l=1}^{L_k - 1} \alpha_{l,k} \boldsymbol{a}_t^H(\theta_{l,k}) \delta(d - d_{l,k}) \right), \ d < d_m \tag{7.2}$$

where d_m is the maximal number of distinguishable taps in the delay domain; L_k is the number of paths; $\alpha_{l,k}$, $d_{l,k}$, and $\theta_{l,k}$ represent the small-scale fading, the propagation delay and the angle of arrival (AoA) associated with the l-th path, respectively. For the direct path, $\alpha_{0,k} \sim \mathcal{CN}(0, 1)$. For other scattered paths, $\alpha_{l,k} \sim \mathcal{CN}(0, 1/\mathcal{K})$ with $\mathcal{K}$ standing for the Rician factor. Suppose the AP adopts a half-wavelength spaced uniform linear array (ULA), then we can

write the array response as $\boldsymbol{a}_t(\theta) = \sqrt{\frac{1}{N_a}}\left[1, e^{j\pi\sin\theta}, \cdots, e^{j(N_a-1)\pi\sin\theta}\right]^T$. Let $\boldsymbol{H}_k$ consist of all effective delay taps between node-k and AP. Therefore, it can be used to describe the effect channel matrix for node-k.

7.2 Rate Fundamentals of 1-bit Multi-casting

Before detailing the specific multi-casting strategy, we first focus on establishing some crucial fundamentals in this section for three types of 1-bit-DAC setups: analog, digital, and hybrid. The theoretical aspects to be covered include the rate limit for each 1-bit structure along with the corresponding energy efficiency.

7.2.1 Analog Structure

We start with the analog type with its schematic shown in Fig. 7.2. Upon the completion of digital signal processing, the output will be processed by 1-bit DAC before being precoded by the 1-bit APS network. The 1-bit APS component acts as an RF comparator thus it is very cost-effective [31]. For simplicity, we drop out the time index, then a valid transmit vector $\boldsymbol{w}$ at the antenna side should satisfy

$$\boldsymbol{w} = \boldsymbol{a}s, \text{ with } \begin{cases} s \in \left\{\pm\sqrt{\frac{1}{2}} \pm \sqrt{\frac{1}{2}}j\right\} \\ \boldsymbol{a}[i] \in \{-1, 1\}, \forall i \in [1, N_a] \end{cases}. \tag{7.3}$$

Lemma 7.1: For an analog 1-bit-DAC setup having N_a antennas, the maximal number of transmit vectors under a fixed value of transmission power is 2^{N_a+1}.

Proof. Since $\boldsymbol{a}s = (-\boldsymbol{a})(-s)$, either s or $-s$ results in an identical constellation with size 2^{N_a}. Thus the eventual number of transmit vectors is 2^{N_a+1}. □

The core hardware upholding these 2^{N_a+1} vectors comprises one RF chain, N_a low noise amplifiers, and N_a 1-bit APS components. An RF chain further consists of a local oscillator, a low pass filter, a base-band amplifier, a mixer, a splitter, and a pair of 1-bit DACs. The power

consumption for each component is listed in Table.7.1. To simplify notation, we use P_{RF} to denote the total power consumed by one RF chain. With taking the communication power P_t into account, the energy efficiency is computed as

$$\eta_a = \frac{N_a + 1}{P_t + P_{RF} + P_{SP} + N_a P_{LNA} + N_a P_{APS}} \ . \tag{7.4}$$

Table 7.1: Hardware power consumption with reference to [1, 3, 4]. c =494fJ/step/Hz according to state-of-the-art HPADC structure and B is the bandwidth and is set as 1GHz in this chapter.

Device	Notation	Value
Based-band processor	P_{BB}	200mW
Low Noise Amplifier	P_{LNA}	40mW
Local oscillator	P_{LO}	5mW
Low pass filter	P_{LNA}	14mW
Base-band amplifier	P_{BAMP}	5mW
Mixer	P_M	16.8mW
1-bit DAC	P_{DAC}	$cB2$
1-bit APS	P_{APS}	10mW
RF adder	P_{ADD}	19.5mW
Splitter	P_{SP}	19.5mW
Transmission power	P_t	1W

7.2.2 Digital Structure

When it comes to a digital setup, regardless of digital signal processing, a valid transmit vector $\boldsymbol{w}$ must obey the following form:

$$\boldsymbol{w}[i] \in \left\{ \pm\sqrt{\frac{1}{2}} \pm \sqrt{\frac{1}{2}}j \right\}, i \in [1, N_a]. \tag{7.5}$$

Recall that a pair of DAC components can output at most four distinct values, one can readily draw the following conclusion:

Lemma 7.2: For a digital 1-bit-DAC setup having N_a antennas, the maximal number of transmit vectors under a fixed value of transmission power is 4^{N_a}.

The involved hardware components here mainly include N_a RF chains and N_a low noise amplifiers. Therefore, the corresponding energy efficiency can be calculated as

$$\eta_d = \frac{2N_a}{P_t + N_a P_{RF} + N_a P_{LNA}} \, . \tag{7.6}$$

7.2.3 Hybrid Structure

Our attention finally lands in a hybrid setup where N_r $(N_r > 1)$ RF chains are deployed. Let $\boldsymbol{A} \in \mathcal{C}^{N_a \times N_r}$ and $\boldsymbol{s} \in \mathcal{C}^{N_r \times 1}$ represent the analog precoder and the DAC output, respectively, then the transmit vector can be expressed as

$$\boldsymbol{w} = \boldsymbol{A}\boldsymbol{s} \text{ with } \begin{cases} \boldsymbol{A}[i][j] \in \{-1, +1\}, i \in [1, N_a], j \in [1, N_r] \\ \boldsymbol{s}[i] \in \left\{ \pm\sqrt{\frac{1}{2}} \pm \sqrt{\frac{1}{2}} j \right\}, , \forall i \in [1, N_r] \end{cases} . \tag{7.7}$$

Lemma 7.3: For a hybrid 1-bit-DAC setup having N_a antennas and N_r RF chains, the maximal number of transmit vectors under a fixed value of transmission power is bounded by

$$(N_r + 1)^{N_a+1} \leq C \leq 2^{N_r}(N_r + 1)^{N_a}. \tag{7.8}$$

Proof. For a given $\boldsymbol{s}$, multiplying its real part with a row of $\boldsymbol{A}$ yields at most $(N_r + 1)$ distinct values, indicating that the real part of $\boldsymbol{w}$ has $(N_r + 1)^{N_a}$ combinations. On the other hand, he imaginary part of the product of $\boldsymbol{s}$ and $\boldsymbol{A}$ will contribute $(N_r + 1)$ combinations at least and 2^{N_r} combinations at most. Thus using these two limits, one can quickly get Eq. (7.8). □

Based on lemmas 7.2and7.3, it is straightforward to verify that once the hybrid structure has no fewer than 3 RF chains, its achievable rate will always exceed its digital counterpart. Such an interesting finding may seem counter-intuitive at the first sight, but it relies on the fact that the hybrid structure is not necessarily simpler than the digital type under the 1-bit

setup. Specifically, the former consists of N_r RF chains, N_aN_r APS components, N_a low noise amplifiers, and N_a RF adders. Once N_a tends to be large, which is usually the case of mmWave systems, taking the logarithm on both sides of Eq. (7.8) gives rise to

$$\frac{R_L}{R_U} = \frac{\log_2(N_r+1)^{N_a+1}}{\log_2\left(2^{N_r}(N_r+1)^{N_a}\right)} = \frac{(N_a+1)\log_2(N_r+1)}{N_a\log_2(N_r+1)+N_r} \simeq 1. \tag{7.9}$$

The above approximation reveals that the derived rate bounds are tightly close. Hence we can take the rate lower bound R_L to assess the energy efficiency for hybrid structures, which is computed as

$$\eta_h(N_r) = \frac{(N_a+1)\log_2(N_r+1)}{P_t + N_r(P_{RF}+P_{SP}+N_aP_{APS}) + N_a(P_{LNA}+P_{ADD})}\,. \tag{7.10}$$

Unlike the other two structures whose energy efficiency is irrelevant to the number of RF chains, η_h in Eq. (7.10) behaves as a function of N_r. In this sense, pinpointing which N_r will yield the highest energy efficiency would be useful for hybrid structures.

Lemma 7.4: Let N_r^* stand for the stationary point of $\eta_h(N_r)$. The maximal energy efficiency of a hybrid 1-bit setup with N_a antennas will be achieved by setting $N_r = \underset{\hat{N}_r\in\mathcal{N}}{\arg\max}\ \eta_h(\hat{N}_r)$ with $\mathcal{N} = \{\max(2, \lfloor N_r^* \rfloor), \min(N_a, \lceil N_r^* \rceil)\}$

Proof. By treating η_h as a function over a continuous argument N_r, we calculate its first-order derivative and find the value first appears positive and then remains negative as N_r increases. Therefore, η_h first ascends with N_r and then keeps descending. Setting N_r leads the derivative to be zero, thereby maximizing η_h. Since N_r has to be a positive integer in practice, we henceforth arrive at the lemma 7.4. □

7.3 Constellation Construction

The rate limit has been established in the previous section. In a massive MIMO setup, the actual rate usually is significantly lower than the limit. Such considerable discrepancy motivates a careful selection from a vast candidate pool to boost the quality of service (QoS). To this end, we will shed light upon the codeword selecting strategy in this part.

7.3.1 Conventional Multi-casting

To better sense the difficulty in 1-bit multi-casting, we first review the conventional paradigm in the absence of 1-bit constraints. A common practice is to transform the multi-casting design into a beamforming optimization problem under a particular metric, say maximizing the weakest received power. Once determining a specific vector $\overline{\boldsymbol{w}}$, the transmit vector will be set as

$$\boldsymbol{w} = \overline{\boldsymbol{w}}s, \tag{7.11}$$

where s is chosen from an M-ary PSK or QAM constellation by convention. Following this manner, we see that modulation in multi-casting essentially takes place in s instead of $\overline{\boldsymbol{w}}$.

For simplicity but without losing any generality, we assume the channel between AP and the considered user is frequency-flat. In addition, we omit the user index because $\overline{\boldsymbol{w}}$ is common to all users, so the received signal can be represented as

$$r = \boldsymbol{a}_t^H(\theta)\overline{\boldsymbol{w}}s + n. \tag{7.12}$$

Eq. (7.12) describes a generic inter-symbol interference (ISI-)free model, where s can be demodulated via simple linear equalization. The function of $\overline{\boldsymbol{w}}$ becomes apparent, that is, enhancing the equivalent channel gain. A summarizing remark is made as follows with reference to convention multi-casting.

Conventional multi-casting equates to finding a beamforming vector that optimizes the link reliability. Either modulation or demodulation relates to the modulated constellation symbol rather than the beamforming vector.

7.3.2 Generic problem formulation for 1-bit-DAC multi-casting

Unfortunately, the prior *one-make-all* paradigm fails in the 1-bit setups because the transmit vector embedded with an arbitrary s in Eq. (7.12) is not necessarily invalid. For this reason, tailoring a new multi-casting paradigm dedicated to the studied constrained system is crucial.

Applying multi-casting relies on a well-crafted constellation. Since the minimum Euclidean

distance (MED) is a key measure of constellation's performance, our overarching goal is to maximize this indicator, which in turn can be roughly translated to optimizing the error performance of multi-casting. As such, an M-ary constellation design problem can be formulated as follows:

$$\mathcal{P}.1: \textbf{ Generic M-ary Constellation Design}$$

$$\max_{\boldsymbol{w}_1,\cdots,\boldsymbol{w}_M} \min_{\substack{\forall i\in[1,M]\\ i\neq j\\ \forall k\in[1,K]}} \left|(\boldsymbol{w}_i-\boldsymbol{w}_j)^H\boldsymbol{H}_k\right|$$

$$\text{s.t.} \begin{cases} \text{Eq.}(7.3) & \text{if analog} \\ \text{Eq.}(7.5) & \text{if digital} \\ \text{Eq.}(7.7) & \text{if hybrid} \end{cases}, \forall\{\boldsymbol{w}_m\}_{m=1}^M$$

Compared with prior formulated problems (e,g., [114]), $\mathcal{P}.1$ exhibits three major challenges:

- It needs to jointly optimize M codewords.
- It entails non-convex 1-bit-DAC constraints.
- It traverses all Euclidean distances in objective function.

Note that the processing difficulty will further be aggravated by the high dimension issue in mmWave systems. Therefore, directly addressing $\mathcal{P}.1$ would be extremely arduous, and seeking a more tractable alternative, despite being sub-optimal, becomes a necessity.

7.3.3 1-bit-DAC constellation: $M \leq 4$

In light of the difficulty in handling $\mathcal{P}.1$, we retreat to perhaps the simplest condition, i.e., $M = 1$. In this case, only one codeword needs to be designed, and the corresponding optimization problem can be formulated as follows:

$$\mathcal{P}.2: \textbf{ Generic Design for the First Basis}$$

$$\max_{\boldsymbol{w}} \min\left\{\left|\boldsymbol{w}^H\boldsymbol{H}_i\right|\right\}_{i=1}^K$$

$$\text{s.t. Eq.}(7.3)/\text{Eq.}(7.5)/\text{Eq.}(7.7).$$

Other than the 1-bit-DAC constraint, the problem is similar to a conventionally formulated one, by solving which we can complete multi-casting design. Although such convenience does not apply here, the obtained $\boldsymbol{w}^*$ via solving $\mathcal{P}.1$ still lays a foundation for constellation expansion.

Proposition 7.1: *If $\boldsymbol{w}^*$ is a valid codeword for a specific 1-bit-DAC setup, the optimal 2-ary constellation in the sense of maximizing the minimum Euclidean distance can be designed as $\{-\boldsymbol{w}^*, \boldsymbol{w}^*\}$.*

Proof. For ease of representation, let us define

$$\boldsymbol{f}(\boldsymbol{w}) = \min \left\{ \left| \boldsymbol{w}^H \boldsymbol{H}_i \right| \right\}_{i=1}^{K}. \tag{7.13}$$

Adding $\boldsymbol{w}$ to $\{\boldsymbol{w}^*\}$ will make the MED be $\frac{1}{2}|\boldsymbol{f}(\boldsymbol{w}^* - \boldsymbol{w})|$, which, according to the triangular inequality, satisfies

$$\begin{aligned} \frac{1}{2}|\boldsymbol{f}(\boldsymbol{w}^* - \boldsymbol{w})| &\leq \frac{1}{2}(|\boldsymbol{f}(\boldsymbol{w}^*)| + |\boldsymbol{f}(\boldsymbol{w})|) \\ &\leq |\boldsymbol{f}(\boldsymbol{w}^*)|. \end{aligned} \tag{7.14}$$

It is clear that $\boldsymbol{w} = -\boldsymbol{w}^*$ will ensure both equalities hold. □

After obtaining $\{-\boldsymbol{w}^*, \boldsymbol{w}^*\}$, a 4-ary constellation calls for two more codewords. As learned from proposition 7.1, we only need to determine one codeword as the other one will automatically be its inverse. The codeword can be found by solving the following optimization problem:

$$\max_{\boldsymbol{w}} \min\{|\boldsymbol{f}(\boldsymbol{w} - \boldsymbol{w}^*)|^2, |\boldsymbol{f}(\boldsymbol{w} + \boldsymbol{w}^*)|^2\} \tag{7.15a}$$

$$\text{s.t. Eq.}(7.3)/\text{Eq.}(7.5)/\text{Eq.}(7.7). \tag{7.15b}$$

Proposition 7.2: *If $\boldsymbol{w}^*$ represents a valid codeword for a specific 1-bit-DAC structure, then the optimal 4-ary constellation in the sense of maximizing the minimum Euclidean distance can be designed as $\{-\boldsymbol{w}^*, \boldsymbol{w}^*, j\boldsymbol{w}^*, -j\boldsymbol{w}^*\}$.*

Proof. Expanding the objective function of $\mathcal{P}.2$ yields

$$\min\{|\boldsymbol{f}(\boldsymbol{w}-\boldsymbol{w}^*)|^2, |\boldsymbol{f}(\boldsymbol{w}+\boldsymbol{w}^*)|^2\} \tag{7.16a}$$

$$\leq |\boldsymbol{f}(\boldsymbol{w})|^2 + |\boldsymbol{f}(\boldsymbol{w}^*)|^2 \tag{7.16b}$$

$$\leq 2|\boldsymbol{f}(\boldsymbol{w}^*)|^2. \tag{7.16c}$$

Equality holds for (7.16b) if $\mathcal{R}\{\boldsymbol{f}_{\boldsymbol{w}}^H \boldsymbol{f}_{\boldsymbol{w}^*}\} = 0$. This condition can be met by setting $\boldsymbol{w} = j\boldsymbol{w}^*$, which meanwhile leads the equality holds for (7.16c) as well because $j\boldsymbol{w}^*$ is a phase-rotated version of $\boldsymbol{w}^*$. Apparently, $j\boldsymbol{w}^*$ is attainable through conjugating the DAC output of $\boldsymbol{w}^*$. □

Now that the optimal constellation follows a PSK pattern if $M \leq 4$, the entire design boils down to finding an optimal codeword, and the corresponding problem is precisely the already formulated $\mathcal{P}.2$. Recall that $\mathcal{P}.2$ contains 1-bit constraints, and together with the massive MIMO configuration, the problem is a large-scale NP-hard one. For tractability, we leverage SDR programming, a widely used optimization tool in prior multi-casting literature, to simplify $\mathcal{P}.2$. It is worth mentioning that one may seek other more advanced optimization techniques to tackle this problem, but the standard SDR approach can generally yield a decent solution. Following rank relaxation, we can transform $\mathcal{P}.2$ into the following problem:

$\mathcal{P}.3$: **Design the First Basis via Relaxation**

$$\max_{\mathbf{W}} \ \min \left\{ \text{Tr}(\boldsymbol{H}_i \boldsymbol{H}_i^H \boldsymbol{W}) \right\}_{i=1}^K$$

$$\text{s.t. } \boldsymbol{W} \succeq \mathbf{0}$$

$$\begin{cases} \text{Tr}(\boldsymbol{W}) = N_a \text{ for hybrid} \\ \text{Diag}(\boldsymbol{W}) = \mathbf{1}_{N_a} \text{ for analog/digital.} \end{cases}$$

Notice that the constraint associated with the hybrid setup slightly differs from the other two with relaxation. The reason is that codewords in the former case are not restricted to be constant-modulus according to Eq. (7.7). By introducing slack variables, we can rewrite $\mathcal{P}.3$ into its equivalent form, which demonstrates to be a standard quadratically constrained quadratic

programming (QCQP) problem.

$$
\begin{aligned}
&\min_{\mathbf{W},t,s} \; -t \\
\text{s.t.} \;\; &-t - s_i + \text{vec}(\boldsymbol{H}_i^* \boldsymbol{H}_i^T)^T \text{vec}(\boldsymbol{W}) = 0 \\
&\boldsymbol{W} \succeq \mathbf{0} \\
&t \geq 0 \\
&s_i \geq 0, i \in [1, K] \\
&\begin{cases} \text{Tr}(\boldsymbol{W}) = N_a \text{ for hybrid} \\ \text{Diag}(\boldsymbol{W}) = \mathbf{1}_{N_a} \text{ for analog/digital.} \end{cases}
\end{aligned}
$$

Thanks to this standard form, we can efficiently get $\mathcal{P}.3$'s optimal solution via the CVX solver. Note that the obtained $\boldsymbol{W}^*$ is an N_a-dimension square matrix instead of vector that we need, thus rank-1 approximation is essential. The overall process basically follows the classic framework proposed in [115], but two more steps are carefully crafted to accommodate 1-bit structures. First, different quantizing operations are applied per the hardware type. Secondly, iterative update [58, 116, 27] has been customized for the hybrid setup for its digital processing and analog processing are mutually coupling. The detailed procedures are listed in **Algorithm 4** for readers' reference.

7.3.4 1-bit-DAC constellation: $M > 4$

Despite the success in getting low-order constellations via a single codeword (basis), further generalization to high-order constellations fails because all the valid phase-rotated versions concerning the first basis have been used up in constructing the 4-ary constellation. While as implied by proposition 7.2, in order to get an 8-ary constellation based on the obtained 4-ary one, we just need to seek the second basis. For notional conciseness, we define $\boldsymbol{w}^{(j)} = \boldsymbol{w} e^{\frac{j\pi}{2}}$,

then the second basis can be sought by solving the following optimization problem:

$\mathcal{P}.4$: **Generic Design for the Second Basis**

$$\max_{\tilde{\boldsymbol{w}}} \min_{\substack{1\le i\le K\\ 1\le j\le 4}} \left|\tilde{\boldsymbol{w}}^H \boldsymbol{H}_i - \boldsymbol{f}(\boldsymbol{w}_j^*)\right|$$

$$\text{s.t. Eq.}(7.3)/\text{Eq.}(7.5)/\text{Eq.}(7.7).$$

Relaxing $\mathcal{P}.4$ is not that straightforward as relaxing $\mathcal{P}.2$ because the objective function contains cross terms. Fortunately, the homogenization trick proposed in [114] comes as a remedy, via which the generic form can be relaxed into a more tractable form described by $\mathcal{P}.5$.

$\mathcal{P}.5$: **Design the Second Basis via Relaxation**

$$\max_{\widetilde{\mathbf{W}}} \min_{\substack{1\le i\le K\\ 1\le j\le 4}} f_{i,j}(\widetilde{\boldsymbol{W}})$$

$$\text{s.t.} \quad \widetilde{\boldsymbol{W}} \succeq \mathbf{0}$$

$$f_{i,j}(\widetilde{\boldsymbol{W}}) = \text{Tr}\left(\begin{bmatrix} \boldsymbol{H}_i\boldsymbol{H}_i^H & -\boldsymbol{H}_i\boldsymbol{f}(\boldsymbol{w}_j^*) \\ -\boldsymbol{f}^H(\boldsymbol{w}_j^*)\boldsymbol{H}_i^H & \boldsymbol{f}^H(\boldsymbol{w}_j^*)\boldsymbol{f}(\boldsymbol{w}_j^*) \end{bmatrix} \widetilde{\boldsymbol{W}}\right)$$

$$\begin{cases} \text{Tr}(\widetilde{\boldsymbol{W}}) = N_a + 1, \widetilde{\boldsymbol{W}}[N_a+1, N_a+1] = 1 \text{ hybrid} \\ \text{Diag}(\widetilde{\boldsymbol{W}}) = \mathbf{1}_{N_a+1} \text{ analog/digital.} \end{cases}$$

At first glance, $\mathcal{P}.5$ may seem much more difficult than $\mathcal{P}.2$. But with a closer look, we observe that these two problems are essentially homogeneous, implying that the former can also be equivalently represented as a QCQP problem. Hence we can rely on the CVX solver to acquire $\mathcal{P}.5$'s global optimum and implement Algorithm-1 to get the corresponding rank-1 approximation, denoted as $\boldsymbol{w}^\circ$. Note that $\boldsymbol{w}^\circ$ is an $(N_a + 1)$-dimension rather than an N_a-dimension vector. The augmented dimension comes from introducing an auxiliary variable in homogenization [114]. Therefore, $\boldsymbol{w}^\circ$ itself is not an ultimate basis. Instead, $\tilde{\boldsymbol{w}}^* = (\boldsymbol{w}^\circ[N_a + 1])^H \boldsymbol{w}^\circ[1 : N_a]$ is what we need as the second codeword basis. Following a similar design flow from $M = 4$ to $M = 8$, we can increase the constellation size to an even higher value. The extension is straightforward, so the details are omitted here.

7.3.5 Low-complexity alternative

In previous subsections we have transformed a generic constellation design problem into a series of QCQP optimization (sub-)problems. SDR programming is adopted to circumvent the intractability of non-convexity and NP-hardness. Despite a generic feasibility, the complexity issue would be outstanding in a mmWave massive MIMO system. For this reason, a low-complexity alternative, albeit losing some technical rigor, would be in favor in practice.

Let us still focus on the generalization of an 8-ary constellation. To do so, the proposed heuristic method first applies SVD within each user's effective channel[1] , i.e., $svd(\boldsymbol{H}_k) = \boldsymbol{U}_k\boldsymbol{\Sigma}_k\boldsymbol{V}_k^H$, and form a matrix as follows:

$$\widetilde{\boldsymbol{H}}_1 = [\boldsymbol{U}_1[:,1], \boldsymbol{U}_2[:,1], .., \boldsymbol{U}_K[:,1]]. \tag{7.19}$$

Another round of SVD will be implemented on $\widetilde{\boldsymbol{H}}_1$ to get its first left singular vector $\boldsymbol{u}_1$. By feeding $\boldsymbol{u}_1$ into Algorithm-1, we set the corresponding output as the first codeword basis. Likewise, the second codeword basis is obtained by refining the first left singular vector of $\widetilde{\boldsymbol{H}}_2 = [\boldsymbol{U}_1[:,2], \boldsymbol{U}_2[:,2], .., \boldsymbol{U}_K[:,2]]$. These two basis vectors finally yield an 8-ary constellation according to lemma 7.2.

Some explanations can be made towards this heuristic method: the first-stage SVD aims at extracting interference-suppressed scatters from the propagation environment between each user and AP. The second-stage SVD essentially calculates the centroid among these scatters, each acting as a decent virtual path *w.r.t.* all users. Although the 1-bit hardware severely degrades centroids' resolution, massive antennas still help separate them. This method is generally more efficient than the SDR-based approach in generating a relatively high-order constellation. The later simulations will show that it performs similarly to the SDR-based method.

[1] We assume all the singulars are sorted in descending order per their amplitudes.

7.4 Constellation Identification

How to demodulate information is rarely touched upon in prior multi-casting studies because the *one-make-all* policy will not bring in any particular challenges to detection. But when the 1-bit system adopts a fundamentally different multi-casting paradigm at the transmitter side, we find that the receiver side also demands accommodation in deciphering the shared information.

Algorithm 4 Rank-1 Approximation for 1-bit-DAC multi-casting

Input: SDR Solution: $\boldsymbol{W}^* \in C^{N_a \times N_a}$, Maximum random generations T_r, Maximum updates T_e, Effective channels $\{\boldsymbol{H}_k\}_{k=1}^K$, Type$\in$\{Analog, Digital, Hybrid\}.

Output: Codeword vector: $\boldsymbol{w}^* \in C^{N_a \times 1}$

Set $i = 0$ and factorize $\boldsymbol{W}^* = \boldsymbol{V}\boldsymbol{V}^H$
for $i \leq T_r$ **do**
    $v_i = \boldsymbol{V}^H e^{j2\pi * rand(N_a,1)}$
    if Type == Analog **then**
        Get $\hat{\boldsymbol{v}}_i$ by (element-wise) quantizing v_1 to $\{\pm e^{\frac{j\pi}{4}}\}$
    else
        Get $\hat{\boldsymbol{v}}_i$ by quantizing v_1 to $\{\pm e^{\frac{j\pi}{4}}, \pm e^{\frac{j3\pi}{4}}\}$
    end if
end for
$l = \arg\max_{j=1,\cdots,T_r} \min \left\{ \left| \hat{\boldsymbol{v}}_j^H \boldsymbol{H}_i \right| \right\}_{i=1}^K$
if Type == Analog or Type == Digital **then**
    $\boldsymbol{w}^* = \hat{\boldsymbol{v}}_l$
else
    Randomly generate $\boldsymbol{A} \in \mathcal{C}^{N_a \times N_r}$ satisfying (7.7)
    $\boldsymbol{s} \in \mathcal{C}^{N_r \times 1}$ that satisfies (7.7) by quantizing $\boldsymbol{A}^\dagger \hat{\boldsymbol{v}}_l$
    Apply T_e complete rounds of entry-wise update
    $\boldsymbol{w}^* = \sqrt{N_a} \frac{\boldsymbol{A}\boldsymbol{s}}{|\boldsymbol{A}\boldsymbol{s}|}$
end if

7.4.1 Generic LMMSE equalizer based detector

We omit the user index without triggering ambiguity since the information delivered via multicasting is common to all users. For an illustration purpose, we assume that the channel between the user and AP contains two effective taps, delayed by 0 and 1 sampling instant, respectively.

Let $\boldsymbol{\Omega}$ stand for a matrix having M columns, each standing for a codeword from an M-ary constellation. The transmit vector can be uniformly represented as:

$$\boldsymbol{w} = \boldsymbol{\Omega}\boldsymbol{e}_i, \tag{7.20}$$

Supposing the length of data frame to be P, we can express the received signals as

$$\begin{aligned}\boldsymbol{r} &= \boldsymbol{H}\boldsymbol{s} + \boldsymbol{n} \\ &= \begin{bmatrix} \boldsymbol{h}_0^H\boldsymbol{\Omega} & 0 & 0 & \cdots & 0 \\ \boldsymbol{h}_1^H\boldsymbol{\Omega} & \boldsymbol{h}_0^H\boldsymbol{\Omega} & 0 & \cdots & 0 \\ 0 & \boldsymbol{h}_1^H\boldsymbol{\Omega} & \boldsymbol{h}_0^H\boldsymbol{\Omega} & \cdots & 0 \\ \vdots & \ddots & \ddots & \ddots & \vdots \\ 0 & \cdots & \boldsymbol{h}_1^H\boldsymbol{\Omega} & \boldsymbol{h}_0^H\boldsymbol{\Omega} & 0 \\ 0 & \cdots & 0 & \boldsymbol{h}_1^H\boldsymbol{\Omega} & \boldsymbol{h}_0^H\boldsymbol{\Omega} \\ 0 & \cdots & 0 & 0 & \boldsymbol{h}_1^H\boldsymbol{\Omega} \end{bmatrix} \begin{bmatrix} \boldsymbol{s}_1 \\ \boldsymbol{s}_2 \\ \vdots \\ \boldsymbol{s}_P \end{bmatrix} + \boldsymbol{n}. \end{aligned} \tag{7.21}$$

with $\boldsymbol{s}_p \in \{\boldsymbol{e}_1, \boldsymbol{e}_2, \cdots, \boldsymbol{e}_M\}, \forall p$, $\boldsymbol{r} = [r_0, \cdots, r_P]^T$, and $\boldsymbol{n} = [n_0, \cdots, n_P]^T$. Amid a plethora of detection solutions, the linear minimum mean square error (MMSE-) based equalizer is widely used to in mainstream wireless standards [117]. Assume that all the codewords are equiprobably selected from the constellation, then $\mathbb{E}\{\boldsymbol{s}\boldsymbol{s}^H\} = \frac{1}{M}\boldsymbol{I}_{PM}$. By applying linear MMSE equalization, $\boldsymbol{s}_p$ can be demodulated as

$$\begin{aligned} \hat{\boldsymbol{s}}_p &= \underset{\boldsymbol{e}_i \in \{\boldsymbol{e}_1, \cdots, \boldsymbol{e}_M\}}{\arg\min} |\tilde{\boldsymbol{s}}_p - \boldsymbol{e}_i| \\ \text{with } [\tilde{\boldsymbol{s}}_1^T, \tilde{\boldsymbol{s}}_2^T, \cdots, \tilde{\boldsymbol{s}}_P^T]^T &= \left(\frac{M}{\epsilon}\boldsymbol{I}_{PM} + \boldsymbol{H}^H\boldsymbol{H}\right)^{-1}\boldsymbol{H}^H\boldsymbol{r}. \end{aligned} \tag{7.22}$$

From Eq. (7.21), we may notice that the signal model involves PM unknowns and P measurements. From the perspective of estimation theory, the model is under-determined, so the

classic LMMSE solution might not be a decent choice. Nevertheless, if focusing on a small-size constellation, i.e., $M \leq 4$, the solution still guarantees decency because at instant p, we can write the transmit vector as

$$\boldsymbol{w}_p = \boldsymbol{w}^* s_p \ , \tag{7.23}$$

with s_p chosen from an M-PSK constellation $\mathcal{C}_{MPSK}$. Eq. (7.21) henceforth degenerates to

$$\begin{aligned} \boldsymbol{r} &= \tilde{\boldsymbol{H}}\tilde{\boldsymbol{s}} + \boldsymbol{n} \\ &= \begin{bmatrix} \boldsymbol{h}_0^H \boldsymbol{w}^* & 0 & 0 & \cdots & 0 \\ \boldsymbol{h}_1^H \boldsymbol{w}^* & \boldsymbol{h}_0^H \boldsymbol{w}^* & 0 & \cdots & 0 \\ 0 & \boldsymbol{h}_1^H \boldsymbol{w}^* & \boldsymbol{h}_0^H \boldsymbol{w}^* & \cdots & 0 \\ \vdots & \ddots & \ddots & \ddots & \vdots \\ 0 & \cdots & \boldsymbol{h}_1^H \boldsymbol{w}^* & \boldsymbol{h}_0^H \boldsymbol{w}^* & 0 \\ 0 & \cdots & 0 & \boldsymbol{h}_1^H \boldsymbol{w}^* & \boldsymbol{h}_0^H \boldsymbol{w}^* \\ 0 & \cdots & 0 & 0 & \boldsymbol{h}_1^H \boldsymbol{w}^* \end{bmatrix} \begin{bmatrix} s_1 \\ s_2 \\ \vdots \\ s_P \end{bmatrix} + \boldsymbol{n}, \end{aligned} \tag{7.24}$$

which is exactly a standard signal model in ISI channels [118]. With this observation, the LMMSE based demodulator is accordingly adapted to

$$\hat{s}_p = \underset{s \in \mathcal{C}_{MPSK}}{\arg\min} \ |s - \tilde{\boldsymbol{s}}[p]| \text{ with } = (\epsilon^{-1}\boldsymbol{I}_M + \tilde{\boldsymbol{H}}^H \tilde{\boldsymbol{H}})^{-1} \tilde{\boldsymbol{H}}^H \boldsymbol{r}. \tag{7.25}$$

Remark: Regardless of the modulation size, block detection still comes as a must in 1-bit setups because OFDM cannot diagonalize the convoluted channel. This restriction, however, does not apply to conventional multi-casting.

7.4.2 Constellation Size: $M > 4$

Moving to a high-order constellation, say 8-ary, we fail to express the codeword using Eq. (7.23). Instead, we have to rely on the primitive Eq. (7.20), which usually leads to an under-determine signal model. Although the LMMSE approach is still workable, a more powerful yet computationally manageable detector is desired. To this end, we revisit the detection problem from an

optimization perspective, giving rise to

$$\min_{\boldsymbol{s}} \ \ |\boldsymbol{r} - \boldsymbol{H}\boldsymbol{s}| \tag{7.26a}$$

$$\text{s.t. } \mathbf{1}^T \boldsymbol{s}_p = 1, \quad \forall p \in [1, P] \tag{7.26b}$$

$$\boldsymbol{s}_p[i] \in [0, 1], \ \ \forall i \in [1, M] \tag{7.26c}$$

The main roadblock of solving the above problem lies in the discrete constraint Eq. (7.26c). If linking it with Eq. (7.26b), $\boldsymbol{s}$ ends up as a structured sparse vector. With this property, we first replace the objective from 1-norm to 2-norm, then remove the constraints via regularization, so the ultimate objective function becomes

$$\begin{aligned} \mathcal{L}(\boldsymbol{s}, \lambda, \mu) &= |\boldsymbol{r} - \boldsymbol{H}\boldsymbol{s}|^2 + \lambda |\boldsymbol{s}|_1 + \mu \sum_{p=1}^{P} |\mathbf{1}^T \boldsymbol{s}_p - 1|^2 \\ &= \left| \begin{bmatrix} \boldsymbol{r} \\ \mu \mathbf{1}^T \end{bmatrix} - \begin{bmatrix} \boldsymbol{H} \\ \mu \mathbf{1}^T \bigotimes \boldsymbol{I}_P \end{bmatrix} \boldsymbol{s} \right|^2 + \lambda |\boldsymbol{s}|_1. \end{aligned} \tag{7.27}$$

The penalizing idea is drawn from [119] where it deals with detecting classic QAM symbols. Specifically, the l-1 penalty term aims at promoting sparsity, and the l-2 term is to absorb Eq. (7.26c) by setting a large μ. The detection optimization problem is finally formulated as

$\mathcal{P}.6:$ **Detection via Sparse Signal Recovery**

$$\min_{\boldsymbol{s}} \ \ \mathcal{L}(\boldsymbol{s}, \lambda, \mu)$$

$$\text{s.t. } \ \boldsymbol{s} \succeq \mathbf{0}.$$

$\mathcal{P}.6$ is a constrained LASSO problem, so we can easily get its global optimum via the projected proximal gradient method. Define $\tilde{\boldsymbol{s}}$ to be the optimal solution, then $\boldsymbol{s}_p$ will be demodulated as

$$\hat{\boldsymbol{s}}_p = \boldsymbol{e}_{i^\star} \text{ with } i^\star = \underset{i=1,\cdots,M}{\arg\max}\ \tilde{\boldsymbol{s}}[(p-1)M + i]. \tag{7.28}$$

Similar to [119], we can further lower the error rate by leveraging interference cancellation. In particular, $\hat{\boldsymbol{s}}_p$ will be regarded as a reliable demodulated result if its maximal value approaches

1. By excluding those "reliable" $\boldsymbol{s}_p$'s, we can proceed with the next-round detection where a fewer number of unknowns will be involved. Let τ be a reliability threshold, then so long as $\max_{i\in[1,M]} \tilde{\boldsymbol{s}}_p[i] > \tau$ satisfies, we will remove the contribution made by the p-th transmit vector. In consequence, the received signal for the next-round detection is updated as

$$\tilde{\boldsymbol{r}} = \boldsymbol{r} - \sum_{p=1}^{P} \boldsymbol{H}[:, (p-1)M+1 : pM]\hat{\boldsymbol{s}}_p \times \mathbb{I}\left(\max_{i\in[1,M]} \tilde{\boldsymbol{s}}_p[i] > \tau\right). \tag{7.29}$$

Apparently, one can apply multiple rounds of iterative cancellation schemes. Nevertheless, we will only implement one additional round in this chapter for an illustration purpose.

7.5 Simulations

In this section, we will showcase some numerical results regarding the multi-casting performance under various configurations. All the system and channel related parameters used in simulations have been listed in Table. 7.2.

Table 7.2: System and channel parameters for simulation.

Parameters	Value
ULA size N_a	64
Effective taps L_k	$3 \sim 8$
Delay taps d_m	64
Tap index $d_{l,k}$	$U \sim [1, 64)$
AoA $\theta_{l,k}$	$U \sim [0, 2\pi)$
l-1 penalty λ	10
l-2 penalty μ	1000
Cancellation threshold τ	0.8

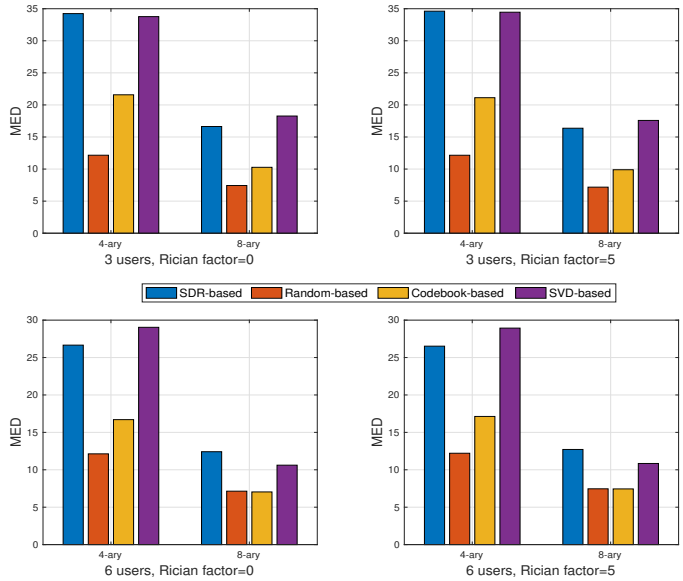

Figure 7.3: MED comparisons among different constellation generating schemes under digital 1-bit.

Multi-casting via various schemes: We take the digital 1-bit as an example to compare the MED achieved via various constellation generation methods. Aside from the proposed two basis iterative approaches, another two heuristic methods are added to the comparison. Specifically, the first one relies on arbitrarily generating valid codewords, and the second one applies exhaustive search over the Hardmard codebook to maximize MED [31]. Multiple configurations are tested by varying the number of paths, the number of users, and the Rician factors.

Fig. 7.3 shows that the MED obtained via the proposed schemes remains at least 50% higher than the other two options in all tested configurations. Such remarkable superiority implies that in spite of severe restrictions imposed by the 1-bit hardware, a careful design still matters because the massive antennas leave us a high degree of freedom in codeword selection generation. As for the proposed two methods, we notice that their performances are pretty similar, especially in the low-order case. Another interesting observation is that all schemes' effectiveness is insensitive to the Rician factor, implying that a single beam can accommodate more than one user due to its coarse resolution. Nevertheless, with more users getting in, all schemes incur a dramatic decline in MED due to the inherent nature of multi-casting.

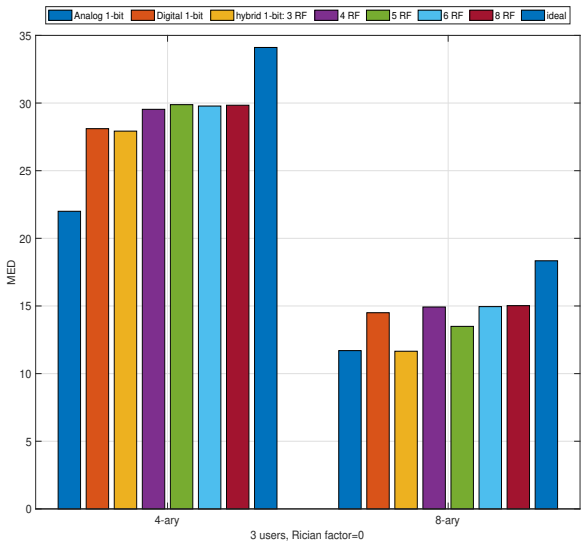

Figure 7.4: spectrum efficiency and energy efficiency comparisons among different 1-bit structures.

Multi-casting via various structures: Fig. 7.4 compares the achievable rate and the energy efficiency for three 1-bit structures. The hybrid type proves to be the most powerful in supporting high-order constellations, while the analog type tends to be the weakest. The rate merit of the hybrid structure over the other two becomes more comprehensive as increasing the number of RF chains for the former. However, the accompanying downside for the hybrid setup is a rapid reduction in energy efficiency due to the use of massive APS components. Still within this structure, we calculated that setting $N_r = 6$ will maximize the energy efficiency based on corollary 1, which is consistent with the simulation result.

Fig. 7.5 illustrates that the MED achieved in the hybrid setup is nearly 25% higher than that in the analog structure for both $M = 4$ and $M = 8$, regardless of how many RF chains are used. Nevertheless, only when the number of RF chains becomes moderately large will the hybrid structure outperform the digital counterpart, and the advantage in MED is also minimal (around 5%) and will soon be saturated. Interestingly, the hybrid setup gets a lower MED when it has an odd number of RF chains because the oddness will corrupt the codewords' symmetry, leading to the MED decrease. Compared with an ideally transparent system, the achieved MED values in digital and hybrid setups are 15% shorter. The result is rather promising if considering the

ultra-simplified expenditure in 1-bit systems. According to Fig. 7.4 and Fig. 7.5, we conclude that either the hybrid setup with very few RF chains or the digital setup can be a suitable option to serve mmWave internet-of-things (IoT) applications for their overall balanced efficacy.

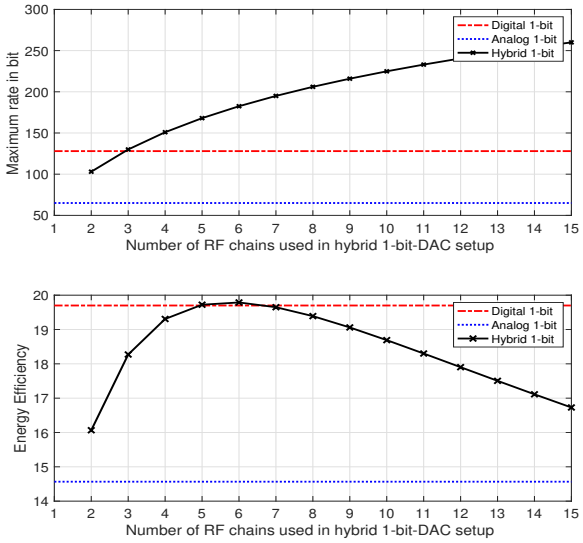

Figure 7.5: MED comparisons among different 1-bit structures using SDR-based method.

Error performance of multi-casting: This part will present the bit error rate (BER) results for $M = 4$ and $M = 8$. All the curves are the average of 3000 independent channel realizations, each with a length-100 sequence. The penalty parameters used in LASSO, corresponding to λ and μ in (7.27) used, are set as 10000 and 100, respectively. It is worth mentioning that extensive tests show that BER performance is insensitive to these two values, so we are free of cumbersome parameter tuning. The BER result using an 8-ary constellation strikingly differs from the above. From Fig. 7.6, it is evident that the LMMSE detector exhibits a huge performance gap to the LASSO one. The underlying reason is that the rank-deficient signal model, on the one hand, aggravates the ambiguity in LMMSE equalization. Still, on the other hand, it helps promote a sparse output via the LASSO-based approach. Unlike the 4-ary case, iterative cancellation here will tremendously benefit detection, as the post round will bring in a 3dB gain. Such a notable improvement relies on the fact that more estimated symbols reside around the

threshold; hence slightly alleviating the inter-symbol interference level will remarkably boost the next-round detection. To eliminate the trend of error floor occurring at high SNR, one can augment the iterations of project gradient descent add more rounds of interference cancellation.

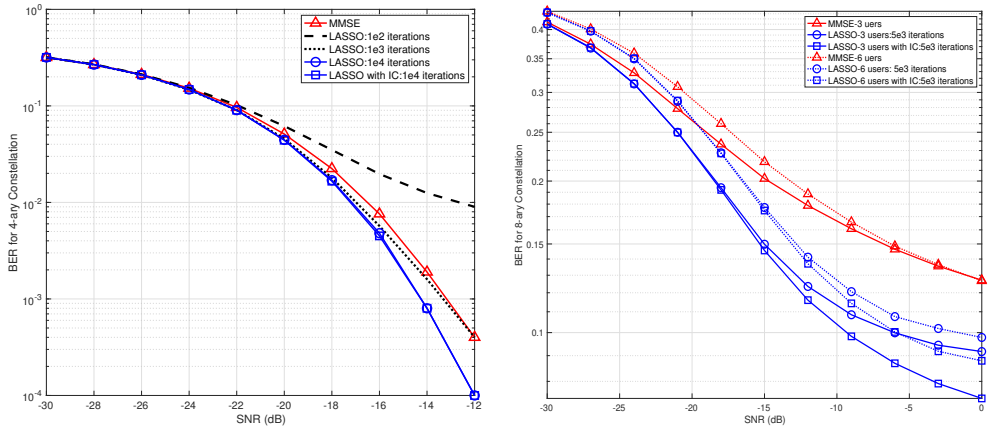

(a) (b)

Figure 7.6: BER comparisons between LMMSE- and LASSO-based methods under digital 1-bit with 3 users(a) 4-ary constellation ; and (b) 8-ary constellation.

7.6 Conclusions

This chapter customized a new multi-casting scheme for 1-bit mmWave systems. The overarching idea is to shift the paradigm from scalar-based modulation to vector-based modulation. Specifically, we first derived theoretical rate fundamentals for different 1-bit configurations. Then, we identified the optimal pattern for low-order constellations and arrived at an iterative scheme to generate high-order constellations. Effective detection solutions were finally individually proposed for low-order and high-order modulations per their constellation structures. The entire design manifests high efficacy under various configurations and promises to reinforce the applicability of 1-bit mmWave IoT.

Chapter 8

Summary and Future Directions

The growing interest earned from and hefty effort made by regulatory, industrial, and academic sectors has transformed mmWave cellular communication systems from a concept to reality. Despite already being deployed in the 5G era, mmWave only take up a small proportion among all cellular infrastructure. Meanwhile, many designs at the nascent 5G stage draw from the sub-6GHz family without being tamed and refined per the mmWave features. As 5G continues to evolve, it is envisioned that future generations will exploit more mmWave frequency bands to support data-intensive applications, including dynamic vehicular communications. To fully unleash the vast potential of mmWave and achieve economic 5G & Beyond networks with low carbon emission, additional venues have to be pursued for mmWave research and development. To this end, the present thesis investigated a few critical aspects of mmWave systems with reduced complexity structure, emphasizing the physical layer and aspiring to harness more with less.

8.1 Summary of Contributions

We first focused on the popular hybrid structures with limited complexity RF chains. Recall that the achievable multiplexing gain generally cannot exceed the number of RF chains. This shortcoming will seriously confine the ultimate spectrum efficiency, particularly in the uplink

transmission. This prompted us to introduce index modulation in order to heighten the multiplexing gain. Its applied domain was carefully constructed as a high-quality (sub-)beamspace. As such, the multiplexing gain of GBM promises to break the limit of RF chains and up to the rank of spatial channels.

With the help of OFDM, we can apply spatial modulation per subcarrier when communicating over frequency-selective channels. However, this does not carry over to GBM because the hybrid structure couples processing across subcarriers. This prompted us to devise an OFDM symbol-based modulating scheme . The time-domain samples in the resulting WGBM obey a regular sparse pattern, which allows transmission via fewer RF chains. Relying on the analog-dictated WGBM, we complemented a near-optimal diagonal digital precoding matrix based on the APEP-minimizing criterion to boost the coding gain. As for the receiver, we demonstrated that a simple first-order Doppler compensator suffices to combat time variation in mmWave mMIMO. Owing to these prominent merits, the proposed (P-)WGBM holds great potential for uplink transmission in vehicular-related scenarios.

The transceiver designs require CSI, which led us to develop our so-called DSDS channel estimator for hybrid structures. On the one hand, the proposed channel estimator exploited the well-known beamspace sparsity by transforming the original channel estimation into a compressed-sensing problem. On the other hand, the delay-domain sparsity was used to help exclude a majority of channel taps, and thus simplify processing. The key to enabling double-sparsity exploitation is a well-customized training pattern. After identifying the effective taps and associated dominant beams, we applied beam steering to capture the amplitudes and Doppler shifts. The entire process requires lightweight storage and computation burden, and has been tested to be effective in combating the double (*time-frequency*) selectivity.

Moving on to the wideband multi-user setup, we designed an overall improved transceiver that can maximize the end-to-end mutual information. This endows the adopted HBD framework with a well defined sense of optimality, in sharp contrast to available ad hoc designs that rely either on the extension from narrowband multi-user transceivers or the compromise of wideband single-user transceivers. Instead, we directly tackled the general wideband multi-user

problem by optimizing the explicit mutual information lower bound. Interestingly, the derived lower bound strictly equals the upper bound in the limit, indicating that the proposed transceiver guarantees the asymptotic optimality.

Transitioning from hybrid to one-bit structures, we commenced by studying a detection problem for the uplink access. A so-called Me-LeaD detector was developed, and offers three prominent advantages: i) It outperforms the conventional linearization method because it bypasses inaccuracies arising from modeling the non-linear quantization noise; ii) It gains over the pure learning-based method because the serial detector needs considerably fewer training templates, thus significantly easing the classification; and iii) It offers high-performance dimension reduction thanks to importing the model information into the classifier, ensuring low computation complexity in online implementation.

Swapping from uplink to downlink, we proceeded with the 1-bit system and investigated the multi-casting setup to underpin network configuration and content sharing. Our initial study shows that the original constellation design problem can be formulated as a large-scale NP-hard optimization problem given the modulation order and the specific criterion. However, the immediate treatment is mathematically intractable, which motivates looking for a sub-optimal solution. We established that the optimal pattern for a low-order constellation is PSK-like. Leveraging this fundamental conclusion, we successfully converted high-order generation into a series of homogeneous yet low-complexity optimization problems. Detectors were customized for both low- and high-order constellations by considering the underlying signal structure. On top of that, we also derived the theoretical bounds regarding the achievable rate and energy efficiency for various types of 1-bit architectures.

8.2 Future Directions

The research thrusts outlined in the last section only cover a tiny tip of the entire map of mmWave communications. Nevertheless, a number of open problems await deeper exploration even within this small field. In the following, we will broadly discuss a few promising directions

in anticipation of stimulating a growing emphasis invested in this exciting field.

Multi-mode cellular communications: Despite diving into the multi-user setup, our current research still focuses on a single-cell scenario. In practical cellular, one must deal with both in-cell and out-cell interference [120]. Due to mmWave's directional nature and sensitivity to blockage, it is critical to optimize the beamforming vector in order to improve the signal-to-interference ratio, especially for edge users. In addition, spatial multiplexing has to be adapted to accommodate various transmission modalities, including broadcasting, uni-casting, as well as multi-casting.

Sub-6GHz assisted downlink transmission: Although mmWave cells are expected to be densely deployed, in the long term they will co-exist with the current sub-6GHz cellulars. The uplink transmission will frequently count on the latter to deliver low-volume but critical data traffic. Parsing uplink signals, especially the pilots, is expected to benefit the downlink mmWave transmission because the two spectrum bands share a similar spatial environment [121]. This prompts one to rely on the unveiled frequency-insensitive factors in order to identify the likely line-of-sight channel. In this manner, the downlink is free of cumbersome training and can project the beam instantly.

Two-dimensional mmWave index modulation: The proposed GBM and its derivatives utilize the beamspace domain only. As mmWave systems tend to employ a considerable number of subcarriers, how to take advantage of the subcarrier domain can be of great significance. A preliminary idea here is to implement index modulation across a 2D beamspace-subcarrier grid. By properly setting the group size in line with the subcarrier correlation, those less correlated subcarriers will form a larger group, giving rise to more index combinations [35]. Due to an elevated indexing dimension, the receiver has to develop a low-complexity detector in practice. The approximate message passing algorithm may help in this direction because the higher dimension increases the accuracy in updating the mean and variance via the central limit theorem.

Integrated mmWave radar communication: The mmWave not only brings in more spectrum resources for communication but also paves the way for integrating sensing. The reason

is that, on the one hand, mmWave's wideband band can offer unparalleled sensing resolution. On the other hand, the frequency itself also approaches or overlaps with the frequency radar ssytems operate on. Therefore, integrated sensing and communication at the mmWave band would be a promising research direction. A few scatterers, for example, can be parsed through the sensed results so that mmWave beamforming can select them for multiplexing [122]. On the contrary, intelligent spectrum allocation can be carried out to boost sensing precision by analyzing the density and quality of communication traffic.

1-bit structure in mobility: Although the 1-bit structure is generally perceived as an alternative for fixed access, a certain degree of mobility is still inevitable. The resulting even mild dynamics may minimally impact transparent systems, but can lead to severe detection errors in 1-bit systems. Our preliminary study reveals that a frequency offset results in a periodic pattern after quantization. This renders it possible to recover the underlying frequency offsets through learning the quantized samples over a relatively long period. This way, post compensation can be applied to correct the phase mismatch, thus combating the mobility effects.

References

[1] W. Abbs, F. Gomez-Cuba, and M. Zorzi. Millimeter wave receiver efficiency: A comprehensive comparison of beamforming schemes with low resolution ADCs. *IEEE Trans. Wireless Communications*, 16(12):8131–8146, December 2017.

[2] M. Kraemer, D. Dragomirescu, and R. Plana. Design of a very low-power, low-cost 60 GHz receiver front-end implemented in 65 nm CMOS technology. *International Journal of Microwave and Wireless Technologies*, 3:131–138, April 2011.

[3] C. Chen, Y. Dong, X. Cheng, and L. Yang. Low-resolution PSs based hybrid precoding for multi-user communication systems. *IEEE Trans. Vehicular Tech.*, 67(7):6037–6047, July 2018.

[4] X. Gao, L. Dai, and A. Sayeed. Low RF-complexity technologies to enable millimeter-wave MIMO with large antenna array for 5g wireless communications. *IEEE Communications Magazine*, 56(4):211–217, April 2018.

[5] T. Huang, W. Yang, J. Wu, J. Ma, X. Zhang, and D. Zhang. A survey on green 6g network: Architecture and technologies. 7:175758–175768, December 2019.

[6] F. Guo, F. Yu, H. Zhang, X. Li, H. Ji, and V. Leung. Enabling massive iot toward 6g: A comprehensive survey. *IEEE Internet of Things Journal*, 8(15):11891–11915, August 2021.

[7] X. You *et al*. Towards 6G wireless communication networks: Vision, enabling technologies, and new paradigm shifts. *Science China Information Sciences*, 64:1–77, November 2020.

[8] Z. Pi and F. Khan. An introduction to millimeter-wave mobile broadband systems. *IEEE Communications Magazine*, 49(6):101–107, June 2011.

[9] T. Rappaport *et al*. Overview of millimeter wave communications for fifth-generation (5G) wireless networks–with a focus on propagation models. *IEEE Transactions on Antennas and Propagation*, 65(12):6213–6230, December 2017.

[10] O. El Ayach, S. Rajagopal, S. Abu-Surra, Z. Pi, and R. Heath. Spatially sparse precoding in millimeter wave MIMO systems. *IEEE Trans. Wireless Communications*, 13(3):1499–1513, March 2014.

[11] X. Gao, L. Dai, S. Han, C-L. I, and R. Heath. Energy-efficient hybrid analog and digital precoding for mmwave MIMO systems with large antenna arrays. *IEEE Journal on Selected Areas in Communications*, 34(4):998–1099, April 2016.

[12] J. Mo and R. W. Heath. Capacity analysis of one-bit quantized MIMO systems with transmitter channel state information. *IEEE Trans. Signal Processing*, 63(20):5498–5512, October 2015.

[13] A. Alkhateeb, O. El Ayach, G. Leus, and R. Heath. Channel estimation and hybrid precoding for millimeter wave cellular systems. *IEEE Journal on Selected Topics in Signal Processing*, 8(5):831–846, October 2013.

[14] V. Va, H. Vikalo, and R. Heath. Beam tracking for mobile millimeter wave communication systems. In *Proc. Global Telecommunications Conf.*, Washington, USA, December 2016.

[15] Z. Xiao, T. He, P. Xia, and X-G. Xia. Hierarchical codebook design for beamforming training in millimeter-wave communication. *IEEE Trans. Wireless Communications*, 15(5):3380–3392, May 2016.

[16] C.-X. Wang, J. Bian, J. Sun, W. Zhang, and M. Zhang. A survey of 5G channel measurements and models. *IEEE Communications Surveys & Tutorials*, 20(4):3142–3168, August 2018.

[17] V. Roth. The generalized LASSO. *IEEE Trans. Nerual Network*, 15(1):16–18, January 2004.

[18] Y. Bian, X. Cheng, M. Wen, H. V. Poor L. Yang, and B. Jiao. Differential spatial modulation. *IEEE Trans. Vehicular Tech.*, 64(7):3262–3268, July 2015.

[19] M. Di Renzo, H. Haas, A. Ghrayeb, S. Sugiura, and L. Hanzo. Spatial modulation for generalized MIMO: challenges, opportunities and implementation. *Proc. the IEEE*, 102(1):56–103, January 2014.

[20] P. Yang, M. Di Renzo, Y. Xiao, S. Li, and L. Hanzo. Design guidelines for spatial modulation. *IEEE Communications Surveys & Tutorials*, 17(1):6–26, June 2015.

[21] M. Zhang, M. Wen, X. Cheng, and L. Yang. Pre-coding aided differential spatial modulation. In *Proc. Global Telecommunications Conf.*, pages 1–6, San Diego, CA, December 2013.

[22] X. Cheng W. Qu, M. Zhang and P. Ju. Generalized spatial modulation with transmit antenna grouping for massive MIMO. *IEEE ACCESS*, 5:26798–26807, 2017.

[23] R. Mesleh, H. Haas, S. Sinanovic, C. W. Ahn, and S. Yun. Spatial modulation. *IEEE Trans. Vehicular Tech.*, 57(4):2228–2241, July 2008.

[24] A. Younis, N. Serafimovski, R. Mesleh, and H. Haas. Generalised spatial modulation. In *Proc. Asilomar Conf. on Signals, Systems, and Computers*, pages 1498–1502, Pacific Grove, CA, November 2010.

[25] X. Gao, L. Dai, S. Han, C-L. I, and X. Wang. Reliable beamspace channel estimation for millimeter-wave massive MIMO systems with lens antenna array. *IEEE Trans. Wireless Communications*, 16(9):6010–6021, September 2017.

[26] Y. Dong, C. Chen, and Y. Jin. Joint beamforming with low-resolution PSs for millimetre-wave communications. *Electronics Letters*, 52(18):1541–1543, September 2016.

[27] F. Sohrabi and W. Yu. Hybrid digital and analog beamforming design for large-scale antenna arrays. *IEEE Journal on Selected Topics in Signal Processing*, 10(3):501–513, April 2016.

[28] S. Han, C.-L. I, Z. Xu, and C. Rowell. Large-scale antenna systems with hybrid analog and digital beamforming for millimeter wave 5g. *IEEE Communications Magazine*, 53(1):186–194, January 2015.

[29] J. Brady, N. Behdad, and AM. Sayeed. Beamspace MIMO for millimeter-wave communications: System architecture, modeling, analysis, and measurements. *IEEE Transactions on Antennas and Propagation*, 61(7):3814–3827, July 2013.

[30] L. He, J. Wang, and J. Song. Spatial modulation for more spatial multiplexing: RF-chain-limited generalized spatial modulation aided mm-wave MIMO with hybrid precoding. *IEEE Trans. Wireless Communications*, 66(3):986–998, March 2018.

[31] S. Gao, Y. Dong, C. Chen, and Y. Jin. Hierarchical beam selection in mmwave multiuser MIMO systems with one-bit analog phase shifters. In *Proc. of IEEE International Conference on Wireless Communications and Signal Processing*, Yangzhou, China, October 2016.

[32] A. Alkhateeb, G. Leus, and R. Heath. Limited feedback hybrid precoding for multi-user millimeter wave systems. *IEEE Trans. Wireless Communications*, 14(11):6481–6494, November 2015.

[33] S. Sun and T. S. Rappaport. Millimeter wave MIMO channel estimation based on adaptive compressed sensing. In *Proc. of Workshop on International Conference on Communications (ICC)*, pages 47–53, Paris, France, May 2017.

[34] B. Zheng, X. Wang, M. Wen, and F. Chen. Soft demodulation algorithms for generalized spatial modulation using deterministic sequential Monte Carlo. *IEEE Trans. Wireless Communications*, 16(6):3953–3967, June 2017.

[35] S. Gao, M. Zhang, and X. Cheng. Precoded index modulation for multi-input multi-output OFDM. *IEEE Trans. Wireless Communications*, 17(1):17–28, January 2018.

[36] C. Gustafson, K. Haneda, S. Wyne, and F. Tufvesson. On mm-wave multipath clustering and channel modeling. *IEEE Transactions on Antennas and Propagation*, 62(3):1445–1455, June 2014.

[37] X. Cheng, M. Zhang, M. Wen, and L. Yang. Index modulation for 5G: Striving to do more with less. *IEEE Wireless Communication Magazine*, 25(2):126–132, April 2018.

[38] M. Wen, X. Cheng, and L. Yang. *Index Modulation for 5G Wireless Communications*. Springer, Cham, Switzerland, 2017.

[39] E. Başar, Ü. Aygölü, E. Panayırcı, and H. V. Poor. Orthogonal frequency division multiplexing with index modulation. *IEEE Trans. Signal Processing*, 61(22):5536–5549, November 2013.

[40] Y. Ding, K. J. Kim, T. Koike-Akino, M. Pajovic, P. Wang, and P. Orlik. Spatial scattering modulation for uplink millimeter-wave systems. *IEEE Communications Letters*, 21(7):1493–1496, July 2017.

[41] J. Li, M. Wen, M. Zhang, and X. Cheng. Virtual spatial modulation. *IEEE ACCESS*, 4:6929–6938, November 2016.

[42] T. Do, J. Wang, L. Song, and Y. Kim. Joint relay selection and power allocation for two-way relaying with physical layer network coding. *IEEE Communications Letters*, 17(3):301–304, February 2013.

[43] I. S. Gradshteyn and I. M. Ryzhik. *Table of Integrals, Series, and Products*. Elsevier, San Diego, USA, 2007.

[44] J. Zhang, Y. Huang, J. Wang, and L. Yang. Hybrid analog and digital beamforming for mmwave OFDM large-scale antenna arrays. *IEEE Trans. Vehicular Tech.*, 67(11):11285–11290, November 2018.

[45] F. Sohrabi and W. Yu. Hybrid analog and digital beamforming for mmwave OFDM large-scale antenna arrays. *IEEE Journal on Selected Areas in Communications*, 35(7):1432–1443, July 2017.

[46] W. Shen, X. Bu, X. Gao, C. Xing, and L. Hanzo. Beamspace precoding and beam selection for wideband millimeter-wave MIMO relying on lens antenna arrays. *IEEE Trans. Signal Processing*, 67(24):6301–6313, December 2019.

[47] J. Li, S. Gao, X. Cheng, and L. Yang. Hybrid precoded spatial modulation (hPSM) for mmwave massive MIMO systems over frequency-selective channels. *IEEE Wireless Communication Letters*, 9(6):839–842, February 2020.

[48] S. Gao, X. Cheng, and L. Yang. Estimating doubly-selective channels for hybrid mmwave massive mimo systems: A doubly-sparse approach. *IEEE Trans. Wireless Communications*, 19(9):5703–5715, 2020.

[49] L. Rugini, P. Banelli, and G. Leus. *Wireless Communications Over Rapidly Time-Varying Channels: OFDM Communications over Time-varying Channels*. New York: Academic Press, Cambridge, USA, 2011.

[50] L. Wei, J. Zheng, and Q. Liu. Approximate message passing detector for index modulation with multiple active resources. *IEEE Trans. Vehicular Tech.*, 68(1):972–976, January 2019.

[51] S. Gao, X. Cheng, and L. Yang. Spatial multiplexing with limited RF chains: Generalized beamspace modulation (GBM) for mmwave massive MIMO. *IEEE Journal on Selected Areas in Communications*, 37(9):2029–2039, July 2019.

[52] R. Zhang, L.-L. Yang, and L. Hanzo. Generalized precoding aided spatial modulation. *IEEE Trans. Wireless Communications*, 12(11):5434–5443, November 2013.

[53] S. Guo, H. Zhang, P. Zhang, S. Dang, C. Xu, and M.-S. Alouini. Signal shaping for non-uniform beamspace modulated mmwave hybrid MIMO communications. *IEEE Trans. Wireless Communications*, 19(10):6660–6674, October 2020.

[54] P. Yang, Y. L. Guan, Y. Xiao, M. Di. Renzo, S. Li, and L. Hanzo. Transmit precoded spatial modulation: Maximizing the minimum Euclidean distance versus minimizing the bit error ratio. *IEEE Trans. Wireless Communications*, 15(3):2054–2068, March 2016.

[55] S. Guo, H. Zhang, P. Zhang, P. Zhao, L. Wang, and M.-S. Alouini. Generalized beamspace modulation using multiplexing: A breakthrough in mmwave MIMO. *IEEE Journal on Selected Areas in Communications*, 37(9):2014–2028, July 2019.

[56] K. Venugopal, A. Alkhateeb, N. Gonzalez-Prelcic, and R. Heath. Channel estimation for hybrid architecture-based wideband millimeter wave systems. *IEEE Journal on Selected Areas in Communications*, 35(9):1996–2009, September 2017.

[57] L. Xiao, L. Dan, Y. Zhang, Y. Xiao, P. Yang, and S. Li. A low-complexity detection scheme for generalized spatial modulation aided single carrier systems. *IEEE Communications Letters*, 19(6):1069–1072, June 2015.

[58] S. Gao, X. Cheng, and L. Yang. Mutual information maximizing wideband multi-user (wMU) mmwave massive MIMO. *IEEE Trans. Communications*, 69(5):3067–3078, May 2021.

[59] E. G. Larsson, O. Edfors, F. Tufvesson, and T. L. Marzetta. Massive MIMO for next generation wireless systems. *IEEE Communications Magazine*, 52(2):186–195, February 2014.

[60] J. A. Tropp and A. C. Gilbert. Signal recovery from random measurements via orthogonal matching pursuit. *IEEE Trans. Information Theory*, 53(12):4655–4666, December 2007.

[61] Q. Qin, L. Gui, P. Cheng, and B. Gong. Time-varying channel estimation for millimeter wave multiuser MIMO systems. *IEEE Trans. Vehicular Tech.*, 67(10):9435–9448, October 2018.

[62] Z. Gao, C. Hu, L. Dai, and Z. Wang. Channel estimation for millimeterwave massive mimo with hybrid precoding over frequency-selective fading channels. *IEEE Communications Letters*, 20(6):1259–1262, June 2016.

[63] J. Fernandez, N. Prelcic, K. Venugopal, , and R. Heath. Frequency-domain compressive channel estimation for frequency-selective hybrid mmwave MIMO system. *IEEE Trans. Wireless Communications*, 17(5):2946–2960, May 2018.

[64] B. Wang, F. Gao, S. Jin, H. Lin, and G. Y. Li. Spatial- and frequency wideband effects in millimeter-wave massive MIMO systems. *IEEE Trans. Signal Processing*, 66(13):3393–3406, June 2018.

[65] C. Carbonelli, S. Vedantam, and U. Mitra. Sparse channel estimation with zero tap detection. *IEEE Trans. Wireless Communications*, 6(5):1743–1753, May 2007.

[66] A. Alkhateeb and R. Heath. Frequency selective hybrid precoding for limited feedback millimeter wave systems. *IEEE Trans. Communications*, 64(5):1801–1818, May 2016.

[67] S. Buzzi and C. D. Andrea. *On clustered statistical MIMO millimeter wave channel simulation*, May 2016.

[68] X. Ma, L. Yang, and G. B. Giannakis. Optimal training for MIMO frequency-selective fading channels. *IEEE Trans. Wireless Communications*, 4(2):453–466, March 2005.

[69] X. He, R. Song, and W. P. Zhu. Pilot allocation for distributed compressed sensing based sparse channel estimation in MIMO OFDM systems. *IEEE Trans. Vehicular Tech.*, 65(5):2990–3004, May 2016.

[70] L. Liu, E. Larsson, W. Yu, P. Popovski, C. Stefanovic, and E. Carvalho. Sparse signal processing for grant-free massive connectivity: A future paradigm for random access protocols in the internet of things. *IEEE Signal Processing Magazine*, 35(5):88–99, September 2018.

[71] Z. Zhang and B. D. Rao. Extension of SBL algorithms for the recovery of block sparse signals with intra-block correlation. *IEEE Trans. Signal Processing*, 61(8):2009–2015, April 2013.

[72] Z.-Q. He, X. Yuan, and L. Chen. Super-resolution channel estimation for massive MIMO via clustered sparse bayesian learning. *IEEE Trans. Vehicular Tech.*, 68(6):6156–6160, June 2019.

[73] J. Ziniel and P. Schniter. Dynamic compressive sensing of time-varying signals via approximate message passing. *IEEE Trans. Signal Processing*, 61(21):5270–5284, June 2013.

[74] L. Chen, A. Liu, and X. Yuan. Structured turbo compressed sensing for massive MIMO channel estimation using a Markov prior. *IEEE Trans. Vehicular Tech.*, 67(5):4635–4639, May 2018.

[75] A. Liu, V. K. N. Lau, and W. Dai. Exploiting burst-sparsity in massive MIMO with partial channel support information. *IEEE Trans. Wireless Communications*, 15(11):7820–7830, November 2016.

[76] A. B. Awoseyila, C. Kasparis, and B. G. Evans. Improved single frequency estimation with wide acquisition range. *Electronics Letters*, 44(3):245–247, January 2008.

[77] T. Zemen and C. F. Mecklenbrauker. Time-variant channel estimation using discrete prolate spheroidal sequences. *IEEE Trans. Signal Processing*, 53(9):3597–3607, June 2005.

[78] J. Wang, S. Kwon, and B. Shim. Generalized orthogonal matching pursuit. *IEEE Trans. Signal Processing*, 60(12):6202–6216, December 2012.

[79] M. A. Davenport and M. B. Wakin. Analysis of orthogonal matching pursuit using the restricted isometry property. *IEEE Trans. Information Theory*, 56(9):4395–4401, September 2010.

[80] Y. Dong, C. Chen, N. Yi, S. Gao, and Y. Jin. Low-complexity hybrid precoding design for MIMO-OFDM millimeter wave communications. *IEICE Transactions on Communications*, 100(8):1228–1237, August 2017.

[81] Q. H. Spencer, A. L. Swindlehurst, and M. Haardt. Zero-forcing methods for downlink spatial multiplexing in multiuser MIMO channels. *IEEE Trans. Signal Processing*, 52(2):461–471, February 2004.

[82] L. Liang, W. Xu, and X. Dong. Low-complexity hybrid precoding in massive multiuser MIMO systems. *IEEE Wireless Communication Letters*, 35(5):653–656, December 2014.

[83] D. H. N. Nguyen, L. Le, T. Le-Ngoc, and R. Heath. Hybrid MMSE precoding and combining designs for mmwave multiuser systems. *IEEE ACCESS*, 5:19167–19181, November 2017.

[84] Z. Wang, M. Li, Q. Liu, and A. L. Swindlehurst. Hybrid precoder and combiner design with low-resolution phase shifters in mmwave MIMO systems. *IEEE Journal on Selected Topics in Signal Processing*, 12(2):256–269, May 2018.

[85] A. Sayeed and J. Brady. Beamspace MIMO for high-dimensional multiuser communication at millimeter-wave frequencies. In *Proc. Global Telecommunications Conf.*, pages 3679–3684, Atlanta, GA, December 2013.

[86] W. Ni and X. Dong. Hybrid block diagonalization for massive multiuser MIMO systems. *IEEE Trans. Communications*, 64(1):201–211, January 2016.

[87] R. Rajashekar and L. Hanzo. Iterative matrix decomposition aided block diagonalization for mm-wave multiuser MIMO systems. *IEEE Trans. Wireless Communications*, 16(3):1372–1384, March 2017.

[88] Q. Zhang, Y. Liu, G. Xie, J. Gao, and K. Liu. An efficient hybrid diagonalization for multiuser mmwave massive MIMO systems. In *Proc. of Global Symposium on Millimeter Waves (GSMM)*, Boulder, CO, USA, May 22-24, 2018.

[89] H. Yuan, J. An, N. Yang, K. Yang, and T. Duong. Low complexity hybrid precoding for multiuser millimeter wave systems over frequency selective channel. *IEEE Trans. Vehicular Tech.*, 68(1):983–987, January 2019.

[90] B. Liu and H. Zhu. Rotman lens-based two-tier hybrid beamforming for wideband mmwave MIMO-OFDM system with beam squint. *EURASIP J. Wireless Commun. Netw*, 267:1–13, 2018.

[91] 3GPP. *TR38.900 Study on channel model for frequency spectrum above 6 GHz*, July 2017.

[92] J. Singh, O. Dabeer, and U. Madhow. On the limits of communication with low-precision analog-to-digital conversion at the receiver. *IEEE Trans. Communications*, 57(12):3629–3639, December 2009.

[93] R. H. Walden. Analog-to-digital converter survey and analysis. *IEEE Journal on Selected Areas in Communications*, 17(4):539–550, April 1999.

[94] J. Mo, P. Schniter, and R. W. Heath. Channel estimation in broadband millimeter wave MIMO systems with few-bit ADCs. *IEEE Trans. Signal Processing*, 66(5):1141–1164, March 2018.

[95] J. Zhang, L. Dai, X. Li, Y. Liu, and L. Hanzo. On low-resolution ADCs in practical 5g millimeter-wave massive MIMO systems. *IEEE Communications Magazine*, 56(7):205–211, July 2018.

[96] C. Wen, C. Wang, S. Jin, K. Wong, and P. Ting. Bayes-optimal joint channel-and-data estimation for massive MIMO with low-precision ADCs. *IEEE Trans. Signal Processing*, 64(10):2541–2556, May 2016.

[97] J. Choi, J. Mo, and R. Heath. Near maximum-likelihood detector and channel estimator for uplink multiuser massive MIMO systems with one-bit ADCs. *IEEE Trans. Communications*, 64(5):2005–2018, June 2016.

[98] Y. Jeon, N. Lee, S. Hong, and R. Heath. One-bit sphere decoding for MIMO systems with one-bit ADCs. *IEEE Trans. Wireless Communications*, 17(7):4509–4521, July 2018.

[99] Y. Jeon, H. Do, S. Hong, and N. Lee. Soft-output detection methods for sparse millimeter wave MIMO systems with low-precision ADCs. *IEEE Trans. Communications*, 67(4):2822–2836, April 2019.

[100] C. Mollén, J. Choi, E.G. Larsson, and R. W. Heath. Uplink performance of wideband massive MIMO with one-bit ADCs. *IEEE Trans. Wireless Communications*, 16(1):87–100, January 2017.

[101] Y. Jeon, S. Hong, and N. Lee. Supervised-Learning-Aided communication framework for MIMO systems with low-resolution ADCs. *IEEE Trans. Vehicular Tech.*, 67(8):7299–7313, August 2018.

[102] D. Kim, S. Hong, and N. Lee. Supervised-learning for multi-hop MU-MIMO communications with one-bit transceivers. *IEEE Journal on Selected Areas in Communications*, 37(11):2559–2572, November 2019.

[103] Y. Jeon, N. Lee, and H. V. Poor. Robust data detection for MIMO systems with one-bit ADCs: A reinforcement learning approach. *[Online]: https://arxiv.org/pdf/1903.12546.pdf*, March 2019.

[104] L. Nguyen, D. Ngo, N. Tran, A. Swindlehurst, and D. Nguyen. Supervised and semi-supervised learning for MIMO blind detection with low-resolution ADCs. *IEEE Trans. Wireless Communications*, 19(4):2427–2442, April 2020.

[105] S. Gao, X. Cheng, and L. Yang. Hybrid multi-user precoding for mmwave massive MIMO in frequency-selective channels. In *Proc. of IEEE Wireless Communications and Networking Conference (WCNC)*, Online, May 26-28, 2020.

[106] T. Cui and C.Tellambura. Superimposed pilot symbols for channel estimation in OFDM systems. In *Proc. Global Telecommunications Conf.*, pages 2229–2233, St. Louis, MO, November 2005.

[107] S. Maeng, Y. Yapici, I. Guvenc, H. Dai, and A. Bhuyan. Hybrid precoding for mmwave massive MIMO with one-bit DAC. *[Online]: https://arxiv.org/pdf/1909.08451.pdf*, 2019.

[108] A. Géron. *Hands-on Machine Learning With Scikit-Learn and TensorFlow: Concepts, Tools, and Techniques to Build Intelligent Systems*. Sebastopol, CA, USA:O'Reilly, 2019.

[109] R. Rifkin. *Multiclass Classification*, February 2018.

[110] N. Sidiropoulos, T. Davidson, and Z. Luo. Semidefinite relaxation based multiuser detection for m-ary psk multiuser systems. *IEEE Trans. Signal Processing*, 54(6):2239–2251, June 2006.

[111] M. Ibrahim, A. Konar, M. Hong, and N. Sidiropoulos. Mirror-prox sca algorithm for multicast beamforming and antenna selection. In *Proc. of IEEE International Workshop on*

Signal Processing Advances in Wireless Communications (SPAWC), Kalamata, Greece, June 2018.

[112] M. Dai and B. Clerckx. Hybrid precoding for physical layer multicasting. *IEEE Communications Letters*, 20(2):1493–1496, November 2015.

[113] L. Abanto-Leon, M. Hollick, and G.Kim. Hybrid precoding for multi-group multicasting in mmwave systems. In *Proc. Global Telecommunications Conf.*, Waikoloa USA, December 2019.

[114] Z. Luo, M. Wen, A. So, Y. Ye, and S. Zhang. Semidefinite relaxation of quadratic optimization problems. *IEEE Signal Processing Magazine*, 27(3):20–34, May 2010.

[115] W. Ma, P. Ching, and Z. Ding. Semidefinite relaxation based multiuser detection for M-ary PSK multiuser systems. *IEEE Trans. Signal Processing*, 52(10):2862–2872, October 2004.

[116] C. E. Chen. An iterative hybrid transceiver design algorithm for millimeter wave MIMO systems. *IEEE Wireless Communication Letters*, 4(3):285–288, June 2015.

[117] A. Scaglione, P. Stoica, S. Barbarossa, G. B. Giannakis, and H. Sampath. Optimal designs for space-time linear precoders and decoders. *IEEE Trans. Signal Processing*, 50(5):1051–1064, May 2002.

[118] Z. Wang and G.B.Giannakis. Wireless multicarrier communications, where fourier meets shannon. 17(3):29–48, May 2000.

[119] A. Elgabli, A. Elghariani, A.O. Al-Abbasi, and M. Bell. Two-stage lasso admm signal detection algorithm for large scale mimo. In *Proc. Asilomar Conf. on Signals, Systems, and Computers*, pages 1–5, Pacific Grove, CA, November 2017.

[120] M. Bashar, K. Cumanan, A. G. Burr, H. Q. Ngo, L. Hanzo, and P. Xiao. On the performance of cell-free massive MIMO relying on adaptive NOMA/OMA mode-switching. *IEEE Trans. Communications*, 68(2):792–810, February 2020.

[121] M. Alrabeiah and A. Alkhateeb. Deep learning for mmwave beam and blockage prediction using sub-6Ghz channels. *IEEE Trans. Communications*, 68(9):5504–5518, September 2020.

[122] Z. Huang and X. Cheng. A general 3D space-time-frequency non-stationary model for 6G channels. *IEEE Trans. Wireless Communications*, 20(1):535–548, January 2021.